

**DEFECT AND THICKNESS INSPECTION SYSTEM FOR CAST
THIN FILMS USING MACHINE VISION AND FULL-FIELD
TRANSMISSION DENSITOMETRY**

A Thesis
Presented to
The Academic Faculty

by

Jay Tillay Johnson

In Partial Fulfillment
of the Requirements for the Degree
Master of Science in Mechanical Engineering in the
School of George W. Woodruff School of Mechanical Engineering

Georgia Institute of Technology
December 2009

**DEFECT AND THICKNESS INSPECTION SYSTEM FOR CAST
THIN FILMS USING MACHINE VISION AND FULL-FIELD
TRANSMISSION DENSITOMETRY**

Approved by:

Dr. Tequila Harris, Advisor
School of Mechanical Engineering
Georgia Institute of Technology

Dr. Levent Degertekin
School of Mechanical Engineering
Georgia Institute of Technology

Dr. Wayne Daley
Principal Research Engineer
Georgia Tech Research Institute

Date Approved: 12 November, 2009

Dedicated to our sustainable future.

ACKNOWLEDGEMENTS

I received a great deal of assistance throughout this project. Firstly, I would like to thank my advisor, Dr. Tequila Harris, for her guidance, positive encouragement, and dedication to my intellectual development. I would also like to thank my reading committee members, Drs. Levant Degertekin and Wayne Daley, for their technical assistance. Dr. Daley provided insight into the vision system, data mining, and neural network structure, and Dr. Degertekin helped brainstorm and investigate thickness profilometry techniques.

The system design and construction would not have been possible without Louis Boulanger, John Graham, Kyle French, and the rest of the machine and electronics shops. They worked with me through various design difficulties regarding the roll-feed system and fabricated many of the components. John Jones and Label Vision Systems graciously provided cameras, lighting, lasers, and other hardware during the conceptualization phase of the project. The preliminary design and construction of the roll-feed system was performed by Mike Gilsdorf, John Nevin, Arthur Toal, and Benjamin Kirk.

I would also like to acknowledge the Design and Manufacturing of Energy Systems laboratory, especially Terry Caston and Kanthi Bhamidipati, whose lighthearted discussions and useful engineering consultations made for a great lab environment. I also must extend my thanks to Nathan Young and Dr. Mervyn Fathianathan, who introduced me to learning algorithms and graduate research, as well as all the students and professors at Georgia Tech who have been wonderfully helpful over the last couple years.

Lastly and most importantly, I am grateful for the love and encouragement from my family and friends. My amazing parents have always listened to my concerns, offered advice, and supported my decisions; and my brother, grandparents, and the rest of the extended family have inspired me to work hard and make a better world. Thank you all.

TABLE OF CONTENTS

ACKNOWLEDGEMENTS	iv
LIST OF TABLES	viii
LIST OF FIGURES	ix
LIST OF SYMBOLS	xv
SUMMARY	xix
Chapter 1 : Introduction	1
1.1 Thin Film Nondestructive Evaluation	1
1.2 Machine Vision Systems for Defect Detection	2
1.3 Profilometry Techniques for Thickness Measurements	4
1.4 Research Motivation and Objectives	5
1.5 Thesis Structure.....	7
Chapter 2 : Background On Inspection Systems and Thin Film Thickness Profilometry.....	8
2.1 Machine Vision Systems for Defect Detection and Classification	9
2.1.1 Plastics Inspection	9
2.1.2 Wood, fabric, and paper inspection	13
2.1.3 Glass Inspection Systems	15
2.2 Thin Film Thickness Determination	16
2.2.1 Optical Thin Film Thickness Profilometry	17
2.2.1.1 Interferometry	20
2.2.1.2 Densitometry	23
2.3 Summary	28
Chapter 3 : Experimental Setup and Roll-Feed System Configuration	29
3.1 Roll-feed Web System and Control.....	31
3.1.1 Load Cell Model and Calibration	34
3.1.2 Brake Model	36
3.1.3 Control Results	38
3.1.4 Web Speed Measurements.....	39
3.2 Tooling System.....	41
3.3 Temperature Control System	43
3.4 Inspection System	45
3.4.1 Thickness Profilometry System.....	45
3.4.1.1 Camera Selection	49
3.4.1.2 Transmission Densitometry Model	51
3.4.1.3 CCD Sensor and Camera Noise	54
3.4.1.4 Optical Distortions from Lensing.....	57
3.4.1.5 Camera and Lens Calibration.....	61
3.4.1.6 Quantification of Densitometry Noise	64

3.4.1.7 Densitometry Calibration	66
3.4.2 Defect Identification System	72
3.4.3 Inspection Control System.....	76
3.5 System Summary	80
Chapter 4 : Fuel Cell Membrane Casting and Inspection	81
4.1 PEMFC Background.....	81
4.2 Motivation for Inspecting Polymer Electrolyte Membranes	82
4.3 Defect Detection in Cast Polymer Membranes	84
4.3.1 Selection of Defects to Identify	84
4.3.2 Image processing	86
4.4 Defect Classification in Cast Polymer Membranes	90
4.4.1 Defect Data Mining	90
4.4.2 Determining the Best Classification Tool.....	97
4.4.3 Neural Network Background.....	99
4.4.4 Neural Network for Defect Classification	101
4.4.5 Network Structure, Training, and Optimization	102
4.5 Summary	106
Chapter 5 : Experimental Results	108
5.1 Defect Identification	108
5.1.1 Batch Material Defects	108
5.1.2 False Alarms and Escapements	111
5.2 Defect Classification	114
5.2.1 Casting Window Analysis	115
5.2.2 Misclassifications	118
5.3 Thickness Profilometry	119
5.3.1 Determining the Membrane Extinction Coefficient	119
5.3.2 Thickness Results	122
5.4 GUI results	127
Chapter 6 : Discussion of Results	131
6.1 Defect Inspection	131
6.2 Casting Window Determination.....	132
6.3 Transmission Densitometry Depth Profilometry.....	133
Chapter 7 : Conclusions, Contribution, and Future Work.....	137
7.1 General Conclusions.....	137
7.2 Contributions to Engineering and Science.....	137
7.3 Future Work	138
7.3.1 Casting System Modifications	139
7.3.2 Inspection Hardware.....	139
7.3.3 Image Processing Refinement	140
7.3.4 GUI modifications	141
7.3.5 Full Automation.....	141
APPENDIX A: LabVIEW Control Program.....	142

APPENDIX B: Web Tension Responses for Different Proportional Controlers....	144
APPENDIX C: Camera Characterization Data for the Photon Transfer Method	146
APPENDIX D: Densitometry Results for Regions of Different Influx	149
APPENDIX E: Parameters for the Neural Network	154
REFERENCES.....	156

LIST OF TABLES

Table 1.1: Features extracted from inspected products with vision systems [12].	4
Table 2.1: Nondestructive thickness measurement techniques, modified from [42]......	17
Table 2.2: Selected Laser and Optical Thickness Profilometry Techniques.	18
Table 3.1: Comparison of camera sensors, adapted from [96].	50
Table 3.2: Sources of radiometric error from CCD arrays (modified from [18])......	55
Table 3.3: The camera objectives for densitometry and defect detection.....	61
Table 3.4: The error results for each of the measurements.....	68
Table 3.5: Error Results for the Densitometry Test.....	71
Table 4.1: Defects present in fuel cell membrane castings.....	85
Table 4.2: Exemplary grayscale, top-hat, and bottom-hat defect regions.	94
Table 4.3: Confusion matrix for the decision table.....	98
Table 4.4: Confusion matrix for the decision tree.	98
Table 4.5: Confusion matrix for the Bayesian network.....	98
Table 4.6: Confusion matrix for a neural network.....	98
Table 4.7: Desirable neural network outputs.	102
Table 4.8: Minimum number of defects for different numbers of hidden layer neurons.	104
Table 4.9: Confusion matrix for a neural network.....	105
Table 5.1: The maximum, minimum, and estimated mode of defect sizes.	108
Table 6.1: Thickness errors for 400 μm measurements of different hypothetical thin films.	134

LIST OF FIGURES

Figure 1.1: Typical industrial vision system [12].	3
Figure 2.1: Wrinkle inspection system [20].	10
Figure 2.2: Defects in a polypropylene cast extrusion manufacturing process [5]. Only the gels and die lines were specifically identified by the Gamage and Xie vision system.	11
Figure 2.3: The optical conceptualization for gel detection [5].	12
Figure 2.4: Comparison of wood veneer defects [35].	14
Figure 2.5: Defects occurring in paper manufacturing: (a) flocculation, (b) macro forming faults, (c) unstable streaks, (d) periodic variations, (e) random variations [40]. ..	15
Figure 2.6: The 2f1 Vision System. (a) Optical principle of the system. (b) The types of image signals indicating no defect, a defect and a dark obstruction [41].	16
Figure 2.7: Laser-VAMFO setup with (a) He-Ne laser, (b) monochromator, (c) xenon lamp, (d) mirror, (e) goniometer, (f) sample, (g) detector [60].	22
Figure 2.8: Shadow moiré pattern of a computer motherboard [64].	23
Figure 2.9: Cross section of a thin film material showing (R) reflection, (A) absorption, (T _d) diffuse transmission, and (T _s) specular transmission.	24
Figure 2.10: Influx and efflux geometry for densitometry measurements [67].	25
Figure 2.11: System configuration for evaluating pecan quality using x-ray densitometry and digital camera [84].	27
Figure 3.1: The roll-feed system with inspection instrumentation.	30
Figure 3.2: The web, tooling, and inspection systems of the roll-feed imaging system... ..	30
Figure 3.3: Physical system with web, heating, and inspection control systems.....	31
Figure 3.4: Roll-feed webbing configuration. The blue arrows indicate the direction of rotation.	32
Figure 3.5: Webbing without tensioning.	33
Figure 3.6: Web tension control loop.	33
Figure 3.7: Calibration Data and Least Squares Linear Fit Line.	35

Figure 3.8: Static analysis of the webbing across the load cell roller.....	36
Figure 3.9: Torque vs current in the Cleveland-Kidder electromagnetic particle brake [92]......	37
Figure 3.10: Web tension vs duty cycle calibration control curves.....	38
Figure 3.11: The drive system. The motor is connected to a belt drive (green) which reduces the angular velocity and increases the torque delivered to the motorized roller (blue). The angular velocity of the motorized roller is then increased as it is passed to the take-up roller (orange).....	40
Figure 3.12: T-shaped slot die. Material enters from the top and is extruded through a very thin rectangular slit at the bottom.	42
Figure 3.13: The casting tank and die setup.	42
Figure 3.14: The heating control panel mounted on the electrical enclosure.	44
Figure 3.15: Insulation on the die and tank viewed from the downstream side.	44
Figure 3.16: Overview of the image station hardware and software.	45
Figure 3.17: Thickness profilometry schematic.....	48
Figure 3.18: The inspection station (a) without and (b) with the blackout fabric.	49
Figure 3.19: Block diagram of the mathematical pixel model from [97].	51
Figure 3.20: The gray value vs thickness for densitometry measurements.	53
Figure 3.21: The signal-to-noise ratio vs. the number of photons for $\eta = 50\%$, $\sigma_{e_dark} = 64$ electrons, $\mu_{e_saturation} = 65,000$ electrons [99]. The image quality improves with light intensity.	56
Figure 3.22: Vignetting on the roll feed imaging system for a large pupil (f/1.4) and a pinhole aperture (f/16). Note that the f-number is larger for smaller pupil diameters.	58
Figure 3.23: The effect of aperture on vignetting, shown by taking a grayscale profile diagonally across the images in Figure 3.22. The image with the larger aperture saturates in the center, whereas the smaller aperture does not.....	58
Figure 3.24: Off-axis lighting causing vignetting in a double-Gauss lens, like those used on the roll-feed system [101]. As the aperture is reduced, the off-axis rays directed to the edge pixels are blocked.	59
Figure 3.25: Geometrical setup with a uniform Lambertian luminaire irradiating the camera sensor through a single lens [99]......	59

Figure 3.26: The histogram of pixels with exposures of (a) 22 ms, (b) 23.5 ms, and (c) 25 ms.....	62
Figure 3.27: Number of saturated pixels for different integration times (gain = 1, f/8)...	62
Figure 3.28: Grayscale vs density for different influxes.....	64
Figure 3.29: Density error from saturated pixels vs number of gray values truncated.....	64
Figure 3.30: The measured density vs true density. The blue line shows perfect matching, so the difference between the red and blue lines represents the mean error.....	68
Figure 3.31: Density error vs measured density with a linear fit used for calibration.....	69
Figure 3.32: Corrected densitometer measurement locations.....	70
Figure 3.33: Comparisons of the measurements using the direct method (left) and the calibrated densitometer (right).....	71
Figure 3.34: Error in the calibrated densitometer.	71
Figure 3.35: Ten density measurements for 1 to 10 PET sheets in 4 locations (left) and their average (right).....	72
Figure 3.36: Low angle laser concept with (a) the laser path for good material, and (b) the camera mounting system.....	73
Figure 3.37: Imaging the die directly to measure the menisci. (a) The system configuration, and (b) the resulting image.....	74
Figure 3.38: Transmission laser with projection screen. (a) The system configuration, and (b) the imaged result when the laser hit bubble defects.....	75
Figure 3.39: The reflected planar laser method, with (a) the setup and (b) the image of the laser striking a bubble defect.	75
Figure 3.40: The backlight system without the opal diffuser. (a) The system in operation, (b) the backlight and support structure, (c) the full system without cast material, and (d) the system in operation from another angle.	76
Figure 3.41: Screen shot of the graphical user interface with a non-cast sample of analogous material.	77
Figure 3.42: GUI real-time processing flow chart.....	79
Figure 4.1: Fuel cell assembly with (1) Bipolar plates, (2) Gaskets, (3) Electrodes, (4) Catalysts, (5) Polymer Electrolyte Membrane [112].	82

Figure 4.2: Defects occurring far from the casting window at low pressures or high web speeds.....	86
Figure 4.3: The steps in the top-hat operation. The original image is morphologically opened to generate a background mask (upper right) which is then subtracted from the original (lower left), renormalized (lower middle), and thresholded (lower right). Rice.png image from MATLAB [132]......	88
Figure 4.4: Image processing procedure to convert the original color image to segmented defect regions.....	89
Figure 4.5: Scatter plot of defect data with good inter-class variation. Normalized bottom-hat mean grayscale vs. normalized center point grayscale. Key: blue – hole, red – bubble, green – thinning, cyan - gel.....	92
Figure 4.6: Scatter plot of defect data with poor inter-class variation. Normalized grayscale median vs. normalized top-hat skewness. Key: blue – hole, red – bubble, green – thinning, cyan - gel.....	92
Figure 4.7: Original image, top-hat and bottom-hat histograms of defect types.	94
Figure 4.8: The histogram of the Laplace transform, the image of the region of interest, and the Laplace transform image for the four types of defects.....	95
Figure 4.9: Grayscale profile vectors from the center of the defect region to each of the corners.....	96
Figure 4.10: Profiles from the center of the defect region to the corners sampled 500 times.....	96
Figure 4.11: Model of a neuron and perceptron [138]......	100
Figure 4.12: The neural network classification process.....	102
Figure 4.13: The average percentage of defects misclassified for 2500 NN training runs vs the number of hidden layer sigmoid neurons for the analogous solution. This network contained 18 inputs and 3 outputs because gels were not classified. ...	103
Figure 4.14: Mean squared error of the data sets during each epoch of NN training.....	105
Figure 4.15: Defect processing flow chart with user-input variables.	107
Figure 5.1: Comparison between identifying all the defects and only the defects with a size greater than 10 pixels.....	110
Figure 5.2: Image processing steps when batch material contains bubbles.....	110
Figure 5.3: Improving top-hat results by removing small bubble defects from the image.	111

Figure 5.4: Superficial light defects created by gels in the casting.	112
Figure 5.5: Thinning (on the left) escaping detection.....	112
Figure 5.6: Image of membrane with different bubbles sizes.....	113
Figure 5.7: False dark identifications due to dense periodic thinning.	113
Figure 5.8: Defect identification and classification results.....	114
Figure 5.9: Defect identification and classification results.....	115
Figure 5.10: Images from a vertical slice of the casting window at $V = 1$ mm/s. The pressure and defects are shown for each of the images.	116
Figure 5.11: Fuel cell membrane casting window results (adapted from [127]). The image shows the defect trends for different locations on the tank pressure vs web speed plot.	117
Figure 5.12: Vertical slice through the casting window. Defects per image vs pressure passing through the casting window at ~ 1 mm/s.	118
Figure 5.13: Misclassification of bubbles as gels.	119
Figure 5.14: Complications with density measurements.	120
Figure 5.15: Finding the extinction coefficient for the fuel cell material using a trend line of micrometer and density measurements.....	121
Figure 5.16: True thickness (from the micrometer) vs densitometer thickness.....	121
Figure 5.17: Background noise in the densitometer with the influx values determined with 20 averaged images.....	124
Figure 5.18: The density of the calibration sheet (a) in grayscale, (b) color contour plot, and (c) a topographical representation. The density for sample 10x10 regions in the 0.00 D, 0.06 D, 0.26 D, and 1.46 D areas are indicated.....	125
Figure 5.19: Volumetric flow rate vs pressure determined with the thickness profilometer.	126
Figure 5.20: Results from the defect identification and classification with the GUI.	128
Figure 5.21: Defect tallies, casting window location, and suggested parameter adjustments.	129
Figure 5.22: Casting window locations and recommendations in the GUI.	129
Figure 5.23: The thickness profilometry system.....	130

Figure 6.1: Theoretical density vs thickness profiles for two materials with a density measurement $\pm 1 \sigma$ shown to illustrate how noise is introduced into the measurement. 134

Figure 6.2: Theoretical thickness error at 400 μm vs extinction coefficient for different dark currents..... 135

Figure 6.3: The spectral absorbance of a theoretical material shown with the two wavelengths which minimize error. 136

LIST OF SYMBOLS

A		Absorption fraction
a		Extinction coefficient
$a_{optimal}$		Optimal extinction coefficient
C		Constant
$C_{correction}$	Correction factor for density measurements	
D		Optical density
D		Neural network desired output
$D_{corrected}$		Calibrated density results
$D_{optimal}$	Material density with the minimum densitometric error	
E		Neural network error vector
f		Neural network activation function
F_{LC}		Load cell force
$F_{loadcells}$		Force acting on the load cell roller
$G_{control}$		Web tension controller transfer function
G_{system}	Transfer function from web tension to brake duty cycle	
h		Luminaire to sensor distance
K		Camera gain
K_p		Proportional gain controller
K_T		Load cell to web tension conversion factor
M		Number of averaged images
m		Slope
N		Number of averaged photosites
N_{hidden}		Number of hidden neurons in neural network
N_{inputs}		Number of input neurons in neural network

N_{output}	Number of output neurons in neural network
$N_{weights}$	Total number of weights in neural network
n_p	Number of photons
n_e	Number of photo-induced electrons
n_{e_dark}	Number of dark electrons
$n_{training}$	Number of neural network input-output training sets
P	Tank pressure
p	Flange focal length
PWM	Pulse width modulation (brake duty cycle)
Q	Volumetric flow rate
q	Mount radius
R	Reflection fraction
r	Luminaire radius
$r_{motorized}$	Motorized roller radius
s	Neuron signal
T	Web tension
T_s	Controller settling time
t	Thickness
$T_{desired}$	Web tension setpoint
T_d	Diffuse Transmission
T_{error}	Web tension controller error
T_{input}	Input tension acting on load cell roller
$t_{integration}$	Integration time
t_{mean}	Average thickness of the material
T_{output}	Output tension acting on the load cell roller

T_s	Specular transmission
t_{set}	Neural network training set (input-output pair)
T_t	Transmission fraction
V	Web velocity
V_{LC}	Load cell voltage
w	Optical axis to corner photosite distance
\mathbf{w}	Synaptic neural network weights
w_{imaged}	Width of the imaged web
\mathbf{x}	Neuron input vector
x_i	i^{th} pixel in the image row
y	Neuron output
y_j	j^{th} pixel in the image column
Z	Feature value without normalization
Z'	Normalized feature value
z	Grayscale value (gray level)
$z_{truncated}$	Number of truncated gray values due to saturation
η	Quantum efficiency
Θ_i	Influx cone angle
Θ_e	Efflux cone angle
$\theta_{measured}$	Angle of the optical encoder
λ	Wavelength
μ	Mean
$\mu_{graylevel}$	Mean grayscale value for one pixel
μ_p	Mean photons over the integration time
σ	Standard deviation

σ^2	Variance
σ_g	Photo-response nonuniformity
σ_{offset}^2	Variance of spatial offset noise
Φ	Radiative flux
Φ_e	Efflux
Φ_i	Influx
φ	Half-angle subtended from a luminaire to the sensor
ϕ_{input}	Input angle between webbing and load cell roller
ϕ_{output}	Output angle between webbing and load cell roller
ξ	Neural network learning coefficient

Subscripts

binning	Binning (averaging) of photosites
dark	Associated with dark noise in the camera measurement
e	Electron
efflux	Obtained from an efflux measurement
graylevel	Grayscale value
influx	Obtained from an influx measurement
p	Photon
photo_induced	Generated from incident light
saturated	Value with saturation
saturation	Value at pixel saturation point
spatial	Location-centric sensor feature (measured between pixels)
temporal	Time-centric sensor feature (measured for a single pixel)
unsaturated	Value without saturation

SUMMARY

Quick mass production of homogeneous thin film material is required in paper, plastic, fabric, and thin film industries. Due to the high feed rates and small thicknesses, machine vision and other nondestructive evaluation techniques are used to ensure consistent, defect-free material by continuously assessing post-production quality. One of the fastest growing inspection areas is for 0.5-500 micrometer thick thin films, which are used for semiconductor wafers, amorphous photovoltaics, optical films, plastics, and organic and inorganic membranes.

As a demonstration application, a prototype roll-feed imaging system has been designed to inspect high-temperature polymer electrolyte membrane (PEM), used for fuel cells, after being die cast onto a moving transparent substrate. The inspection system continuously detects thin film defects and classifies them with a neural network into categories of holes, bubbles, thinning, and gels, with a 1.2% false alarm rate, 7.1% escape rate, and classification accuracy of 96.1%. In slot die casting processes, defect types are indicative of a misbalance in the mass flow rate and web speed; so, based on the classified defects, the inspection system informs the operator of corrective adjustments to these manufacturing parameters.

Thickness uniformity is also critical to membrane functionality, so a real-time, full-field transmission densitometer has been created to measure the bi-directional thickness profile of the semi-transparent PEM between 25-400 micrometers. The local thickness of the 75 mm x 100 mm imaged area is determined by converting the optical density of the sample to thickness with the Beer-Lambert law. The PEM extinction coefficient is determined to be 1.4 D/mm and the average thickness error is found to be 4.7%. Finally, the defect inspection and thickness profilometry systems are compiled into a specially-designed graphical user interface for intuitive real-time operation and visualization.

CHAPTER 1: INTRODUCTION

1.1 Thin Film Nondestructive Evaluation

Automated inspection systems and nondestructive evaluation (NDE) have become ubiquitous in manufacturing systems because the technology is an inexpensive and reliable method to measure product requirements. NDE robustly and autonomously identifies defects or other flaws in components or assemblies in real-time, so manufacturing companies can increase production rates while minimizing costs associated with scrap components and paid labor from human inspectors. As automated inspection technologies have matured and more engineers have become aware of their capabilities, current manufacturing lines are not only designed for cost and quality, but also designed for inspection (DFI). DFI-incorporated manufacturing systems typically use some form of machine vision along with software analysis to ensure the resulting output is functional, maintained within tolerance, and/or defect-free.

In the last two decades the thin film market has rapidly expanded and diversified. This has led to a wide range of industries now requiring highly accurate and consistent manufacturing of thin film materials, such as semiconductor wafers [1, 2], photovoltaics and photoconductors [3], plastics [4, 5], graphic arts papers and films [6], optical films [7], and various organic and inorganic membranes [8, 9]. Additionally sol-gel coatings on polymer films are gaining scientific interest because they can be used in photography, radiography, holography, reprography (for printers, photocopiers, etc.), optical coatings (e.g., colored, anti-reflectant, electro-optic polymers, photo-anodes) and protective coatings (e.g., adherent, corrosion resistant) [6, 10]. To mass produce these thin film products, there exist a number of technologies such as doctor blade extrusion, film applicator blade, melt compression, stencil printing, and slot die extrusion [11], however in all these techniques it is necessary to ensure the quality of the final product.

Increasingly thin film industries are turning to non-destructive evaluation techniques to give manufacturers confidence in the quality of the final product. In [5], Gamage and Xie note the shortcomings of the long-held conventional approach of statistical sampling and human inspection for polymer casting inspection tools; the

bottom line revealed that statistical sampling resulted in 14.8% or \$550,000/year in total production scrapped and 2% or \$88,000/year lost due to customer returns, which also hurt the image of the company. These losses were incurred solely from the statistical sampling method the company employed: inspectors used a light table to examine a sample from the end of each polymer roll. Gamage and Xie pointed out that this sample represented as little as 0.01% of the total product and was often not inspected for some time after production. As a result, the cast material occasionally contained defects which did not appear in the statistical sample; or if the sample did contain defects, there was a delayed response before identification—costing the company money in wasted material and reduced efficiency.

In human inspection, one or more inspectors are stationed along the manufacturing line to flag catastrophic defects. Especially in high speed manufacturing applications, human inspectors are prone to error—missing defects and/or sighting false defects. Additionally, human inspectors have difficulty with fatigue, inconsistency between inspectors, and turnover and training [5]. Labor costs have also made continuous human inspection unattractive from the managerial point of view. Furthermore, inspectors often physically place a flag on the fast-moving web, which may result in injuries. Therefore, by creating an automated inspection system,

1. costs from labor and materials are decreased,
2. the quantity of waste material and wasted production time are reduced,
3. the overall quality of the product is maintained and/or assessed, reducing the number of customer returns,
4. and, the safety of the staff is improved.

The benefits from automated web inspection systems have led to widespread implementation in textile, plastics, foils, and other thin film lines.

1.2 Machine Vision Systems for Defect Detection

Traditionally, trained experts performed the highly tedious and often dangerous task of inspecting resulting parts from a manufacturing process. However, in some environments such as underwater inspection, nuclear and chemical industries, and high temperature applications, it is unsafe and impractical to employ inspection experts.

These challenges lead to the advancement of machine vision, which is an inexpensive nondestructive evaluation technique. Although machine vision systems vary depending on the application, environment, and objectives, the typical setup includes a computer capturing images from one or more cameras mounted above or around the illuminated area of interest, as shown in Figure 1.1. In general, digital images are captured to identify, locate, inspect, count, measure, or otherwise analyze physical objects in order to determine shape, color, or spatial relationships. Features are extracted and analyzed with image processing by applying mathematical or logical operations on the digital data in order to reduce noise, adjust for lens distortion, remove unwanted reflections, lighten, darken, threshold, or otherwise alter the image to make feature detection simpler. Often time-constrained or computationally intensive operations are processed with in-camera digital signal processors (DSPs), application specific integrated circuits (ASICs), or field programmable gate arrays (FPGAs) [12]. Image analysis then manipulates the processed image to produce a much smaller data set of binary or numerical feature variables, such as those in Table 1, which indicate the quality of the product. This computation is done by employing qualitative, heuristic, statistical, model-based, or other computational tools like neural networks or fuzzy logic. The choice of the tool is based on the application and selected to improve the quality of the final data by reducing escape rates (defects that go undetected) and false alarms (acceptable quality which is flagged as a defect).

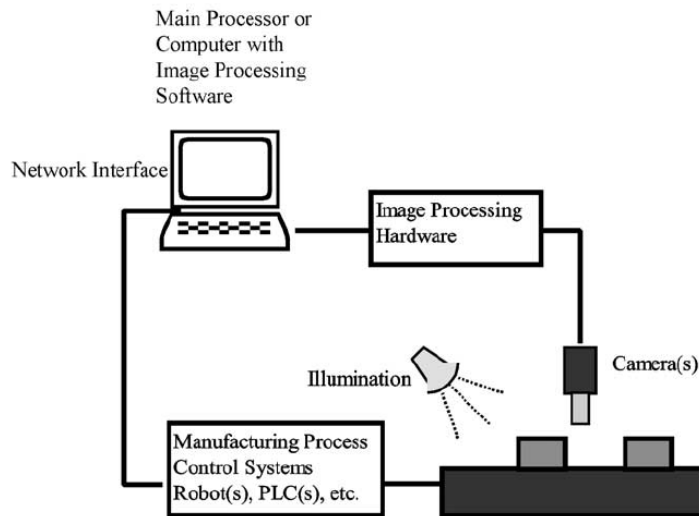


Figure 1.1: Typical industrial vision system [12].

Table 1.1: Features extracted from inspected products with vision systems [12].

Dimensional	Dimensions, shape, positioning, orientation, alignment, roundness, corners
Structural	Assembly (Holes, slots, rivets, screws, clamps), foreign objects (dust, bur, swarm)
Surface	Pits, scratches, cracks, wear, finish, roughness, texture, seams-folds-laps, continuity
Operational	Incompatibility of operation to standards and specifications

Although available for industrial inspection systems since the early 1970s, machine vision has not been universally adopted in manufacturing systems because each application requires unique illumination and heuristic approaches to image processing and analysis [13-15]. Without general-purpose tools, engineers have been forced to create custom machine vision solutions for each inspection problem, which along with the required computing power and cost, kept machine vision usage from becoming more widespread. However, with the help of computer advancements and the need to quickly and inexpensively produce more accurate parts, vision systems have been growing in use, particularly for industries with high manufacturing or processing rates. Currently machine vision inspection is applied to a wide range of manufacturing systems including electronics manufacturing, textile production, metal machining, glass manufacturing, machine parts, printing products, food quality, integrated circuits assembly, and many other fabrication processes [13]. For these reasons, vision systems have become ubiquitous in manufacturing systems with large batch production, high quality manufacturing, or fabrication in specialized environments because of their ability to provide low cost reliable solutions to quality control problems of metrology and defect identification.

1.3 Profilometry Techniques for Thickness Measurements

In cases requiring specific physical characteristics for product functionality, nondestructive testing (NDT) tools are commonly incorporated into the manufacturing process. Many NDT techniques are capable of determining thin film topography, thickness, surface characterization, chemical composition, multilayered structures, dimensional variations, damage, or defects. Since thin film thicknesses on the order of 0.5-500 μm are now being mass produced in numerous niche markets, NDT tools for these materials are employed for a range of measurements. As Power recapitulates, NDT of thin film is capable of identifying a variety of defect such as, “processes of corrosion

and weathering, the segregation of phases in films composed of polymer blends, near surface oxidation processes induced optically or by thermal contact, the out-diffusion of additives such as stabilizers, plasticizers and/or lubricants, processes of thermal or photodegradation, changes in crystallinity or morphology..., and, also processes affecting adhesion between surfaces” [16]. In many cases, thin film failure can be predicted or detected by measuring the material thickness, especially when tolerance across and through the thickness are not maintained. Regardless of possible mechanisms causing the thickness variation—either during manufacturing or operation—monitoring thickness provides assurance that the thin film will function according to specifications.

It was not until the mid 1980s that depth profilometry on the 0.5-500 μm scale became truly nondestructive by basing the metrology on optical absorption, reflection, photoluminescence, and elastic and inelastic scattering [16]. Earlier techniques (such as gas chromatography, infrared spectroscopy, and microtitration analysis) required extracting layers of known thicknesses to profile the sample, thereby destroying the samples. Over the course of the last 25 years, a wide range of optical depth profilometry techniques have been developed to provide localized thickness measurements for thin films. To make the measurements, principles of microscopy, spectroscopy, photoacoustic and photothermal imaging, radiometry, photometry, and interferometry were employed. These metrology tools were an improvement over traditional methods because they provided quick, accurate, and repeatable measurements without requiring any special lighting or atmospheric conditions. These technologies are discussed in more detail in the following chapter.

1.4 Research Motivation and Objectives

Thin films are manufactured in bulk for a broad range of commercial products which require material homogeneity and maintenance of tight thickness tolerances. It is practical and economical to employ computerized machine vision and/or nondestructive evaluation tools for quality assurance purposes in mass production systems because they improve the inspection accuracy, reduce human error, and allow faster production speeds. Hence, the primary research question addressed by this thesis is: what hardware and software tools should be implemented to create a robust, real-time, accurate NDE system

for (a) determining the bi-directional thickness profile and (b) identifying and classifying defects in semi-transparent thin film during production in order to improve manufacturing quality?

Unfortunately, off-the-shelf inspection systems are not capable of quantifying thin film defects or measuring full-field thickness profiles. Defect inspection typically is performed with vision systems, but due to environmental and material variations, specialized systems must be designed for different manufacturing situations; and although there have been defect identification and classification systems developed for a number of applications, the situation of semi-transparent material cast onto a transparent substrate has not been studied. Similarly, instrumentation for full-field thickness measurements of semi-transparent material has not been addressed. Non-contact NDE tools for thickness profilometry are typically single point measurements or in the case of moving webbing, line scan tools. Thus, to recreate the bi-directional thickness profile, the instrument must be scanned laterally (which is difficult for high speed applications) or a linear array of instruments is required (which adds cost and may not be possible due to space constraints). This work investigates inspection methods by employing a single, stationary instrument to recreate the full-field thickness profile in real-time on a dynamic roll-feed production line.

The objective of this work is to manufacture high precision defect-free thin film material by informing the manufacturer of errors in thickness, defect quantities, and tooling adjustments to improve production. The goal of the thickness profilometer and defect inspection instrumentation is to measure errors in either material thickness or homogeneity, such that tooling parameters (e.g., tank pressure, web speed) can be modified to produce acceptable material. In some manufacturing cases, a misbalance in tooling parameters is indicated by the types of defects present in the resulting film, and therefore operational parameter recommendations or adjustments can be made autonomously based on the results of the inspection system. Thus, with only limited knowledge of production operations, a manufacturer can improve thin film fabrication by following the inspection system recommendations. To provide this capability, a graphical user interface containing the thickness and defect inspection subsystems has

been designed to visually display results of the inspection process and allow quick modifications to the system as necessary.

A custom designed roll-feed imaging system (RFIS) has been developed to bulk manufacture defect-free thin film materials and to test prototype NDE solutions. A case study, utilizing the RFIS system, has been performed based on a high temperature polymer electrolyte membrane (PEM) material used in fuel cells (FCs), which is particularly challenging to manufacture [11]. Furthermore, PEMFC production is currently limited by manufacturing cost and product durability resulting from defects, among other things. Fuel cells are currently manufactured at low volume because they are not cost competitive with traditional energy sources. However, as fuel cell manufacturing and inspection technologies progress, manufacturing costs will drop and production quality will improve. Quality improvements are particularly crucial because fuel cell implementation has been stifled by poor durability results due to membrane degradation. Studies have indicated defects and nonuniformity in the membrane is closely linked to the lifetime of the fuel cell system [17]. Hence, with better manufacturing and inspection systems, it is anticipated that PEMFC durability will be improved. Although, this research has been applied to materials used in the fuel cell industry, it has a much broader impact in areas requiring thin film quality control, such as the paper, plastics, fabric, wafer, and food industries.

1.5 Thesis Structure

This thesis describes thin film defect and thickness inspection background, theory, experimental setup, and results. Chapter 2 contains a survey of vision systems employed for defect detection and classification, as well as background on non-contact, nondestructive thickness profilometry techniques. Chapter 3 discusses the design and construction of the roll-feed manufacturing system and integrated inspection station. Chapter 4 explains the additional analysis, programming, and calibration required for the fuel cell membrane inspection case study and Chapter 5 presents the experimental results from this study. Chapter 6 discusses the results of the case study and assesses the inspection system and Chapter 7 concludes the thesis with a summary of contributions to engineering and science, and recommendations of future work.

CHAPTER 2: BACKGROUND ON INSPECTION SYSTEMS AND THIN FILM THICKNESS PROFILOMETRY

Thin film manufacturing processes (e.g. extrusion, coating, sputtering, film deposition, condensation, thermal evaporation, or casting methods) produce sheet materials with a range of magnetic, electrical, mechanical, optical, layering, and dimensional characteristics. Due to the wide scope of material characteristics and processing methodologies, there is no universal thin film inspection system. Instead, to ensure their products meet quality standards, manufacturers either employ human inspectors, develop specialized NDE or machine vision systems, or use a combination of the two. The decision to use human or automated inspection depends on manufacturing processes, batch quantities, line speed, worker safety, and cost. Roll-feed systems are turning to automated inspection systems as the technology matures and hardware and software prices decrease relative to inspector wages [5]. Paper and plastic production have been especially quick to shift to automated inspection systems because the web speeds which these systems operate (1-5 m/s), are too quick for human inspectors to identify small defects.

In thin film web systems, defects are generated in two ways: (1) poor batch material or solution yields particulates, gels, and other defects infused in the final product; or (2) incorrect processing parameters yield holes, die lines, streaks, fisheyes, air entrainment, or thickness variations. To produce defect-free material, the solution must be properly prepared and the processing parameters must be set correctly. The work in this thesis focuses on identifying and quantifying different defects in order to inform the manufacturer which operating parameter adjustments are required to improve film quality. Furthermore, thin films must be fabricated at the specified thickness for assembly and functionality. Therefore, this review focuses on roll-feed related technologies which perform defect identification and classification, as well as full-field thickness profilometry to ensure uniformity in the material.

2.1 Machine Vision Systems for Defect Detection and Classification

Although challenging, there have been number of web manufacturing inspection systems designed to monitor product quality with machine vision. Xu and Floeder noted difficulties with real-time, continuous inspection were due to high data rates and environmental conditions, but companies—e.g., Cognex, Datacube, Honeywell, Systronics, and Webview—have still created commercially available systems for \$20,000-\$1,000,000 [15]. These systems are typically composed of linear or 2-D array cameras, lighting, image processing system, user interface, and other sensors and controls. They inspect the quality or grade of the material by capturing images and extracting qualitative information about the web through intensity, saturation, or hue of the image.

Many machine vision-based or NDE defect detection systems measure the electromagnetic energy (luminous intensity) of light being reflected, transmitted, or refracted from the material. These measurements are often performed by radiometric and photometric instruments consisting of CCD (charge-coupled device) photodetectors. Radiometry measures all irradiance from a point or surface, whereas photometry only measures the visible wavelengths (360-830 nm) [18]. Thus, depending on the inspection application, different electromagnetic bands are measured to determine the quality of the material. Although this work focuses on roll-feed manufacturing, attention has been given to defect detection and classification across a broad range of fabrication areas because of the commonality in inspection approaches. Inspection of plastic, wood, paper, circuit boards, and glass generally share similar techniques where reflected or transmitted visible radiation is measured via image thresholding, grayscale measurements, or photodiode comparisons.

2.1.1 Plastics Inspection

Plastic sheet production is a common application for web inspection systems. These systems typically run continuously, at high feed rates, and with limited human inspection. For this reason, the plastics industry has been one of the key contributors to roll-feed imaging development. Smith investigated roll and web defects common to cast

films, tenter-frame processes, co-extrusions, and laminations, including film, foil, paper, fabrics and non-woven materials [19]. He found that web defects can be classified into categories of property defects, point defects, linear defects, space-filling patterns, and flatness defects.

In roll-to-roll manufacturing, web quality is an important consideration for machine vision analysis; often the shape of the webbing or substrate indicates problems with the product, such as material variations or other defects in the material. To et al. created a system to measure wrinkles across the width of 300 mm wide web materials with structured light [20], shown in Figure 2.1. Using a planar laser, they were capable of monitoring the shape of the reflected light with an off-axis area scan camera; and then by performing data reduction on the bright pixel bead, they determined out-of-plane web deflections.

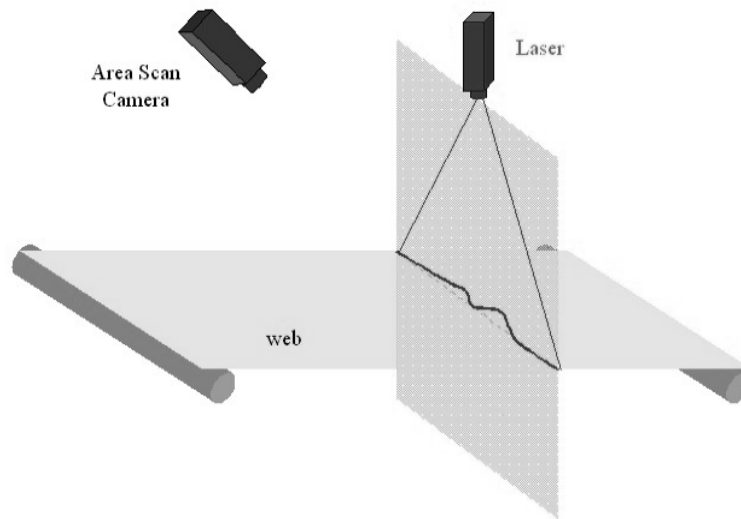


Figure 2.1: Wrinkle inspection system [20].

In 1992, Kona et al. created a robust method of inspecting plastic bags for pinholes using an area camera by taking microscopic images of vibration-flex tested specimens [21]. By mapping the 1.2 x 1.239 mm images to 6-bit grayscale, thresholding the photos to pull out light regions (pinholes) and dark regions (potential pinhole boundaries), and using Papert's boundary tracing algorithm, the authors were able to locate pinholes as small as 40 μm^2 for different plastic bag thicknesses.

Bowman et al. created a prototype system to detect clear gels and black spots in gusseted plastic bag roll-feed manufacturing [4]. They employed two inspection stations with backlighting and 2048-element line-scan cameras to search for each of the defects separately. The authors graded each of the bags continuously by identifying and classifying defects. By exploiting the optical characteristics of the gel (bending the light like a lens) and black spots (absorbing incident light), a robust system for identifying the defects was created. Bowman et al. made a correlation between light input and the scatter thereof to differentiate dark and light spots, because dark spots absorbed the light whereas clear gels scattered the light. The authors reported excellent reliably detecting spots down to 0.25 mm with bag grading processing times of 1.8 s/bag, which was not possible for a human inspector.

Gamage and Xie inspected defects in clear cast films with a real-time vision system [5]. They replaced human inspection with a vision system in a 2 m wide polypropylene casting system operating at 50 m/min. The defects in the material could be classified as wrinkles, gels, coating voids, and streaks, seen in Figure 2.2, but the authors focused on identifying gels and die lines (streaks). By inspecting the shadow cast by Mie scattering (refraction of collimated light, shown in Figure 2.3), they were able to identify 87% of $\sim 360 \mu\text{m}$ gel granules and 94% of $\sim 320 \mu\text{m}$ die lines at a web speed of 0.8 m/s and nearly 100% of the defects at 0.1 m/s. To do this, an 800 x 600 digital image was imported into LabVIEW, smoothed, converted to binary with a histogram-based threshold, and denoised with a lowpass filter to remove small particles. This image was then segmented into the defect regions for automatic classification via shape and grayscale analysis.

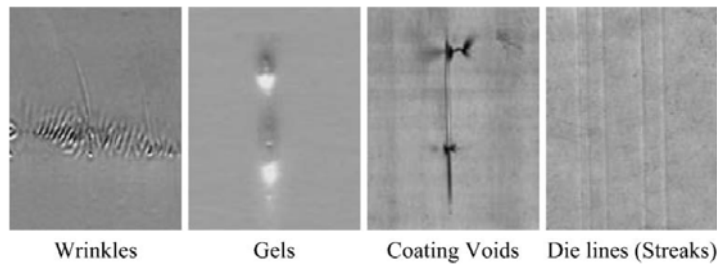


Figure 2.2: Defects in a polypropylene cast extrusion manufacturing process [5]. Only the gels and die lines were specifically identified by the Gamage and Xie vision system.

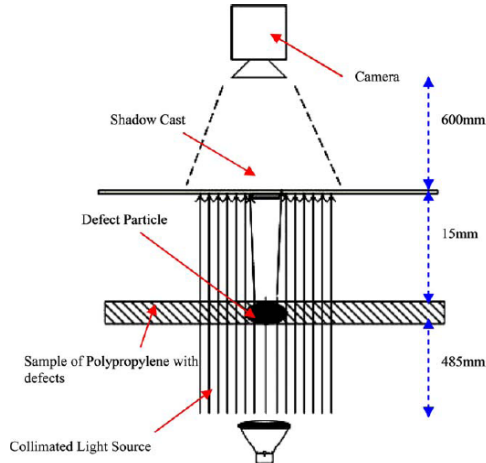


Figure 2.3: The optical conceptualization for gel detection [5].

Another web-based defect identification system is reflectometry. Reflectometry compares the ratio of intensity of incident radiation to reflected radiation at the specular angle. Reflectometry and X-Ray Reflectometry (XRR) are primarily used to characterize surfaces and determine roughness in thin films and multilayered polymers [7]. In multilayered materials the Abeles matrix method is typically applied to calculate the specular reflectance, similar to neutron reflectometry and ellipsometry. The basis for these methods comes directly from phenomena associated with electromagnetic radiation passing between different media; thus, by using the Fresnel equations and Snell's law (described in detail in [22]), surface non-uniformity is detected.

Larena et al. found a correlation between surface roughness of a multilayer polymer film and reflected diffuse and specular radiation [6]. To create the rough surface they added an emulsion agent to adhere spherical granules to the surface. The measurements of different surface roughnesses were done at angles of 20°, 60°, and 85°. It was found that for all angles the reflectometer value decreased with average roughness because granule roughness scattered the incident rays. The authors also characterized photo-degradation from oxidation using this same method in [23]. They discovered similar correlations between degradation and reflectance. Larena et al. later investigated measuring surface roughness in multilayer polymer films with optical transmittance of different wavelengths [7]. They found that in the visible, near infrared (NIR), and certain bands of the infrared (IR) spectra, different roughnesses changed the transmittance according to a power law.

Due to the commercialization potential for plastic inspection systems, there is limited published research but multiple web inspection patents. These systems often rely on specialized sensors or precision lasers. Weber invented an inspection system which first generated a scanning laser line with a mirror wheel and then expanded the beam with concave mirrors [24, 25]. This laser line was then reflected off the surface of the web material and directed by another series of concave mirrors to a photo-receiver; if a defect was present, the reflected light would not reach the photo-receiver. Matzan created another defect identification system with a pair of side-by-side planar lasers [26]. If any defect (e.g., a hole in the material) passed through the parallel laser planes one of the lasers would impinge on the surface at a slightly different height, which was measured by photo-detectors and indicated a flaw.

2.1.2 Wood, fabric, and paper inspection

Wood processing plants and sawmills are a well-established areas for machine vision systems. There is significant work in vision-based cutting, inspecting, and grading in the field. For example, surface quality of wood veneer has been a significant area for the development of inspection systems because the aesthetic aspects of the veneer rely heavily on the number, type, and size of defects. Human inspection of the veneer grading is limited to an accuracy of 55% [27], which led to the development of automated visual inspection (AVI) tools. The sub-tasks involved in the AVI were to detect the defects [28], perform image segmentation [29-32] and classify the defects [33-35].

In wood grading, detecting defects using AVI systems is challenging. Often it is not possible to detect all the types of defects (like those shown in Figure 2.4) using a single edge detection or thresholding algorithm. For example, Pham et al. completed defect detection with global adaptive thresholding for hard rot; multi-level thresholding for holes, splits, and rotten knots; row-by-row adaptive thresholding for sound knots, pin knots, colored streaks and worm holes; and vertical profiling for streaks [31]. Then Pham et al. used an *Accumulation of Evidence* fuzzy logic tool to eliminate false objects and a self-organizing neural network clustering method to combine separated regions representing the same defect [34]. The advancements of Pham et al. lead to implementation of more advanced systems for which features of the defect were extracted

from a segmented region of interest around the defect. Features were either object-based (size, shape, etc.) or tonal-based (mean grey level, grey level standard deviation, number of dark pixels, etc.). These features were then normalized and entered as inputs into a neural network. Feed-forward neural networks with one hidden layer have shown the best results [29, 33]. The neural network classified defects with 87% mean accuracy compared to 63% for non-neural networks techniques [35].

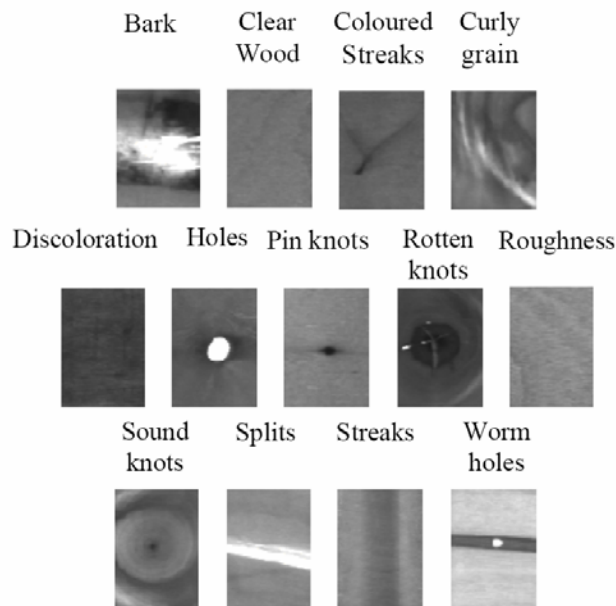


Figure 2.4: Comparison of wood veneer defects [35].

It should be noted that very similar defect identification and neural classification systems exist for the textile industry. Mitropulos et al. performed similar steps of image processing and detection, segmentation, and classification for wrinkle and spot defects on woven structure [36]. They report a classification accuracy of 82%. Other defect detection and classification systems for fabric web systems have used fuzzy classification [37], Bollinger brands [38], and Gabor filters [39].

Parker patented an array of illumination and sensor units to inspect paper in real-time [40]. The types of defects the inventor was interested in are shown in Figure 2.5. The inspection stations used a lens to focus the light onto the web while fiber optic cabling routed the reflected illumination to photodiodes. The electrical signals were then

converted to digital, multiplexed, and sent to a computer to analyze the data to determine which, if any, of the defect types were present.

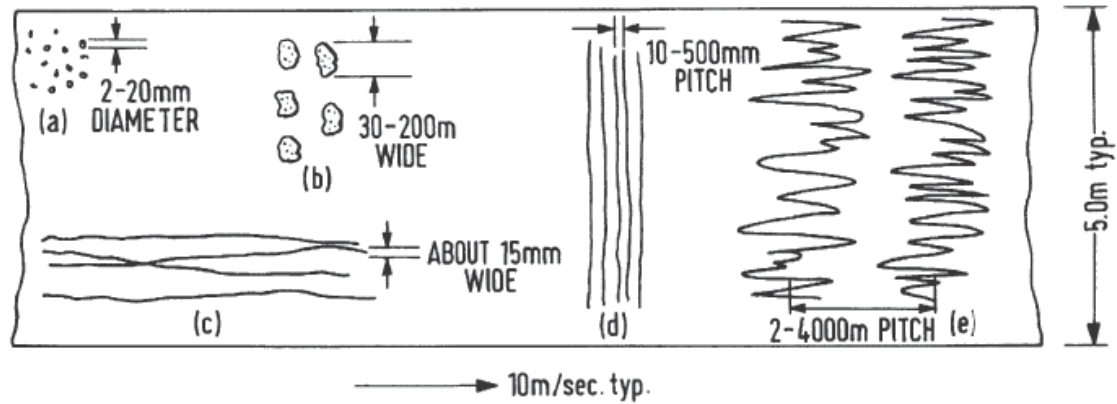


Figure 2.5: Defects occurring in paper manufacturing: (a) floculation, (b) macro forming faults, (c) unstable streaks, (d) periodic variations, (e) random variations [40].

2.1.3 Glass Inspection Systems

A glass inspection system was developed by Lasor/Systronics called the 2f1 Vision System which detected defects in the glass and recorded optical deflection in the lengthwise and width directions [41]. Up to 12 cameras were mounted on the system with each camera pixel representing a 0.1 x 0.1 mm area. The system used web-speed-synchronized line-scan cameras to detect an alternating 2 or 4 LED configuration located behind the web. The testing configuration in Figure 2.6(a) resulted in different intensity values for normal material and defective material, shown in Figure 2.6(b). It was found that using the sum of I_1 and I_2 (brightness), the difference of I_1 and I_2 (deflection), and first deviation of I_1 and I_2 (refractive power), the type of defect could be determined. The system then plotted a web map showing the grayscale level for the glass, and the locations of the spot defects, allowing operators to avoid these areas when finalizing the product. This system demonstrated that transmission properties through transparent material are capable of indicating defects and that displaying inspection results in real-time is of significant value for the manufacturing operator. The display allowed the manufacturers to make quick decisions about the product quality and change manufacturing parameters of the glass production line if necessary.

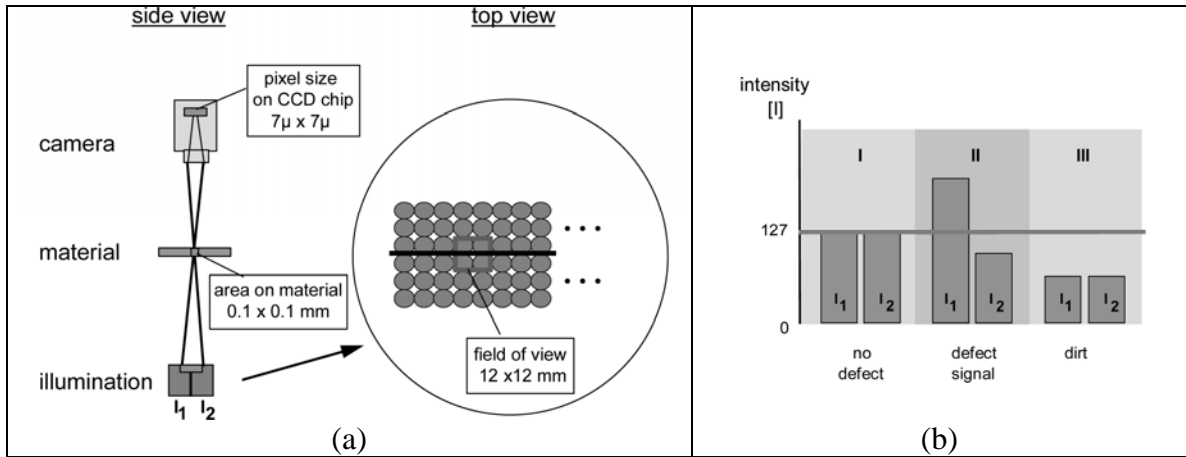


Figure 2.6: The 2f1 Vision System. (a) Optical principle of the system. (b) The types of image signals indicating no defect, a defect and a dark obstruction [41].

2.2 Thin Film Thickness Determination

In the thin film manufacturing processes, the material thickness must be kept as close to tolerance as possible. If the material is produced thin, there is a greater chance that it will fail due to corrosion, impact, or static or fatigue loads; if the material is produced thicker than specified, bulk material is wasted and there is added cost from production and handling; and if the material varies in thickness across the web, uneven loading would cause stress concentrations and greater potential for failure. Therefore, it is vital that thin film manufacturing systems inspect the thickness of the material. Similar to defect detection, it is imperative that the process used to inspect film thickness be nondestructive. There are many technologies which determine thickness for thin films, ranging from mechanical to magnetic, as shown in Table 2.1. The selection of thickness measurement tools is based on the range, accuracy, and precision of the instrument, as well as the environment and material characteristics. For instance, techniques are often limited by material state, corrosivity, viscosity (e.g., a micrometer is not applicable for thickness measurements of fluid materials). In other cases the material characteristics allow specific instruments to be used, e.g. magnetic induction is only applicable on ferromagnetic materials and interferometry is limited to thin materials. In this work, optical thickness techniques are further explored because they offer excellent versatility and robustness for the roll-feed system.

Table 2.1: Nondestructive thickness measurement techniques, modified from [42].

Technique	Range	Notes on accuracy or precision
Mechanical		
Caliper, micrometer	1 μm -100 mm	$\pm 3 \mu\text{m}$ accuracy
Weighing	Area dependent	
Electronic gages	0-1 m	Precision dependent on noise
Optical/focusing, shadowing, comparing		
Microscope	5 μm minimum	$\sim 1\%$ accuracy
Comparators/projectors	25-250 nm	
Laser caliper	100 μm -100 mm	6 μm precision
Capacitive gages	$< 1 \mu\text{m} - 1 \text{ cm}$	
Inductive gages (eddy current sensors)	0 – 1.5 mm	2.5 μm precision
Magnetic induction	0-4 mm	10% accuracy
Hall effect gage	0-10 mm	1-3% accuracy
Far-field/time-of-flight		
Sonar/ultrasound	0.5-250 mm	25 μm accuracy
Far-field/resonance		
Interferometry (spectral and spatial)	1 nm-100 μm	About $\lambda/50$ accuracy
Ellipsometry	0.3 nm-10 mm	0.1 nm accuracy
Far-field/absorption, scattering, emission		
Gamma-ray backscatter	Range to 25 mm	0.5% precision
Beta-transmission	2 mm-1mm	0.2% precision
Beta-backscatter	100 nm-50mm	3-20% precision
X-ray fluorescence	0-30 mm	
Infrared absorption	Material dependent	

2.2.1 Optical Thin Film Thickness Profilometry

Optical thickness profilometry tools have many advantages over traditional thickness measurement techniques. They are non-contact, nondestructive measurements with high accuracies and real-time readings. Heavens [22] breaks down the optical tools for thin film thickness measurement into the following categories:

- **Interferometric and fringe-displacement methods** generate interference of electromagnetic radiation to produce periodic signals related to the light wavelength and thickness of the material.
- **Photometric methods** relate the intensity of light to the thickness of the material either through transmission, reflection, or backscatter.
- **Polarization methods** use p- and s-polarized light properties to measure the thickness. The different polarizations of light reflect from the surface of materials differently, so by comparing the different irradiances, the thickness of the material can be calculated.
- **Stepped angle methods** adjust the angle of the incident radiation to generate data about the thickness. For instance, in attenuated total reflectance infrared

spectroscopy, the absorption and depth of penetration depend on the angle of incidence.

- **Spectrophotometric methods** rely on spectral measurements of the transmitted or reflected light.

A selection of optical thickness tools are described in Table 2.2. The method for full-field thickness measurements is limited depending on budget constraints and the desired measurement precision, accuracy, and range. For films less than 25 μm , beta and x-ray gauges are not sensitive enough to measure changes in thickness, and IR and UV absorption gages are known to have difficulty measuring thickness when there are chemical changes or temperature variations [43]. Furthermore, gamma-ray and other transmission thickness gages are not designed to give full-field results. Alternatively, interferometric and densitometry techniques are economical and well-suited for thickness measurements between 1-400 μm . To this end, the succeeding section will further describe these optical techniques.

Table 2.2: Selected Laser and Optical Thickness Profilometry Techniques.

Nondestructive Evaluation Technique	Brief Explanation
<i>Interferometric and Fringe-Displacement Methods</i>	
Interference spectroscopy	Incident light reflects on the top and back surfaces of the thin film to create interference [44]. Adjusting the wavelength of light used, a period pattern of reflected light intensity is used to determine the material thickness.
Multiple-beam interference fringes (e.g. Fizeau fringes)	The top surface of the material and the substrate are silvered on one edge. A monochromatic source is used to create a fringe pattern by reflecting the light off the silvered surfaces and reference mirror [45].
Haidinger fringes and Fabry-Perot interferometry	Circular fringes are created by using wide angle illumination via the reflections from the front and back surfaces. The diameter or number of fringes can be used to estimated the thickness of the material [46].
Scanning white-light interferometry	Similar to the Michelson interferometer configuration, a white light source is split with one path reflected off the sample and the other path reflected off a scanning reference mirror. When the path lengths are equal, the wavelengths destructively interfere and a fringe pattern is created.
<i>Photometric Methods</i>	
Confocal microscopy	A laser with a very small pinhole aperture irradiates the sample and images of the sample are taken. After correcting for different nonlinear effects, the intensity profiles correspond linearly to true thickness [47].
Confocal laser scanning microscopy (CLSM)	The subject is illuminated with a single laser point and optically sectioned by raster scanning point-by-point to create the 3D surface [48].

Table 2.2: Selected Laser and Optical Thickness Profilometry Techniques (continued).

Nondestructive Evaluation Technique	Brief Explanation
Fluorescence microscopy	Fluorophore molecules absorb a certain wavelength of light (generally UV) and re-emit a different wavelength (usually visible light). Using this principle, a UV light is used with a microscope to view a dyed or naturally fluorescent sample. The intensity of the fluorescence is then correlated to the thickness of the material [49].
<i>Densitometry and Absorptiometry Methods</i>	
Light profile microscopy	Collimated light passes through the material in the thickness direction while images are captured through a microscope, which views the film in the through-plane direction. From this simple setup, the thickness along with optical absorption, photoluminescence, light scattering, and other depth-dependent properties of the material can be determined from the images taken of the sample [50].
Optical computed tomography (CT)	Photo-detectors record the absorption of laser beam or collimated light through sample material at different angles (often by a rotating the sample) [51]. A 3-D representation is recreated of the sample by triangulating areas of specific density based on the absorption data.
Transmission Densitometry	Thickness is determined by quantifying the attenuation of transmitted radiation by photometrically measuring the influx and efflux.
Reflection Densitometry	Thickness is measured by quantifying the amount of reflected radiation.
<i>Laser-based Thermal Methods</i> [16]	
Photopyroelectric effect spectrometry and photothermal spectroscopy	Material is heated with a laser and the conduction through the material is measured with a pyroelectric detector on the back of the material or substrate. Due to the well-understood relations between material thickness and conduction, the thickness of the material can be determined from the thermal signals.
Photoacoustic spectroscopy	A laser warms a sample with a gaseous medium on the surface. The thermal expansion of the medium forces acoustic waves through the gas to a microphone which records the results over a 20 kHz bandwidth [52]. The thickness is related to the recorded acoustic frequencies.
Photothermal infrared radiometry (PT-IR)	The IR radiation emitted from a sample heated with a laser is measured (often with an IR camera) to determine the spatial temperature change in the material, and based on conduction calculations determines the material thickness.
Attenuated total reflectance (ATR) or internal reflection spectroscopy	A high refractive index medium is placed on the front of a 0.1-10 μm sample so that an IR laser passes through the medium above the critical angle and an evanescent wave propagates into the sample. The spectral content of the evanescent wave is then measured to determine the thickness.
<i>Polarization Methods</i>	
Ellipsometry	Ellipsometry can classify nanometer-thick films by sending light through a polarizer, off the surface of the material, through another polarizer and then into a detector. The light reflects off the top and bottom surfaces of the thin film, which creates interference that is measured by the change in polarization state. Metrologically, ellipsometry also gives information on refractive index and dielectric properties.
Polarization interference microscope (and Savart plate method [22])	Two interference images are produced by using a polariscope made from birefringent crystals cut 45° to the axis [53]. Then using a polarizer and analyzer, the thickness of transparent samples can be found similar to a Michelson interferometer.

2.2.1.1 Interferometry

Interferometry takes advantage of wave-like phenomena of light in order to produce constructive or deconstructive interference. When electromagnetic waves are in-phase, they amplify the radiation signal, whereas when the waves are out-of-phase, the waves cancel each other and there is a signal reduction. This basic principle of wave interference has led to a number of interferometry techniques used to measure opaque thin films including holographic interferometry (holography), white light interferometry, and electronic speckle pattern interferometry. In holography, the surface of the object is recorded and then replayed on the object. When the physical surface remains in the same location, the waves constructively amplify the signal and there is no fringe pattern, however when the surface translates or deflects by half a wavelength, there is deconstructive interference and dark bands appear in the fringe pattern. By measuring fringes directly or with a Fourier transform, the displacement and strain of the surface can be determined [54], but it becomes challenging at displacements larger than 50 μm because the fringes become dense [55].

White light interferometry works on the same interference principle, except that all the visible wavelengths of light are split into two pathways; one impinges on the surface of the object and the other off a reference mirror. When these waves are recombined, the only way all the wavelengths constructively interfere is when the distances off the mirror and the object are equal [56]. Hence, by adjusting the distance that the control beam takes, the height of the upper surface is found. There are multiple white light interferometry configurations possible to determine thin film thickness. Flournoy et al. have illustrated multiple methods of determining transparent material thickness using interferometry, including generating Brewster's fringes with the web material, using an optical wedge, or employing a Michelson interferometer [43].

Some industrialized systems use interferometry to ensure sheet glass is the proper thickness and has no distortions. Pilkington Glass Lahti Ltd. created an off-line interferometry system to inspect the glass slope and an on-line system to measure thickness [57]. The off-line system measured the fringe pattern from the interference of

laser light reflected off the top and bottom surfaces of the glass in a 10 x 10 mm area. The fringe pattern indicated the slope of the surface with submicron accuracy for a 10 mm range. The on-line system used a CCD camera to measure the interferometric signal generated from a laser reflecting off the top and bottom surfaces of the 1-6 mm plate glass [13]. The accuracy was reported to be 0.01 mm and the system scanned back and forth across the lateral dimension of the glass surface with 3.8 m of travel.

Over the past decade, thin film measurements and methods of determining characteristics of coatings on polymer substrates have been investigated [3, 6, 7, 23]. Applying interference spectrometry, Larena et al. developed a technique to determine the total thickness of multilayered materials using IR absorption and Beer's law to find the thickness of a 1-10 μm photoconductor coating on a PET substrate [3]. Their interference spectrometry system used the internal reflectance of the material to create interference fringes and simultaneously determine the refractive index and thickness for 100 nm to 5 μm thick films [44]. To test the system, photoconductor layers were observed with the spectrophotometer. From the results, the optical thickness of the material was found using a relationship between periodicity of maxima and minima in the interference spectrum and the optical thickness. Unfortunately, this method did not determine the thickness of the coating alone, but rather included all the layers. The authors believed there were no interference fringes created from the coating-substrate interface because the index of refraction was similar between PET substrate and the coating.

As early as 1937, Blodgett and Langmuir found that interference fringes from low-angle reflected polarized light could be used to determine thickness in crystalline thin films [58], given the refractive index of the film and substrate. Shelley et al. found that optical low coherence reflectometry (OLCR) using a Michelson interferometer was capable of determining the thickness of 10-75 μm PET films while in motion, but the calculations required 1 min to find the thickness [59]. Another technique called Variable Angle Monochromatic Fringe Observation (VAMFO) was studied with respect to a wide range of transparent thin films, where laser light reflected and refracted as it impinged the surface of the thin film. Photometer extrema only occurred when the refracted path was a multiple of half the wavelength, so by rotating the sample and measuring the extrema,

the thickness of the material could be determined. After investigating 28 semiconductor-related materials, Warnecke and LoPresti found that if the refractive index of the material was known, the thickness of the film could be found with the reflectance results [60]. Pliskin discovered that refractive index and the thickness of a transparent layer could be found with the VAMFO when two wavelengths were used [61]. However, in all cases this required the sample be carefully rotated with respect to the incident laser beam, as shown in the general VAMFO setup in Figure 2.7.

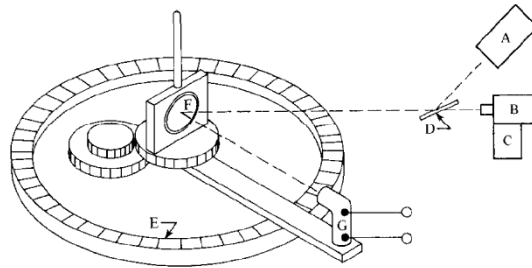


Figure 2.7: Laser-VAMFO setup with (a) He-Ne laser, (b) monochromator, (c) xenon lamp, (d) mirror, (e) goniometer, (f) sample, (g) detector [60].

Goodman further investigated reflectance interferometry and demonstrated that an approximation of refractive index and the thickness of the material can be determined with a single sweep using Constant Angle Transmission Interference Spectroscopy (CATIS) [62]. The concept relied on successive reflections of the incident light in the substrate to create interference patterns before reaching the detector. A drawback of this system was that uncertainty caused significant deviation from the surface profile analyzer results. Goodman reported that CATIS provided results within 6% of the thickness for submicron thick wafers [62]. However, the method required the sample be uniformly deposited on a flat substrate and neither absorb nor scatter light. Assuming the base of the thin film was placed on a flat surface, the surface topography indicated the thickness of the material.

Real-time, full-field moiré measurements have shown excellent resolution for surface characterization. In projection moiré or shadow moiré techniques, interference patterns are used to determine surface topography for an entire (preferably opaque) surface. Projection moiré uses two images of laser grating to create interference patterns, which computer algorithms can analyze to reproduce the surface geometry. This

approach was studied to identify circuit board warpage during soldering processes [63], whereby a laser was expanded and then reflected through a Michelson interferometer to create the grating pattern. The interferometer reference mirror was attached to a piezoelectric transducer and two images of the grating were captured at different times; then the images were superposed to create the moiré pattern. Shadow moiré has also been implemented to measure circuit board warpage [64]. Shadow moiré patterns appeared from the interference of the suspended grating above the surface and the grating shadow on the surface. These two sets of periodic lines were imaged with a CCD camera, shown in Figure 2.8, such that the fringe pattern could be equated to out-of-plane board bending through computer analysis. Fringes occurred every $8.47 \mu\text{m}$ and the resolution of the system using an 8-bit camera was between 0.01-0.1 fringe order or $0.085\text{-}0.847 \mu\text{m}$.

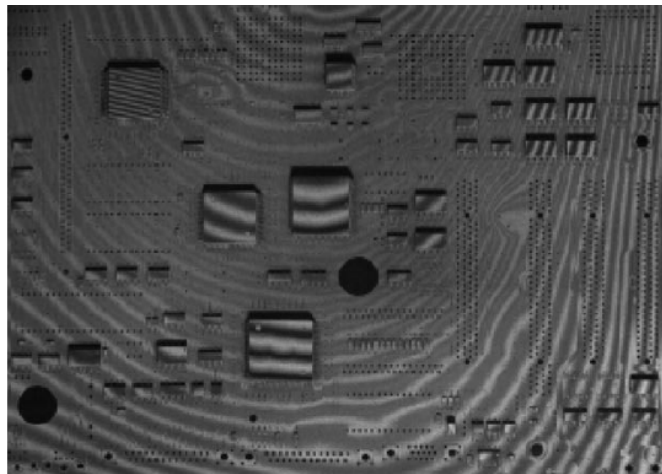


Figure 2.8: Shadow moiré pattern of a computer motherboard [64].

2.2.1.2 Densitometry

As shown in Figure 2.9, when electromagnetic radiation passes through a semi-transparent material, some radiation is reflected, absorbed, and transmitted. By the conservation of energy, the respective fractions of the flux can be written as

$$R + A + T_t = 1 \quad (2.1)$$

where R is reflectance, A is absorbance, and the total transmittance (T_t) is the sum of specular and diffuse transmittance ($T_t = T_s + T_d$). The transmission or transmittance factor is defined by the emergent to incident flux ratio, given by

$$T_t = \frac{\Phi_e}{\Phi_i} \quad (2.2)$$

where Φ_e is the efflux (radiative flux exiting the material), Φ_i is the influx (radiative flux entering the material), and the optical transmission density, D , defined as

$$D = -\log_{10} T_t \quad (2.3)$$

which is synonymous with absorbance. Therefore, the transmission density of the material can be found with flux measurements with and without the sample in front of a radiation source.

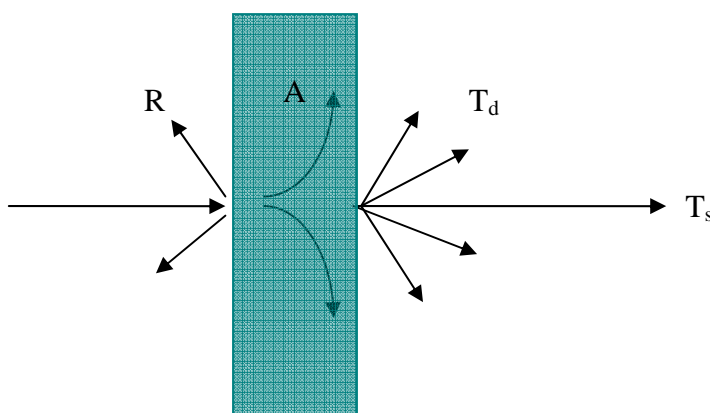


Figure 2.9: Cross section of a thin film material showing (R) reflection, (A) absorption, (T_d) diffuse transmission, and (T_s) specular transmission.

To fully describe densitometry measurements the angular substance of the influx and efflux beams, spectral power distribution of the influx beam, and the spectral sensitivity of the receiver must be described [65]. For this reason, a joint American National Standards Institute (ANSI)/International Organization for Standardization (ISO) standard was created to normalize densitometry influx and efflux cone angles, Θ_i and Θ_e , respectively, shown in Figure 2.10. Historically, specular densitometry attempted to capture all efflux radiation with an integrated sphere (e.g., $\Theta_e = 90^\circ$) [66]. However, with the development of the ANSI IT2.19-1994 and ISO 5-2 standards, it is now required to mate the back of the material with an opal glass diffuser and use a small angle lens with a large aperture ($f/4.5$ - $f/1.6$) to measure the radiometric flux [67]. The ANSI standard

allows for diffuse influx, diffuse efflux, and projection density measurements. Off-the-shelf point measurement instruments which adhere to the ANSI standard are available from Tobias Associates, Inc. [68] and X-Rite, Inc. [69] with aperture diameters of 1, 2, and 3 mm. Commercially available transmission densitometers are capable of measuring optical densities of 0.0-6.0 with ± 0.01 repeatability [70]. However, there are no commercially available full-field instruments.

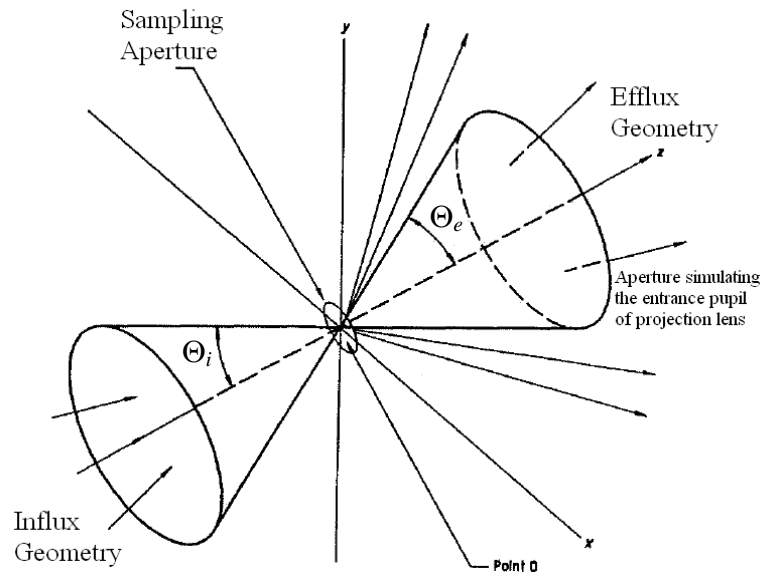


Figure 2.10: Influx and efflux geometry for densitometry measurements [67].

Thin film densitometry has been used for a wide-range of applications where the optical density changes proportionally with the parameter of interest. Teasdale et al. measured the amount of dissolved sulfide in thin films by imaging the sheet with a flat-bed scanner [71]. The scanner was configured such that if there was no sulfide gel the 8-bit image would read slightly darker than pure white and at the highest concentration the image would not saturate to black. Photon transmission methods have also been used to monitor the formation of plastic films. Experimental work has investigated the void-closure coalescence of latex particles via optical clarity [72], polymer-polymer interactions in annealed films [73, 74], and molecular weight effects on latex formation [75]. Further, reflection spectrodensitometers use reflections off web material to verify the color of printed material, paints, plastics, textiles, and analyze powdered chemicals. X-ray scanning densitometry was used to study changes in waferboard samples during

various mechanical tests [76], and ExxonMobil Chemical, Inc. used transmission densitometry to measure the thickness of metalized films with optical densities typically between 2.0 to 3.0 [77].

Densitometry measurements are also heavily used in biology and medical applications. Densitometry is often employed for analyzing x-rays for bone density measurements, radiation dosimetry [78], ophthalmology [79] or in mammography [80]. Also, transmission densitometry is implemented for scientific applications where parameters of interest are dependent on photographic translucency. For instance, laser transmission densitometry and reflectance densitometry were explored to characterize protein immunoblot membranes in tissues via gel electrophoresis [81].

Of the surveyed medical applications for densitometry, only one investigated full field densitometry, in which breast arterial calcification was calculated by full field X-ray digital mammography with a phantom overlay [80]. The phantom was a calibration sheet with calcium deposits of known thickness and mass. This sheet was then used to create a gray level to calcium (Ca) mass conversion, given the X-ray dosage. The authors report excellent linearity between the log signal intensity and Ca mass, 9% systematic error and a maximum uncertainty of 15%. This study indicated full field transmission densitometry was possible but with less accuracy or repeatability than localized densitometry measurements.

Densitometric measurements are also widely used to characterize chemical solutions using spectrophotometers. Optical density, D , is related to the Lambert-Beer law—also referred to as Beer’s law—in which the chemical properties of the material define the absorbance, i.e.,

$$D = A = \varepsilon ct \tag{2.4}$$

where, ε is the molar absorptivity, c is the concentration of the solution, and t is the path length of the radiation through the sample (usually in a cuvette). Thus, with knowledge of the concentration of the solution (mol/L) and the molar absorptivity (L/mol-cm), the thickness of the sample can be calculated.

Although, Beer’s law is widely used for quantifications of chemical solutions, it has been rarely utilized for thin film thickness measurements—likely because (a) molar

concentrations are not known for the material and (b) ε and c can be combined to form a more practical absorption/depth attenuation or extinction coefficient, $a = \varepsilon c$. However, Beer's law has been cited in some thin film thickness profilometry experiments. The extinction coefficient which describes the linear relationship between density and thickness has been shown to exist for thin carbon films [82] and Beer's law has been used to verify interference spectroscopy results for photoconductor coatings [3]. Similar Lambert-Beer law results were found for PET films with IR transmittance radiation using a Mattson Galaxy FT-IR spectrophotometer [83].

X-ray densitometric imaging operates as a NDE tool for a variety of agricultural products. Kotwaliwale et al. used the system configuration in Figure 2.11 to generate x-ray attenuation coefficients of pecans and their shells in order to perform quality evaluation via nutmeat quantification [84]. They used a 1024 x 1024 camera and Gd₂O₂S scintillator screen to convert the x-ray radiation to grayscale. The signal was digitized to 12 bits and used to create linear fits for the nutmeat and shell attenuation coefficients using samples of known thickness. Although there were variations in extinction coefficients between nuts, detector variations were less than 4%, with 80% of this error attributed to random noise and 20% from pixel sensitivity variation.

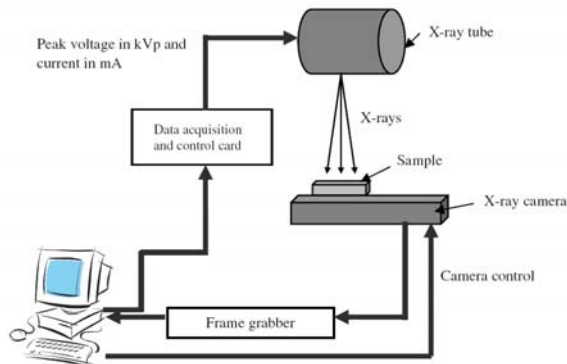


Figure 2.11: System configuration for evaluating pecan quality using x-ray densitometry and digital camera [84].

There are also a number of thickness profilometry patents which rely on the decay or transmission radiation to determine the thickness of the materials. Ashford of the Aluminum Company of America patented a method for using beta ray radiation to measure the thickness of metallic web material [85]. IR transmission measurements have also been used to inspect paper webbing to determine humidity and basis weight [86].

Flook and Moore of DuPont patented a transversely scanning UV signal/sensor pair to determine thickness at different locations across a web of cast material [87]. Kimberly Clark created a similar system for analyzing the quality of tissue product by illuminating the webbing and recording two frequencies of electromagnetic radiation with an array of filter spectrometers [88]. One of the frequencies was used as a reference signal to adjust for baseline changes and help remove noise from web flutter and surface conditions, and the other frequency measured the density of the tissue. The inventors claimed the composition of material could be determined based on either reflectance or absorbance using Beer's law.

2.3 Summary

Inspection systems are common in the plastics, wood, fabric, paper, glass, and thin film industries. These systems determine the quality of the product with machine vision and nondestructive evaluation tools by quantifying the defects and/or thickness of the material directly or by post-processing the data. Defect detection systems generally use machine vision to capture images of the product and flag defective regions when there are localized radiometric differences. Defect classification determines the type of defect with heuristic rules, a neural network, or some other classifier. Although fabric and wood inspection systems often classify defects for the purpose of grading, polymeric inspection generally does not classify the defects because differentiating defects adds little value to the inspection system and the types of defects are generally limited.

Of the broad range of thickness instruments, optical thickness profilometry techniques were most applicable for non-contact thickness measurements of thin film material in a dynamic roll-feed environment. Based on the thickness range, accuracy, and ability to make full-field measurements, interferometry and densitometry were further studied for implementation on the roll-feed system. Both of these techniques have advantages and disadvantages. Interferometry has excellent accuracy but requires more hardware and scanning to make measurements. Densitometry is less accurate but the thickness is determined with quick, simple full-field measurements. The following chapter considers these tradeoffs when designing the thickness profilometry instrument for the roll-feed system.

CHAPTER 3: EXPERIMENTAL SETUP AND ROLL-FEED SYSTEM CONFIGURATION

The roll-feed imaging system (RFIS), shown in Figure 3.1, is a continuous roll-feed system that incorporates imaging and thickness profilometry to analyze defect generation in semi-transparent thin film using various casting and extrusion processes (e.g. slot die extrusion). The RFIS has been designed to be modular, adjustable, and adaptable for different types of cast materials and different inspection systems. The structure was constructed with 80/20 Inc. components to allow for variable positioning of the manufacturing tooling components, heating elements, and inspection station because different materials required different system configurations. Additionally, there were a wide range of NDE and machine vision systems in literature (as discussed previously in Chapter 2), so the RFIS was designed to accommodate different inspection technologies and sensors. The system can be subdivided into the following modules:

- roll-feed and web control system – controls the speed and tension of the webbing
- tooling system – produces the extrusion with a temperature- and pressure-controlled tank, die, and piping
- temperature control system – ensures tank, die, and platen temperatures during casting
- inspection system – measures the thickness and quantifies defects in the manufactured product with a graphical user interface

The web, tooling, and inspection systems are illustrated in Figure 3.2. Components of the temperature control system are pictured in Figure 3.3, along with web and inspection control hardware, where the temperature control system provides tooling and platen heating with Watlow PID (proportional-integral-derivative) controllers. The web tension control is performed with National Instruments LabVIEW 7.1 program and the inspection system is operated with a dedicated MATLAB 2008a graphical user interface (GUI) on a second computer. The RFIS modules are discussed in more detail in the following sections.

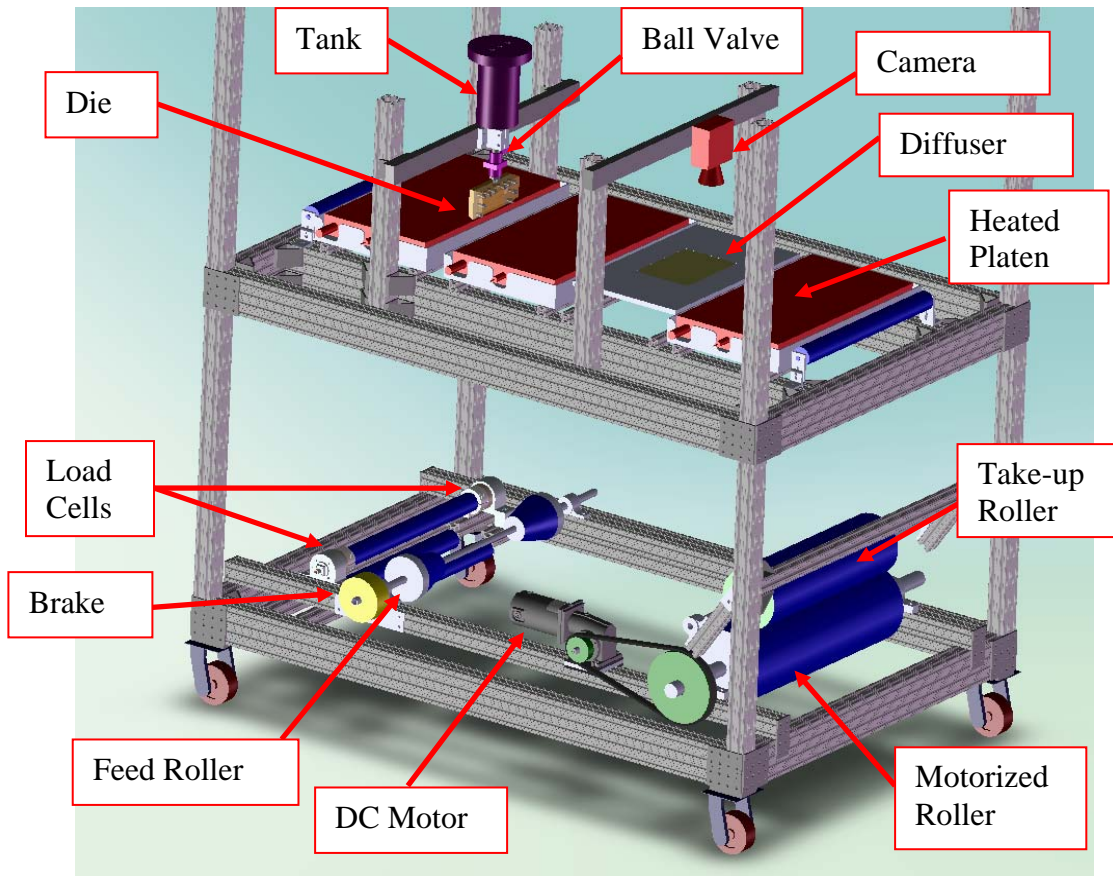


Figure 3.1: The roll-feed system with inspection instrumentation.

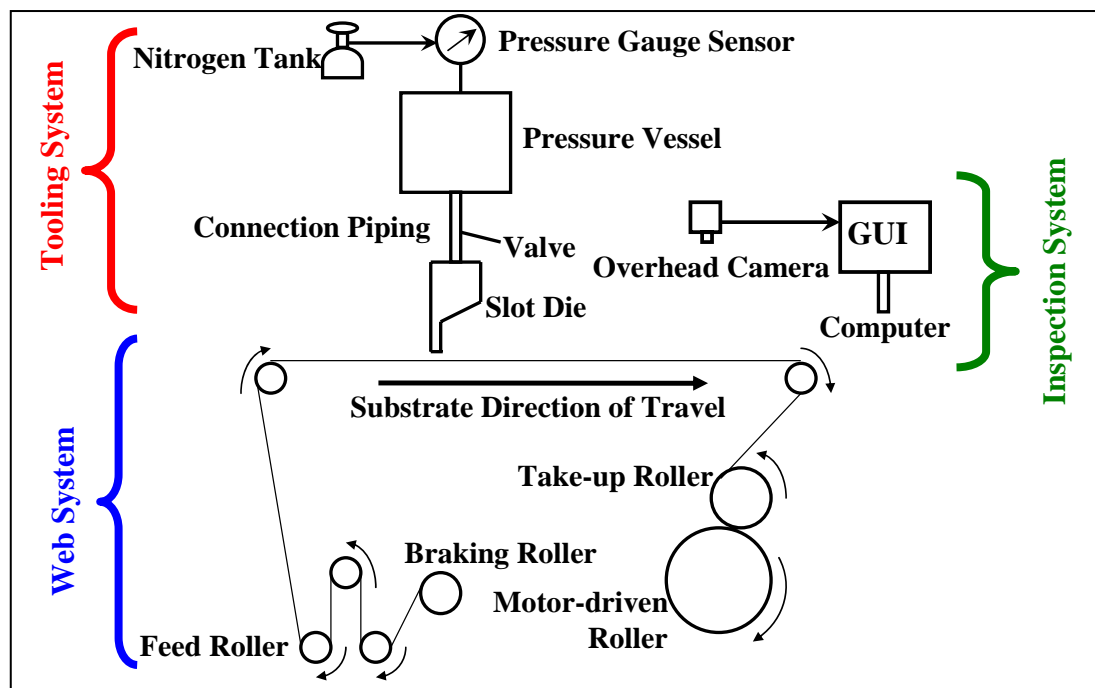


Figure 3.2: The web, tooling, and inspection systems of the roll-feed imaging system.

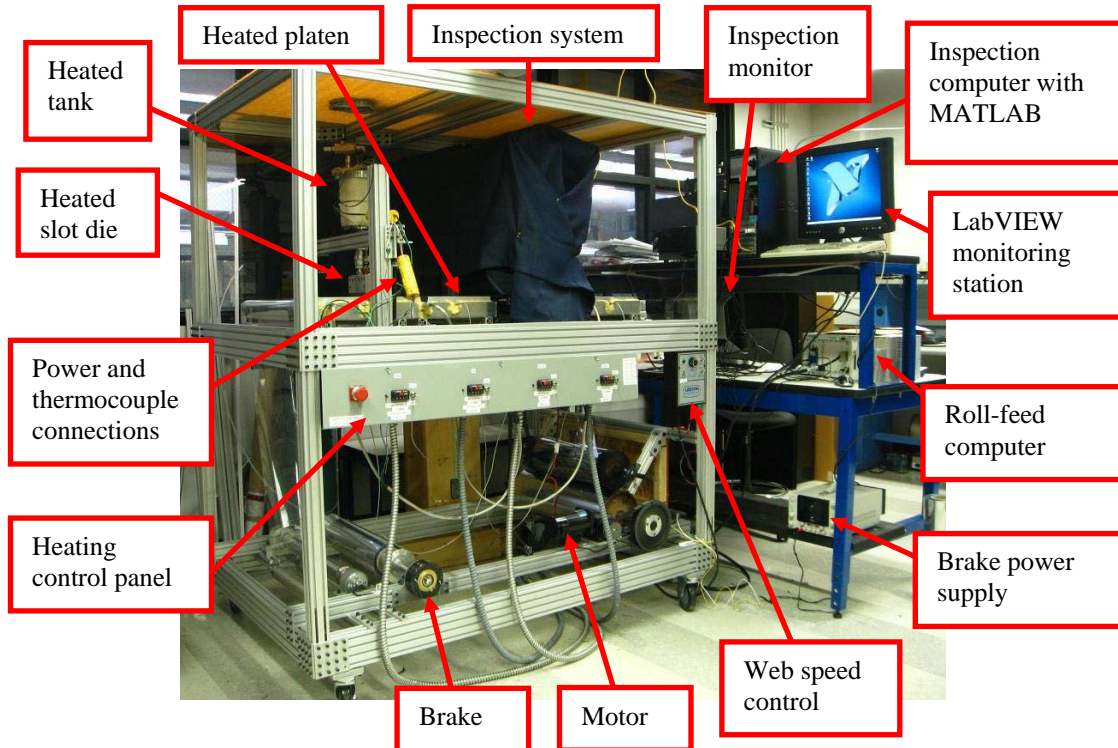


Figure 3.3: Physical system with web, heating, and inspection control systems.

3.1 Roll-feed Web System and Control

Acting not only as webbing, but also as a substrate to cast material, polyethylene terephthalate (PET) is streamed across the system as shown in Figure 3.4. The webbing is pulled through the system with a motor coupled to a take-up roller. The tension is controlled by a brake attached to the substrate roll which adjusts the resistance torque, $Q_{\text{resistance}}$.

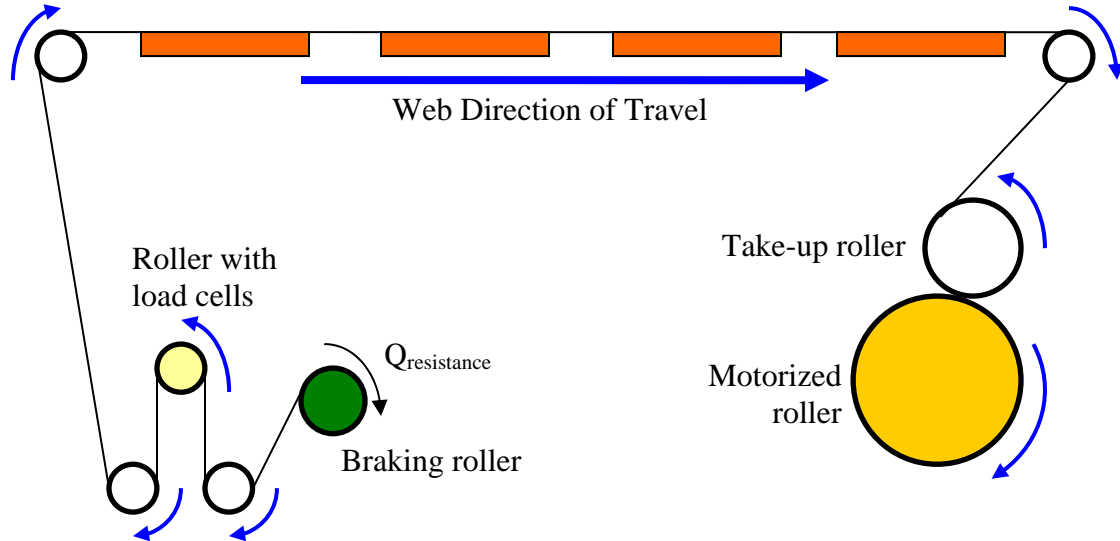


Figure 3.4: Roll-feed webbing configuration. The blue arrows indicate the direction of rotation.

The roll feed system is controlled with a Tesson DC motor and Cleveland Motion Controls brake. A potentiometer is used to adjust the web speed between 0 and 0.25 m/s depending on the casting process by regulating the voltage across the motor. Although, limited by the hardware of the current design, web speeds of 1 m/s and higher are possible for casting membrane material, and likely a requirement for industry-scale versions of the die cast system [89].

The brake is used to adjust the web tension by varying the voltage with a 1000 Hz pulse width modulated (PWM) signal. The signal is controlled with National Instruments (NI) LabVIEW [90] and is sent through a NI PXI-1010 DAQ card connected to a NI PXI-8186 Embedded Controller with a SCB-68 I/O board. The web tension is controlled with a feedback control system using Ultra Cartridge Transducer load cells, which are mounted at the ends of the roller shown in Figure 3.1.

The system operator determines the desired tension to keep the substrate taut around the rollers. Since PET has high bending stiffness, friction in the system alone does not keep the substrate in full contact with the rollers, shown in Figure 3.5. If the substrate is not held taut against the platens, out-of-plane vibrations or deflections may cause non-uniform casting, as described in 2.1.1. The control system, shown in

Figure 3.6, is a model-based, feedback control system which maintains constant web tension as the casting applies forces on the web and the diameter of the feed and take-up rolls change.



Figure 3.5: Webbing without tensioning.

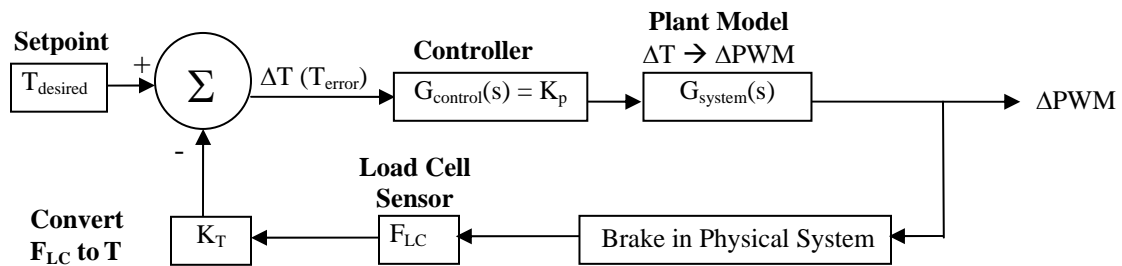


Figure 3.6: Web tension control loop.

The control can be described as a series of steps:

1. Based on experience, the desired tension (T_{desired}) is input into the system by the operator. Generally, this is between 60-75 N.
2. T_{desired} is subtracted from the measured tension to determine the error in tension (T_{error}), which is also the desired change in tension (ΔT).
3. The controller takes ΔT and based on the control algorithm, adjusts this value to correct for system lag and overshoot issues.
4. A model of the system converts the ΔT to the equivalent change in Pulse Width Modulation (ΔPWM) duty cycle signal.
5. The signal is sent from the PC through the NI system to trigger the transistor and apply the brake, which changes the resistance torque of the feed roller.
6. The new tension is measured by the two load cell sensors and sent back into LabVIEW.
7. The data from the load cells is averaged and converted from a load to a tension with the constant transfer function, K_T .
8. This tension is then fed back into the LabVIEW control program to maintain constant tension in the webbing.

In addition to the control system, the LabVIEW program—shown in Appendix A—allows the user to fix the PWM signal.

The following sections explain how the transfer functions were determined and calibrations were completed. Specifically, Section 3.1.1 finds the calibration curves for the conversion from load cell voltage to load cell force ($V_{LC} \rightarrow F_{LC}$) and the transfer function taking the mean load cell force to web tension ($F_{LC} \rightarrow T$); Section 3.1.2 determines the predicted web tension as a function of duty cycle ($PWM \rightarrow T$); and Section 3.1.3 shows the results for different controllers.

3.1.1 Load Cell Model and Calibration

The load cells were calibrated by measuring the voltage from the Cleveland-Kidder Ultra Cartridge Transducers by hanging known masses on the roller, as proposed by Roisum [91]. Cleveland-Kidder generally connects their load cells to an amplifier circuit in order to boost the signal strength and smooth the output, but for the RFIS the amplification was done in the LabVIEW program. Like a strain gauge, the transducers were configured in a Wheatstone Bridge circuit with a 5 V differential placed across the circuit. To determine the relationship between the load and voltage, the load cells were zeroed in software to account for the weight of the roller and ensure the calibration curves would have a y-intercept of zero. Weights of 5.0, 10.0 and 15.0 lbs were attached at the load cell location and the mean DC voltage was read from LabVIEW.

As shown in Figure 3.7, there is a linear relationship between the change in voltage and the applied force. When the system is operated, the LabVIEW program initially re-zeros the load cells to account for any drift in the transducers. Over the range of loads expected in the webbing, the following relationship has been derived:

$$F_{LC}(V_{LC}) = \frac{1000V_{LC} - C}{m} \quad (3.1)$$

where F_{LC} is the average load measured by the load cell, V_{LC} is the voltage for the load cells averaged over a 0.100 s time period, C is a constant which zeros the voltage when there is no web tension, and m is the slope of the $\Delta V_{LC}/F_{LC}$ linear fit.

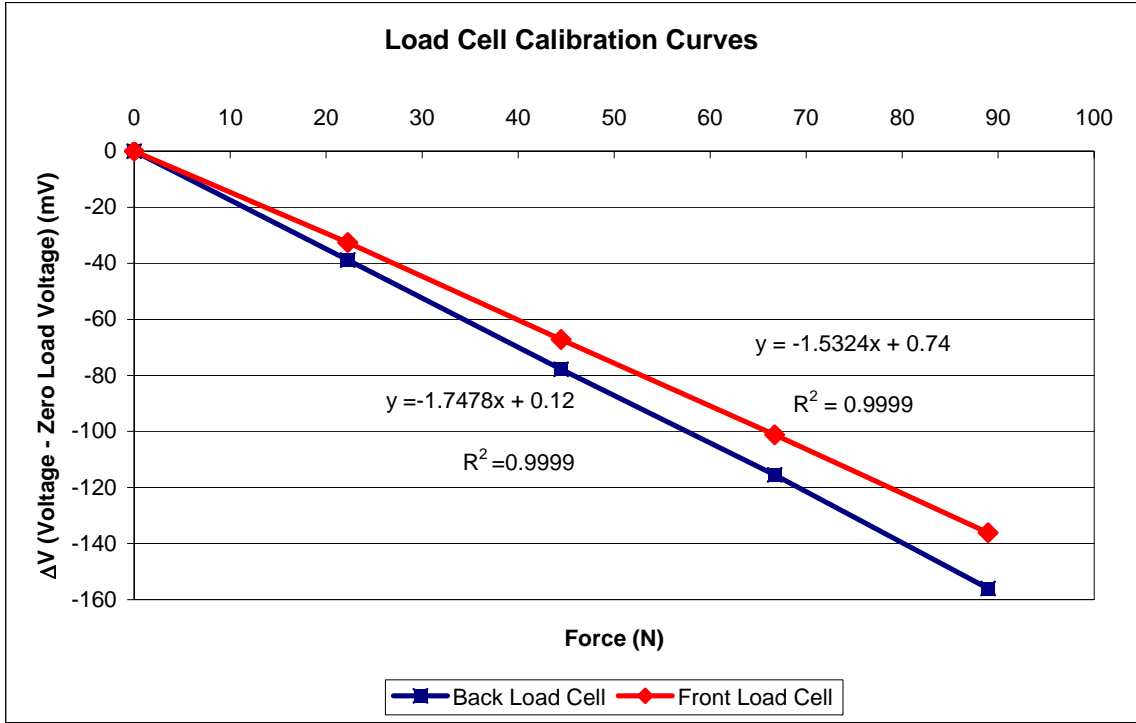


Figure 3.7: Calibration Data and Least Squares Linear Fit Line.

A static analysis was used in order to convert the load cell force measurement to web tension. The force recorded by the load cells was a function of the tension in the web and the angle that the web intersected the load cell roller. The load cell only recorded the vertical component of the force acting on the roller, so as Figure 3.8(a) illustrates, the vertical force can be found by

$$F_{loadcells} = T_{input} \cdot \cos \phi_{input} + T_{output} \cdot \cos \phi_{output} \quad (3.2)$$

where T_{input} and T_{output} are web tensions for the substrate coming into contact and separating from the load cell roller at angles of ϕ_{input} and ϕ_{output} , respectively. By assuming the rolling resistance is small, the input and output tensions are equivalent, so $T_{input} = T_{output} = T$ and the static equation simplifies to

$$F_{loadcells} = T (\cos \phi_{input} + \cos \phi_{output}) \quad (3.3)$$

Thus, the transfer function, K_T , is

$$K_T = \frac{T}{F_{loadcells}} = \frac{1}{(\cos \phi_{input} + \cos \phi_{output})} \quad (3.4)$$

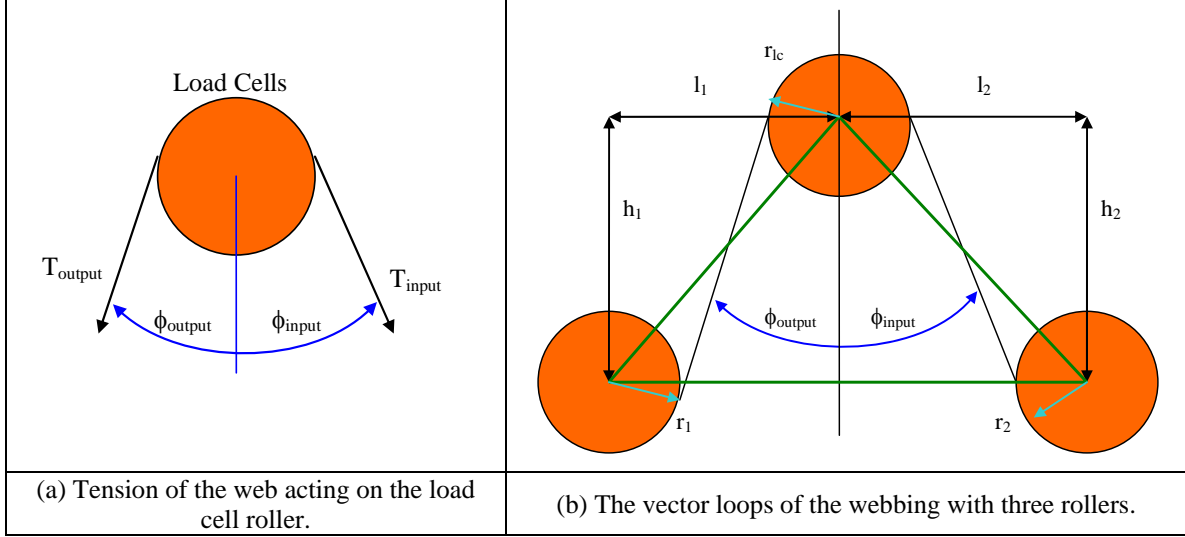


Figure 3.8: Static analysis of the webbing across the load cell roller.

Since the webbing runs tangent to the rollers, to determine the input and output angles—which due to system geometry were the same—a vector loop was created for the left side of Figure 3.8(b),

$$\vec{r}_1 + \vec{r}_{web} - \vec{r}_{lc} = l_1 \hat{i} + h_1 \hat{j} \quad (3.5)$$

where \vec{r}_{lc} and \vec{r}_1 are vectors from the roller centers to the tangent webbing and \vec{r}_{web} is the web vector from the r_1 roller to the r_{lc} roller. In scalar form, this becomes,

$$\begin{aligned} r_1 \cos \phi_{output} + r_{web} \sin \phi_{output} + r_{lc} \cos \phi_{output} &= l_1 \\ -r_1 \sin \phi_{output} + r_{web} \cos \phi_{output} - r_{lc} \sin \phi_{output} &= h_1 \end{aligned} \quad (3.6)$$

with two unknowns: the length of the web, r_{web} , and the angle, ϕ_{output} . The roller diameters are 1.90", $h_1 = 4.30$ " and $l_1 = 2.00$ ", so the angle is 1.3° and K_T is 0.500.

3.1.2 Brake Model

The electromagnetic particle brake is located on the feed roller and is controlled with a duty cycling signal from the LabVIEW control program. Static analysis of the

web system has shown that since the friction acting on the web is significantly lower than the tension force, the tension in the web can be approximated by a function of brake duty cycle. The torque induced by the brake is proportional to the brake current, shown in Figure 3.9. Note the internal resistance of the brake is 23.1Ω , so at 100% duty cycle, the circuit becomes a voltage divider circuit with 5.95 V and 0.26 A across the brake, so the maximum brake torque is $\sim 5.8 \text{ N}\cdot\text{m}$, as indicated in Figure 3.9. One key advantage to using an electromagnetic brake over a conventional DC brushless brake is that the time constant is much smaller because there is little internal inductance. This means that the frictional torque applied to the web acts quickly when the duty cycle is changed by the control. Additionally, there is no back electromotive force (EMF) because the brake does not rely on coiled wire to generate the angular resistance.

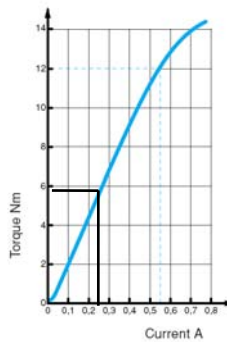


Figure 3.9: Torque vs current in the Cleveland-Kidder electromagnetic particle brake [92].

The relationship between duty cycle and voltage across the brake was determined by placing a voltmeter across the brake as the duty cycle was adjusted. Unfortunately, the voltage across the brake did not scale linearly with the duty cycle due to the time-dependant electrical components in the control circuit and brake. As a result, the transfer function between duty cycle and web tension were determined directly, as shown in the calibration curves in Figure 3.10. The relationship between duty cycle (DC) and voltage explains some of the nonlinearity and hysteresis error. It is believed that the strong hysteresis error was caused by a combination of web stretch, roller and webbing backlash, slop in the take-up roller mounts, and roller friction. The load cell data was also noisy because the web tension force drifted between the left and right load cells due to roller misalignment. Despite the system nonlinearity and sensor error, the final

calibration curves in Figure 3.10 can be represented as linear functions with coefficients of determination of $R^2_{increasingDC} = 0.988$ and $R^2_{decreasingDC} = 0.968$ using Eqs. (3.7) and (3.8).

$$T_{increasingDC} = 9.40DC + 41.5 \quad (3.7)$$

$$T_{decreasingDC} = 9.66DC + 60.9 \quad (3.8)$$

This showed the necessary linearity required to apply the proportional controller. Also since the slopes of these transfer functions were similar, it was not necessary to create separate control strategies for the increasing and decreasing tension scenarios.

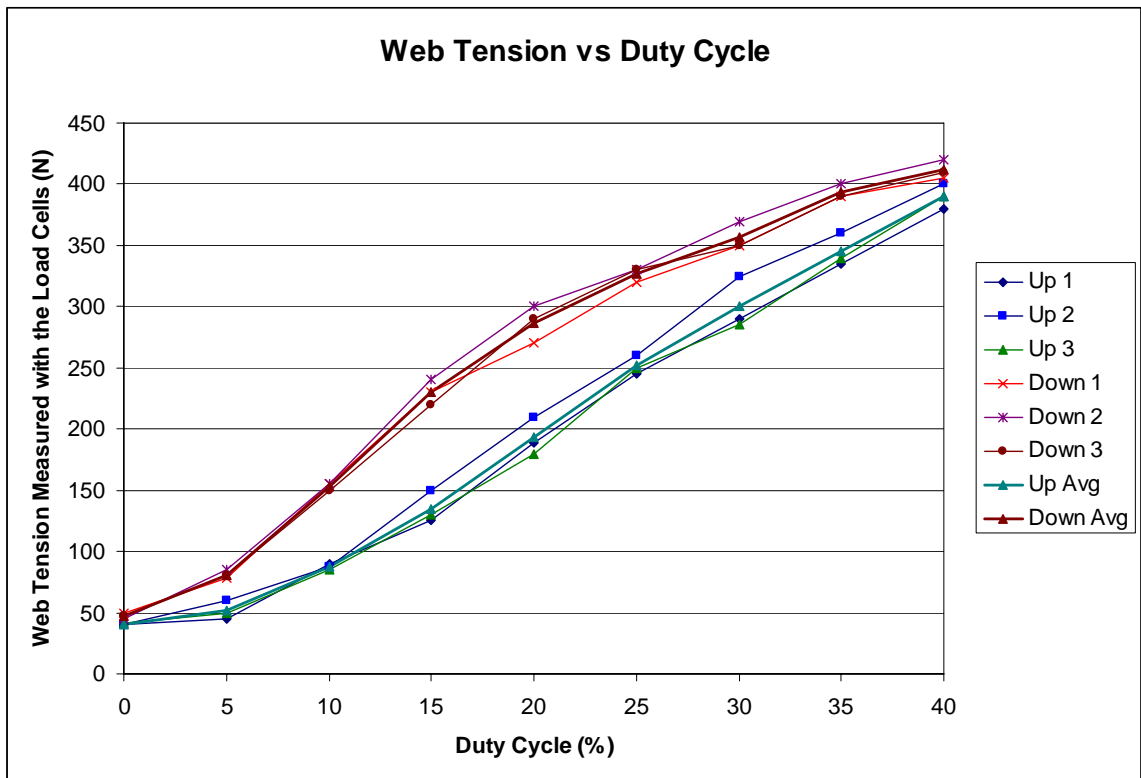


Figure 3.10: Web tension vs duty cycle calibration control curves.

3.1.3 Control Results

Since the braking control system can be represented linearly and the system did not have strict constraints on the settling time, percent overshoot, or damping, a proportional controller was created. The proportional constant, K_p , was adjusted to find

an acceptable control routine by watching the system respond to a 0-150 N step in desired tension. To produce these results the following steps were taken:

1. Web was slackened and the load cells were zeroed.
2. Linear web velocity was set to ~3 cm/s.
3. The natural tension in the web was allowed to stabilize (at ~35-50 N).
4. The control was initiated and the tension from the load cells was recorded.
5. If another test was performed, the duty cycle was zeroed and the web tension was allowed to restabilize.

The results for trials with $K_{p1} = 5 \times 10^{-3}$, $K_{p2} = 10 \times 10^{-3}$, $K_{p3} = 20 \times 10^{-3}$, and $K_{p4} = 30 \times 10^{-3}$ are shown in Figures 1-4 in Appendix B. It was found that for increasing K_p values the controller responded quicker which resulted in shorter rise times but larger percent overshoot values. The settling time, T_s , could not be calculated for the different controllers because the $\pm 2\%$ gap around the setpoint was never terminally entered due to system noise. The plant became severely underdamped with K_{p3} and marginally stable with K_{p4} , depending on initial conditions and system noise. The challenges with stability can be attributed to the system response time, which is driven by the time that it takes to tighten and provide slack in the webbing. The system itself did not become significantly unstable because at large tensions the motorized roller and take-up roller slip, but K_{p3} and K_{p4} are not suitable controllers because of their oscillatory behavior. It is more desirable to maintain the tension close to the setpoint than to reduce the overshoot or settling time, so K_{p2} was chosen as the control. The parameters and models discussed in Sections 3.1.1-3.1.3 are used in the web tension control program to maintain a constant web tension.

3.1.4 Web Speed Measurements

Although not directly fed into the control loop for the web tension, another important factor of the web system was controlling web speed. The web speed was determined with a BEI Technologies EX11 series miniature incremental rotary optical encoder attached to the motorized roller, shown in Figure 3.11.

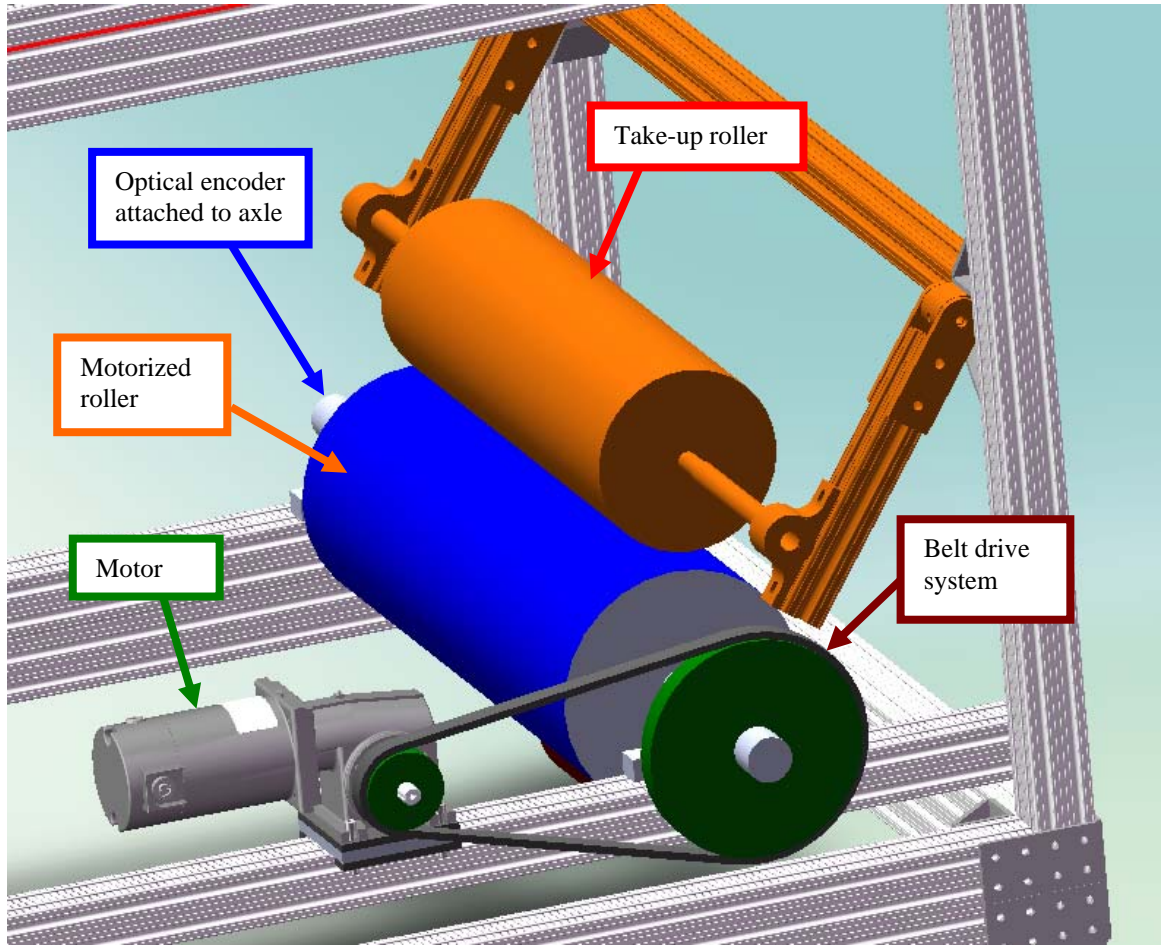


Figure 3.11: The drive system. The motor is connected to a belt drive (green) which reduces the angular velocity and increases the torque delivered to the motorized roller (blue). The angular velocity of the motorized roller is then increased as it is passed to the take-up roller (orange).

Since the take-up roller and motorized roller have the same linear velocity at the frictional contact joint, the linear web speed, V , is calculated by

$$V = r_{\text{motorized}} \dot{\theta}_{\text{measured}} \quad (3.9)$$

where $r_{\text{motorized}}$ is the radius of the motorized roller and the measured angular velocity of the roller, $\dot{\theta}_{\text{measured}}$, is calculated in LabVIEW by reading in the number of optical counts, n_{encoder} , and dividing by 1024 to get the revolutions,

$$\text{revolutions} = \frac{n_{\text{encoder}}}{1024} \quad (3.10)$$

and then converting to rad/s,

$$\dot{\theta}_{measured} = 2\pi \left(\frac{revolutions}{time} \right). \quad (3.11)$$

By substitution, the web speed is given by

$$V = 2\pi \cdot r_{motorized} \left(\frac{n_{encoder}}{1024 \cdot time} \right) \quad (3.12)$$

3.2 Tooling System

There are a wide range of manufacturing techniques which can be adapted to the RFIS to create thin films, such as those investigated by Harris et al. [93]: doctor blade, film applicator blade, melt compression, stencil printing, and slot die extrusion. However, slot die extrusion is implemented for this research, because it was found to be the best alternative for handling high viscosity, non-Newtonian polymeric solutions [89]. The T-shaped slot die was manufactured from 316 stainless steel due to its chemical resistance and mechanical properties. The slot die, shown in Figure 3.12, was assembled by bolting two die halves together which were offset by a thin 316 stainless steel shim. As shown in Figure 3.13, the full casting system was constructed such that a pressurized tank was connected to the slot die via straight piping and a ball valve, which controlled the release of material. The tank lid was equipped with the thermocouple probe, 150 psi pressure relief valve, and pressure gauge to ensure operator safety and that casting parameters were met. The tank and die heating system are discussed further in Section 3.3.

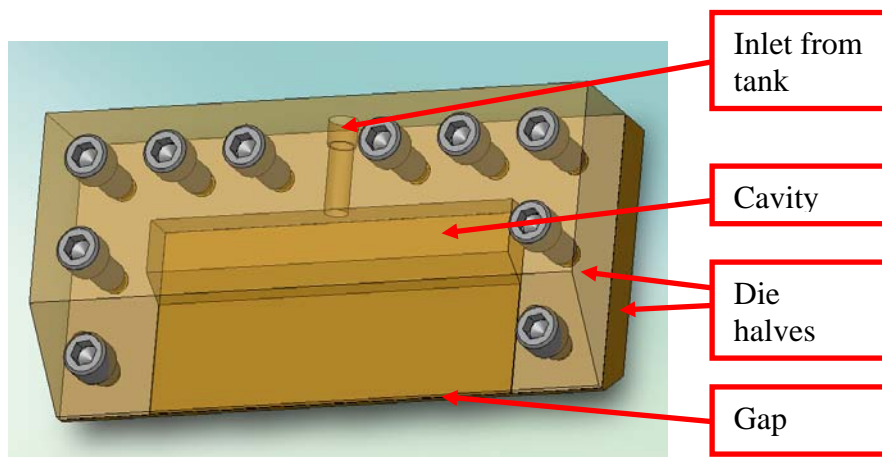


Figure 3.12: T-shaped slot die. Material enters from the top and is extruded through a very thin rectangular slit at the bottom.

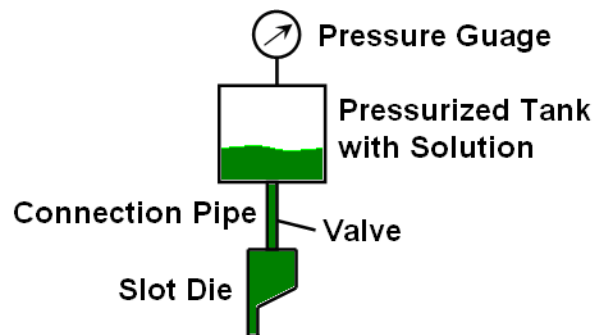


Figure 3.13: The casting tank and die setup.

To prepare the system for a batch run, the die was assembled and connected to the pipe and valve. This subassembly was then clamped into place on an 80/20 vertical rail system with plastic linear bushings and the tank was threaded into place. The system was heated to the proper temperature, the solution added to the tank, and the tank pressurized. A feeler gauge of the desired stand-off height was placed under the die to ensure proper spacing between the die and substrate. The height of either side of the rail system was adjusted with worm gears attached to rail guide blocks. This method was believed to produce a gap to within $\pm 10 \mu\text{m}$ of the desired height. The error was due to slop in the rail system and feeler gauge inaccuracy. The tooling system was susceptible to perturbations due to vibrations from the roll-feed motor and the environment, as well as misalignments in the two die plates and shim. These issues were investigated by Romero and Carvalho, who found that higher frequency noise in the inlet flow rate caused less

variation in the thickness; higher die stand-off height frequency (10 Hz vs 500 Hz) led to greater thickness variation; and when the stand-off height was varied, the overbite (downstream plate lower than upstream) exacerbated the thickness variation at lower frequencies, whereas the underbite yielded higher variation at high frequencies [94]. Their work illustrated that slot die systems are susceptible to certain forms of noise and die misalignment leads to different thickness errors. Thus, when assembling the die for each run, the shim and two die sides were carefully aligned.

3.3 Temperature Control System

In order to cast highly viscous, polymeric materials onto the substrate, the tooling system and casting surfaces were maintained at an elevated temperature. For this reason, a heating control system was installed to change the material viscosity within the tank, piping, die, and on the platens. The system has four heating circuits with type J thermocouples and EZ-ZONE PID auto-tuning controllers which run i) the tank band heaters, ii) the die cartridge heaters, iii) heated platen 1, and iv) heated platen 2. The tank is wrapped with two 800 W Watlow band heaters and two 400 W Watlow cartridge heaters are inserted into the back plate of the T-slot die. The two heated platens act as the lower surface for casting and are 6,500 W custom built Star Electric Inc. cast aluminum heaters with bayonet thermocouples running to the center of the blocks. The top surfaces were fly cut to a flatness specification of 0.001" to ensure uniformly flat surface. The tank has a bayonet thermocouple centered in the tank lid, which contacts the interior tank wall approximately 1.5 mm of the bottom surface of the tank. The thermocouple is put in contact with the tank wall to accommodate controller overshoot and prevent material overheating and degradation. Another thermocouple is attached to the exterior of the die near one of the cartridge heaters to control die heating. Since the thermocouples for the platens are located inside the blocks, the thermocouples do not directly measure the surface temperatures. So for different desired surface temperatures the thermal system was measured by an infrared pyrometer and external thermocouple until the controller setpoint was found which provided the proper surface temperatures. Based on this study, the controller setpoint temperatures for the platens are set approximately 8°C above the desired temperature to obtain the proper surface temperature.

Four different outlets were installed to provide the 208 VAC power to the four different heating circuits. Since the amperage for each of the circuits is large (two 15 A and two 40 A circuits), each of the outlets have a separate breaker to ensure the breaker will trip in the event of an electrical short.

Each of the heating stations is activated independently by flipping a toggle switch on the main panel of the enclosure. There are four LEDs next to the four controllers to indicate when the heaters receive wall power, shown in Figure 3.14. This allows the operator to easily determine the duty cycling rate and if the heater controller is functioning correctly. The tooling system (e.g., die, pipe and tank) is insulated with fiberglass fabric sown into wraps with Velcro attachments, shown in Figure 3.15. The insulation is wrapped around the tooling system to provide better thermal uniformity and reduce power usage, during system operation.

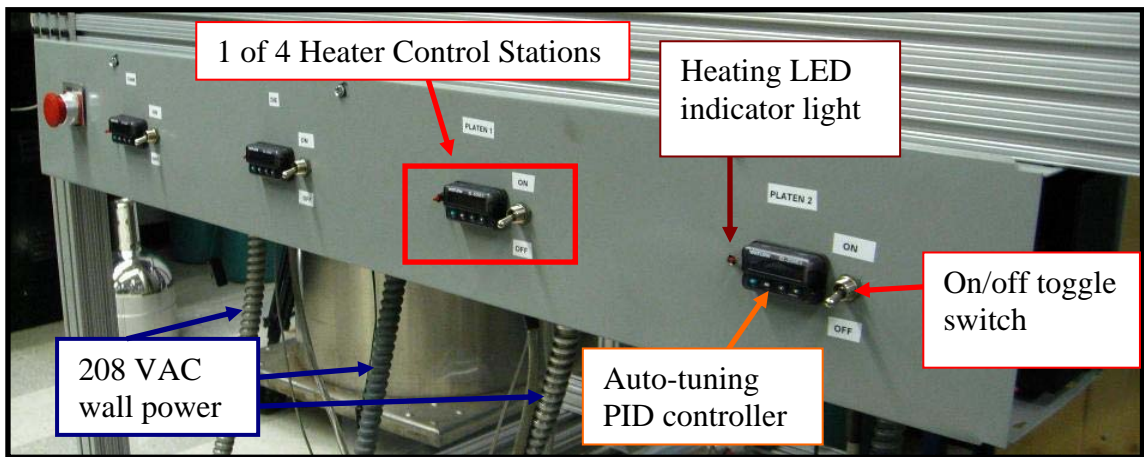


Figure 3.14: The heating control panel mounted on the electrical enclosure.

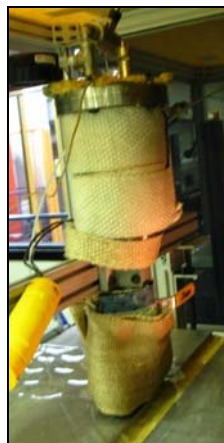


Figure 3.15: Insulation on the die and tank viewed from the downstream side.

3.4 Inspection System

The inspection system is composed of defect identification and thickness profilometry sub-components which utilize the same hardware (backlight, diffuser, lens, and camera) and are integrated into the same graphical user interface (GUI) software program. However, the defect detection system and thickness profilometer are independent in the computer program and only the image data is shared between them, as shown in Figure 3.16. The thickness profilometry hardware and calibration are discussed in Section 3.4.1 and the defect identification system conceptualization and design are investigated in Section 3.4.2. Last, the graphical user interface, which integrated both these systems, is elaborated in Section 3.4.3.

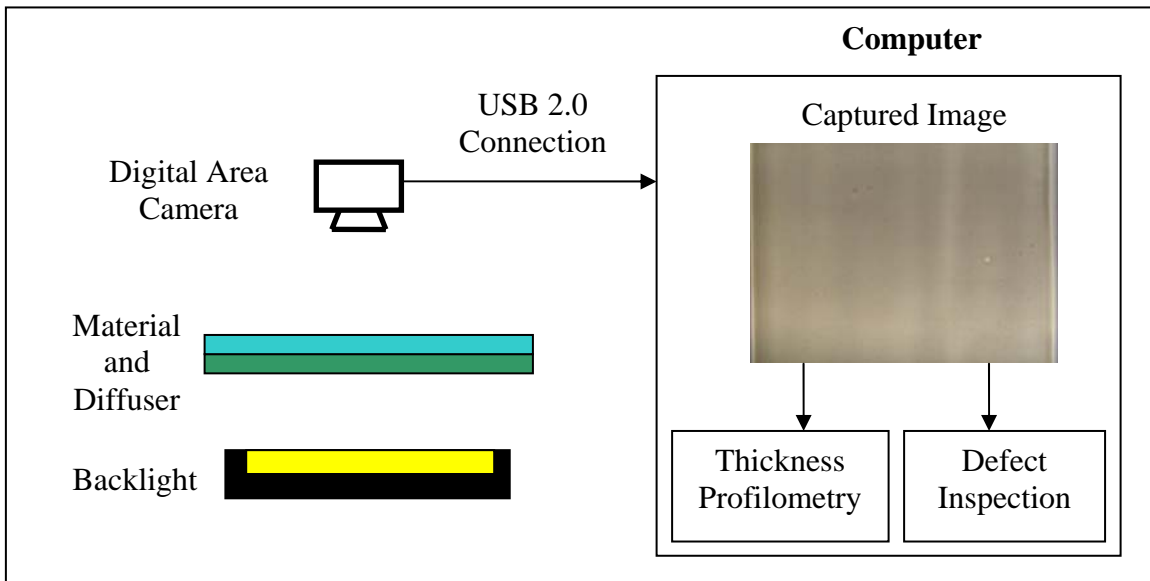


Figure 3.16: Overview of the image station hardware and software.

3.4.1 Thickness Profilometry System

Determining design specifications for the optical thickness profilometry system was not trivial, due to the range of sizes, thicknesses, and optical characteristics of the material and substrates utilized on the system. Further, due to casting variability from configuration or operational issues—e.g., uneven die heating, die shim misalignment, improper die orientation—measurements across the entire web were necessary to perform quality assurance operations. In addition, when casting parameters are adjusted or other undesired perturbations change the casting thickness, there is a real-time need to visualize

the thickness in the direction of travel. As a result, a full-field profilometer was incorporated into the system to measure the web thickness.

Since thickness variability and surface roughness are specific to the material and application, producing accuracy requirements for the thickness profilometer was difficult. As stated earlier, one of the RFIS objectives was to make a modular and flexible manufacturing and inspection system. However, based on the perceived industrial needs for the cast material, a design objective was formulated: thickness measurement errors should be less than $\pm 10 \mu\text{m}$ (or 4-5%) for 200-250 μm films. Based on the state-of-the-art profilometry methods discussed in Section 2.2, only a small subsection of techniques and no off-the-shelf products were capable of fully meeting all the design constraints. The design criteria included:

- The instrument must find thicknesses at as many locations across the web as possible to (a) match experimental studies with numerical simulations and (b) identify errors or miscalibrations in the tooling system.
- The instrument must be non-contact.
- The instrument must make in-line thickness measurements while the web is moving.
- The instrument cannot determine thickness based on scanning methods because at high web speeds it will be unable to render full-field measurements.

Additionally, it is assumed that the material is not magnetic or dielectric. Therefore, optical (interferometric) and absorption-based (X-ray, gamma ray, beta-ray, UV, IR, or visible transmission) methods were determined to be the best options for in-line thickness profilometry. After investigating the potential of these systems, transmission densitometry with visible light was found to be the best candidate profilometry tool, although CCD array detectors have photometric/radiometric measurement limitations (i.e. large numbers of pixels, nonuniformities, aliasing effects, subpixel response, and dependence on operating conditions [18]). Transmission densitometry was chosen over interferometry and other densitometry techniques because it was:

1. Applicable to a dynamic roll-feed environment

2. Capable of full-field nondestructive thickness measurements on a 25-500 μm range with an estimated 5 μm resolution
3. Simple: not requiring complex optics or controls
4. Inexpensive: a diffuse backlight, industrial camera, and lens were needed, as opposed to larger systems with multiple lenses, mirrors, or specialized sensors
5. Robust: web speed, web flutter and other vibrations would not disrupt measurements, and it was easily recalibrated for changes in temperature, camera and backlight orientation and location, and new cast material
6. Repeatable: re-zeroing the system was very simple
7. Could utilize the same hardware as the defect detection system, reducing costs and inspection system space requirements on the roll-feed machine
8. The system was adaptable for the following changes:
 - i. web speed – the camera operated at 30 fps so it could inspect the entire product at ~ 1 m/s (although a strobe light may be required for these speeds)
 - ii. casting width – the camera height could be changed or camera lens replaced for cast material width adjustments
 - iii. cast material or substrate – backlight could be replaced with different LED arrays to tailor the wavelength transmitted through the material, or if the new material were very dense, reflection densitometry could be pursued with off-axis or annular lighting
 - iv. thickness range – the intensity of the backlight could be adjusted for more or less dense materials

When specifying full-field thickness profilometry hardware, the illumination is critical. Commercial densitometer measurements are recorded with a monochromatic light source and a small aperture to the sensor. It was desired to maximize the material absorption, so multiple attempts were made to locate the maximum absorption wavelength for cast samples using spectrophotometers. However, due to difficulty associated with handling the material in its fluidic state and the samples being very thick (optically dense), obtaining the peak absorbance using spectrophotometers was

unsuccessful. As a result, halogen light is used to backlight the thin film. Although this is not optimal for specific materials, the logarithmic radiation attenuation described by Beer's law is wavelength-independent, so maximization of extinction rates through the material is unnecessary. For different materials, optical filters can be applied to the system to artificially adjust sample density.

The final transmission densitometer was simple, robust, inexpensive, and good repeatability and accuracy were expected based on the literature. The final system, conceptualized in Figure 3.17 and shown in Figure 3.18, was constructed with a Fostec fiber optic diffuse backlight connected to a Fostec ACE halogen light source, opal glass diffuser, and a Lumenera LM135M camera with a 25 mm Pentax lens. This system measured the optical density of the material by estimating influx and efflux radiation of the sample using grayscale values of the image. The optical density was then converted to the thickness of the material using the Beer-Lambert law. The Beer's law extinction coefficient, which converts optical density to thickness, must be derived experimentally for each material, but once this value is determined, the full-field thickness of the material can be measured in real-time.

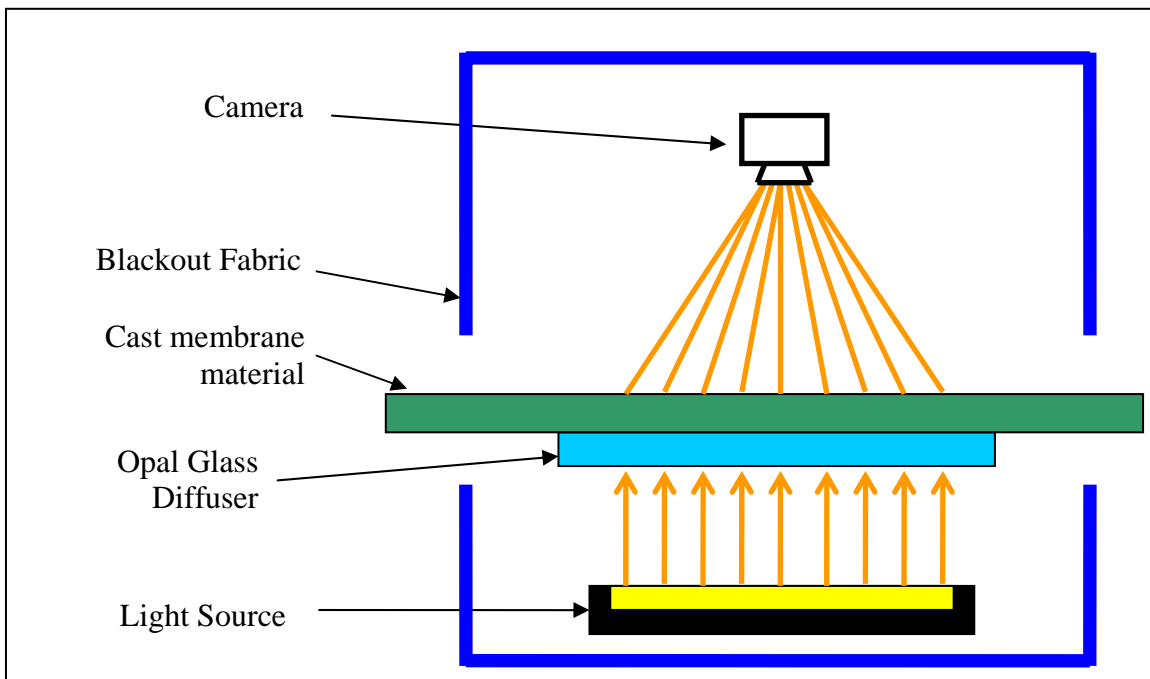


Figure 3.17: Thickness profilometry schematic.

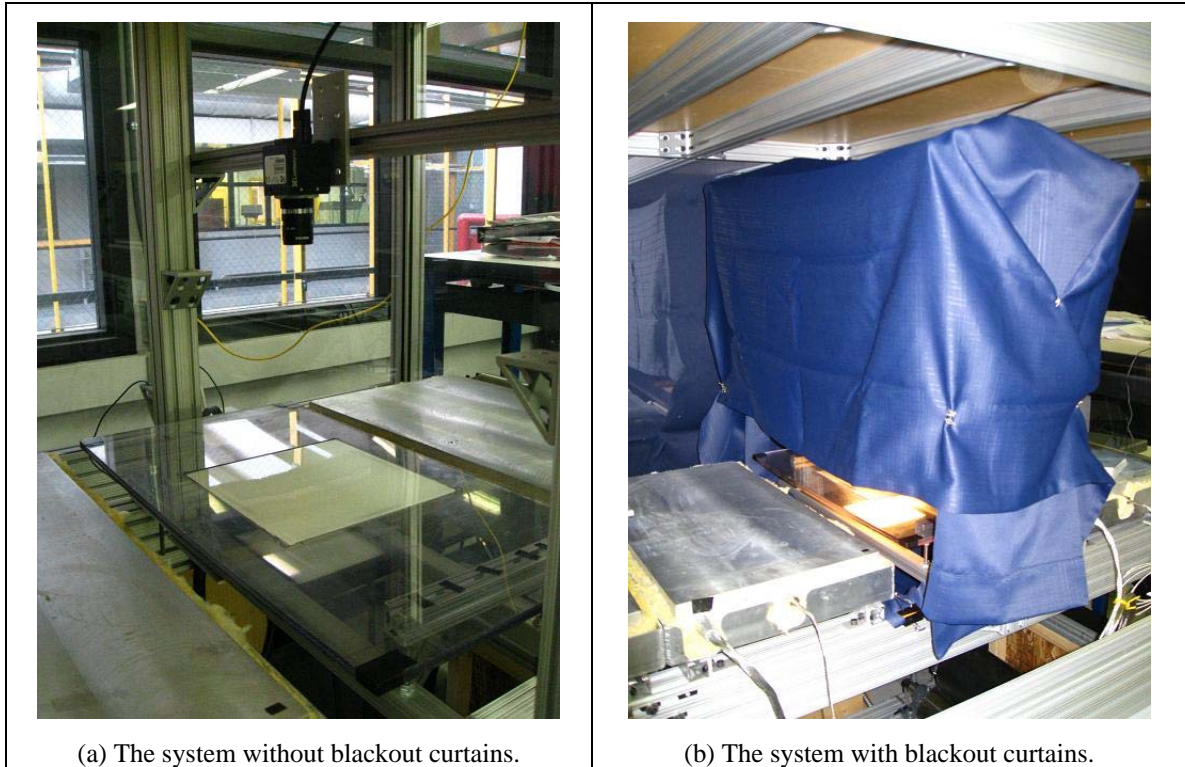


Figure 3.18: The inspection station (a) without and (b) with the blackout fabric.

3.4.1.1 Camera Selection

Due to the applicability and abundance of digital video cameras, vision systems have become increasingly popular for manufacturing inspection and therefore a wide range of camera options exist. One of the most critical decisions was selecting a proper sensor, because optical depth profilometry measurements are highly sensitive to image sensor (imager) readings since the grayscale values are converted directly to thickness values. Therefore, any noise in the image is passed to the thickness measurements, so by understanding imager characteristics, noise effects and other errors can be mitigated. Most modern web inspection systems use line scan techniques to improve the resolution of the captured images [95], however image capture must be coordinated with web position using time-delay integration (TDI). On the RFIS, the encoder did not measure the web location well—due to slack in the substrate and slipping between the motorized and take-up rollers—and high resolution images (greater than 1600 pixels in width) were not necessary, so an area scan camera was chosen. The two main types of photon-detecting sensor readout circuits are charge-coupled device (CCD) and complementary metal–oxide–semiconductor (CMOS). These camera readouts have different advantages

and disadvantages, shown in Table 3.1. One of the most significant CMOS disadvantages is its low sensitivity to light, which requires longer integration times, and therefore is susceptible to more environmental noise. As a result, a camera with a CCD sensor was selected for the densitometer.

Table 3.1: Comparison of camera sensors, adapted from [96].

CCD	CMOS
+ low noise images	- fixed pattern noise
+ pixel-to-pixel uniformity	- pixel-to-pixel nonuniformity
+ electronic shutter without artifacts	- electronic shutter effects
+ 100% fill factor	- less than 100% fill factor
+ high sensitivity to light	- low sensitivity to light
- high power consumption	+ low power consumption
- multiple voltages required	+ windowing (random pixel readout)
- clocks required (added system complexity)	+ additional control circuitry on sensor chip

For the RFIS, selecting the proper camera options was critical for effective defect and thickness inspection. The camera needed to have high resolution to capture small defects; while also having high linearity, high dynamic range, low temporal and spatial noise, high light sensitivity, and high fill factor to produce accurate densitometry measurements. While there have been some proposed methods to select a camera with application modeling [95], it is far more common to experimentally validate proposed camera configurations are satisfactory. To help hone in on critical camera parameters, early experimental work on the RFIS was performed with an 800 x 600 Banner PresencePLUS P4 color camera. Based on experimentation with membrane material and an analogous solution, the following conclusions were made regarding defect identification:

1. Higher resolution would help identify small bubble defects which were often on the order of 1-2 pixels in diameter.
2. Increasing the resolution would provide better information on the defect regions to the classification system.
3. The color information (in RGB and HSI color spaces) was unhelpful in identifying the membrane defects. Therefore a black and white camera sensor was acceptable for the vision system.
4. Since the web speeds for the prototype roll-feed system were small (under 20 mm/s), the frame rate did not need to be high.

5. Images would blur slightly if the exposure was set too long.

Furthermore, camera dynamic range and signal-to-noise ratio (SNR) play a critical role in thickness profilometry measurements, so it was important to find a 12-bit CCD area scan camera with a high SNR. Point Gray Research, Cooke, and PCO high performance cameras were considered, but a 1392x1040 Lumenera LM135M was ultimately selected based on device cost and image quality.

3.4.1.2 Transmission Densitometry Model

The approach taken to model the transmission densitometer was to couple Beer's law with a model of the CCD camera. The European Machine Vision Association (EMVA) has created a standard model for CCD cameras [97], shown in Figure 3.19. In the model, a number of photons, n_p , are photo-absorbed into the semiconductor sensor based on the wavelength-dependent quantum efficiency, $\eta(\lambda)$, and converted to a number of electrons, $n_e = \eta(\lambda)n_p$. These photo-induced electrons combine with dark noise, n_{e_dark} , which are additional electrons collected on the semiconductor due to thermal energy and other effects. All the electrons are then sent through the amplifier and discretized to the digital value, z . (For additional information on CCD sensor processes, see [18, 98]).

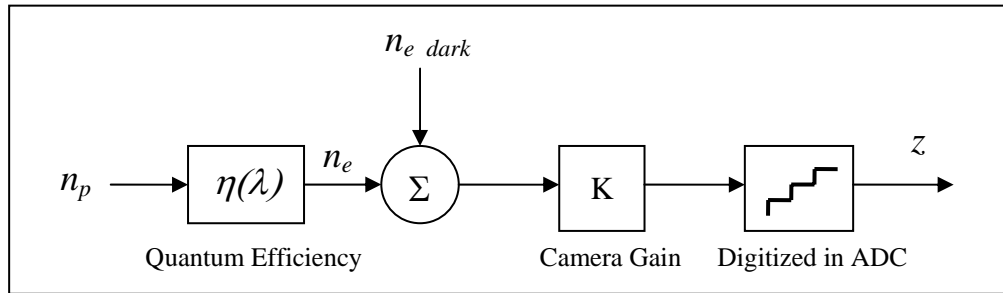


Figure 3.19: Block diagram of the mathematical pixel model from [97].

If backlighting produces an influx of Φ_i photons/s measured by a single photosite, then the optical density of the material is described as a function of photon rates, according to

$$D = -\log\left(\frac{\Phi_e}{\Phi_i}\right) \quad (3.13)$$

where Φ_e is the efflux from the material. To model steady-state illumination, the radiation fluxes are converted to the average number of photons collected by one pixel during the integration time, $\mu_p = \Phi \cdot t_{\text{integration}}$. Using the EMVA model, the grayscale readout from a pixel is represented by

$$\mu_{\text{graylevel}} = \langle K(\eta(\lambda)\mu_p + \mu_{e_dark}) \rangle \quad (3.14)$$

where K is the camera system gain (grayscale/electron), μ_{e_dark} is the average number of fictive dark electrons collected on the photosite during the exposure and $\langle \bullet \rangle$ performs the ADC by mapping continuous current values to discrete grayscale values $[0, 2^{\text{bits}}-1]$.

Density of the material is related to thickness by Beer's Law, $D = at$, so the thickness of the material can be calculated at one location using the gray value of the pixel corresponding with the influx and efflux. The thickness is calculated by

$$\begin{aligned} t &= -\frac{1}{a} \log \left(\frac{\mu_{p_efflux}}{\mu_{p_influx}} \right) = -\frac{1}{a} \log \left(\frac{K\eta(\lambda)\mu_{p_efflux}}{K\eta(\lambda)\mu_{p_influx}} \right) \\ &\approx -\frac{1}{a} \log \left(\frac{\langle K(\eta(\lambda)\mu_{p_efflux} + \mu_{e_dark_efflux}) \rangle}{\langle K(\eta(\lambda)\mu_{p_influx} + \mu_{e_dark_influx}) \rangle} \right) = -\frac{1}{a} \log \left(\frac{\mu_{\text{graylevel_efflux}}}{\mu_{\text{graylevel_influx}}} \right) \end{aligned} \quad (3.15)$$

where the extinction coefficient, a , is a function of the material and illumination wavelengths, and μ_p is a function of aperture and integration time.

Therefore, once the influx gray level has been determined, the thickness is estimated simply by reading the gray level of the pixel corresponding to material in that location. By adjusting the aperture, integration time, and gain, the function becomes a combination of the previously determined zero thickness value and the measured efflux value

$$t \approx \frac{1}{a} \left[\log \underbrace{\langle K(\eta\mu_{p_influx} + \mu_{e_dark_influx}) \rangle}_{\text{known}} - \log \underbrace{\langle K(\eta\mu_{p_efflux} + \mu_{e_dark_efflux}) \rangle}_{\text{measured}} \right] \quad (3.16)$$

with a determined experimentally. An example of this function is shown in Figure 3.20 for a hypothetical material with $a = 1.61$. The curve assumes that the mean influx gray

level is 4095 at 0 thickness. The difficulty with gray value error (from discretization, dark noise, etc.) in thick films measurements is illustrated by the dashed lines. At larger thicknesses, the accuracy of the instrument is handicapped because grayscale resolution, signal noise, and ADC yield larger measurement errors.

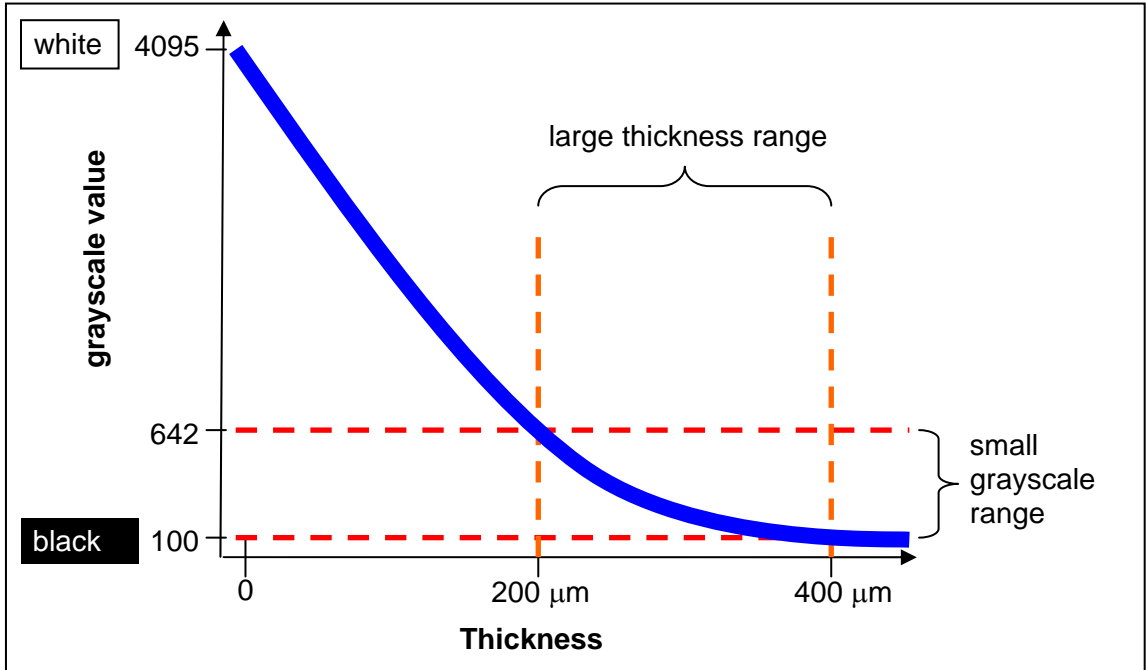


Figure 3.20: The gray value vs thickness for densitometry measurements.

However, these types of limitations are common among optical depth profilometry techniques because underlying most of these techniques are inverse problems. Forward theory takes a known depth profile and experimentation provides profile data, whereas in the inverse problem, measured data is used to reconstruct a model of an unknown thickness profile [16]. Inverse problems are inherent in optical thickness profilometry systems because the thickness is not measured directly with a micrometer, caliper, or other instrument; but rather, a non-contact optical instrument measures a thickness-dependent effect such as thermal waves, transmission radiation, or fringe patterns. For transmission densitometry, a photosensor (CCD camera pixel) is used to reconstruct the depth profile by measuring a depth sensitive parameter (grayscale), as opposed to the thickness directly.

Unfortunately, there are a number of difficulties that arise from inverse problems because they are ill-posed, i.e., they do not have the properties of existence, uniqueness,

and stability for all measured data values. The issues of existence and uniqueness manifest themselves in the densitometer measurement from the analog-to-digital conversion (ADC) and noise in the camera. Densitometer results are not unique because the image is discretized from a continuous spectrum with stochastic noise so there are different thickness values which produce the same digital value. Further, there exist different thickness values which are measured as the same grayscale. Thus, there is not a 1:1 mapping from any grayscale value, z , to a unique thickness, t . These challenges will be discussed further in Section 5.3.

3.4.1.3 CCD Sensor and Camera Noise

CCD cameras are the primary measurement detectors for radiometry. They provide precise measurements from the near IR to the x-ray wavelengths of the electromagnetic spectrum with high quantum efficiency, high linearity, large dynamic range, and low noise [98]. However, there are a number of sources of noise that must be minimized for accurate radiometric measurements. Various noise sources, their causes, and specific mitigation strategies for the RFIS are shown in Table 3.2.

Of the errors in Table 3.2, the most significant source of noise in the radiometric measurements is from the dark current. To quantify and design additional mitigation measures for the dark current, the EMVA model introduced in the proceeding section will be studied further.

Photons arrive at the sensor with a Poisson distribution [99], so the mean number of incident photons equals the variance ($\mu_p = \sigma_p^2$). Thus, the variance in the gray level is

$$\begin{aligned} \sigma_{graylevel}^2 &= \sigma_{graylevel_temporal}^2 + \sigma_{graylevel_spatial}^2 \\ &= K^2 \left[\underbrace{\eta(\lambda)\mu_p + \sigma_{e_dark}^2}_{temporal} + \underbrace{\sigma_g^2\eta^2\mu_p^2 + \sigma_{offset}^2}_{spatial} \right] \end{aligned} \quad (3.17)$$

So the temporal portion of the gray level variance is a combination of the photo-induced variance and the dark signal variance, described by

$$\sigma_{\text{graylevel_temporal}}^2 = \underbrace{K^2 \eta \mu_p}_{\text{photo_induced}} + \sigma_{\text{dark_signal}}^2 \quad (3.18)$$

The mean of the digitized dark signal noise, $K\mu_{e_dark}$, and variance, $\sigma_{\text{dark_signal}}^2$, were determined statistically by capping the lens and taking multiple readings of the gray level.

Table 3.2: Sources of radiometric error from CCD arrays (modified from [18]).

Source of Noise	Explanation	Mitigation Strategy
Quantum efficiency	The quantum efficiency (ratio of irradiant photons to produced electrons) is dependent on imager temperature and wavelength	Maintain the system at a constant temperature with the ventilation system
On-chip amplifier and electronics response (amplifier and 1/f noise)	Analog amplifier gain and offset can be affected by temperatures and voltages – these effects are generally small for good power supplies	Ventilation system circulates cool ambient air, computer USB supplies uniform voltage
Off-chip electronics (amplifier and ADC) nonlinearity	Temperature can affect the gains in the amplifier and the digitization process introduces ‘rounding’ errors	Ventilation system circulates cool ambient air
Fixed pattern noise and photo-response nonuniformity (PRNU)	Certain photosites consistently responding more or less sensitively to captured photons than others	This does not affect the densitometry measurement
Dark current and dark signal nonuniformity (DSNU)	Thermal energy produces electrons on the sensor. Strongly varies with temperature – the error doubles approximately every 8°C	Ventilation system circulates cool ambient air
Reset noise	After the capacitor used for converting electrons to voltage is reset, there is a variable number of remaining electrons in the capacitor	
Stray light	Ambient light can artificially and significantly amplify radiometric measurements	Blackout fabric surrounded the test setup
Dead pixels	Photosites which no longer are sending voltage information	Max exposure demonstrated that there were no dead pixels.
Analog-to-digital conversion	Quantizes the signal and can introduce error in the conversion from a continuous analog range to discrete values	Nothing can be done to correct for this, but it is a very small value—at most $0.5/4095 = 0.01\%$ of the full dynamic range
Saturation and blooming	Saturation occurs when the photosite ‘well’ is at full capacity. In some cases, when saturation occurs, the pixel will bloom, or spillover into another photosite.	The maximum exposure was kept below saturation
Dirt/debris on the opal glass, substrate, lens or imager	All optical surfaces which have light pass through them must be perfectly clean so that the light is not refracted or absorbed.	All optical surfaces were cleared with optical cleaning wipes
Vignetting	The periphery of the imager does not receive the same light intensity because of illumination falloff away from the optical axis	Aperture is reduced to a pinhole, discussed in Section 3.4.1.5

The spatial variance results from nonuniformity in the sensor sites. The spatial noise does not directly affect the accuracy of the densitometry system since each pixel

uses the ratio of efflux to influx photons for the density measurement. Thus, different pixel photo-sensitivities do not affect the accuracy of the instrument. However, due to vignetting and fixed pattern noise (FPN) not all the pixels use the full dynamic range (pixel bit depth) since the in-camera gain amplifies all values returned from the camera.

It is common to measure the camera error as a ratio of the pixel level to camera noise, called the signal-to-noise ratio (SNR),

$$SNR = \frac{\mu_p}{\sigma_p} = \frac{\mu_{\text{grayscale}} - \mu_{\text{grayscale_dark}}}{\sigma_{\text{grayscale}}} \quad (3.19)$$

which for the Lumenera LM135M camera is specified by the manufacturer as 60 dB (SNR = 3) [100]. However, the SNR changes depending on the amount of light incident on the sensor, as shown in Figure 3.21. The SNR is improved when photo-induced signal increases with respect to dark current noise.

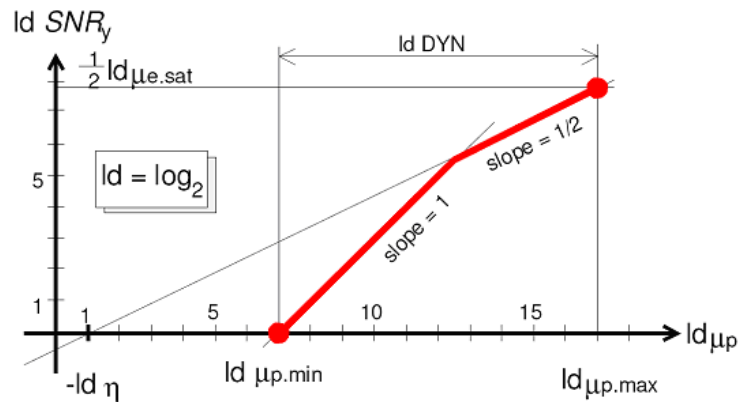


Figure 3.21: The signal-to-noise ratio vs. the number of photons for $\eta = 50\%$, $\sigma_{e_dark} = 64$ electrons, $\mu_{e_saturation} = 65,000$ electrons [99]. The image quality improves with light intensity.

Although dark current noise reduces the accuracy of the thickness measurements, binning options help provide more accurate readings. Higher resolution cameras often offer binning, which groups two or more photosites, adds their signals and reads them as one photo-detector. This is the same concept as averaging a region of pixels in post processing. In both cases, the SNR is improved. A single photosite reads the grayscale value with a normal probability distribution function $Norm(\mu_{\text{graylevel}}, \sigma_{\text{dark_signal}})$ [99]. Therefore, the mean for N number of averaged photosites becomes

$$\tilde{\mu}_{graylevel} = \sum_{i=1}^N \mu_{graylevel_i} \approx N \mu_{graylevel} = NK \eta \mu_p \quad (3.20)$$

The new variance is

$$\tilde{\sigma}_{graylevel_temporal}^2 = K^2 \sum_{i=1}^N (\eta \mu_{graylevel_i} + \sigma_{e_dark_i}^2) \approx NK^2 (\eta \mu_p + \sigma_{e_dark}^2) \quad (3.21)$$

so the signal to noise ratio is

$$SNR_{binning} = \frac{\tilde{\mu}_{graylevel}}{\tilde{\sigma}_{graylevel}} \approx \frac{N \eta \mu_p}{\sqrt{N (\eta \mu_p + \sigma_{e_dark}^2)}} = \sqrt{N} \frac{\eta \mu_p}{\sqrt{(\eta \mu_p + \sigma_{e_dark}^2)}} = \sqrt{N} \cdot SNR \quad (3.22)$$

Thus, the averaging or binning of N pixels will improve the SNR by a factor of \sqrt{N} . This noise reduction technique is used for RFIS densitometry measurements by averaging regions of 10 x 10 pixels to improve the SNR by 10. Further increasing the size of this region would improve the SNR, but it would also decrease the number of density readings.

3.4.1.4 Optical Distortions from Lensing

Ideally the radiance of a point in an imaged scene maps directly to the digital image intensity of that point. However, due to vignetting—a gradual darkening away from the optical axis—this is not the case. Vignetting in this document will encompass the combination of various optic effects including lens geometry, light refraction, and pupil aberrations. Optical vignetting occurs when periphery pixels do not share the same lines of sight as interior pixels. Thus, by reducing the aperture, the irradiance on each pixel is more uniform because the sensor is exposed to fewer off-axis rays, shown in Figure 3.22 and Figure 3.23. Essentially, some of the object rays normally incident on the peripheral photosites are obstructed by the lens barrel. Aggarwal et al. found that with a 16 mm lens, even with a relatively small field of view (10°) would yield grayscale variations as large as 31% [101]. When using a 16 mm lens with the RFIS, the variance was found to be even higher (>100%), illustrated in Figure 3.23.

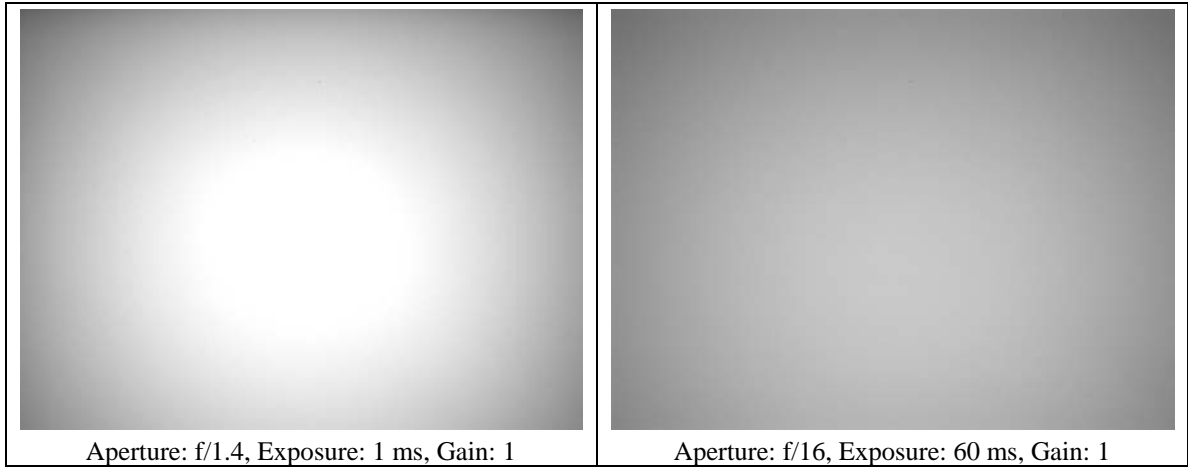


Figure 3.22: Vignetting on the roll feed imaging system for a large pupil (f/1.4) and a pinhole aperture (f/16). Note that the f-number is larger for smaller pupil diameters.

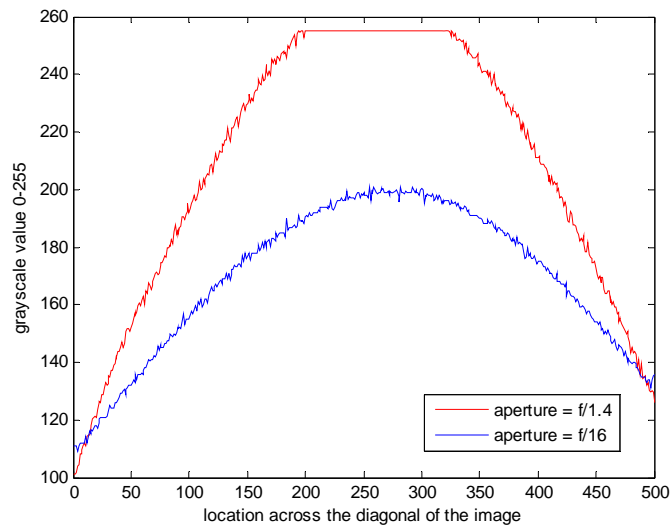


Figure 3.23: The effect of aperture on vignetting, shown by taking a grayscale profile diagonally across the images in Figure 3.22. The image with the larger aperture saturates in the center, whereas the smaller aperture does not.

Vignetting is particularly pronounced when there is significant off-axis lighting, because these rays do not converge at the focal point and create nonuniformity across the sensor. As shown in Figure 3.24, when the aperture is decreased from A-A' to B-B' the pupil is illuminated more evenly and sensor pixels are not exposed to the off-axis light. Although it appears that the side of the sensor would be brighter in Figure 3.24, when all the off-axis rays enter the sensor, the center of the sensor receives the greatest irradiance, and therefore appears the brightest.

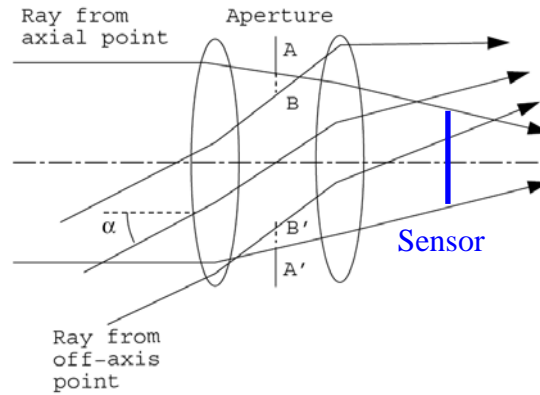


Figure 3.24: Off-axis lighting causing vignetting in a double-Gauss lens, like those used on the roll-feed system [101]. As the aperture is reduced, the off-axis rays directed to the edge pixels are blocked.

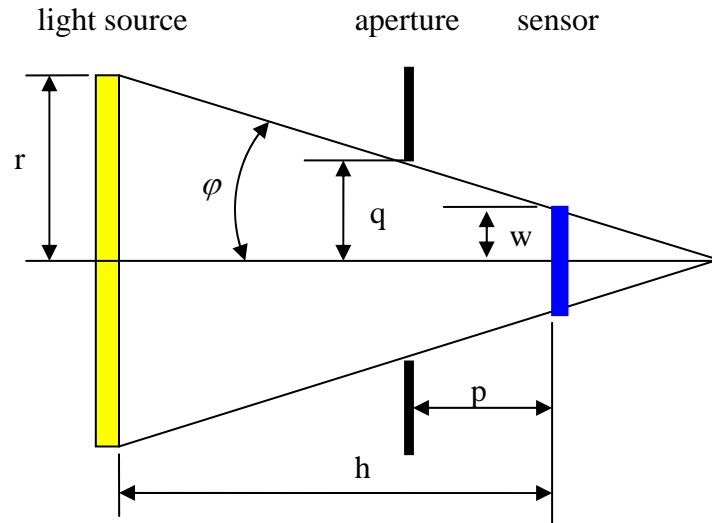


Figure 3.25: Geometrical setup with a uniform Lambertian luminaire irradiating the camera sensor through a single lens [99].

Even with the aperture reduced to a pinhole and a uniform light source centered on the optical axis, vignetting still occurs because of lens geometry. This is evident with a simplified lens model developed by Dierks [99]. As shown in Figure 3.25, a uniform light source is subtended by a cone with an interior half-angle φ , such that

$$\tan \varphi = \frac{q - w}{p} = \frac{r - w}{h} \quad (3.23)$$

where q is the mount radius, p is the flange focal length, r is the luminaire radius, and w is the distance from the optical axis to the edge of the sensor. The lens used on the RFIS

was a Pentax C-1614 16 mm C-mount lens with $q = 12.5$ mm and $p = 17.5$ mm. The Lumenera 1392x1040 pixel sensor format was $\frac{1}{2}$ " (6.5 mm x 4.8 mm), so the largest distance to a pixel from the optical axis was 4.04 mm and $\varphi = 25.9^\circ$. The cosine-fourth law [102] states that the pixel irradiance, Φ_{pixel} , decreases proportionally with the cosine of the half-angle to the fourth power,

$$\Phi_{pixel} = \frac{\Phi_e \pi \cdot q^2 \cos^4 \varphi}{4p^2} \quad (3.24)$$

So, for the Pentax lens and Lumenera camera geometry, there is a $\sim 3.5\%$ drop in the irradiance on the corner pixels in comparison to the center pixels. However, Aggarwal et al. noticed that in practical applications the cosine-fourth law significantly underestimates the true photometric drop-off and found that pupil aberrations accounted for a significant amount of the grayscale drop-off when the aperture was small [101].

Pupil aberrations create additional darkening away from the optical axis via nonlinear refractions through the lens. The aberrations are not caused by imperfections in the lens, but rather from the refraction through spherical lenses. Lens calculations rely on a paraxial approximation—or a small angle assumption—which presumes the light rays converge to a single point [103]. In reality, spherical aberration cause the light to converge within a region which creates additional nonuniformity through

1. pupil centroid shift – as the aperture is reduced, the centroid of the pupil may shift, causing the optical axis to not align with the center of the pupil
2. pupil shape – when the pupil is constricted the shape becomes polygonal, but the geometry is often irregular so pixels are unevenly irradiated
3. sensor tilt – the sensor was not held perpendicular to the optical axis of the lens

Another form of aberration which leads to vignetting is astigmatism, in which a point off the optical axis has the point converge on the sensor at different locations depending on the plane through which the optical axis is viewed [103]. Furthermore, there are spatial distortions caused by the lens, commonly called barrel or pincushion distortion, because they appear to bend the sides of the image inward or outward. Distortion changes the magnification of the image relative to the distance away from the optical axis. Therefore, on the RFIS a lens with a large focal length was desired to mitigate distortion.

Some research has gone into correcting vignetting effects in images [104, 105], however these algorithms only normalize the data using mapping functions or nonlinear look-up tables. They do not improve radiometric measurements because they denoise the image via pixel normalization. Thus, the vignetting effects were minimized on the RFIS by reducing the aperture and using a lens with a long focal length. In the final RFIS optical setup, vignetting effects reduced corner pixel influx grayscale values by approximately 35% of the full dynamic.

3.4.1.5 Camera and Lens Calibration

The Lumenera LM135M parameters were selected to improve densitometry measurements. There were a number of tradeoffs considered when choosing the camera operating settings, listed in Table 3.3. The settings were carefully selected based on their influence on the objectives, however in many cases the objectives had conflicting adjustments recommendations, so they were balanced through an iterative method.

Table 3.3: The camera objectives for densitometry and defect detection.

Objective	Sub-objectives	Parameters Adjustments to Achieve Objective
Maximize densitometry accuracy	Maximize SNR	↑ aperture, ↑ integration time, ↑ gain, ↑ binning, ↑ backlight intensity, ↓ lens focal distance. Maximizing the amount of light will increase the SNR and provide more accurate readings as per Figure 3.21.
	Minimize saturation	Reduce the light reaching all the sensors such that very few—preferably none—of the pixels reach a gray value of 4095. ↓ aperture, ↓ integration time, ↓ gain.
	Reduce spatial error/noise and vignetting	↓ aperture, ↑ binning, ↑ lens focal distance. Depending on when the noise enters the signal, ↑ gain, see [99].
Maximize densitometry resolution	Maximize dynamic range of each pixel	This requires balancing aperture, gain, and integration time to not saturate the pixels, while keeping them as close to saturation as possible when there is no material ($D = 0$).
Capture clear images	Reduce blur	↓ integration time

It was desired to have all the pixels just below the saturation level (4095) when there was no material on the backlight. To do this, the gain, aperture and integration time were set. Since the in-camera gain is part of the system gain, K , which amplifies the dark current noise along with the light-induced signal, the camera gain was kept to the lowest value (1). The aperture influenced inter-pixel gray value variation (i.e., vignetting), so a small aperture was set, f/8—albeit, not the smallest possible, which was f/16. f/8

allowed four times more sensor illumination, so the exposure could be reduced which alleviated blur and temporal noises. Also, Aggarwal et al. showed that there was little difference in vignetting effects between f-numbers of 4 through 16 [101]. Since there were different offsets and gains for each of the pixels (some of the pixels were ‘hotter’ or ‘colder’ than others) and there was strong vignetting in the optical setup, the integration time was carefully selected to maximize the gray values across the sensor, while also minimizing the number of saturated pixels. The pixel gray value histograms for integration times of 22, 23.5 and 25 ms are shown in Figure 3.26. With large integration times (25 ms), there was significant saturation, but with lower integration times (22 ms), there were nearly no saturated pixels. The saturation trend versus integration time is plotted in Figure 3.27. At approximately 23.5 ms the number of saturated pixels increased drastically, so the integration time was chosen to be 23.25 ms, because this maximized the densitometry resolution while minimizing the saturation error. For this integration time, less than 0.25% of the pixels were saturated for influx measurements.

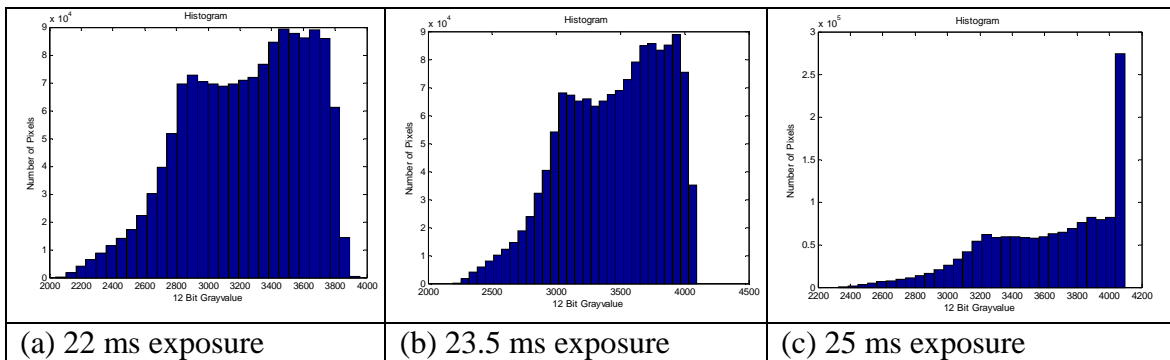


Figure 3.26: The histogram of pixels with exposures of (a) 22 ms, (b) 23.5 ms, and (c) 25 ms.

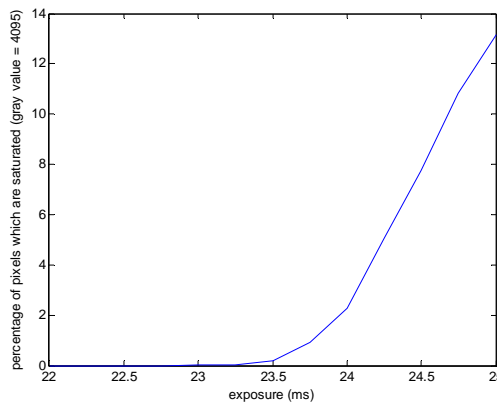


Figure 3.27: Number of saturated pixels for different integration times (gain = 1, f/8).

Even after calibration, not all the pixels were capable of measuring just below a gray value of 4095 at $D = 0$ due to fixed pattern noise and vignetting effects. Once the camera gain, exposure, and aperture were set, the distribution of pixel locations for $D = 0$ was known. The grayscale influx determines the efflux grayscale-to-density mapping for each of the pixels. The ‘Optimal Pixel,’ shown in Figure 3.28, utilizes the full range of digital values in the camera and therefore has the greatest SNR, because it produces more photo-induced current for a given density. In the case of the ‘Dark Pixel’ curve, there is less photo-induced current with respect to dark current, so the SNR is poor. However, the number of bits responsible for this signal is still more than 11 (a gray value of 2048), so the pixel still provides good resolution. Lastly, the ‘Saturated Pixel’ curve is shown in Figure 3.28. In reality, this curve truncates at 4095 because it maximizes the ADC output. Therefore, it is undesirable to have saturated pixels because densities from $D = 0$ to the density associated with a digital value of 4095 have the same measurement, resulting in thickness errors for all densities. The degree of the error is dependent on the number of gray levels that are truncated, e.g.

$$z_{truncated} = K \left(\eta n_p + n_{e_dark} \right) - \left(2^{bits} - 1 \right) \quad (3.25)$$

However, it is impossible to know $z_{truncated}$ via experimentation because the ADC loses this information. The truncation results in a density shift given by

$$D_{shift} = D_{actual} - D_{predicted} = -\log \left(\frac{z_{efflux_unsaturated}}{z_{influx_unsaturated}} \right) + \log \left(\frac{z_{efflux_saturated}}{z_{influx_saturated}} \right) \quad (3.26)$$

where $z_{influx_unsaturated}$ and $z_{efflux_unsaturated}$ are not truncated if above 4095. When the efflux grayscale is in the range $[0, 4095]$, $z_{efflux_unsaturated} = z_{efflux_saturated}$ and the shift in density simplifies to

$$D_{shift} = \log \left(z_{influx_unsaturated} \right) - \log \left(z_{efflux_unsaturated} \right) \quad (3.27)$$

where $z_{influx_saturated} = 4095$ for a 12 bit camera. The density shift versus number of truncated gray values is shown in Figure 3.29. The result shows that the density shift

increases nearly linearly with the number of truncated gray values, and that even for small truncations, there is significant density error. Therefore, the number of saturated pixels and the degree of saturation must be minimized because the density shift maps directly to thickness error.

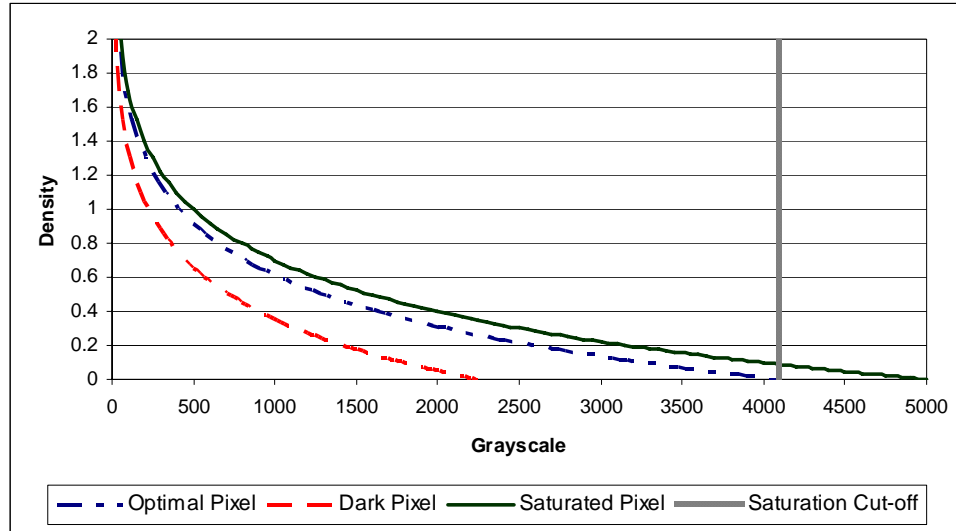


Figure 3.28: Grayscale vs density for different influxes.

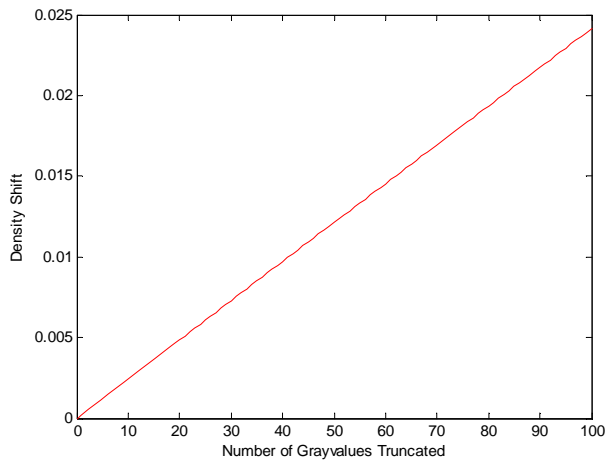


Figure 3.29: Density error from saturated pixels vs number of gray values truncated.

3.4.1.6 Quantification of Densitometry Noise

Using the procedure outlined in [97, 99, 106], the camera parameters were calculated through a series of tests. Initially a dark run was performed (leaving the lens cap on) to measure $\sigma_{\text{graylevel_temporal_dark}}^2 = K^2 \sigma_{e_dark}^2$ and $\mu_{\text{graylevel_dark}} = K \mu_{e_dark}$. Then

light-induced runs calculated, μ_p , $\mu_{graylevel}$, and $\sigma_{graylevel_temporal}^2$, by stepping through the range of integration times available in the camera. The mean gray values and temporal gray value variance for the dark and light-induced cases were determined by

$$\mu_{graylevel} = \frac{1}{N} \sum_{i,j} z(x_i, y_j) \quad (3.28)$$

$$\sigma_{graylevel_temporal}^2 = \frac{1}{2N} \sum_{i,j} [z_A(x_i, y_j) - z_B(x_i, y_j)]^2 \quad (3.29)$$

where N is the total number of photosites and i and j are the indices for the x and y directions, z is the measured grayscale at that location, and A and B represent different photos. The total grayscale variance was found by looking at adjacent pixels in a single image

$$\sigma_{graylevel_total}^2 = \frac{1}{N} \sum_{i,k} (z(x_i, y_{2k}) - z(x_i, y_{2k+1}))^2 \quad (3.30)$$

The results from the EVMA photon transfer calibration method are shown in Appendix C. The results show that for the integration times used on the RFIS, the mean dark grayscale was around 2.1, although one pixel was consistently 10 gray levels larger than all other pixels. As a result, this “hot pixel” was removed from all further studies and densitometry measurements. Excluding this pixel, the maximum temporal grayscale from dark current was typically between 18-20. The temporal variance for numerous dark image pairs was always between 0.71 and 0.78; and for multiple dark images the grayscale variance was about 2.75. From the data in Appendix C, the overall system gain was found to be 0.1716 using the regression line formula,

$$K = \frac{\sigma_{graylevel_temporal}^2 - \sigma_{graylevel_temporal_dark}^2}{\mu_{graylevel} - \mu_{graylevel_dark}} \quad (3.31)$$

Since the dark grayscale shift occurred as a result of the capacitor unsuccessfully removing all the charge (reset error) and dark electrons collecting at the pixel with a Poisson distribution, the dark grayscale probability of each pixel can be modeled with a normal distribution,

$$P(z_{dark}(x_i, y_j)) = Norm(\mu_{graylevel_dark}(x_i, y_j), \sigma_{graylevel_dark_temporal}(x_i, y_j)) \quad (3.32)$$

Therefore, by averaging a number of images, the grayscale variance at each pixel decreases. However, averaging images this way is only practical for calculations of the grayscale influx because the grayscale efflux is determined while the material on the web is moving. As the number of images, M , included in the influx gray level estimation increases, the standard deviation approaches 0, and the probability approaches the mean, i.e. $P(z_{dark}(x_i, y_j)) = \mu_{grayscale_dark}(x_i, y_j)$, by the law of large numbers. The density probability function can then be defined as

$$P(D) = -\log \left(\frac{P(z_{efflux})}{\sum_{k=1}^M P(z_{influx_k})} \right) \quad (3.33)$$

$$\approx -\log \left(\frac{z_{efflux_graylevel_photo_induced} + Norm(\mu_{graylevel_dark}, \sigma_{graylevel_dark_temporal})}{\mu_{influx_graylevel_photo_induced} + \mu_{graylevel_dark}} \right)$$

with the assumption that photo-induced gray values have no variance. This equation illustrates that (a) even averaging the influx images, there will be dark grayscale values in the influx, and (b) the noise is a larger portion of the efflux signal in the case of small photo-induced gray levels. The camera has $\mu_{graylevel_dark} = 2.1$ and the $\sigma_{graylevel_dark_temporal} = 0.9$, so the dark grayscale values represent a small portion of the signal when the photo-induced grayscale value is large, but for dense material measurements, these errors reduce density accuracy. Therefore, this limitation must be taken into consideration when selecting this instrument for measurements of specific materials.

3.4.1.7 Densitometry Calibration

The densitometry system was calibrated to remove error in the measurements. The tests were run at night with the lights turned off and a thick blackout fabric placed around the testing system to eliminate extra photo-induced gray values from skewing

results. When the backlight was off, this setup had a mean gray level of 2.44 and a variance of 0.93—slightly higher than $\mu_{\text{graylevel_dark}}$ and $\sigma_{\text{graylevel_temporal}}^2$. When the room lights were on, but the fabric was in place, the mean and variance increased to 11.25 and 2.1.

The first study determined if the location on the backlight affected the density measurements. In order to determine the accuracy of the densitometry instrument at these locations, an X-Rite Standard Densitometer Calibration Sheet conforming to ANSI PH2.19-1986 and ISO 5/2-1985 standards was used as reference for density values of 0.06, 0.26, 1.46, 2.87, and 3.62 ± 0.02 D. A series of images of the X-Rite calibration sheet were taken so that four locations with varying degrees of vignetting (or $\mu_{\text{graylevel_influx}}$) had images of 0.00, 0.06, 0.26, and 1.46 calibrated densities. D = 2.87 and 3.62 values were not used, because these measurements approached the dark current noise floor, and therefore did not assist in the calibration. An average of 15 images of the backlight without material was used to find the influx grayscale values for all the pixels. To reduce the temporal noise in the measurements, the grayscale, z , was averaged over 11 x 11 pixel areas, so the density was found by

$$D = \log \left(\sum_{\text{images}} \sum_{i,j} z_{i,j}(\Phi_{\text{influx}}) \right) - \log \left(\sum_{i,j} z_{i,j}(\Phi_{\text{efflux}}) \right) \quad (3.34)$$

where i and j were indices of the 11x11 areas. The locations of these regions and the data for each of the regions are shown in Appendix D. A summary of the empirical results is shown in Table 3.4. All the density measurements were smaller than the “true” density from the calibration sheet, but the discrepancy was far larger than could be attributed to grayscale dark current or ambient lighting. Therefore, all the measurements under-predicted the density and would under-predict the thickness of thin films. The degree of density under-prediction and the thickness error for a theoretical material with an extinction coefficient of 1.2 D/mm are shown in Table 3.4. Note that the grayscale errors for 0.06 D were the largest, but this did not produce the largest density or thickness errors because of the logarithmic mapping from grayscale to density. The source of the density shift can likely be attributed to the X-Rite sheet being calibrated for a different light source and sensor. Transmission is wavelength dependant, so density changes based on

the illumination source and sensor. Since the Fastec halogen light did not provided the same spectral influx and the sensor did not have the same quantum efficiency as the X-Rite densitometer, there was a drift in all the density measurements, shown by the density error values.

Table 3.4: The error results for each of the measurements.

	Density	Grayscale Error	Density Error	Thickness Error for a = 1.2 D/mm
Region 1 ($\mu_{\text{graylevel_influx}} = 2687$)	0.00 D	31.6970	-0.0034	-2.83 μm
	0.06 D	94.4620	-0.0039	-3.25 μm
	0.26 D	18.1606	-0.0061	-5.08 μm
	1.46 D	44.5791	-0.0877	-73.08 μm
Region 2 ($\mu_{\text{graylevel_influx}} = 3503$)	0.00 D	43.6088	-0.0047	-3.92 μm
	0.06 D	119.3951	-0.0054	-4.50 μm
	0.26 D	37.3957	-0.0085	-7.08 μm
	1.46 D	64.5811	-0.1189	-99.08 μm
Region 3 ($\mu_{\text{graylevel_influx}} = 3992$)	0.00 D	46.4303	-0.0057	-4.75 μm
	0.06 D	294.5364	-0.0066	-5.50 μm
	0.26 D	80.2958	-0.0104	-8.67 μm
	1.46 D	54.9904	-0.1406	-117.17 μm
Region 4 ($\mu_{\text{graylevel_influx}} = 4087$)	0.00 D	17.3273	-0.0028	-2.33 μm
	0.06 D	223.6601	-0.0032	-2.67 μm
	0.26 D	152.8370	-0.0051	-4.25 μm
	1.46 D	82.8027	-0.0741	-61.75 μm

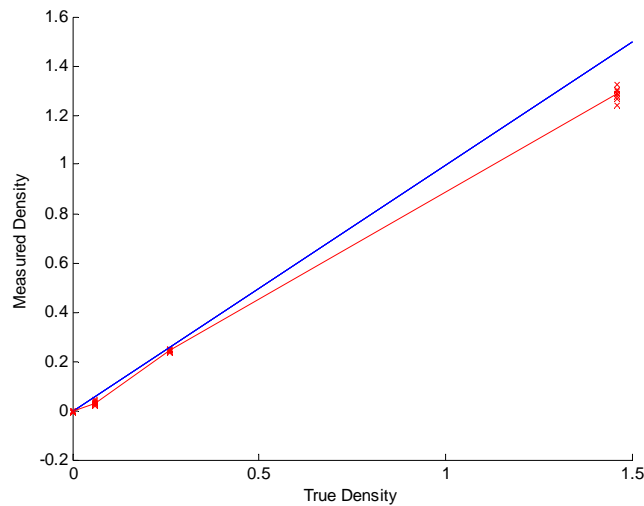


Figure 3.30: The measured density vs true density. The blue line shows perfect matching, so the difference between the red and blue lines represents the mean error.

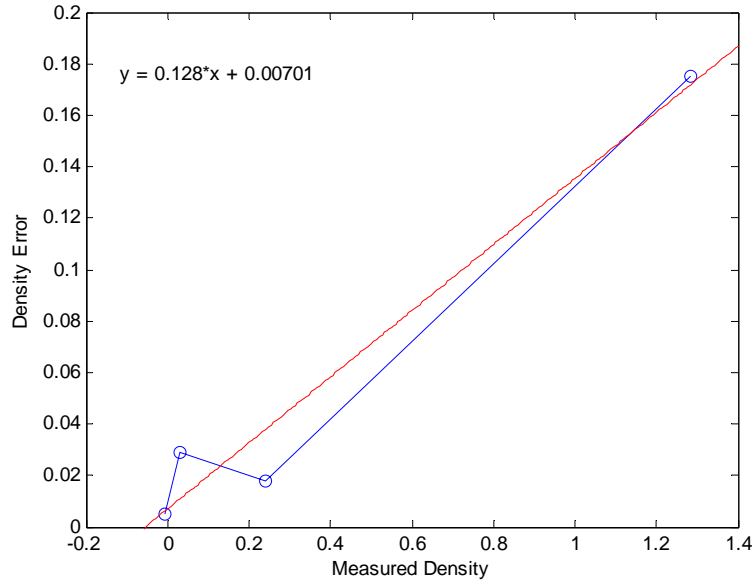


Figure 3.31: Density error vs measured density with a linear fit used for calibration.

Since the error had the same trends regardless of the location on the image, a universal correction for each of the pixels was applied to match the calibration data. First, densities of 0.00, 0.06, 0.26, and 1.46 were found for 9 images at various locations on the backlight, shown in Figure 3.30. Then the density correction function was derived, based on a least-squares line through the error data in Figure 3.31, such that

$$\begin{aligned}
 D_{corrected} &= -\log\left(\frac{\mu_{grayscale_efflux}}{\mu_{grayscale_influx}}\right) + C_{correction}(\mu_{grayscale_efflux}, \mu_{grayscale_influx}) \\
 &= -1.128\log\left(\frac{\mu_{grayscale_efflux}}{\mu_{grayscale_influx}}\right) + 0.00701
 \end{aligned}
 \tag{3.35}$$

Using the calibrated equation for density, 129 images of the calibration sheet were taken and the four densities were calculated. The locations of the measurements are shown in Figure 3.32. The results for the calibrated and uncalibrated equations are shown in Figure 3.33. It was found that the corrected densitometry readings were significantly more accurate. The errors for the calibrated system are displayed in Figure 3.34 and quantified in Table 3.5. The errors for the full-field densitometer were slightly larger than commercially available systems. For instance, the X-Rite 361T has a ± 0.01 D

repeatability and ± 0.02 D linearity for densities between 0–5 D [70]. The full-field system also did not have the same range as off-the-shelf systems. However, the full-field system offers the ability to measure an area which is 1200 times larger than available off-the-shelf systems.

The results show that with increasing density, the absolute mean error and error range increased. It should also be noted that the spike in error standard deviation at high densities was due to poor SNR, but when comparing the standard deviation and error range percentages to the other densities, the high density measurements at 1.46 D performed comparably to 0.26 D. Although, densities on the order of 1.46 D were not required for thickness measurements studied in this thesis. For semi-transparent materials with extinction coefficients in the range of 0.5-2 D/mm (e.g., the material studied in Chapter 4), 1.46 D measurements correspond to 730-2920 μm thick samples, which are outside the 25-400 μm manufacturing range studied in this work. However, these measurements indicated how sensor noise affects density measurements at lower gray values. It should also be noted that the mean error results were not considered a limitation of the instrument. The X-Rite calibration sheet guaranteed density accuracies to within ± 0.02 D, so much of the mean error was likely caused by this variation and explains why 0.06 D measurements were consistently low and the 0.26 D measurements were consistently high.

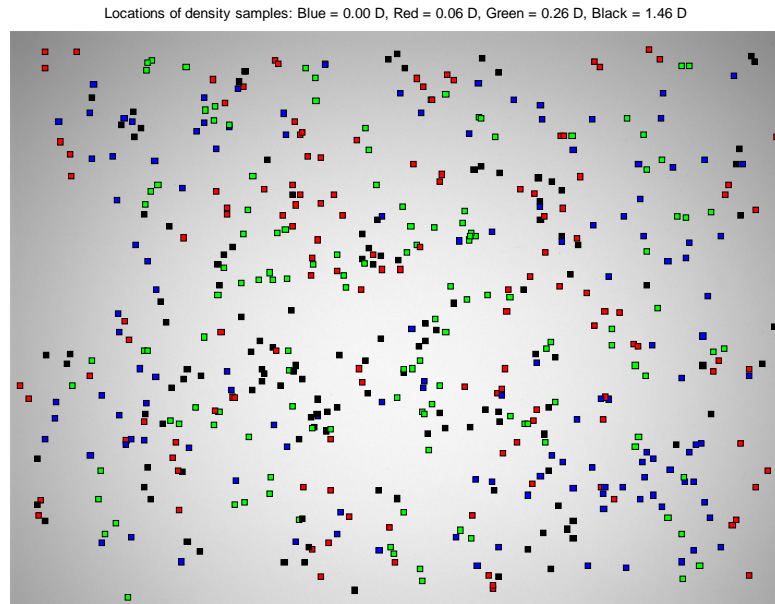


Figure 3.32: Corrected densitometer measurement locations.

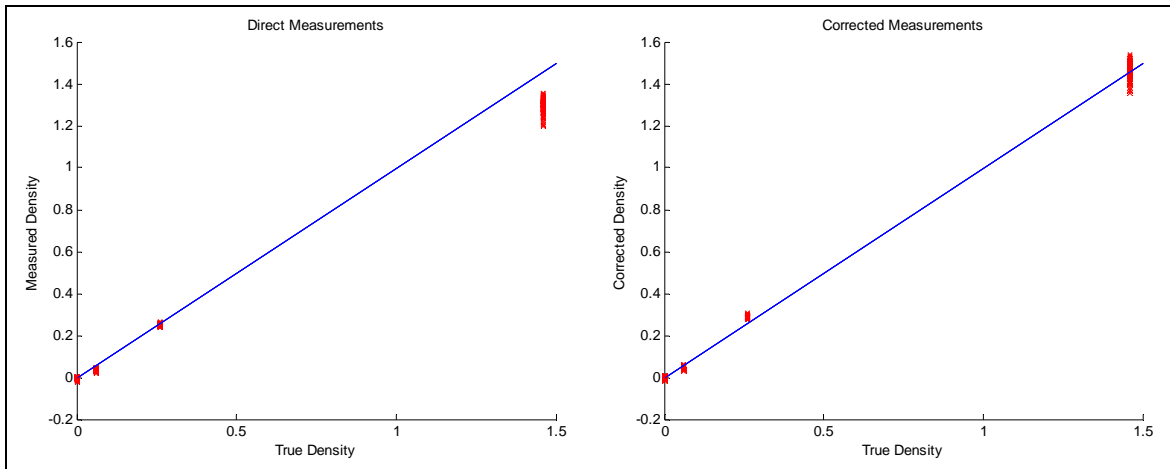


Figure 3.33: Comparisons of the measurements using the direct method (left) and the calibrated densitometer (right).

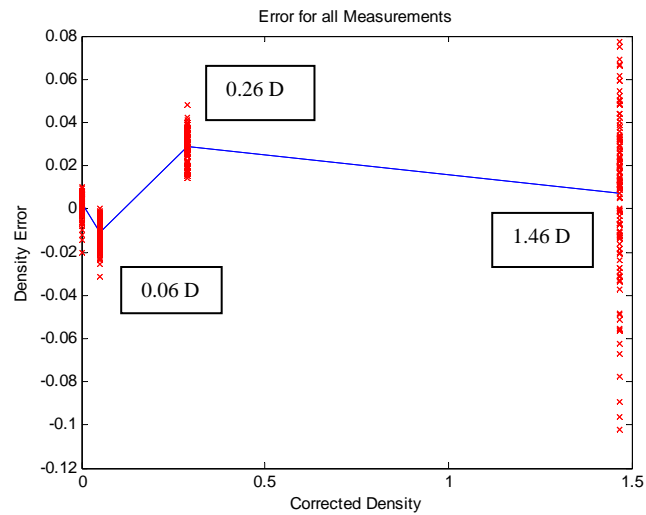


Figure 3.34: Error in the calibrated densitometer.

Table 3.5: Error Results for the Densitometry Test.

True Density	Mean Error	Standard Deviation	Max Error	Min Error	Error Range
0.00 D	0.0026 D	0.0051 D (N/A)	0.0100 D	-0.0200 D	0.03010 D (N/A)
0.06 D	-0.0111 D	0.0061 D (10.1%)	0.0000 D	-0.0316 D	0.0316 D (52.6%)
0.26 D	0.0290 D	0.0065 D (2.5%)	0.0480 D	0.0145 D	0.0335 D (12.8%)
1.46 D	0.0710 D	0.0352 D (2.4%)	0.0774 D	-0.1022 D	0.1796 D (13.3%)

The last verification of densitometric accuracy and resolution was performed using ten 130 μm sheets of the PET material. The influx grayscale was determined with 20 averaged images without material. Then 10 images were taken with 1 to 10 sheets of PET on the opal glass and the density at four 11 x 11 pixel locations was found for each

of the images and averaged, as shown in Figure 3.35. These results showed a slightly nonlinear densitometry trend which was likely caused by additional surface reflections with more sheets. Since light reflected off the front and back surfaces for each layer, more sheets artificially increased the density. Also each of the sheets added more dirt, scratches, and surface imperfections which increased density results and measurement variance. However, from these results, the number of layers was visible and the density for a single sheet and extinction coefficient were estimated to be ~ 0.005 D and 0.038 D/mm.

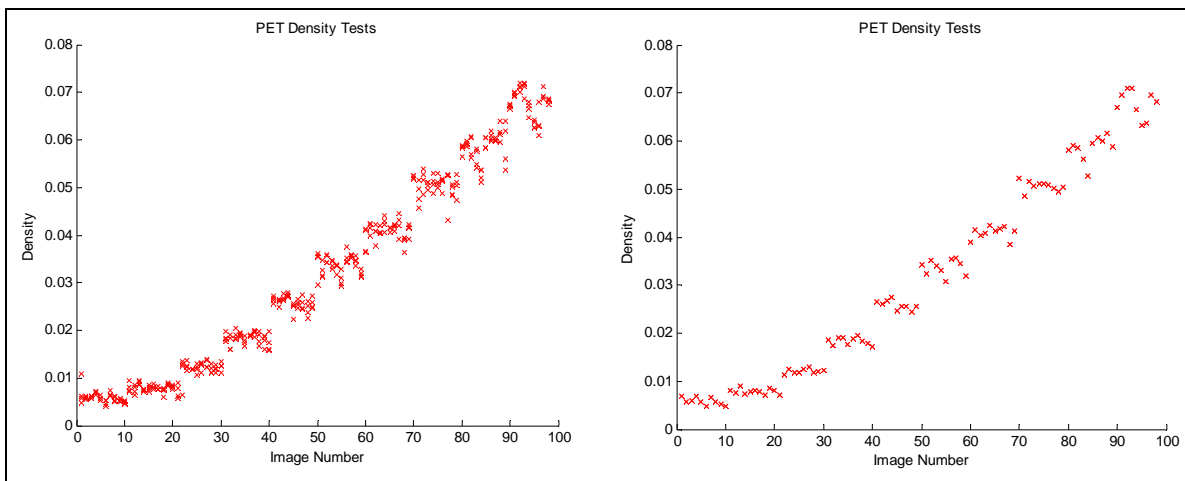


Figure 3.35: Ten density measurements for 1 to 10 PET sheets in 4 locations (left) and their average (right).

3.4.2 Defect Identification System

Based on different methodologies discussed in Chapter 2, several methods were investigated for inspecting the thin film after casting. These defect identification system configuration tests were performed with a readily available, non-volatile analogous solution (molasses), in place of traditional polymeric material, based on its rheological and optical characteristics, e.g., viscosity and semi-transparency. Some of the methods considered included:

1. Using a reflected low angle laser line to detect the defects. The plane of the laser would reflect specularly except when a surface anomaly caused the beam to reflect at a lower or higher angle. The camera would pick up a bright bead of light unless a defect caused the light ray to diverge. The setup is shown in Figure 3.36. In

practice this method worked, but was very sensitive, even for very small surface defects. Additionally, it was not possible to discern the different types of defects from one another using this method; it was only useful for identifying that there was nonuniformity in the casting.

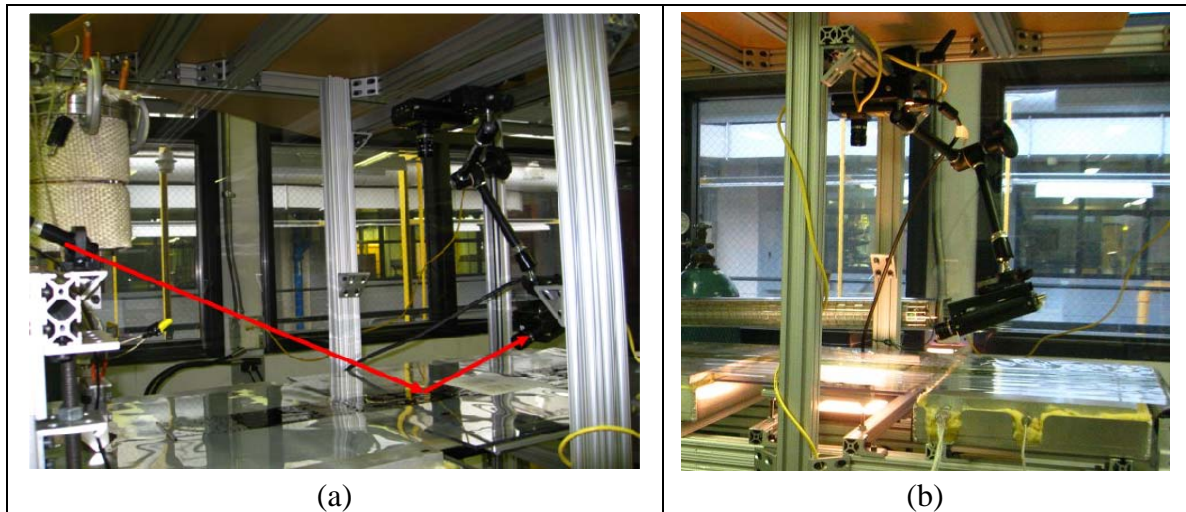


Figure 3.36: Low angle laser concept with (a) the laser path for good material, and (b) the camera mounting system.

2. Direct imaging of the casting menisci using a side-mounted camera provided information on the pressure and web speed. A backlight was used to illuminate the back of the die and generate a silhouette of the die and cast material, as utilized in [107]. The experimental setup and results, shown in Figure 3.37, illustrated that reflection from the substrate and membrane solution led to difficulties viewing the menisci. Unfortunately, the low reflectance angle ensures a large percentage of the light will reflect off the solution and substrate to the sensor. Improved results may be possible with a smaller or collimated backlight, which would project a silhouette of the casting to the camera; however, a microscopic camera would still be required to get acceptable spatial resolution of the small region of interest (ROI).

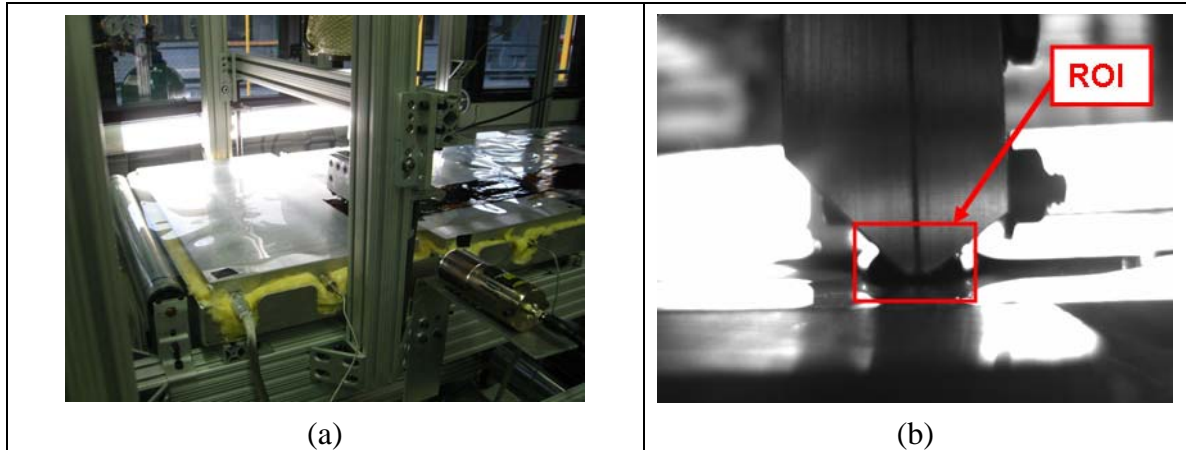


Figure 3.37: Imaging the die directly to measure the menisci. (a) The system configuration, and (b) the resulting image.

3. Mounting the laser line below the material and viewing the line characteristics from a top mounted camera. While the line did brighten and distort when a defect was present, the line quality was poor and false positives were common.
4. Mounting the laser line below the material and monitoring the line behavior on a projection screen, seen in Figure 3.38. This method was similar to the one Gamage and Xie [5] implemented on their system (see Figure 2.3), but since the laser light refracted for all defects it was difficult to classify the defects.
5. Projecting the laser line from above the web and imaging the reflection, as depicted in Figure 3.39. Since the specular laser light reflection was not aligned with the camera lens, when bright spots appeared in the captured image, these areas indicated a defect, shown in Figure 3.39(b). However the bright flash of light was brief and unless the camera was operating with a high frame rate, the defect may go undetected.
6. Using a diffuse backlight to illuminate the semi-transparent material. The material passed over a Plexiglas panel while a 4" x 5" Fastec fiber optic diffuse backlight illuminated the sample. This system is shown in Figure 3.40. Based on this thorough investigation, it was found that using a diffuse backlight to illuminate the semi-transparent material in combination with an overhead camera worked best for defect identification. This method also provided a more efficient means of classifying the defects of interest, e.g., pinholes, air entrainment, gels, and thinning, because they appeared differently in the captured image.

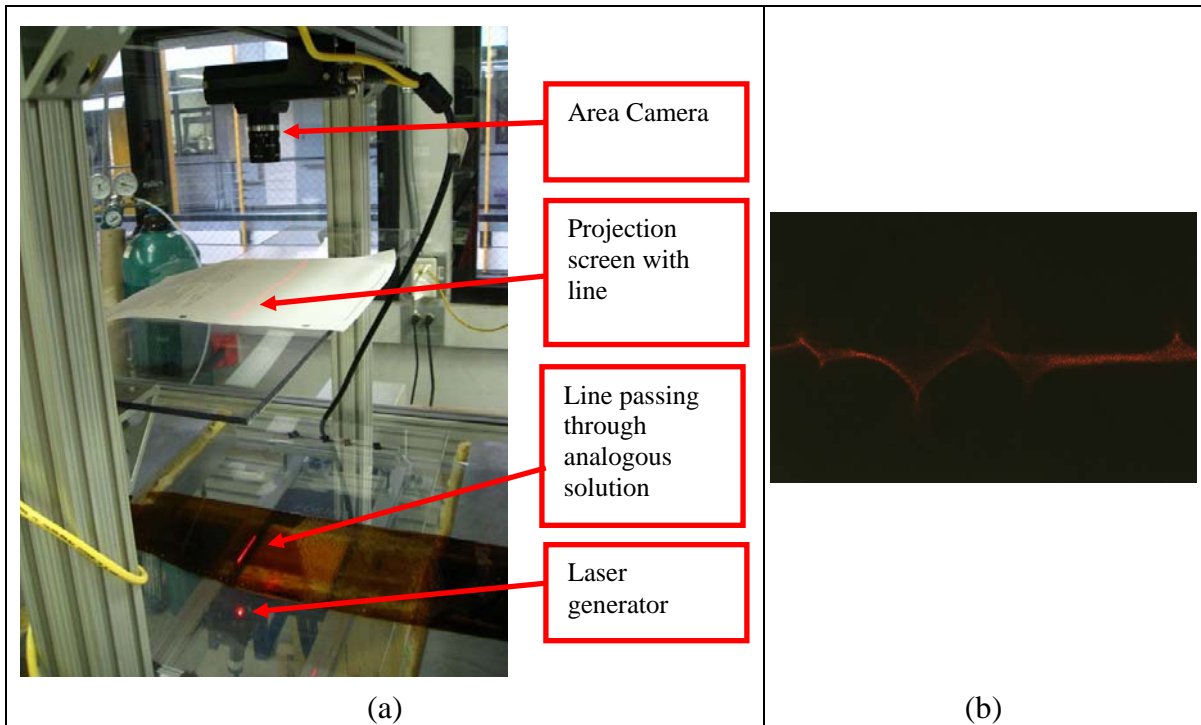


Figure 3.38: Transmission laser with projection screen. (a) The system configuration, and (b) the imaged result when the laser hit bubble defects.

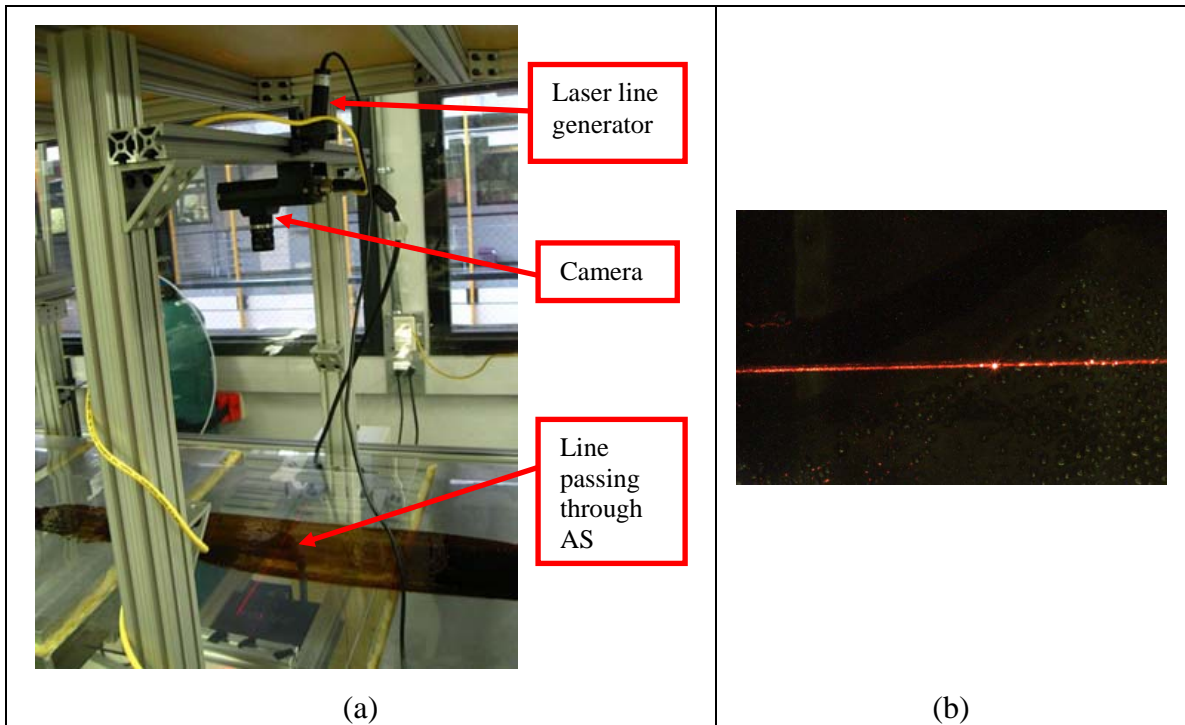


Figure 3.39: The reflected planar laser method, with (a) the setup and (b) the image of the laser striking a bubble defect.

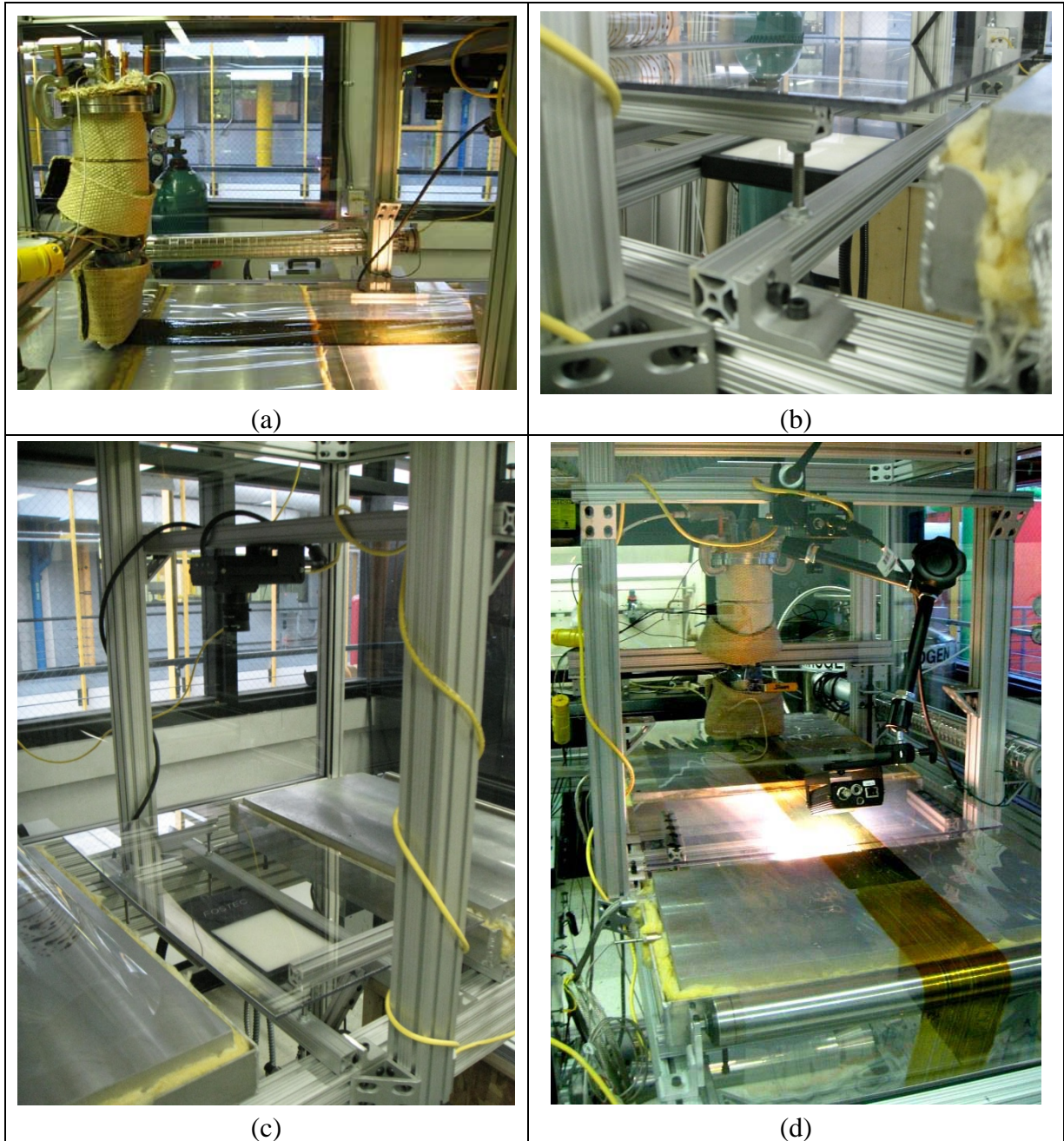


Figure 3.40: The backlight system without the opal diffuser. (a) The system in operation, (b) the backlight and support structure, (c) the full system without cast material, and (d) the system in operation from another angle.

3.4.3 Inspection Control System

As shown in Figure 3.3, web handling was controlled with a National Instruments LabVIEW 7.1 program (discussed in Section 3.1) and the inspection system was

controlled with a MATLAB 2008a graphical user interface (GUI). These programs were located on separate computers to allow manufacturers the ability to monitor or control the web and inspection systems simultaneously. The GUI program received digital image data from the Lumenera camera via a USB 2.0 connection. Then image processing and image analysis was performed on the image data to extrude the thickness profile and defects in the manufactured product. The GUI was created to allow manufacturers simple and intuitive control over the inspection system. The system was coded to include the full-field thickness profilometer and defect inspection system, along with a number of system adjustments for changing the camera settings, image processing values, and other classification and processing options. The interface is shown in Figure 3.41. This discussion only covers the real-time processing mode of the GUI, however single snapshot and post-processing modes were also available.

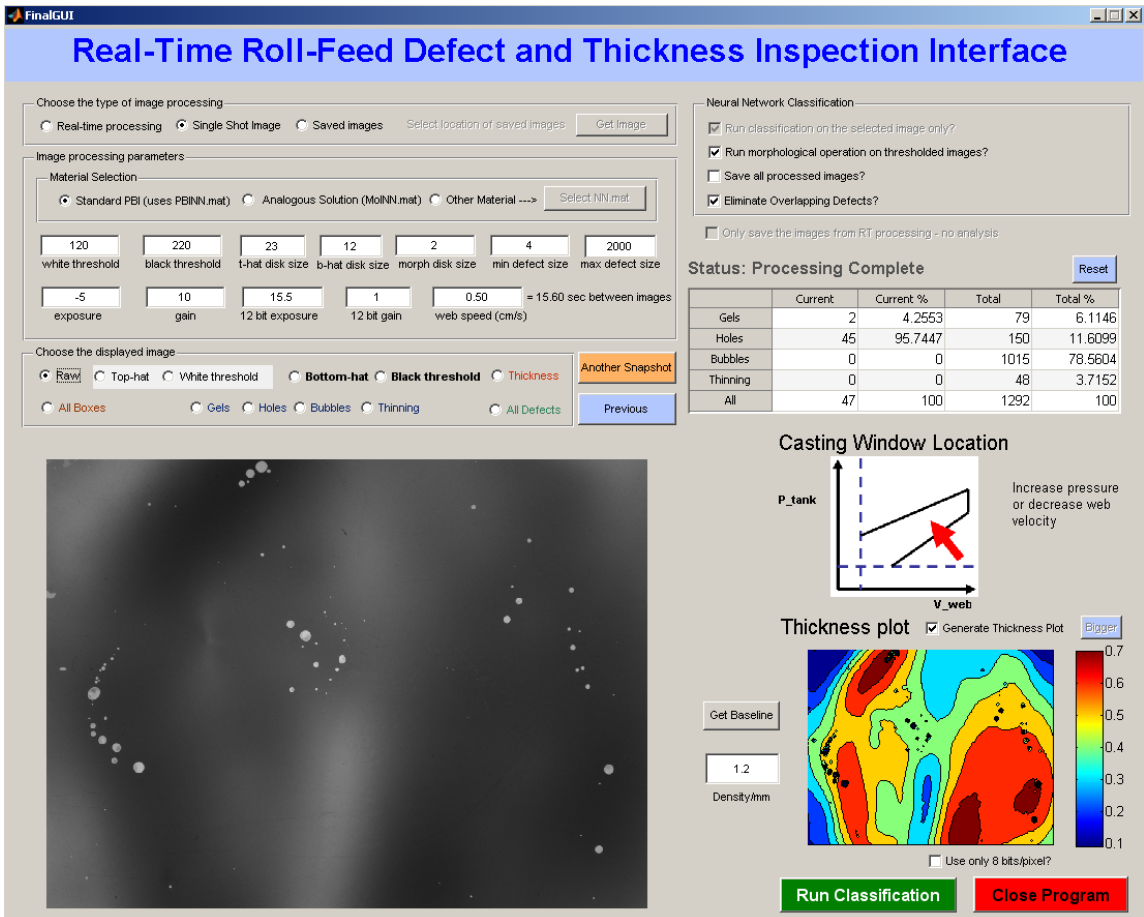


Figure 3.41: Screen shot of the graphical user interface with a non-cast sample of analogous material.

To perform the defect identification and classification, the GUI system captured images and processed them to extract defect regions (discussed in Section 4.3). These regions then had a set of characteristic features extracted and sent to an artificial neural network (ANN) to classify the defects as holes, bubbles, thinning, or gels (discussed in Section 4.4). The GUI was designed to be versatile and capable of operating on a range of cast materials, but there were some material-specific options in the final version. One of the material-specific features was a tool which informed the manufacturer of improperly set casting parameters (e.g., tank pressure, web speed) based on the type of defects in the material (discussed in Section 4.3). This tool determined if the casting parameters were set too high or low based on the existence of certain defects, e.g., via the following pseudocode algorithm:

```
IF total defects < 5
    Status: Casting is good.
    Changes: None.
ELSE IF defect 1 > defect 2
    Status: "Above" the casting window.
    Changes: Lower parameter 1 and/or increase parameter 2.
ELSE
    Status: "Below" the casting window.
    Changes: Increase parameter 1 and/or decrease parameter 2.
END
```

The primary goal of the GUI was to provide real-time information to the manufacturer about the quality of the product and what adjustments could be performed to remedy poor manufacturing. When the system was running in real-time, the program operated according to the flow chart in Figure 3.42, the details of which are covered in Chapter 4. The primary features of the system were:

1. setting the camera and image processing parameters
2. visualizing defect identification and classification results in real-time
3. visualizing thickness measurements in real-time
4. autonomously determining the location on the casting window (Section 4.3) based on classified defects, then notifying the user of the adjustments which should be made to improve the casting

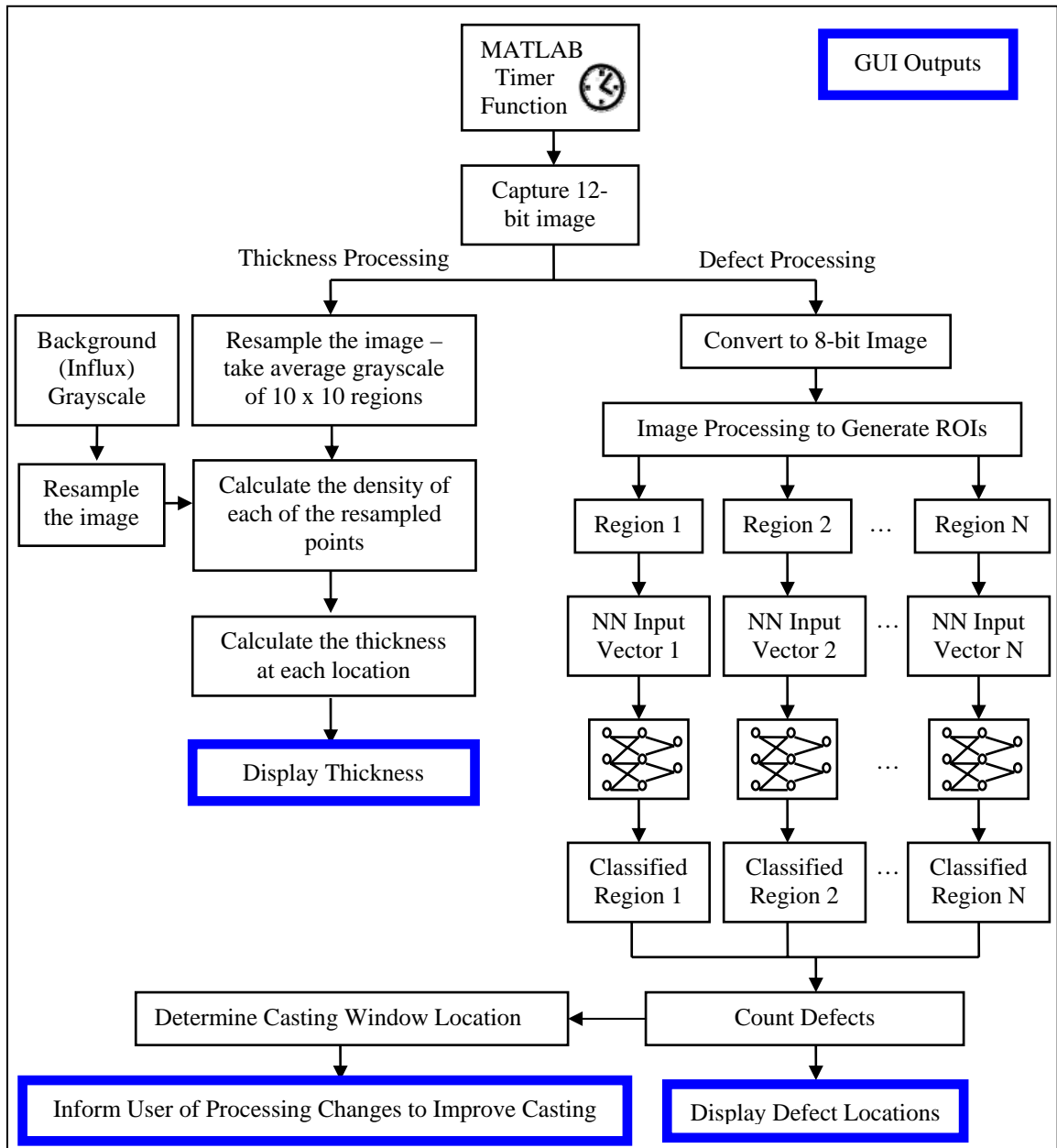


Figure 3.42: GUI real-time processing flow chart.

3.5 System Summary

In Chapter 3, the roll-feed imaging system (RFIS) used to cast and inspect polymeric thin film is described. The imaging system has been designed to measure the thickness and identify, classify, and quantify defects generated in semi-transparent polymeric materials in real-time using NDE techniques. The remainder of this thesis investigates the feasibility of using such technology for the inspection of polymer electrolyte membrane (PEM) used for fuel cells.

CHAPTER 4: FUEL CELL MEMBRANE CASTING AND INSPECTION

4.1 PEMFC Background

Although fuel cell usage first occurred in the 1960s as part of the Apollo Missions [108], they remain poised to revolutionize the automotive industry [109], improve electric grid stability through storage [110], and provide on-demand power for off-grid communities or individuals with technologies such as wind-to-hydrogen (W2H2) [111]. There are many different types of fuel cells (FCs), including polymer electrolyte membrane (PEM) FCs (also known as proton exchange membrane FCs), phosphoric acid FCs, solid oxide FCs, and many more, which operate at different temperatures based on the chosen fuel, oxide, and electrolyte. To demonstrate the RFIS discussed in Chapter 3, polymeric materials used in PEMFCs are considered, because of all the FC technologies, PEMFCs are experiencing the most development and are expected to penetrate the transportation and energy sectors in the next two decades [109, 110].

The PEMFCs are composed of two bipolar plates and repeating membrane electrode assemblies (MEAs), shown in Figure 4.1. Each MEA is composed of two electrodes separated by the polymer membrane. The bipolar plates separate the fuel (H_2) and oxidant (O_2 or air) streams. The bipolar plate has machined or stamped serpentine channels to distribute the reactant flows to the gas diffusion layers (GDLs) mated to the anode (-) the cathode (+). When the fuel and oxidant are present at the anode and cathode, the electrochemical potential is large enough to pass the H^+ cations across the ionomer membrane, but because of the chemical properties of the PEM material, the electrons must pass around an external circuit creating an electrical current similar to a conventional battery. As shown in Eq. (4.1), water and heat byproducts emerge on the oxidant side of the PEM, which are exhausted with the oxidant stream.



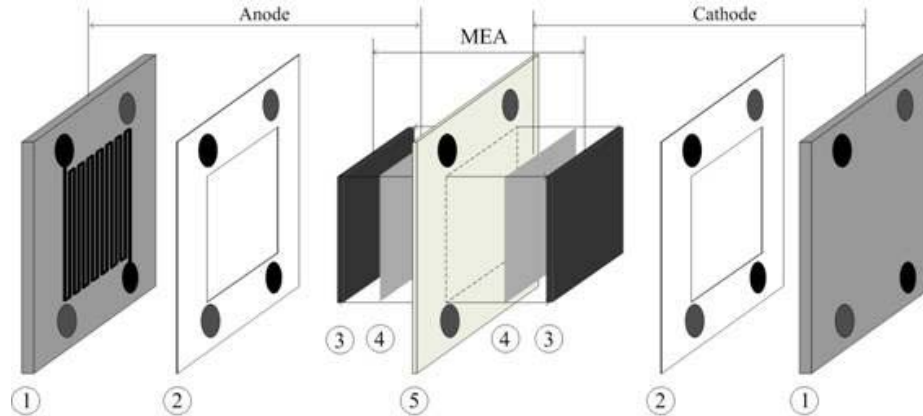


Figure 4.1: Fuel cell assembly with (1) Bipolar plates, (2) Gaskets, (3) Electrodes, (4) Catalysts, (5) Polymer Electrolyte Membrane [112].

For the last 40 years, the state of the art PEMFC electrolyte material has been Nafion[®], a perfluorosulfonic acid/polytetrafluoroethylene copolymer [113]. Although Nafion has remained the market leader, scientists have been working to create more efficient and less expensive ionomer membranes, such as polybenzimidazole doped with phosphoric acid (PBI/PA) [114]. New classes of PEM allow for high temperature PEMFC operation (between 120-200°C) which is infeasible with state-of-the-art membranes. The increase in operating temperature provides higher efficiencies and current density, reduces the need for water management, and allows for higher platinum catalyst tolerance to carbon monoxide poisoning [115-117]. However, both types of ionomers have manufacturability challenges.

4.2 Motivation for Inspecting Polymer Electrolyte Membranes

Since commercial development of both low and high temperature PEMFCs is in its infancy, there lies a host of challenges associated with their mass production. One of the major hurdles is producing PEMFCs cost competitively for transportation and electrical grid storage, as compared to traditional or other alternative energy sources. A National Renewable Energy Laboratory (NREL) report indicated that in order for fuel cells to become cost competitive, they must be less than \$125/kW for transportation and less than \$750/kW for stationary applications [109]. However, since fuel cells are currently manufactured at low volume, the current price is \$3,000/kW with approximately \$1,200/kW for manufacturing [118]. Moreover, up to \$600/kW (i.e., 13-

20%) of the total cost is from the membrane and its manufacture [119, 120], although these studies do not take into account wasted material from defective production. NREL has stated that the total stack price may increase 5-50% solely from quality control checks and conditioning after assembly [109]. Thus, technological developments to fabricate defect-free, uniform membranes inexpensively and reliably will help reduce the overall cost of the PEMFC.

Durability of fuel cells is another impediment to wide spread commercialization of fuel cell systems. The US Department of Energy has set the their 2010 target durability at 5,000 hours (150,000 miles) for automotive applications in order to be competitive with the current vehicle technologies [121]. The reliability of fuel cell membranes is currently limited by the formation of pinhole or tear defects—either in manufacturing or operation—which lead to gas crossover due to chemical, mechanical, and/or thermal degradation [17]. There have been a number of initiatives to identify the source of the pinholes, but there is no consensus to date. Luke first investigated the problem and concluded that the membrane was not getting proper water transport, drying and then cracking [17]. Another theory, originating from a study by La Conti et al., found that MEA failure was due to peroxide formation and degradation of the polymer [122]. More recently Peineche et al. determined the surface roughness of the GDL could cause pinhole creation and Stucki et al. found that the membrane dissolution was the cause of local stress and backed this up with experimental evidence of pinhole formation solely from electrolyzation [123]. Stanic and Hoberecht put forth a hybrid theory that claimed membrane aging, localized heating (from electrochemically-induced current densities), fuel cell component configuration, and operating conditions caused pinhole failures of the fuel cell [124]. Stanic and Hoberecht also experimentally tested 30 membranes between ~30-170 μm and concluded that pinhole defects occurred due to stress concentrations where the membrane thickness was reduced. Furthermore they found that other pinholes had precipitates in the membrane which caused polymer blistering. Harris et al. and Bhamidipati et al. showed experimentally and numerically that holes and bubbles will form during membrane fabrication [89, 125].

The first step in assuring the membrane can withstand harsh automotive or other portable product environmental conditions is to maintain high quality standards in the

manufacturing process. If the cast membrane contains any holes or pinhole defects, the fuel cell will not function; and if there is thinning or air entrainment regions, the membrane will likely fall far short of the desired 5,000 hrs of operation. Moreover, since these studies often point to membrane creep causing the failure, maintaining a uniform membrane casting without particulates or other stress concentration zones is critical to longer fuel cell life. In short, there must be a strong quality control system to ensure optimal membrane fabrication. The RFIS is believed to offer such control.

4.3 Defect Detection in Cast Polymer Membranes

In certain thin film manufacturing situations the types of defects are an indication of improperly set casting parameters, e.g., casting temperature, pressure, and web speed. The range of casting parameters which generate acceptable material defines a “casting window.” Outside of this window, different defects occur based on the misbalance of casting parameters. Thus, by monitoring and classifying the types of defects, the location on the casting window can be determined, and therefore the necessary adjustments in the casting parameters ascertained.

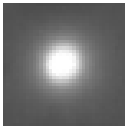

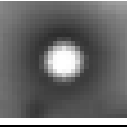

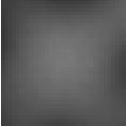

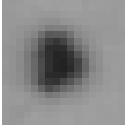

Experimental work based on slot die extrusion has shown that the casting window depends on rheology, capillary number, particle size and concentration because these properties change inter-particle forces, i.e., Brownian, van der Waals, electrostatic, steric, and hydrodynamic forces in the material [107]. Chu et al. showed that when the flow rate was too high or casting speed was too small, material built up behind the die; if the flow rate was too low relative to casting speed, air entrainment would occur; and if the flow rate and casting speed were both high, die lines would occur [107]. Liu et al. showed that changing material properties affected the slot die casting window [126]. In addition to experimental analysis, numerical simulations of the slot-die casting process also exemplified the careful balance between inlet flow rate and web speed [127].

4.3.1 Selection of Defects to Identify

The RFIS produced a range of defects depending on the location on the casting window, specified by the flow rate and substrate speed. When the web speed was too large or the tank pressure (i.e., mass flow rate) was too small, the material could not fill

the volume beneath the die and holes and thinning occurred. If the web was moving too slowly in relation to the tank pressure, too much material was extruded from the die and the coating bead expanded beyond the die and air pockets appeared in the material. There were also dark gels and particulates due to poor material handling practices, not fully cleaning the tooling system between batches, or debris on the substrate. Therefore, the defects of interest are illustrated in Table 4.1.

Table 4.1: Defects present in fuel cell membrane castings.

Defect	Backlit Image	Side View	Qualifications
Hole or Pinhole			There is no material covering the substrate in a localized area.
Air Entrainment or Bubble			A pocket of air below the material surface.
Thinning			Concavity on the surface of the material.
Gel or Particulate			A dark contaminant in the thin film, often caused by hydrolyzed material.

By design, not all the defects in the membrane were detected by the imaging system. A primary objective of the RFIS was to autonomously direct the processing parameters into the casting window, so identifying defects which occurred far from the casting window would only add superfluous system complexity, and the processing parameters would be adjusted prior to reaching these extremes. The unidentified defects were die lines (caused by wrinkling in the substrate), uneven die flow, or gels in the die, and a repeating pattern of thinning or bubbles. These defects are shown in Figure 4.2. Holes, thinning, and air entrainment were the only defects which were necessary for the control system. However, gels occurred within the casting window because they were in the batch solution, so they were also identified and classified to ensure they were not mistaken for other defects. For a more thorough discussion of the causes of these defects and how they occur, see [125, 127-129].

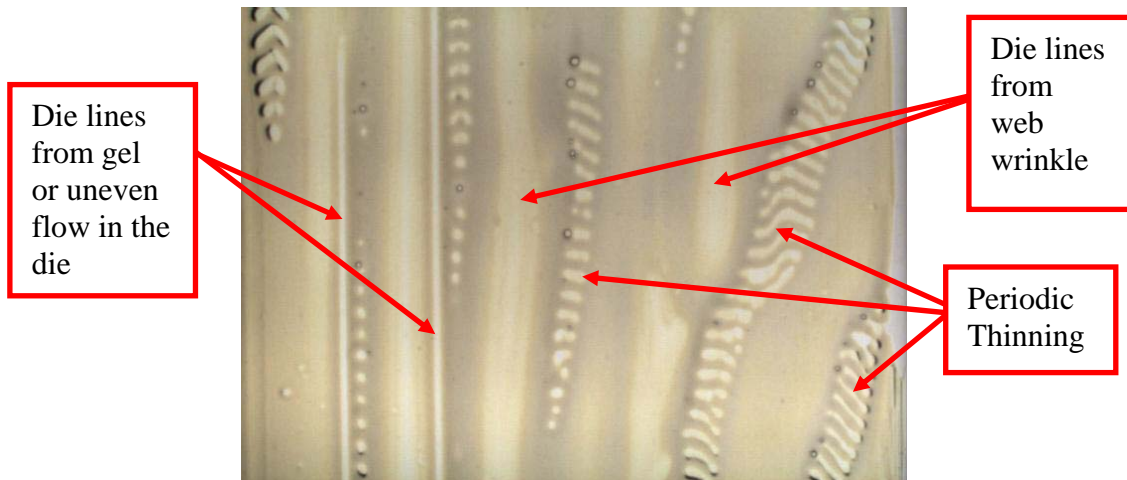


Figure 4.2: Defects occurring far from the casting window at low pressures or high web speeds.

4.3.2 Image processing

In general, it is preferred to adjust camera settings and lighting to optimize defect contrast rather than to post-process images, but it is often unavoidable to process the images in order to extract features of interest. As a result, standard techniques for image processing, including point transformations, spatial transformations, and morphological operations have been developed. The objective of these processing techniques is to remove noise and enhance features of interest, e.g. the defect regions. Using preliminary image data from the RFIS, a wide range of image segmentation methods (many of which are covered in [130]) were attempted, including:

1. Thresholding the grayscale image
2. Thresholding using Otsu's method [131]
3. Attempting to take advantage of the spectral content of the images by thresholding the red, green, or blue values individually
4. Converting the RGB image to the HSI or CMY color space and thresholding each of the tristimulus values
5. K-means clustering
6. Top-hat operation and then thresholding
7. Reconstruction and then thresholding
8. Region growing
9. Split-and-merge algorithm

10. Watershed segmentation

The most promising of these methods was thresholding after taking the top-hat operation, which essentially returned an image containing all the objects which were brighter than the localized background and smaller than a binary kernel. The steps of the operation are shown in Figure 4.3 based on a MATLAB example image. Notice that when the image is directly thresholded (upper middle), processing does a poor job of identifying the rice grains in the lower part of the image, but the thresholded top-hat image (lower right) does identify them. The same processing steps are also performed for dark regions, in which case it is called the bottom-hat operation. The top-hat and bottom-hat operations also help remove the vignetting effects in the images, so that all the defects have equal chance of being detected. Otherwise either the center or the periphery defects would be thresholded at a relatively larger value and more likely classified. After taking the top and bottom-hat operations, using similar steps as Gamage and Xie [5], candidate defect regions were located. The operations in the defect identification program are shown for the four types of defects in Figure 4.4. The operations are as follow:

- 1 – The image is captured from the area camera.
- 2 – If the image is color it is turned to grayscale. The image then is separated into two parallel processing operations. The left side finds defects which are lighter than the local background and the right side finds defects which are darker than the local background.
- Left 3 – The top-hat operation highlights the light regions.
- Left 4 – The image is thresholded at a gray value selected by the user. (Otsu's method and using functions based on grayscale standard deviation were attempted, but with little success.)
- Left 5 – The closing operation is performed where a structuring element dilates and then erodes the blob regions. This removes noise around the light blobs, but also combines multiple defects if a large structuring element is used. For this reason, only a 2 pixel radius disk is used.
- Left 6 – Bounding boxes are placed around the blobs and then expanded by 25% in each direction to capture some of the surrounding area (similar to the methodology of Pham and Alcock [34]).

- Right 3 – The bottom-hat operation finds the dark regions.
- Right 4 – The image is thresholded.
- Right 6 – Bounding boxes are placed around the blobs and expanded by 25% on each side.
- 7 – The boxes from the light and dark processes are compared and combined. If any of the regions are completely enclosed in another box, the smaller boxes are deleted. This helps remove the redundant regions associated with bubbles, and in some cases gels. (For this application, this method performed the desired task, but other joining schemes have been suggested in [34].)
- 8 – The final defect regions are obtained, which are then segmented and classified.

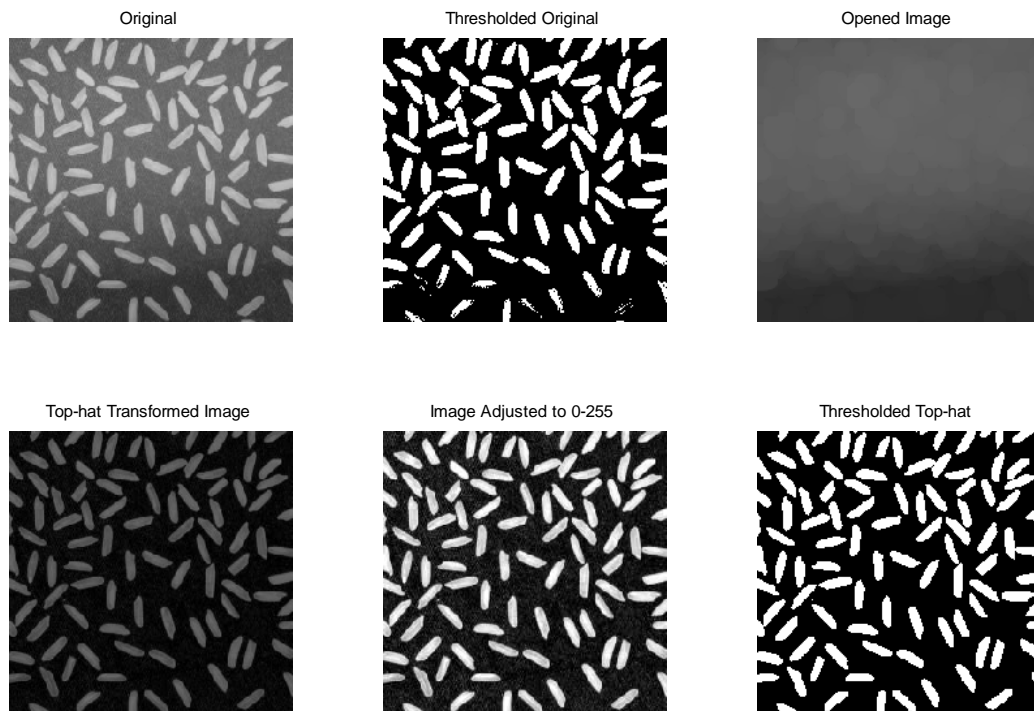


Figure 4.3: The steps in the top-hat operation. The original image is morphologically opened to generate a background mask (upper right) which is then subtracted from the original (lower left), renormalized (lower middle), and thresholded (lower right). Rice.png image from MATLAB [132].

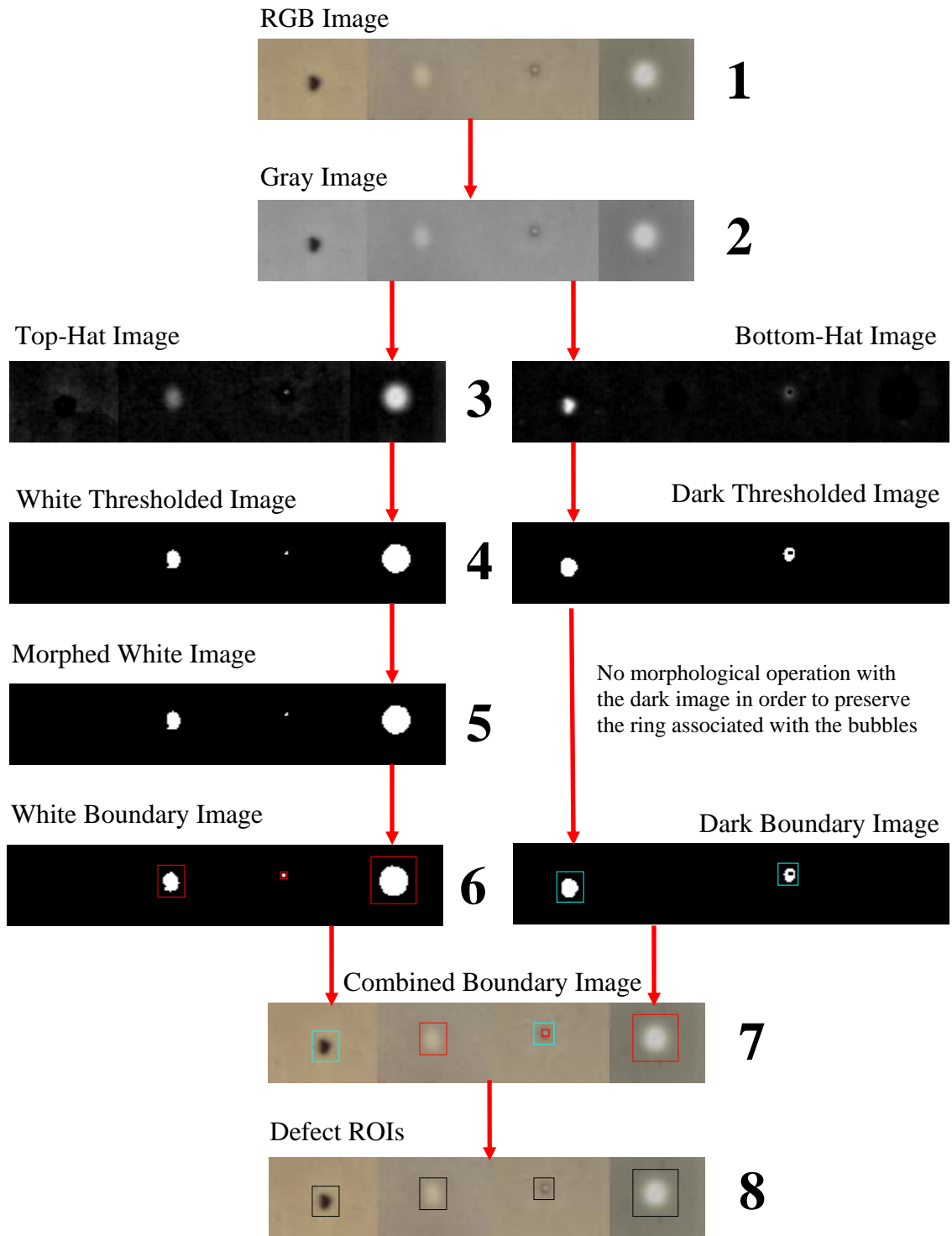


Figure 4.4: Image processing procedure to convert the original color image to segmented defect regions

4.4 Defect Classification in Cast Polymer Membranes

The classification of the defects into categories of holes, bubbles, gels, and thinning was a challenging engineering problem because of the diversity of parameters which accompany the same defect type. For instance, a hole may have an area of 30 pixels or 3000 pixels. Human vision and comprehension is particularly good at detection and classification of defects, so the difficulty in automating this process is often underestimated.

This section describes the motivation and steps in creating a classification tool for the RFIS. Casting defects appeared when certain casting controls were too high or low, so by classifying the defect types, corrective tuning of these controls was possible. In order to create the classification tool, defect parameters—i.e., extracted region-of-interest (ROI) features—from each of the defect regions were collected and analyzed. A data mining tool was used to determine which classification method should be implemented. The results showed that neural networks were the most accurate classifier, so the network structure was further studied to optimize classification accuracy before being implemented within the inspection system.

4.4.1 Defect Data Mining

Classification routines—e.g., decision trees and lists, instance-based classifiers, multilayer perceptrons, Bayesian networks, etc.—all work by dividing the parameter space into different classification regions. The parameters must contain information that can be used to separate different defect types by dividing the parameter space. Thus, the input vectors to any classification routine must be populated with features which are characteristic to certain defects. For example, difficulty arises when segregating holes and bubbles from one another because they have the general geometric form. However, bubbles have a darker ring around the white region, so by taking the Laplace transform of the ROI, patterns to discern the two defects are revealed.

Ultimately, a collection of 59 parameters were believed to designate regions of interest as specific defect types. These candidate inputs fell in broad categories of size, histogram, topography, geometry, and topology shown in Appendix E. The set of features was heavily influenced by the work of Packianather et. al [33], but as opposed to

using uniform 85x60 pixel images for all defects, the segmented images had no size limit. As a result, directly counting pixels was not applicable so the percentage of pixels for each of the regions was determined.

Once this list was finalized, images of the membrane solution were taken over a range of casting parameters to produce different defects. 75 images were selected and segmented to create 6,663 individual defect regions, which were saved with their 59 features. The majority of the defects were bubbles, so only 2,100 of the 6,663 regions were hand classified, resulting in 246 hole defects, 774 bubble defects, 766 thinning defects, and 314 gel defects. It should be noted that there was often difficulty classifying holes and thinning since they have the same general trends, and in some cases thinning looks nearly identical to a hole. Fortunately, if these defects are later misclassified, because they generally appear in the same location on the casting window, the system recommendations will remain the same. Some consideration was given to combining hole and thinning defects, but thinning can occasionally appear in the high pressure/low web speed casting window location where holes do not appear, so it was desired to have them differentiated.

At this point all the data was normalized by assuming the features, Z , formed a Gaussian distribution. By subtracting the feature average, μ , and dividing by the feature standard deviation, σ ,

$$Z' = \frac{Z - \mu}{\sigma} \quad (4.2)$$

99.7% of the normalized features Z' were expected to fall within the range of -3 to 3. This was important for some of the classification schemes (e.g., neural networks) because training the classifier used an error minimization method. If one defect was numerically larger than the others, the training would favor this feature over the others.

Next, the input-output data was analyzed for trends in the data mining software WEKA 3.6 [133] to remove unnecessary feature inputs. Initially, the number of features was reduced from 59 to 19 using a WEKA tool which considered the predictive nature of each feature as well as the redundancy between features [134]. Removing superfluous or redundant features from the classification program makes the classification routine quicker. To remove features, the tool measured the inter-class and intra-class variation of

the parameter space. The intra-class variation described how well the features of a given class were clustered, whereas the inter-class variation quantified the separation of classes. It was important to minimize the overlap of different defects in the feature space, so the mean of the four data sets required a large separation (e.g., large inter-class variation), but small intra-class variations were also important so that the distributions were not broad. For example, a clear division between the holes/thinning and gels/bubbles can be seen using the mean grayscale from the bottom-hat and the ROI center grayscale value shown in Figure 4.5; however, this was not the case for the ROI median grayscale and top-hat skewness, shown in Figure 4.6. Thus, the median grayscale and top-hat skewness were not included in the final feature set.

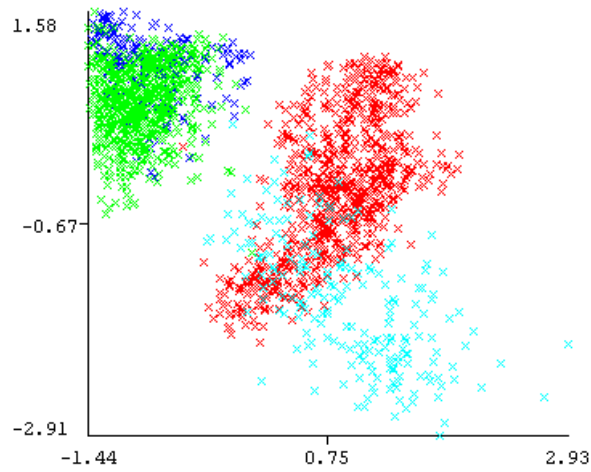


Figure 4.5: Scatter plot of defect data with good inter-class variation. Normalized bottom-hat mean grayscale vs. normalized center point grayscale. Key: blue – hole, red – bubble, green – thinning, cyan - gel.

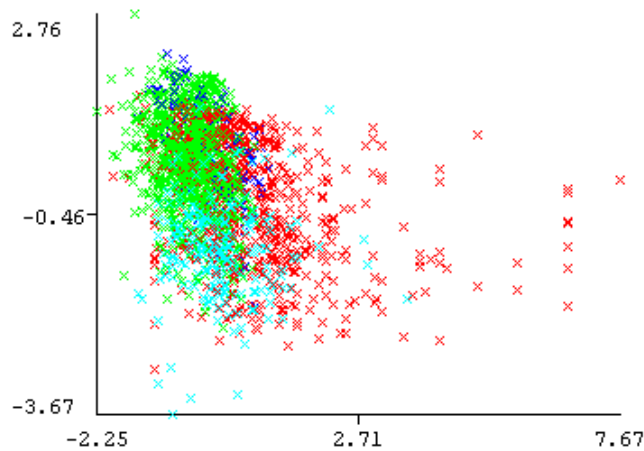











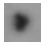


Figure 4.6: Scatter plot of defect data with poor inter-class variation. Normalized grayscale median vs. normalized top-hat skewness. Key: blue – hole, red – bubble, green – thinning, cyan - gel.

After eliminating redundant and unhelpful features from the feature set, the final 19 features were:

1. Standard deviation of the grayscale image
2. Skewness of the grayscale image
3. Percentage of grayscale pixels less than the mean grayscale (μ)
4. Percentage of grayscale pixels greater than $\mu + 40$
5. Dark outliers: threshold grayscale at $\mu + 1.5\sigma$ and count white pixel percentage
6. 3rd lightest pixel in the top-hat
7. Mean bottom-hat value (μ_{bh})
8. Bottom-hat mode
9. Bottom-hat standard deviation
10. Bottom-hat peakedness (Kurtosis)
11. Percentage of bottom-hat pixels less than μ_{bh}
12. Blob region eccentricity of an ellipse fit around the region
13. Blob region extent (% of white pixels in bounding box)
14. Blob region Euler number ($N_{blobs} - N_{holes}$)
15. Laplace transform of grayscale, threshold at 12, and count white pixel percentage
16. Profile is monotonically decreasing (Y/N)
17. Profile increases more than 20 levels (Y/N)
18. Profile increases more than 60 levels (Y/N)
19. Center Pixel Grayscale

Features 1-11 were histogram-based parameters derived from of the grayscale, top-hat, and bottom-hat images of defect regions. Examples of a hole, a bubble, thinning, and a gel grayscale, top-hat, and bottom-hat regions and their associated histograms are shown in Table 4.2 and Figure 4.7, respectively. The ability of these features to divide the parameter space can be seen with the histograms. For example, Feature 6 is the 3rd lightest pixel in the top-hat. As shown in Figure 4.7, the hole value for this feature is 245, the bubble is 100, thinning is 126, and the gel is 52. Hence, there was a clear separation in the four defect types based on this parameter, albeit additional samples would be required to make any definitive claim about the merit of the feature.

Table 4.2: Exemplary grayscale, top-hat, and bottom-hat defect regions.

	Gray Image	Top-hat Image	Bottom-hat Image
Hole			
Bubble			
Thinning			
Gel			

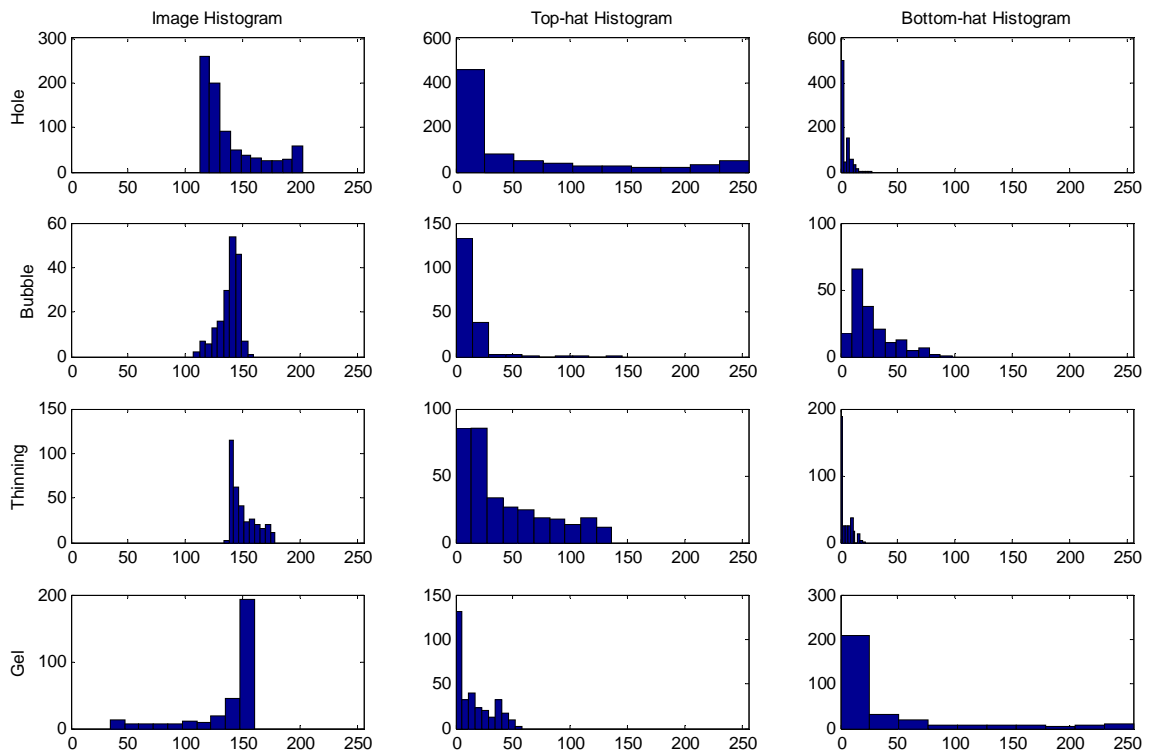


Figure 4.7: Original image, top-hat and bottom-hat histograms of defect types.

Features 12-15 were based on the blob regions. These blob regions are located in Figure 4.4 at Step 6. The eccentricity was a measure of the blob circularity, so elongated defects were differentiated from circular ones. The blob extent measured the percentage of the white pixels in the bounding box and the Euler number was the number of blobs minus the number of holes; both of which measured the defect geometry by indicating if there were cavities or other nonuniformities in the blob shape. Features 15-19 were based on the topology of the defect region. Feature 15 was generated by taking the Laplace

transform of the image, as shown in Figure 4.8, binarizing the image, and then counting the white pixel percentage. Laplace transformations are often used for edge finding, so this showed how rapidly the grayscale profile changed in the vicinity of the defect. Features 16-19 utilized the averaged grayscale profiles measured from the center of the region to the corners, shown in Figure 4.9. These profiles were normalized based on the center pixel grayscale (Feature 19), such that the center of the profile began at the origin, as shown in Figure 4.10. Feature 16 determined if the profile only decreased away from the center, which indicated a hole or thinning. Feature 17 queried if the profile at some point increased 20 gray levels, which typically indicated a gel or bubble; and Feature 18 determined if the grayscale levels increased 60 pixels, which generally indicated a gel. Based on these features there was enough information to segregate the defect types with different classification tools. Each defect provided feature information to the classifier about the region, and using the *a priori* information from the hand classified data, the classifier assigned the region to a defect category based on how closely it matched the other defects of the same type.

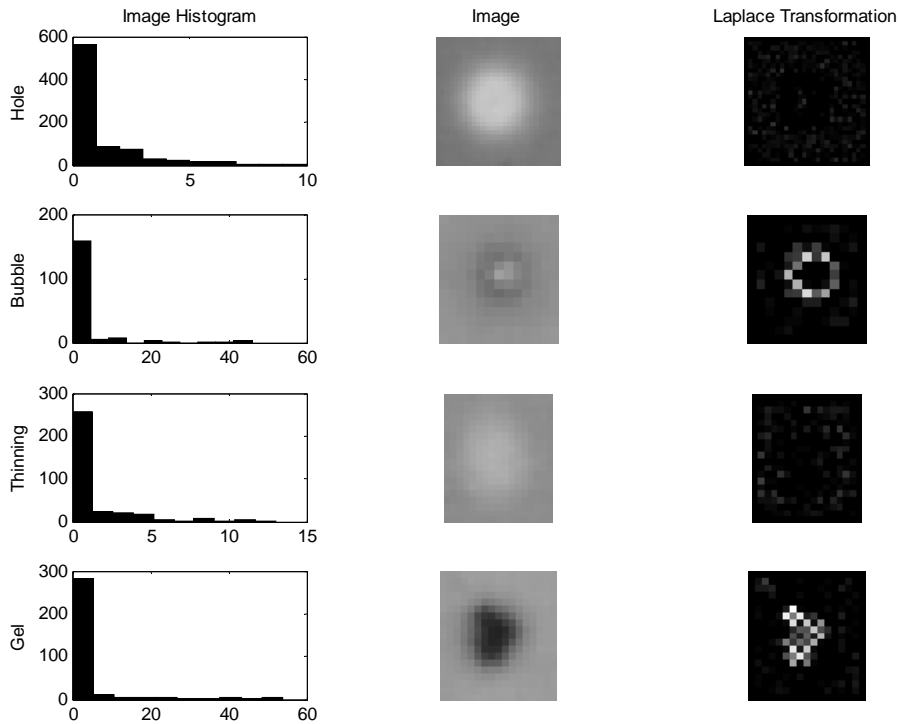


Figure 4.8: The histogram of the Laplace transform, the image of the region of interest, and the Laplace transform image for the four types of defects.

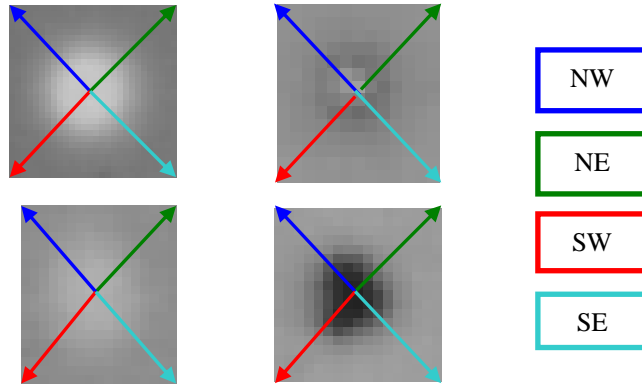


Figure 4.9: Grayscale profile vectors from the center of the defect region to each of the corners.

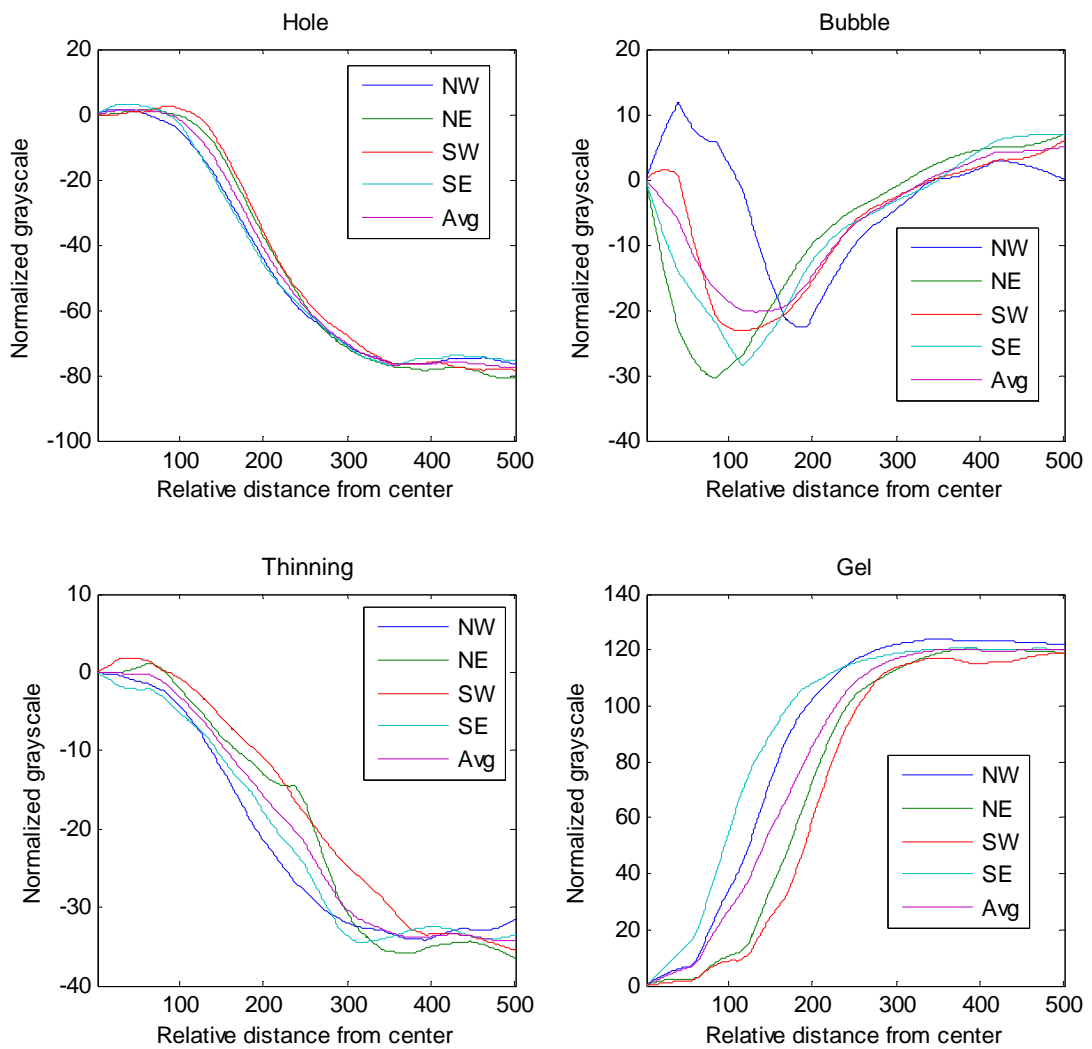


Figure 4.10: Profiles from the center of the defect region to the corners sampled 500 times.

4.4.2 Determining the Best Classification Tool

There are a range of classification methods which divide the parameter space into the different defect types. Each method has its own advantages and disadvantages. For instance, decision trees are simple, and therefore fast, but cannot produce the sophisticated divisions possible with a neural network. For the membrane defect classification problem, a decision table, decision tree, Bayesian network, and neural network were investigated.

Decision tables are essentially a method of stringing together successive IF-THEN-ELSE statements which divide the parameter space [135]. Based on the defect classification problem, WEKA created 162 rules using features 1, 3, 5, 14, and 16. The decision table correctly classified 87.33% of the defects with the confusion matrix shown in Table 4.3.

Decision trees operate under a similar methodology as the decision table. By creating a series of logic statements, e.g.,

```
IF  $\sigma > 1$ 
    classify as hole
ELSE
    classify as gel
END
```

A pruned decision tree was created using the C4.5 algorithm [136]. The final tree included 45 leaves, 89 forks, and classified 93.33% of the defect correctly, shown in the confusion matrix in Table 4.4.

A Bayesian network was generated to perform the classification with different hill climbing and genetic search algorithms. Bayesian networks describe probabilistic relationships between the features and the defect types [137]. The best Bayesian network classifier produced a network with 91.67% accuracy and a confusion matrix shown in Table 4.5.

Multiple multilayer perceptron neural networks were also generated with 12, 14, 16, and 18 hidden layer nodes. All of them performed slightly better than the decision tree, but the 16 node hidden layer had the best accuracy with 94.19%. The confusion matrix is shown in Table 4.6.

Table 4.3: Confusion matrix for the decision table.

		Classified as the Following Defects			
		Holes	Bubbles	Thinning	Gels
Actual Defects	Holes	160	6	79	1
	Bubbles	7	745	0	22
	Thinning	55	12	699	0
	Gels	17	63	4	230
Accuracy		66.9%	90.2%	89.4%	90.8%

Table 4.4: Confusion matrix for the decision tree.

		Classified as the Following Defects			
		Holes	Bubbles	Thinning	Gels
Actual Defects	Holes	192	0	52	2
	Bubbles	0	754	1	19
	Thinning	41	0	722	3
	Gels	0	17	5	292
Accuracy		82.4%	97.8%	92.6%	92.4%

Table 4.5: Confusion matrix for the Bayesian network.

		Classified as the Following Defects			
		Holes	Bubbles	Thinning	Gels
Actual Defects	Holes	193	0	53	0
	Bubbles	0	763	1	10
	Thinning	97	0	678	1
	Gels	1	22	0	291
Accuracy		66.3%	97.2%	92.6%	96.4%

Table 4.6: Confusion matrix for a neural network.

		Classified as the Following Defects			
		Holes	Bubbles	Thinning	Gels
Actual Defects	Holes	201	0	45	0
	Bubbles	0	757	1	16
	Thinning	39	0	725	2
	Gels	0	16	3	295
Accuracy		83.8%	97.9%	93.7%	94.2%

In each of the confusion matrices, the difficulty in separating thinning from holes and gels from bubbles is shown. The holes and thinning have very similar characteristics and it is even difficult for human inspectors to distinguish between the two. In the case of gels and bubbles, for larger defects the differences are clear, but when the defects are less than 10 pixels in size, they have nearly identical characteristics. Therefore small bubbles can occasionally be classified as gels, and vice versa.

Since the neural network performed the best of the four classification methods, it is implemented as the classifier in this work. However, the decision tree produced

similar results and would likely be quicker to run in the code. Therefore, if faster processing time is required, a decision tree is identified as a good option.

4.4.3 Neural Network Background

Neural networks are a type of learning algorithm based on the biological structure of neurons in the brain and are used to solve complicated problems where the complexity of the data does not lend itself to direct solutions. Applications include data processing (e.g., filtering, clustering, separation, compression), time series prediction, regression analysis, data mining, and classification (e.g., pattern and sequence recognition) [138]. Neural networks (NNs) have been shown to be highly robust for classification problems. For the RFIS application, the NN was used to differentiate between the different types of defects based on mathematical characteristics of the defective region. Once the types of defects were known, the location on the casting window could be found, and the proper casting parameter adjustments performed. The application of a NN to solve classification problems requires five basic steps:

1. Identify a set of input vector parameters through data mining
2. Create the structure of the network
3. Train the network with input-output vector pairs
4. Test the network with known solutions
5. Run the network with new data

In the biological network, billions of neurons exchange information through axon-dendrite interactions. Some neurons send stimulating signals and others send suppressing signals, so only when the sum of these signals cross the threshold will the neuron send a signal to other neurons [138]. The model for a single neuron with n input signals is shown in Figure 4.11, where $\mathbf{x} = [x_1, \dots, x_n]^T$ are input signals, $\mathbf{w} = [w_0, w_1, \dots, w_n]^T$ are synaptic weights, w_0 is a bias value, and f is the activation function with signal s given by

$$s = \sum_{i=1}^n x_i w_i \quad (4.3)$$

Perceptrons are one type of neuron that NNs often utilize. They are either bipolar (outputting -1 or 1) or unipolar (outputting 0 or 1). The bipolar perceptron is shown in Figure 4.11.

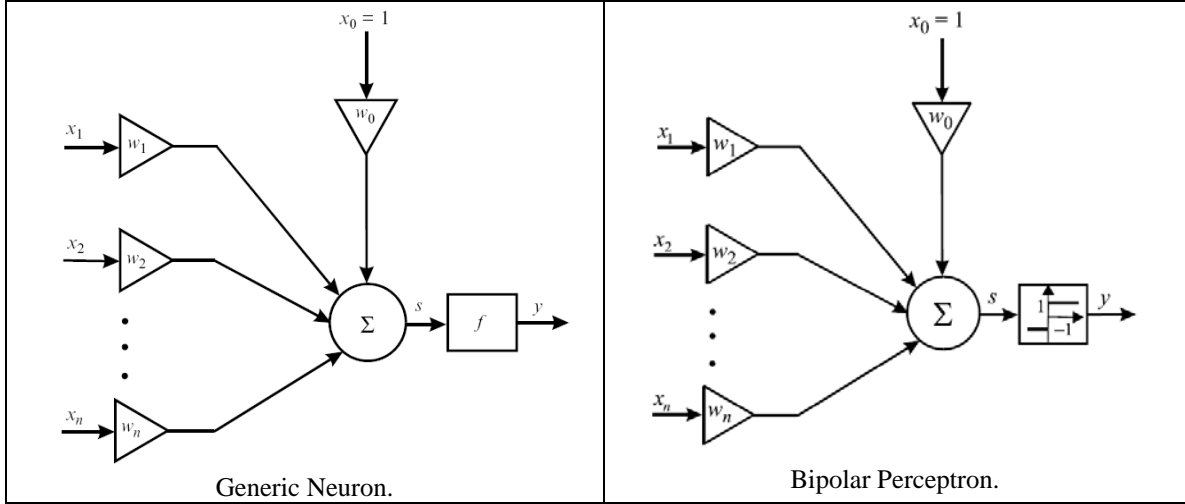


Figure 4.11: Model of a neuron and perceptron [138].

A single perceptron acts to divide the n -dimensional input space into two half spaces. Perceptrons use a type of algorithm called *supervised learning* (or *learning with teacher*) to modify the weights. Perceptron learning is performed by using *a priori* knowledge of input signals $\mathbf{x}(t_{set}) = [x_1(t_{set}), \dots, x_n(t_{set})]^T$ and the associated desired output (target) signals $\mathbf{d}(t_{set})$ for $t_{set} = 1, 2, \dots, n_{training}$, where $n_{training}$ is the number of training data sets. For a given t_{set} , there is a training sequence composed of an input vector \mathbf{x} and a desired output \mathbf{d} . The *learning with teacher* algorithm follows these basic steps [138]:

1. Randomize the perceptron weights.
2. Calculate the outputs of the neuron for the next training sequence.
3. Compare perceptron output with the desired output.
4. Adjust weights to minimize the error between \mathbf{d} and the perceptron output.
 - a. if $y(\mathbf{x}(t_{set})) \neq d(\mathbf{x}(t_{set}))$ then $w_i(t_{set} + 1) = w_i(t_{set}) + d(\mathbf{x}(t_{set}))x_i(t_{set})$
 - b. if $y(\mathbf{x}(t_{set})) = d(\mathbf{x}(t_{set}))$ then $w_i(t_{set} + 1) = w_i(t_{set})$
5. Training takes the next training sequence, $t_{set} = t_{set} + 1$ and goes back to step 2.

This algorithm is repeated until the error for all t_{set} is smaller than some assumed tolerance for an independent set of input-target data. Each time all the training data are used in the algorithm it is called one epoch.

There are other types of neurons which use more sophisticated schemes of weighting updates, such as the Adaptive Linear Neuron (Adaline model), the Hebb neuron model and the sigmoidal neuron model. The sigmoidal neuron, which is used in this thesis, does not use a binary activation function, but a continuous function, which for the bipolar case is

$$f(x) = \frac{1 - e^{\beta x}}{1 + e^{-\beta x}} \quad (4.4)$$

The weights are updated for each training set by creating an error vector for each of the weights,

$$E(\mathbf{w}) = \frac{1}{2} \left[d - f \left(\sum_{i=0}^n w_i x_i \right) \right]^2 \quad (4.5)$$

and then the steepest decent method is used to update the weights

$$w_i(t_{set} + 1) = w_i(t_{set}) - \xi \frac{\partial E(w_i)}{\partial w_i} \quad (4.6)$$

where ξ is the learning coefficient. From these basic neuron building blocks and error reduction methodologies, highly robust classification neural networks are constructed.

4.4.4 Neural Network for Defect Classification

The neural network classification system takes segmented defect ROI features and determines which defect type the region most closely matches. This is done in three steps, shown in Figure 4.12:

1. Each of the defect regions have 19 features extracted from them.
2. The features are used as the input vector for the neural network.
3. Outputs 1-4 form a vector representing holes, bubbles, thinning, and gels.

Although the desired output contains only ones and zeros, as shown in Table 4.7,

a “winner-takes-all” algorithm is employed, such that the classification is based solely on the defect with the largest output value.

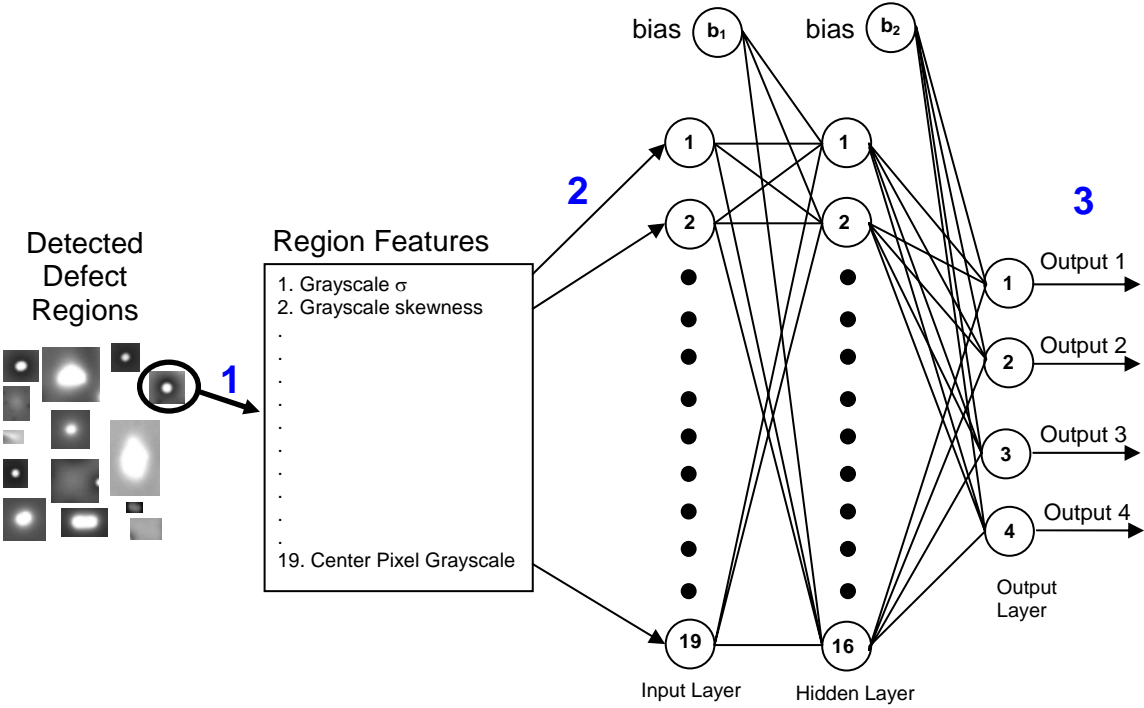


Figure 4.12: The neural network classification process.

Table 4.7: Desirable neural network outputs.

Defect	Desired Output Vector
Hole	$[1, 0, 0, 0]^T$
Air Entrainment	$[0, 1, 0, 0]^T$
Thinning	$[0, 0, 1, 0]^T$
Gel	$[0, 0, 0, 1]^T$

4.4.5 Network Structure, Training, and Optimization

The structure of the neural network describes the number of input neurons, hidden neurons and layers, and output neurons. The number of neurons was chosen to achieve the best classification results, minimize the hand-classified input-output pairs required to train the NN, and reduce the number of training runs to produce an accurate network. To do this, the number of input neurons was first minimized—as previously described with the WEKA data mining software—to reduce computational time in NN classification and image processing. Then the number of hidden layer nodes was selected based on NN Monte Carlo training simulations with a analogous solution network. The mean

classification error for different numbers of hidden layer nodes is shown in Figure 4.13 for the analogous solution network training. Since the analogous material network had a different set of training data and structure (e.g., 18 inputs, 3 outputs), only the general trend of Figure 4.13 should be considered. It shows that small networks did not have enough complexity to map all the inputs to correct defects; medium network sizes had the best mean classification accuracy; and with large networks, the average network accuracy gradually became worse. However, larger networks produced the best classifiers—but due to their complexity, they also occasionally produced very poor networks, and these outliers increased the misclassification mean.

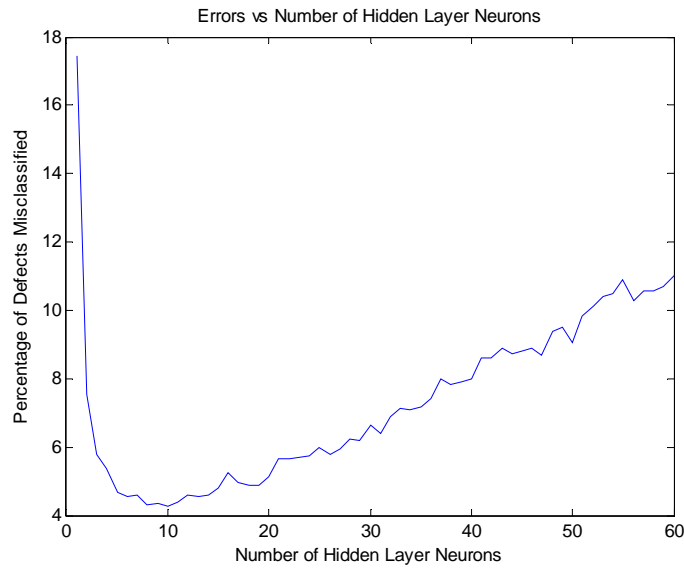


Figure 4.13: The average percentage of defects misclassified for 2500 NN training runs vs the number of hidden layer sigmoid neurons for the analogous solution. This network contained 18 inputs and 3 outputs because gels were not classified.

As expected, for the PEM material network, the top performing networks had more hidden layer nodes (25+). After running 1000 training runs for 14-30 and 54 nodes, the greatest accuracy was 96.86% with 30 hidden nodes. Unfortunately, larger networks took longer to train and required more training data to optimize the network weights. However, with 2,100 input-output sets of training data, good results were expected for large networks, since the total number of weights was

$$N_{weights} = (N_{inputs} + 1)N_{hidden} + (N_{hidden} + 1)N_{output} \quad (4.7)$$

The strong network results for higher numbers of nodes indicated that increasing the number of nodes would produce better classifications, but in doing so the computation time also increased. Packianather and Drake [33] had 3 times as many hidden layer nodes as input nodes but their system had 13 outputs. For the RFIS classification computation time was important, because for each ROI, the time-consuming processes of creating an input vector and running the network were required. In some cases, when the batch material was poor, there were over 1,000 identified defects in the captured image, which led to long processing times since the number of weights is proportional to the number of mathematical operations. Considering all these factors, it was determined that the minimum network complexity which still produced 96% classification accuracy would be the optimal network. Therefore, based on the results in Table 4.8, the final network contained 19 input nodes, 16 hidden nodes, and 4 output nodes. It should also be noted that since only the general trends were needed to determine where on the casting window the casting was located, any classification above 90% would give acceptable results.

Table 4.8: Minimum number of defects for different numbers of hidden layer neurons.

Number of hidden layer neurons	Minimum number of errors for 1000 training sets
14	86 (95.9%)
16	77 (96.3%)
18	67 (96.8%)
20	82 (96.1%)
24	76 (96.4%)
30	66 (96.9%)
54	70 (96.7%)

In order to train the neural network, a set of input vectors with known outputs was created and imported into MATLAB. Then using the Neural Network Toolbox, the collection of input-output pairs was randomly separated as follows:

- 70% or 1470 were used for training, which the network used for error reduction.

- 15% or 315 were used for validation, which were used to stop the training when generalization terminated. This insured that the back propagation routine was not over-constraining the NN to the training data.
- 15% or 315 were used for independent testing of the network.

The training was executed using a scaled conjugate gradient back propagation training routine. The training was terminated when the validation data did not decrease performance error over 6 epochs, shown in Figure 4.14. The test data was an independent means of measuring the accuracy of the NN, as it had no effect on the training or validation of the network.

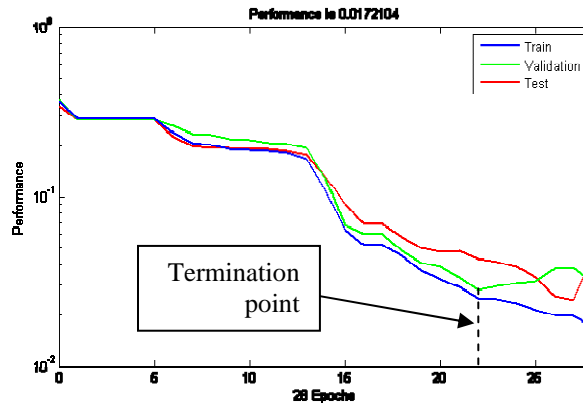


Figure 4.14: Mean squared error of the data sets during each epoch of NN training.

After selecting the network structure, the network was trained until the accuracy of the network was 96% or better. The final network confusion matrix had an accuracy of 96.05% and is shown in Table 4.9.

Table 4.9: Confusion matrix for a neural network.

		Classified as the Following Defects				Total
		Holes	Bubbles	Thinning	Gels	
Actual Defects	Holes	198	0	48	0	80.5% 19.5%
	Bubbles	0	770	1	3	99.5% 0.5%
	Thinning	19	0	746	1	97.4% 2.6%
	Gels	0	10	1	303	96.5% 3.5%
Total		91.2% 8.8%	98.7% 1.3%	93.7% 6.3%	98.7% 1.3%	96.1% 3.9%

Of the 83 misclassifications, 67 of these were holes being misclassified as thinning or vice versa. Since these defects are present in the same location of the casting window, the misclassification is acceptable. However, when bubbles are classified as holes/thinning or vice versa, this could potentially indicate the incorrect location on the casting window and falsely inform the user of parameters changes. Fortunately, only once was a bubble misclassified as a thinning, and never were thinning/holes misclassified as bubbles.

4.5 Summary

The RFIS inspection subsystem was prepared for image processing and classification of FC membrane material by experimenting with different image processing and classification methods. It was found that the best method to classify defects in this material was to perform the top-hat and bottom-hat operations to locate defective regions of interest and then send region data to a neural network for classification. After defects are classified, a GUI indicates which casting parameters must be changed, if any, to correct for existing defects. The complete process is shown in Figure 4.15. With the defect identification and classification systems finalized, the RFIS was prepared for experimental validation, as discussed in Chapter 5.

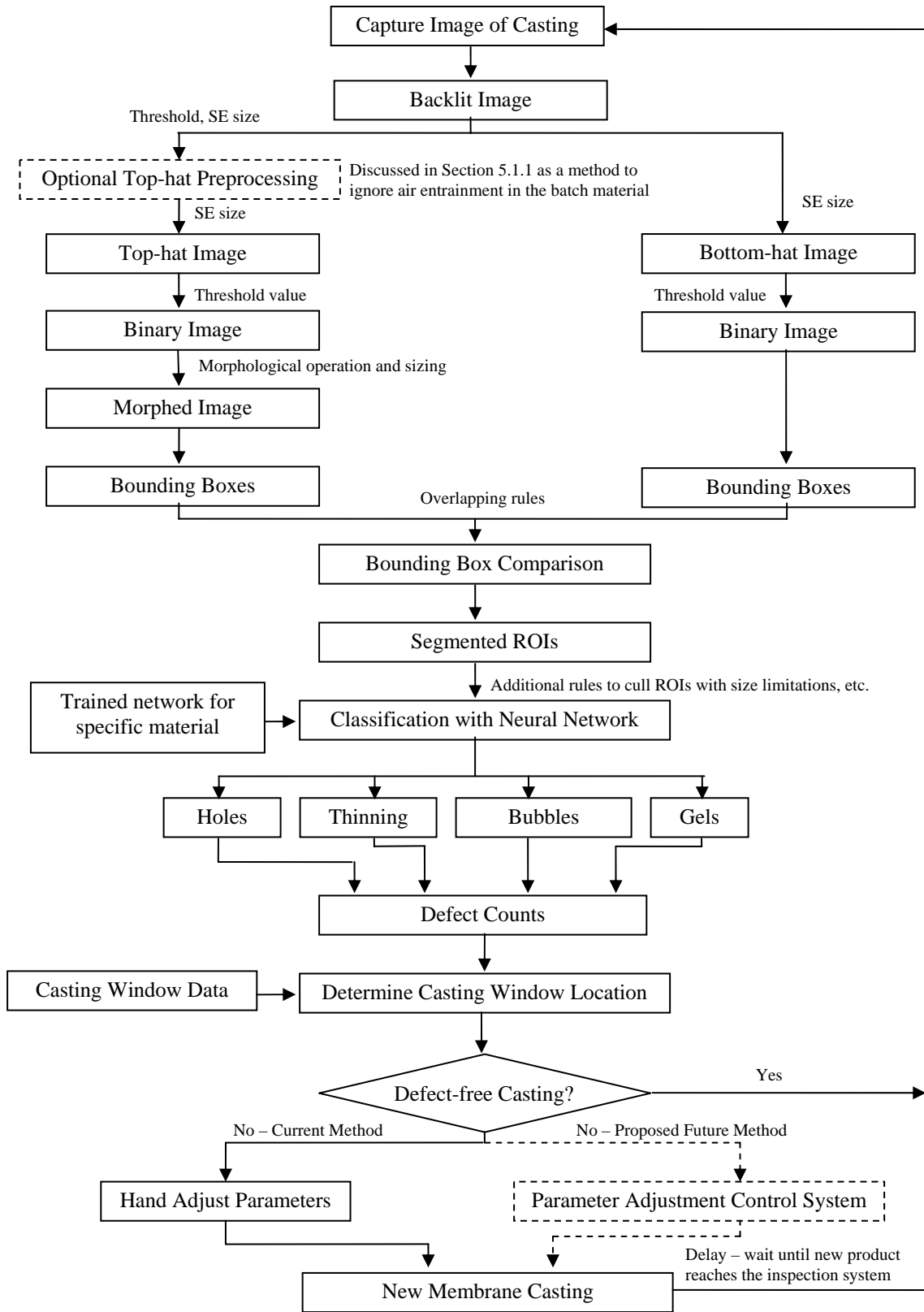


Figure 4.15: Defect processing flow chart with user-input variables.

CHAPTER 5: EXPERIMENTAL RESULTS

5.1 Defect Identification

Defect identification is a challenging problem for machine vision systems when the environment or subject changes. For the RFIS, the thickness and types of defects varied widely depending on the casting parameters and die geometry. Since there was a wide range of defect types and sizes, shown in Table 5.1, selecting thresholds and structuring element sizes to capture only the holes, gels, thinning, and bubbles, was not trivial. However, once the proper structuring element sizes and thresholds were determined for the white and black processing paths, the candidate defect regions were correctly located on the image. To first determine these processing parameters, a single snapshot of the material was captured and the image processing parameters were adjusted until acceptable results were recorded. Then real-time processing of the web was initiated with the previously optimized parameters.

Table 5.1: The maximum, minimum, and estimated mode of defect sizes.

	pixel size			size (mm)		
	min	typical	max	min	typical	max
Holes (and Pinholes)	6	12	25	0.438	0.876	1.825
Gels (and Particulates)	1	8	22	0.073	0.584	1.606
Thinning	4	10	14	0.365	0.730	1.022
Bubbles (i.e., Air Entrainment)	1	12	18	0.073	0.876	1.314
Bubbles in the batch material	1	4	12	0.073	0.292	0.876
Bubbles in periodic defects	4.5	30	45	0.328	2.190	3.284
Thinning in periodic defects	15	30	55	1.095	2.190	4.015
Die lines from web wrinkle (width)	20	35	60	1.460	2.555	4.379
Die lines from gel in die	7.5	12	20	0.547	0.876	1.460

5.1.1 Batch Material Defects

Image processing required a relatively uniform casting to perform the top-hat operation with large structural element sizes. When there were many dark defects the hot-hat operation had difficulty correctly determining the background value. This was particularly prevalent when the batch material contained many small bubbles (which appeared as dark spots) because the localized gray value average was lowered. This

caused good material to be falsely identified as light defects. Since the primary goal of defect classification was to determine the location on the casting window, variations in the batch material—such as bubbles, changes in extinction coefficient, etc.—were unimportant because they appeared regardless of the casting window location. These false alarms were most prevalent in the light defect detection, but this phenomenon could also happen in the bottom-hat operation; however, because the bottom-hat operation used a smaller structural element (usually 12, as opposed to 20 for the top-hat) and the light defects were typically spaced farther apart, this was rarely a problem. A comparison between identifying all the defects in bad batch material and only the defects larger than 10 pixels is shown in Figure 5.1. Therefore, when the batch material contained small bubbles, before the top-hat operation was taken, the dark pixels (from the bottom-hat threshold) were removed from the image and replaced with the average grayscale from the 25 pixel region surrounding the dark pixel. Then the image was smoothed with a 3x3 spatial transformation to remove localized variations. Finally, the resulting image was processed for light defects as normal. The process is shown in Figure 5.2. An example of normal processing and this new method are shown in Figure 5.3. The original top-hat shows many light regions which correspond to good material. As a result, a large number of false alarms occur in these locations. In contrast, on the right side, the new top-hat method located the defects with much higher accuracy and there were significantly fewer places which risked being thresholded into false alarm regions. The danger in using this method was that small light defects would be smoothed out of the image and unidentified. However, if there were bubbles, they would appear in the dark thresholding, so only small thinning and hole defects were potentially ignored. Small thinning regions were nearly always accompanied by larger holes and thinning, so it was believed that leaving these defects unidentified and unclassified was acceptable.

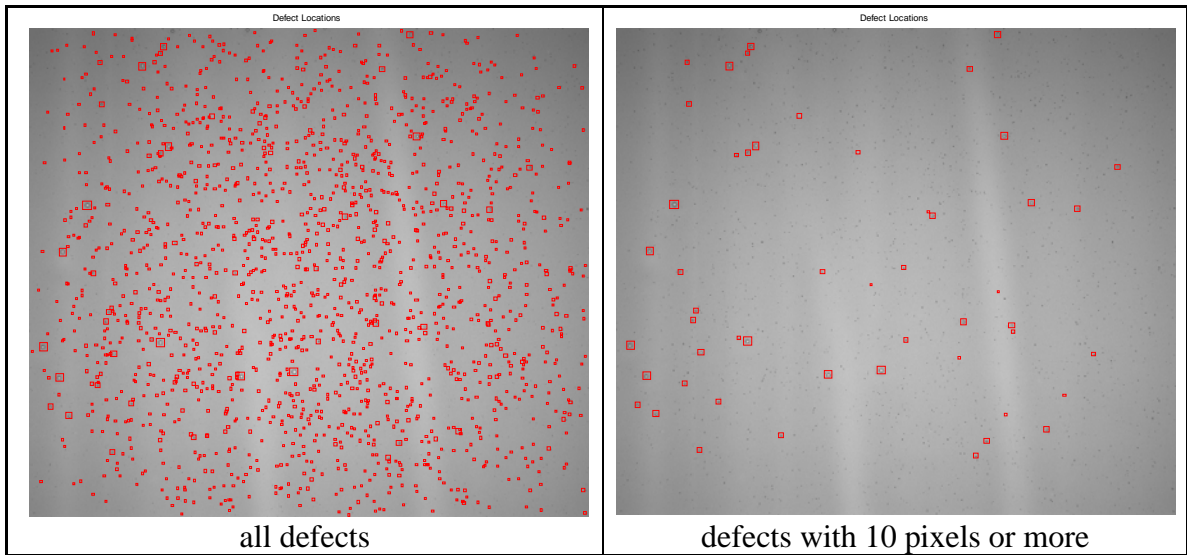


Figure 5.1: Comparison between identifying all the defects and only the defects with a size greater than 10 pixels.

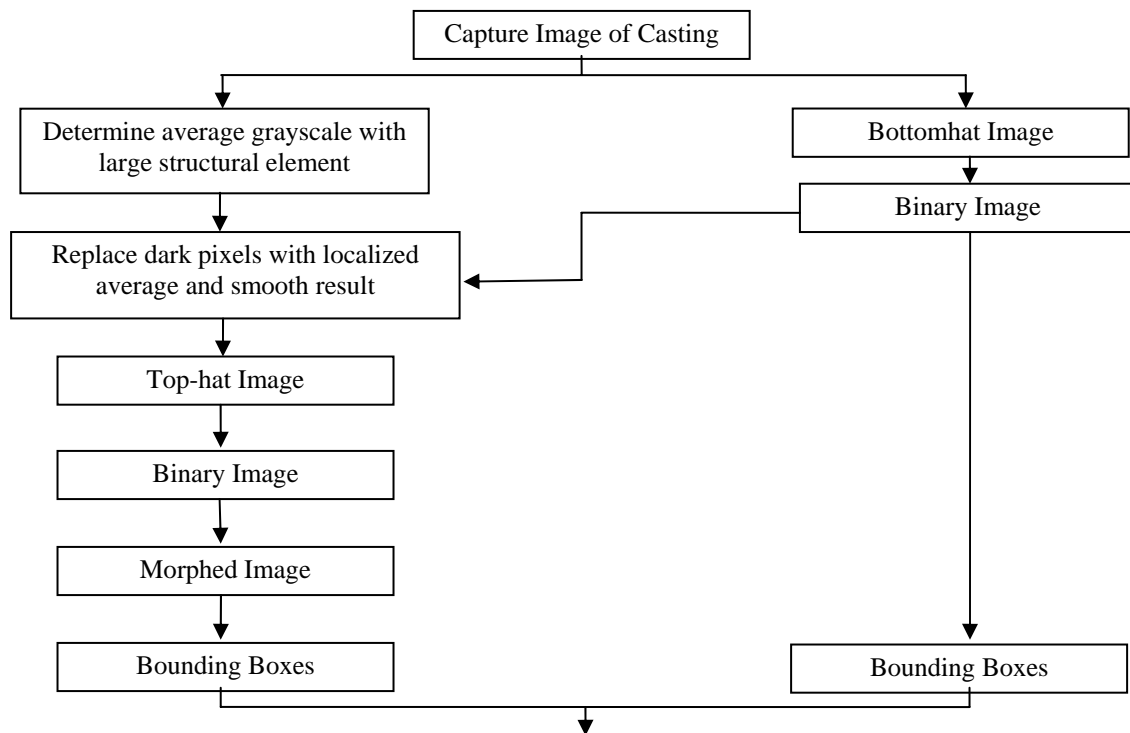


Figure 5.2: Image processing steps when batch material contains bubbles.

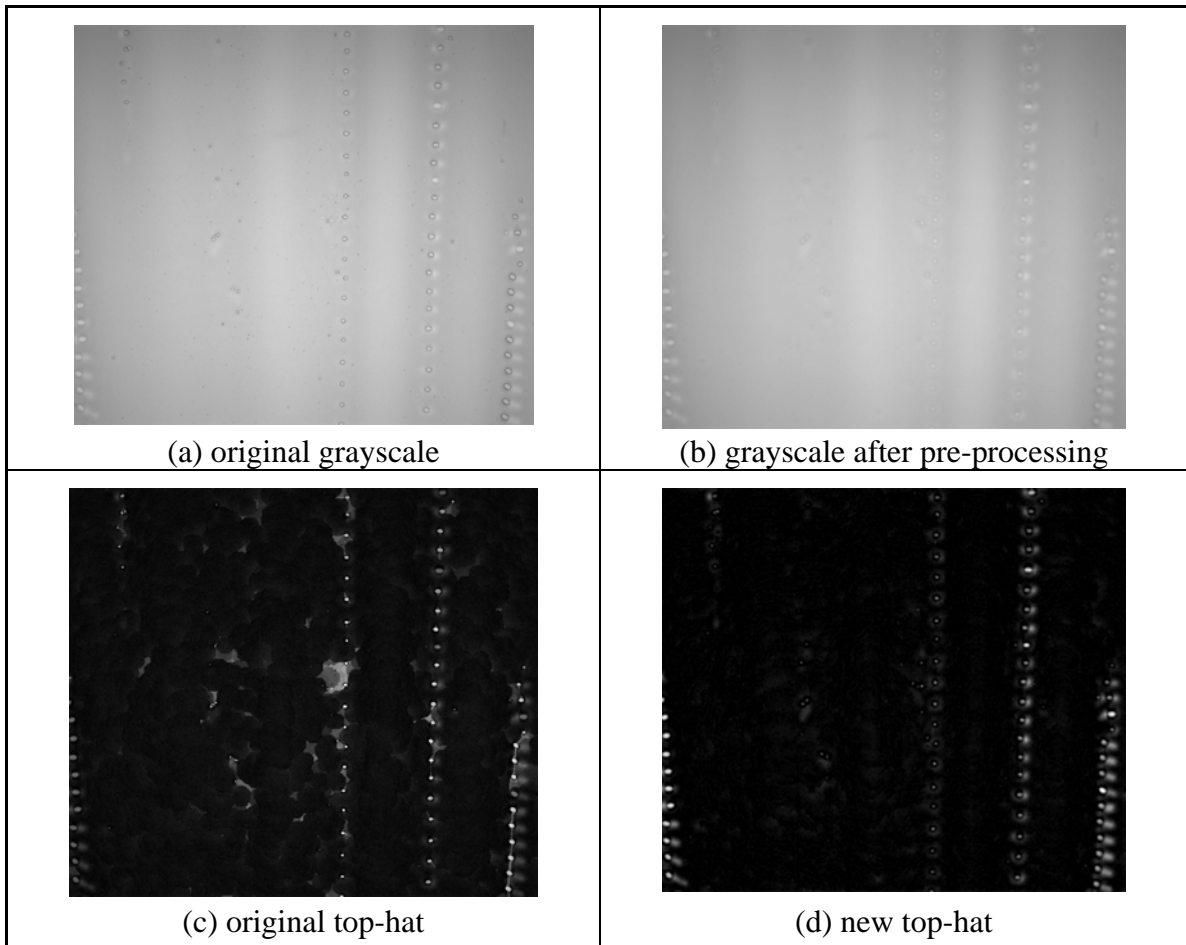


Figure 5.3: Improving top-hat results by removing small bubble defects from the image.

5.1.2 False Alarms and Escapements

The two types of defect identification processing errors were false alarms (flagging good film as defective) and escapements (not identifying a defective region). After processing more than 100 images using the modified processing scheme described in Section 5.1.1, the RFIS proved to identify defects robustly if the image processing parameters were set correctly. 25 images of poor casting were identified by hand and with the image processing algorithms. This resulted in 2758 identified defects, 33 false alarms, and 196 escapements—or a false alarm rate of 1.2% and an escape rate of 7.1%. The false alarms were generally located around other defects because the film disruption or the spatial operations misinterpreted the mean grayscale. The escapement rate was most often a result of missing very light thinning. These regions may have been unidentified with the algorithm because the smoothing operation or because the region

was less than 10 pixels in size. Escapements also occurred in some situations where multiple defects were identified as a single defect. From this analysis the following list of recurrent errors were identified:

1. Around certain defects, there was a region of disturbed thin film which was falsely identified as another defect. For instance, in Figure 5.4, a gel defect caused thinning on the periphery, which artificially created three light defect regions. Although these regions were thinning defects, they were not indicative of the casting window, and therefore were false alarms.

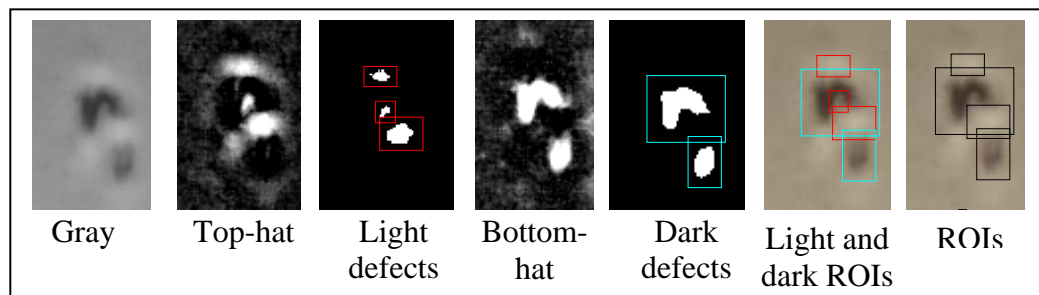


Figure 5.4: Superficial light defects created by gels in the casting.

2. Thinning was often difficult to capture, because depending on the grayscale variation of the particular defect, it could often slip under the threshold. For instance, the thinning on the left of Figure 5.5 was below the threshold but the other three thinning regions were not.

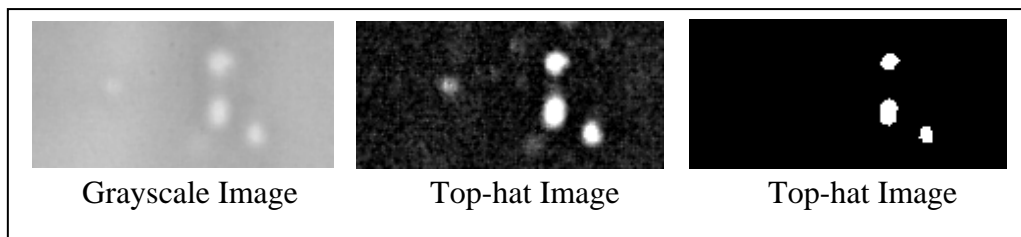


Figure 5.5: Thinning (on the left) escaping detection.

3. Defects which were close together could be identified as a single defect because they were thresholded into the same blob region.
4. As with all inspection systems, at some point the pixel resolution limits the size of the defects which can be identified. In the case of the RFIS each of the pixels represented a $73 \times 73 \mu\text{m}$ region of webbing, so anything below that size escaped

detection. As shown in Table 5.1, the defects on this order were holes, bubbles and gels. Figure 5.6 shows examples of bubbles on this order.

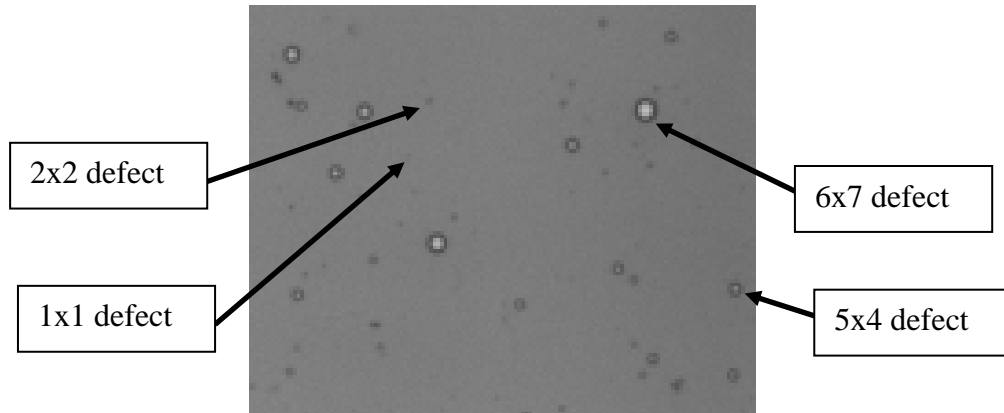


Figure 5.6: Image of membrane with different bubbles sizes.

5. Due to the image processing algorithms, e.g., top- and bottom-hat operations, there were occasionally false identifications around other defects because the top- and bottom-hat operations measured the local background. Therefore false alarms were often the result of periodic defects where the mean background was not identified correctly, as shown in Figure 5.7. However, these types of defects occurred 10-20 psi below the casting window, so this limitation would be rarely encountered.

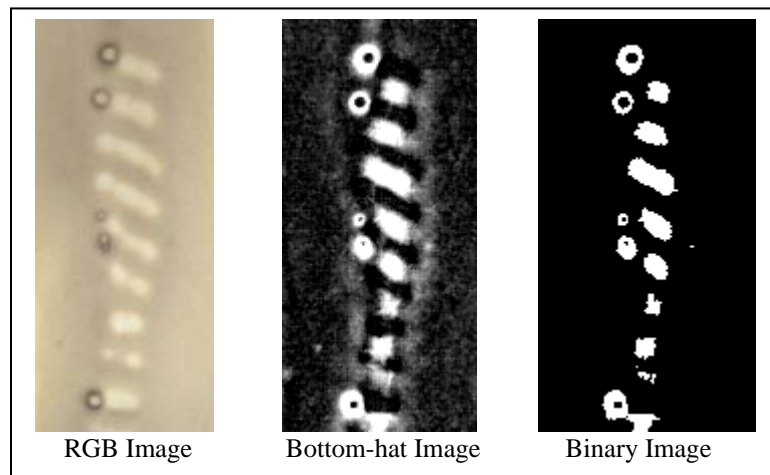


Figure 5.7: False dark identifications due to dense periodic thinning.

5.2 Defect Classification

The neural network was used to take segmented defect regions of interest and classify them into one of the four defect categories. After training the network with 2,100 hand classified defects, the network reported 96% classification accuracy, with the majority of the misclassifications resulting from hole/thinning confusion. To verify the neural network was operating correctly, the images used for the training data were classified, as shown in Figure 5.8. After the neural network was shown to produce accurate classifications, additional images were classified with the network, such as in Figure 5.9. It was found that the new classification images performed less accurately than the images which the training data was extracted. However, this reduction in accuracy remained acceptable for determining the defect trends and locating the position on the casting window.

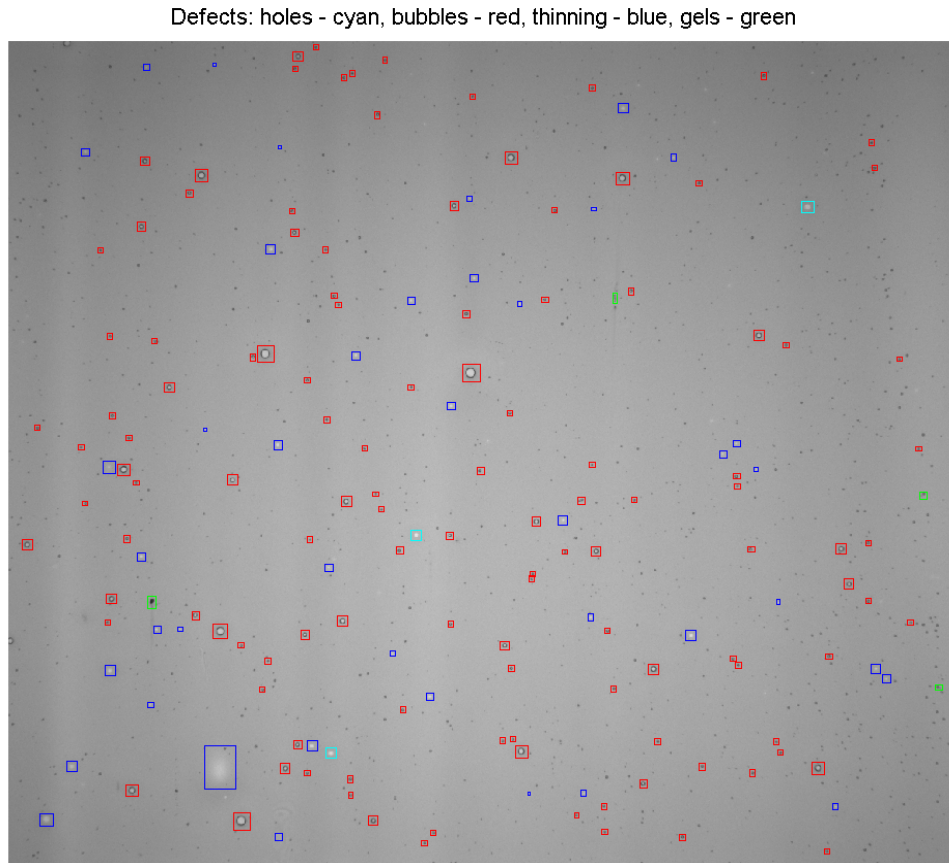


Figure 5.8: Defect identification and classification results.

Defects: holes - cyan, bubbles - red, thinning - blue, gels - green

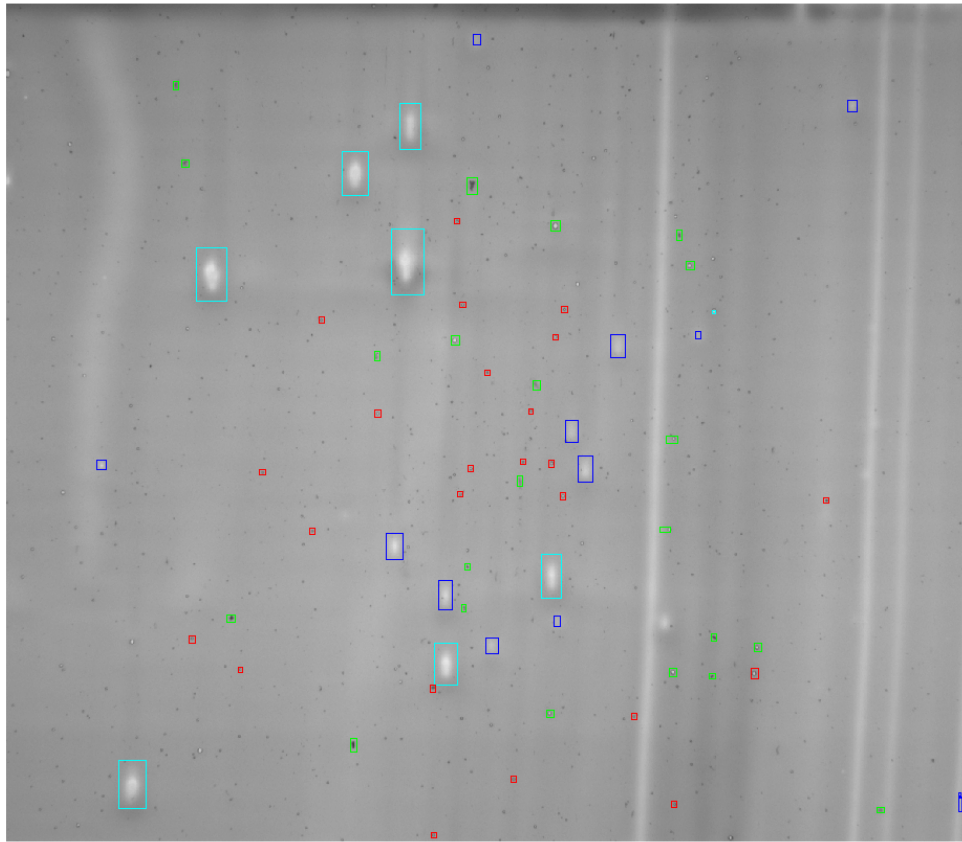
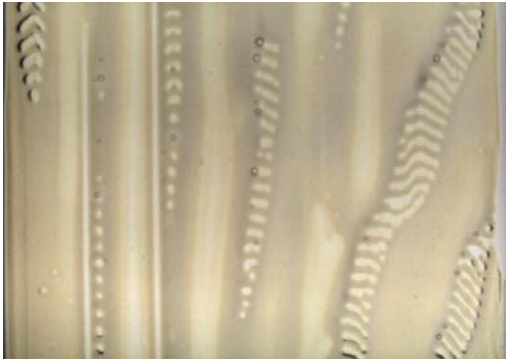


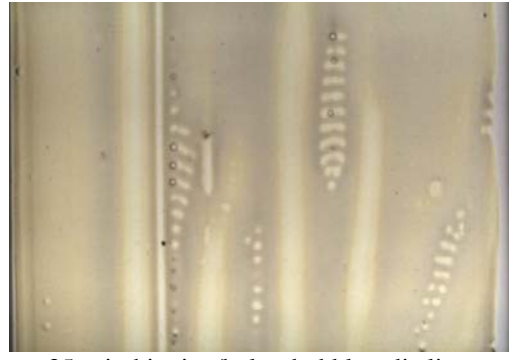
Figure 5.9: Defect identification and classification results.

5.2.1 Casting Window Analysis

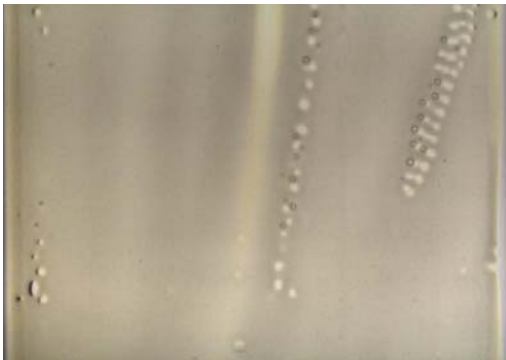
Experimental work was required to verify numerical simulations of the slot die extrusion process conducted by Bhamidipati et al. [125]. Multiple points on the casting window were obtained experimentally by fixing the web speed. Casting points were collected every 5 psi for fixed web speeds of 1.0, 1.5, 2.5, 4.0 and mm/s. One of these vertical passes (or slices) through the casting window is shown in Figure 5.10. The experimental casting window showed the casting window trends in Figure 5.11. When the web speed was too large, the volumetric flow rate was not capable of meeting the required thickness, and voids were created. When the pressure was too high with respect to web speed, there was excess material extruded from the die, the solution flowed upstream of the die, caused dripping, and resulted in castings with air entrainment.



30 psi: thinning/holes, bubbles, die lines



35 psi: thinning/holes, bubbles, die lines



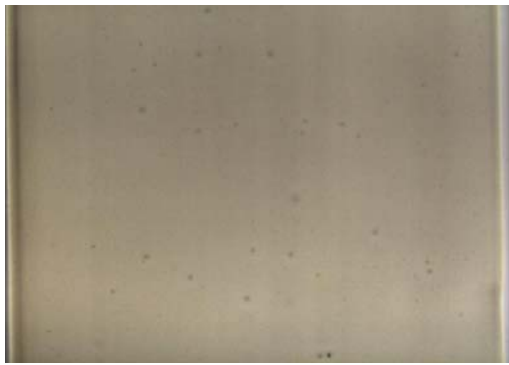
40 psi: thinning/holes, bubbles



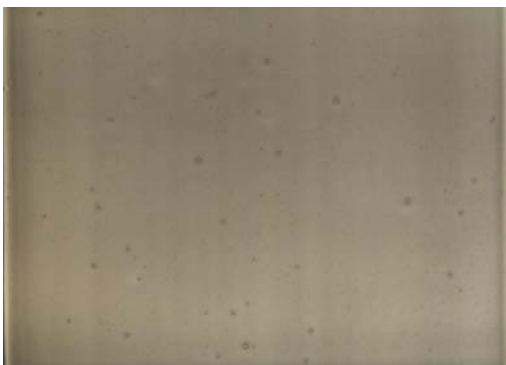
45 psi: thinning/holes, few bubbles



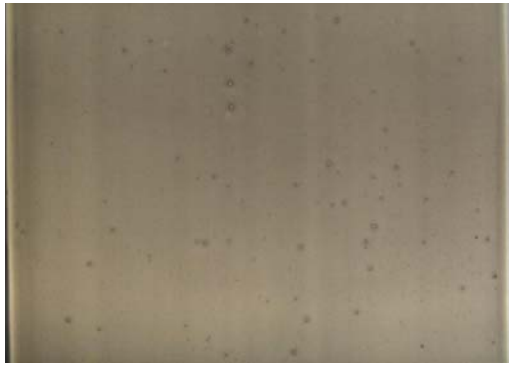
50 psi: nearly no defects



55 psi: bubbles



60 psi: bubbles



65 psi: bubbles, slight thinning

Figure 5.10: Images from a vertical slice of the casting window at $V = 1$ mm/s. The pressure and defects are shown for each of the images.

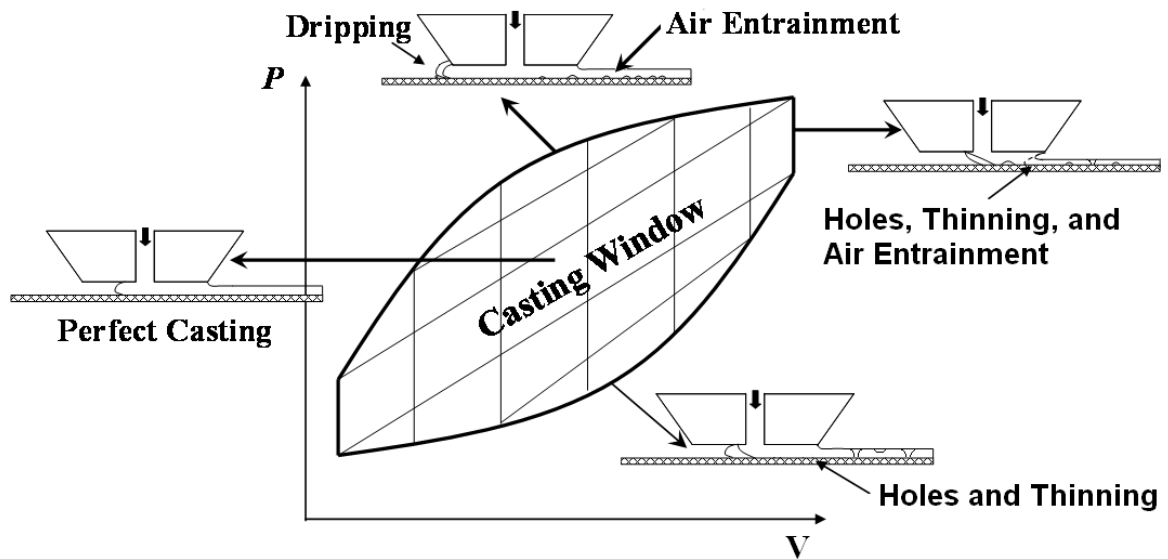


Figure 5.11: Fuel cell membrane casting window results (adapted from [127]). The image shows the defect trends for different locations on the tank pressure vs web speed plot.

Counting the number and type of defects, with the image processing system and by hand, corroborated the defect trends for the P versus V casting window plot in Figure 5.11. The defect trends are summarized in Figure 5.12 for one web speed. For web speeds of 1.0, 1.5, 2.5 and 4.0 mm/s the defect trends were consistent with those in Figure 5.12. At high pressures there was more air entrainment due to dripping, and at low pressures, there were holes and thinning defects in the membrane. The casting window did not have strict edges, as shown in Figure 5.11 and Figure 5.12. Instead, there were gradually increasing numbers of defects as the parameters were adjusted away from the defect minimum. Thus, the casting window boundaries were ambiguous and could only be defined if an acceptable defect quantity was specified. The maximum web speed which produced good castings was not determined because of hardware limitations, but it was expected to exist based on the literature review and numerical simulations.

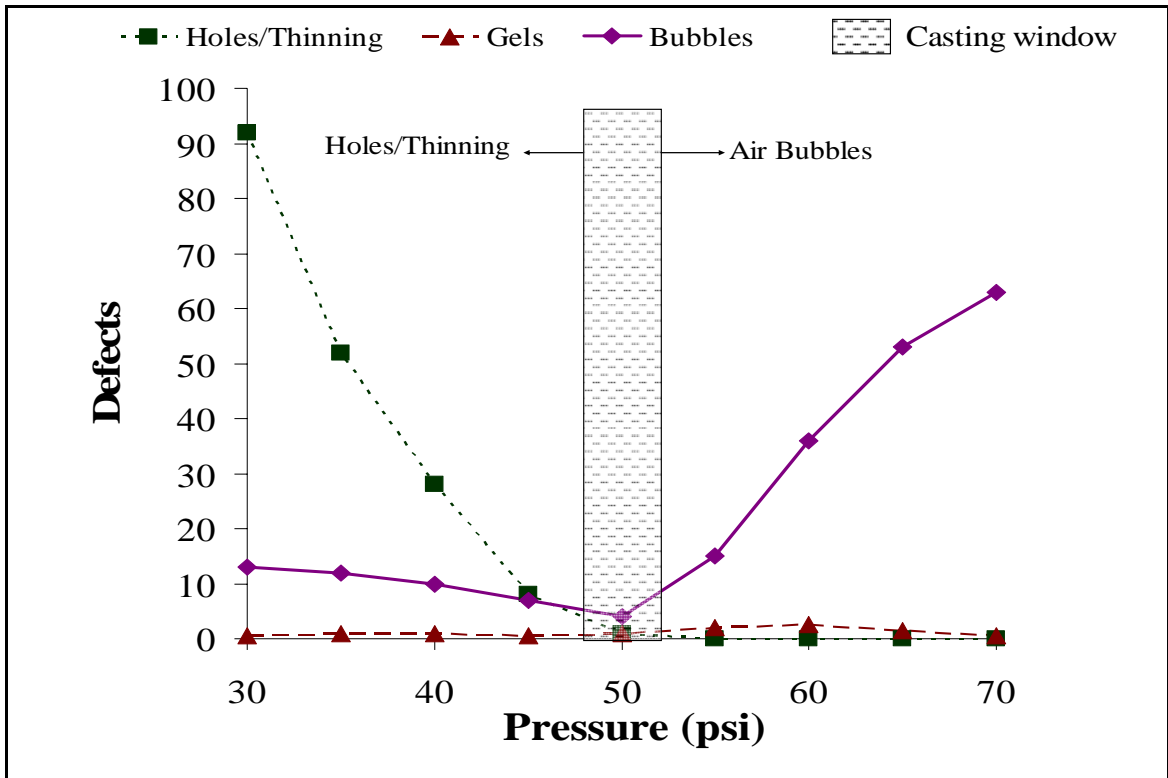


Figure 5.12: Vertical slice through the casting window. Defects per image vs pressure passing through the casting window at ~1 mm/s.

5.2.2 Misclassifications

Although, the training reported 96% classification accuracy, the system did not consistently produce that paramount accuracy. The primary reason for this deficiency was that the specific types of defects were not included in the training data—e.g., large non-circular bubbles, defects less than 10 pixels, oddly shaped holes and thinning.—so the division of the defect feature space with the NN did not factor in these features. As a result, there were hardly any large bubbles included in the training data, so they were often classified as gels, shown in Figure 5.13. Furthermore, because defects less than 10 pixels were not included in the training data, when the minimum defect size was decreased, the small bubbles were classified as gels. Thus, a more thorough collection of possible defects should be included in the training data in the future.

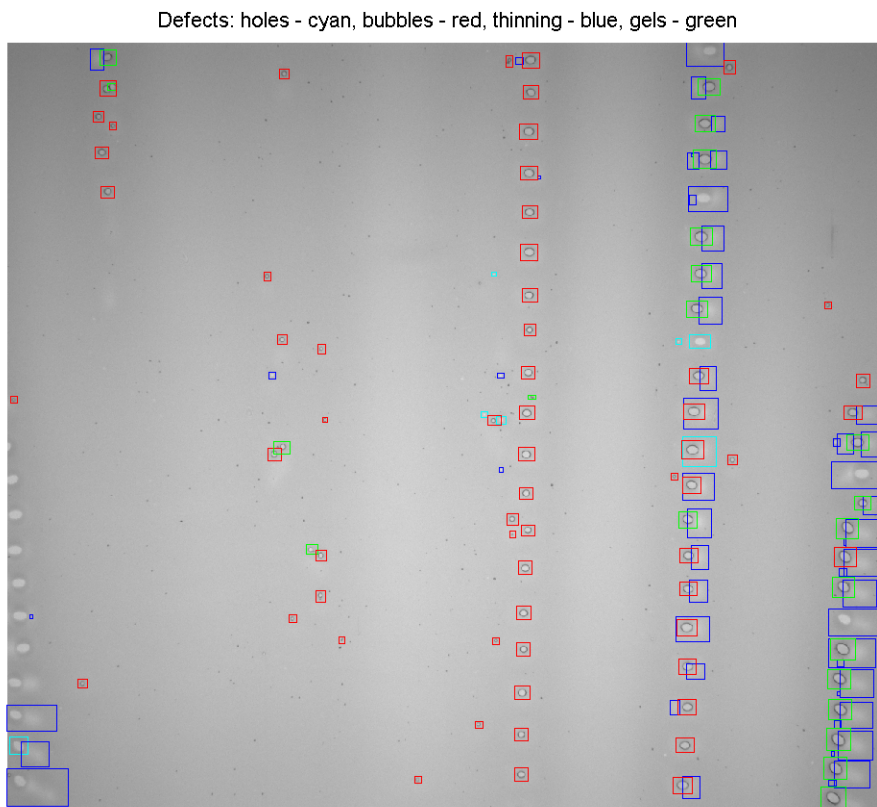


Figure 5.13: Misclassification of bubbles as gels.

5.3 Thickness Profilometry

The transmission densitometer produced full-field density values for the imaged area. Since the 12 bit images were averaged in 10 x 10 pixel regions, there were 139 x 104 thickness measurements for the influx and efflux images. These two images were used to calculate the density at 14,456 locations on the imaged membrane.

5.3.1 Determining the Membrane Extinction Coefficient

In order to determine the extinction coefficient for the membrane, the true thickness of membrane in liquid form was determined by a digital Mitutoyo Absolute Thickness Gage while the density was found using the transmission densitometer. The membrane was cast onto the PET substrate, and then a small sheet of PET with an identification number and location marker was placed on top of the cast membrane. By sandwiching the membrane between the PET sheets, the material was no longer exposed to the moisture in the air, and therefore, did not hydrolyze. This allowed time to cut out the samples and measure them with the micrometer. The marked locations were imaged with the

densitometer while passing through the inspection system to determine the density. $0.01 D$ was subtracted from the density to account for the two PET sheets (see Figure 3.35), and the thickness of two PET sheets was subtracted from the micrometer thickness measurement. The density measurements were subject to a number of challenges as shown in Figure 5.14. There were new sources of densitometric error because (a) placing the top sheet of PET on the membrane would occasionally trap air between the membrane and PET, (b) there were bubbles and other defects in the membrane which caused localized density changes, and (c) handling the numbered reference sheets may have left smudges on the sheets, although latex gloves were worn to minimize this. These new sources of potential error are possible causes for the large thickness deviation seen in the calibration data in Figure 5.15.

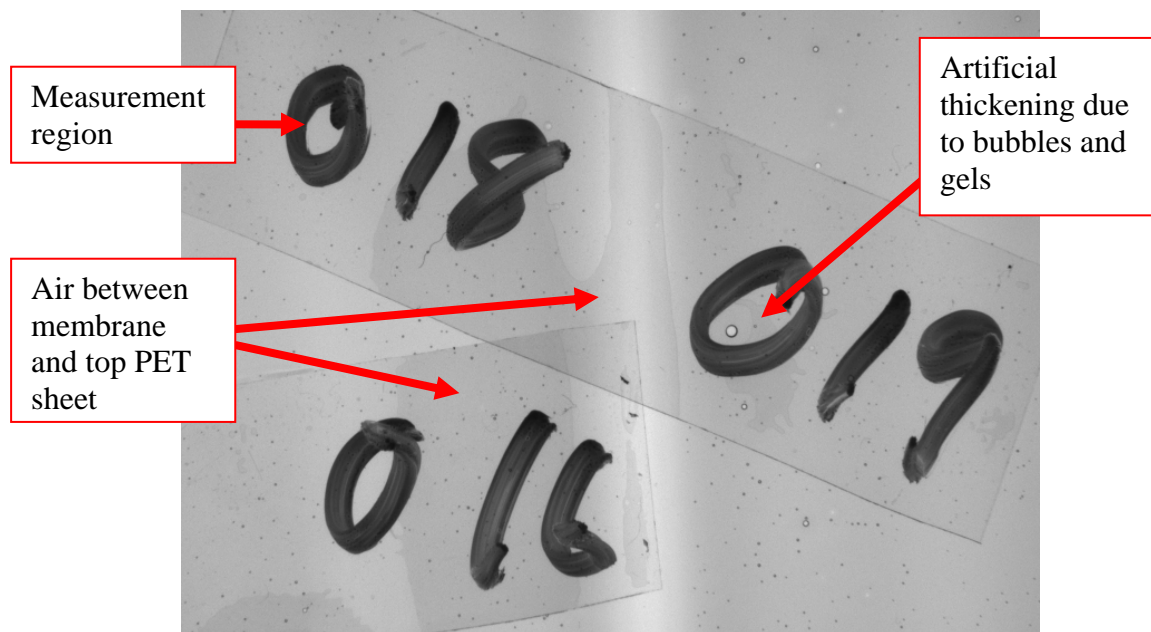


Figure 5.14: Complications with density measurements.

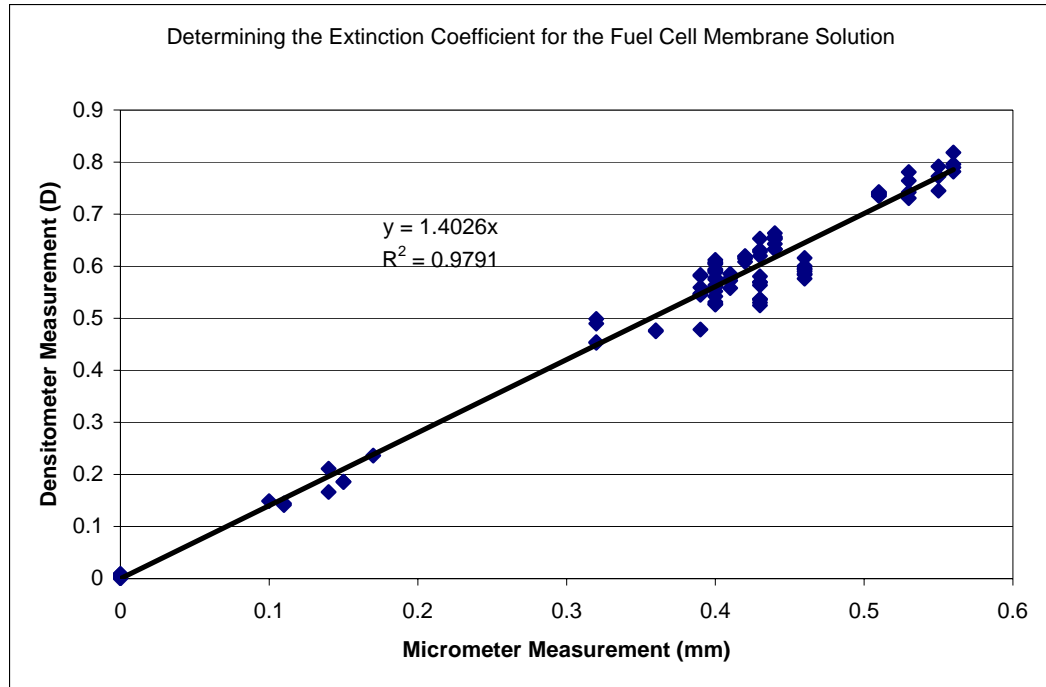


Figure 5.15: Finding the extinction coefficient for the fuel cell material using a trend line of micrometer and density measurements.

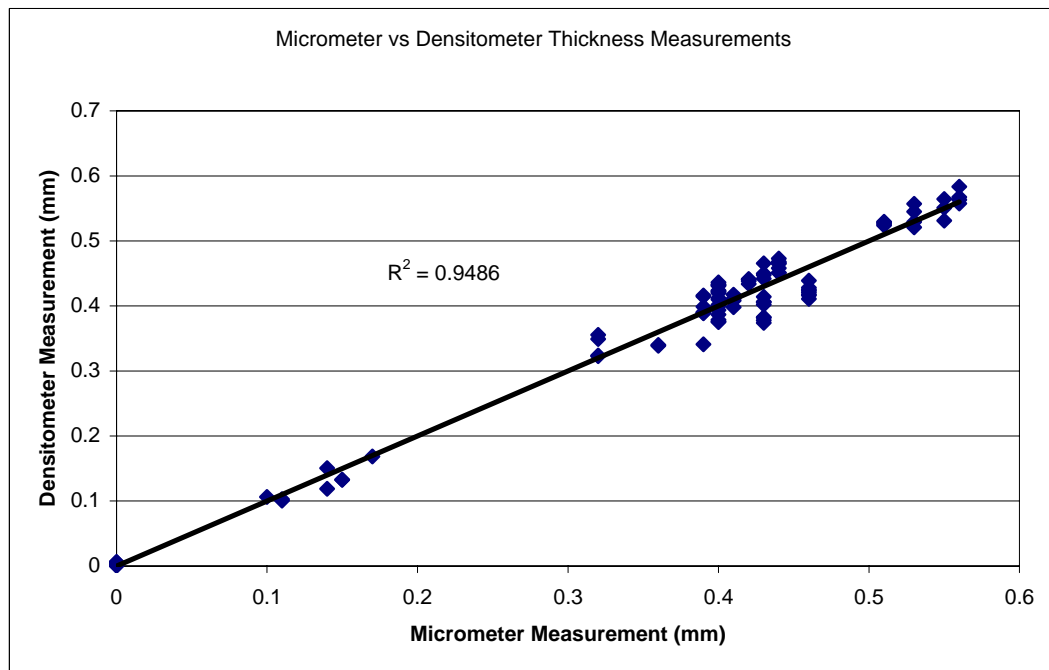


Figure 5.16: True thickness (from the micrometer) vs densitometer thickness

Based on the linear regression of 100 independent thickness measurements, it was found that Beer's law matched the experimental data well. The extinction coefficient for

the membrane was determined to be 1.403 D/mm using the trend line in Figure 5.15. The extinction coefficient was then used to convert densities to thickness values, shown in Figure 5.16. The average error was 4.7% with a standard deviation of 3.73%, and a maximum error of 15.3%. However, the thickness comparison was subject to errors in both the densitometer as well as the Mitutoyo micrometer. The sample in the micrometer had to be kept flat so that the clamping anvil recorded the correct thickness. Therefore, variation in the reference thickness may have caused a portion of the densitometer thickness error.

Further, it was believed that the spring in the thickness gage could compress the thin film slightly—even with its high viscosity—so the membrane thickness was compared to frozen membrane thickness. The sample was measured, placed in liquid nitrogen for 10 s and then re-measured. It was found that the sample was very brittle after being frozen and the freezing process expanded the film by approximately 30%. Therefore only the non-frozen measurements were used for the thickness to density correlation. It was also proposed to create a step between the substrate and top of the membrane and use a Zygo white light interferometer to measure the thickness through non-contact means, but the scanning range of the instrument was limited to 100 μm , so it was impractical for the large thickness ranges needed for an extinction coefficient fit.

During another set of tests, using a different batch of membrane material but the same method for determining the extinction coefficient, the coefficient was found to be 0.62—drastically different than the first test. This was due to the change in material chemistry, clearly identified by lower viscosity, entrained small bubbles, and different optical properties. Changes in material chemistry were problematic because they affected the transmission characteristics of the material and the extinction coefficient had to be recalculated for each chemical composition. Without doing so for each new chemistry, the thickness profilometry would provide inaccurate depth profilometry results and therefore only qualitatively measure thickness uniformity.

5.3.2 Thickness Results

Using the MATLAB graphical user interface, thickness measurements were made of the efflux to determine the background noise. A typical example image of the

background noise is shown in Figure 5.17. The background density noise was found to be at most ± 0.006 D, or approximately ± 4 μm for the membrane material. To verify the calibration results in Section 3.4.1.7, the densitometric accuracy at 0.00, 0.06, 0.26, and 1.46 D was investigated with the X-Rite densitometry calibration sheet, shown in Figure 5.18. As expected from the previous densitometry calibration results, measurements of 0.00 and 1.46 D were the most accurate, 0.06 under-estimated the density, and 0.26 over-estimated the density, which matched the results from Table 3.5. Based on these results, the variation in thickness (as seen in Figure 5.15) was determined to be the combination of instrumentation error, local grayscale deviations, and variation in “true” thickness from the micrometer measurements.

Since the calibration sheet only had four calibrated densities, it was difficult to determine what portion of the error was from instrumentation (e.g., backlight intensity variability, optical surface smudging, camera noise) and what portion was due to the experimental design (e.g., density variations in the membrane, PET films, etc.). Cast membrane thicknesses were typically specified between 200-400 μm on the RFIS and the extinction coefficient for this material was about 1.4 D/mm, so the density values for the system ranged between 0.280 D and 0.560 D. When comparing these densities to known densitometry errors in Figure 3.34 and Table 3.5, it was found that the large instrumentation errors and variance associated with dense measurements (i.e. 1.46 D) were avoided. Furthermore, the density from the calibration sheet showed the instrumentation was reasonably consistent (maximum error range of 0.0335 D for 129 0.26 D calibration tests), but the membrane density measurements varied significantly more (e.g., 0.14 D range at 0.43 D with fewer tests). Thus, the difference in these values can be attributed to variability inherent in the experiment due to the membrane and PET. It was likely that there were local variations in grayscale from debris or scratching on the PET surfaces. Additionally, defects and localized thickness variations changed the density measurement while the reference thickness from the micrometer did not account for surface roughness. Thus, it is believed that the accuracy of the instrument contributed only a small portion of the thickness noise to the measurements and it was the design of the experiment which caused the majority of the error in the results.

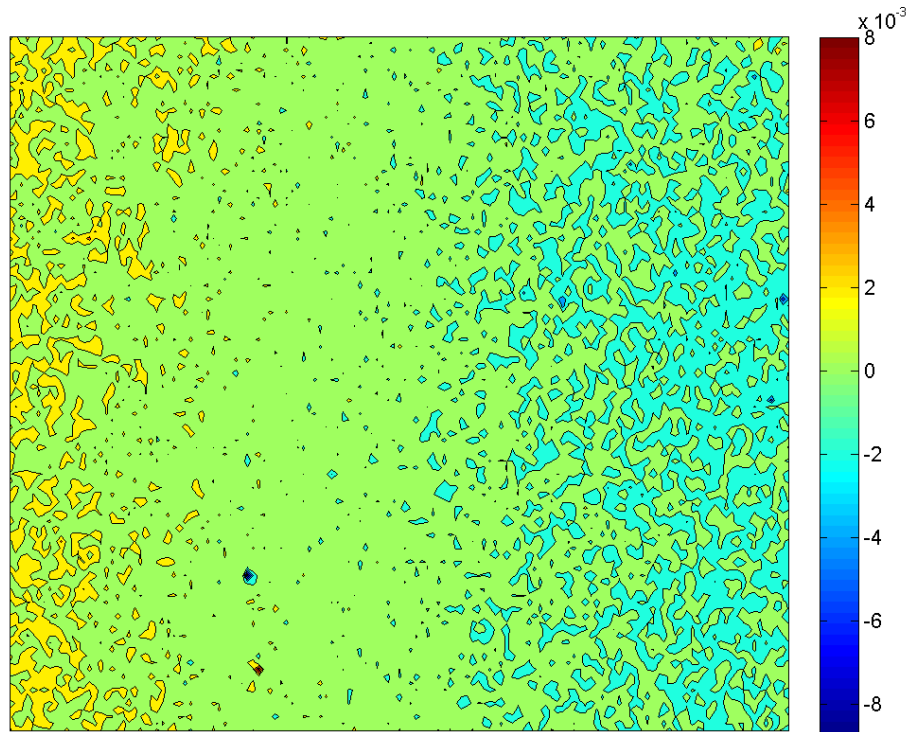


Figure 5.17: Background noise in the densitometer with the influx values determined with 20 averaged images.

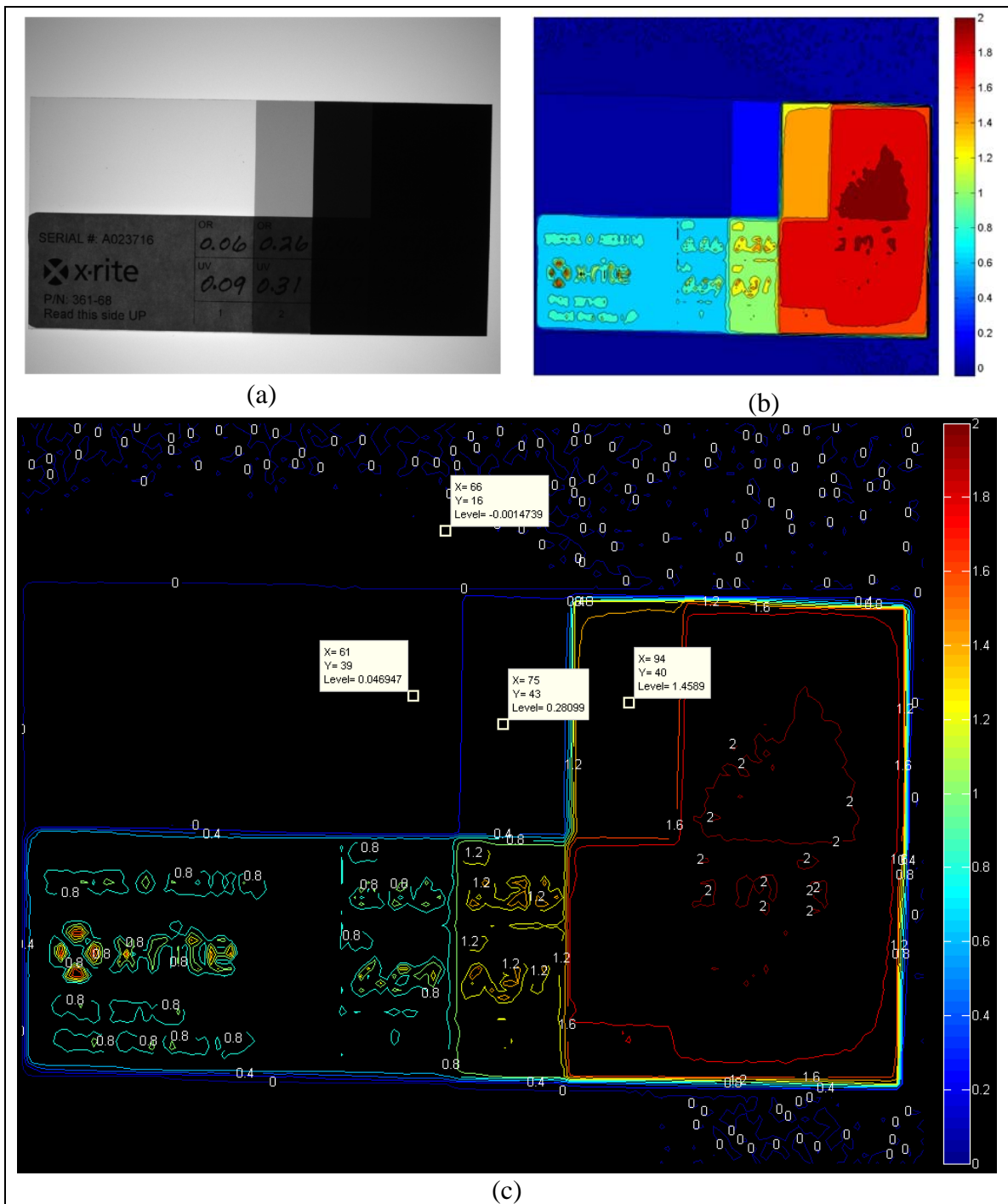


Figure 5.18: The density of the calibration sheet (a) in grayscale, (b) color contour plot, and (c) a topographical representation. The density for sample 10x10 regions in the 0.00 D, 0.06 D, 0.26 D, and 1.46 D areas are indicated.

In another experiment, the volumetric flow rate of the tooling system was calculated with the thickness profilometer. The flow rate was prescribed in the numerical simulations so it was important to obtain the volumetric flow rate versus pressure relationship. Using thickness measurements of relatively defect-free castings, the volumetric flow rate for different pressures was calculated by

$$Q = w_{imaged} V \left[\sum_{i=10}^{end-10} \left(\sum_{j=1}^{end} t_{ij} \right) \right] \quad (5.1)$$

where V was the web speed, w_{imaged} was the width of the imaged membrane, and t_{ij} was the thickness at location (i,j) . The image was cropped in the x -direction to remove edge effects from affecting the calculation. A plot of these measurements is shown in Figure 5.19. The results show a linear trend between the volumetric flow rate and pressure. The mean thickness across the web was determined more accurately than the local measurements because the data points were an average of nearly 10,000 local measurements.

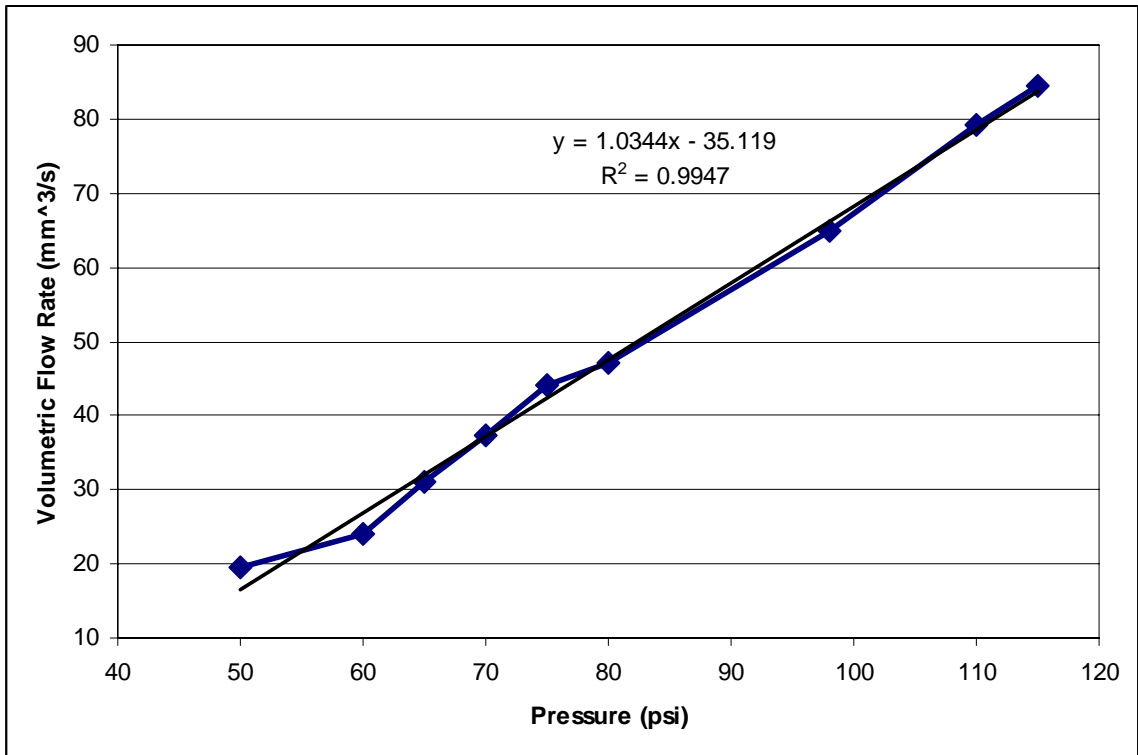


Figure 5.19: Volumetric flow rate vs pressure determined with the thickness profilometer.

5.4 GUI results

As discussed in Section 3.4.3, the GUI displayed the membrane thickness and defect results. The system operated fully autonomously, collecting image data at regular intervals, and processing it to produce and display defect and thickness results. As new material entered the inspection station, a snapshot of the membrane was taken and the following operations were performed:

- the locations and types of defects were determined and displayed
- the thickness profile was calculated and displayed
- the location on the casting window was heuristically ascertained and displayed

Once classification of an image was completed, the GUI allowed the user to visualize image processing results (i.e., top- and bottom-hat and thresholded images) as well as identification and classification results using the following display options:

- Raw – the original image
- Top-hat – the top-hat operation of the grayscale image
- White threshold – the result of thresholding the top-hat
- Bottom-hat – the bottom-hat of the grayscale image
- Black threshold – the thresholded bottom-hat image
- Thickness – the thickness profile with color map showing the localized material thickness
- All boxes – bounding boxes shown with the color-indicated blobs (shown in Figure 5.20)
- Gels/Holes/Bubbles/Fisheyes boxes – displayed specific bounding boxes on the raw image (as shown in Figure 5.20)
- All defects – the raw image with all the defects labeled (shown in Figure 5.20)

The processed images were highly useful for both setting the image processing parameters and understanding errors in the GUI defect identification system. The classification images were designed for the manufacturer to better visualize the manufacturing defects. These images clearly indicated locations where the material was

defective and what type of defects were present. An example of these are shown in Figure 5.20.

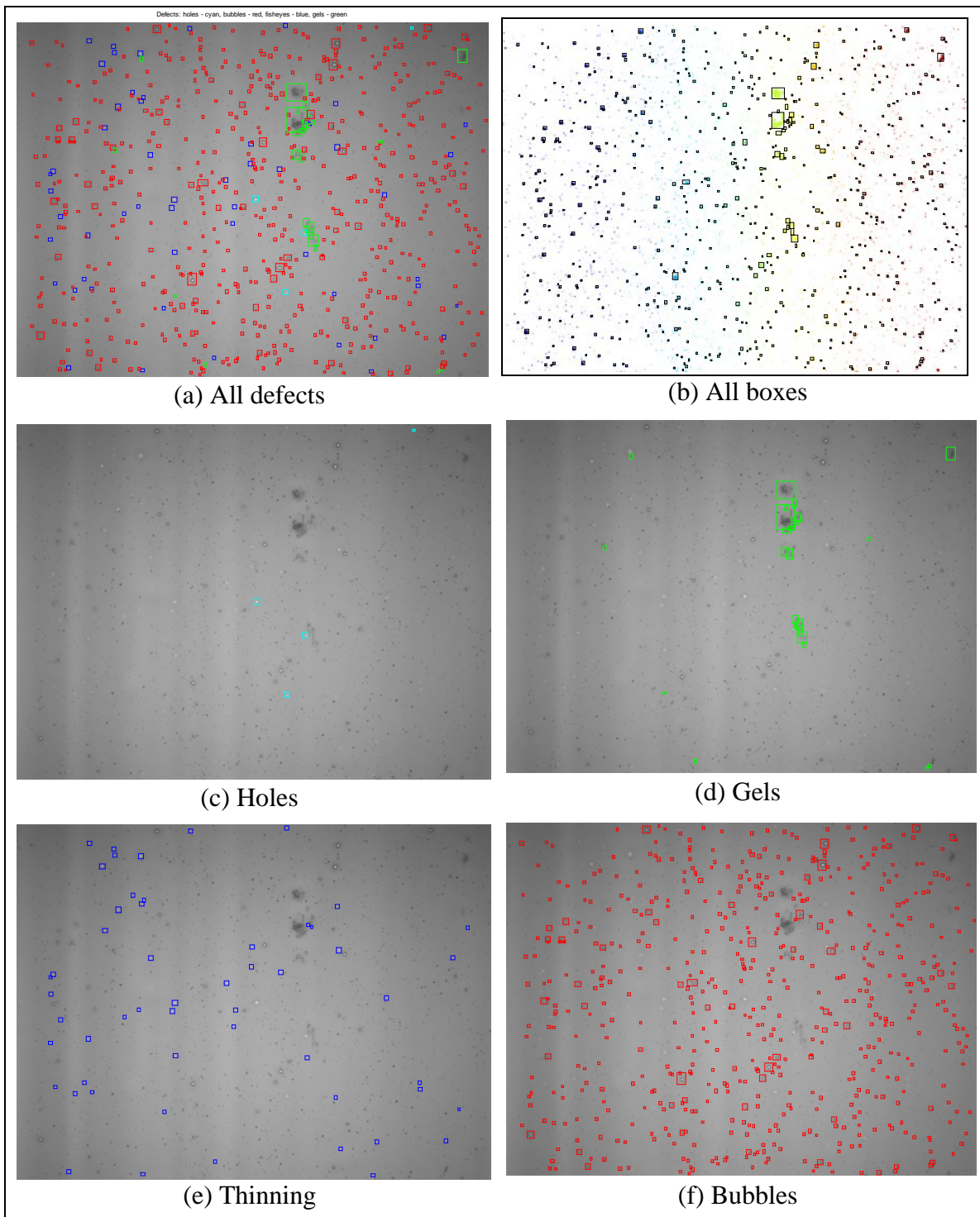


Figure 5.20: Results from the defect identification and classification with the GUI.

The GUI also tallied the defect types and alerted the user to the status of the casting parameters, as shown in Figure 5.21. The defect table showed the number and percentage of defects for the most recently classified image as well as the total number and percentage of defects for the entire batch run. Based on the classification results, the current location on the casting window was displayed. As the casting window analysis indicated in Section 5.2.1, there were two regions of poor manufacturing: the region “below” the casting window where the web speed was too high for the current tank pressure, and the region “above” the casting window, where the web speed was too low for the tank pressure. The three casting window locations are illustrated in Figure 5.22. Thus, by integrating all this information, the GUI displayed pictorial recommendations and written instructions of corrective measures necessary to return to the interior of the casting window.

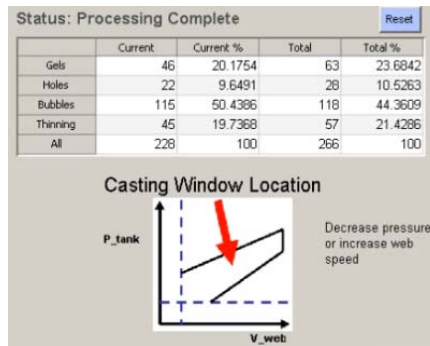


Figure 5.21: Defect tallies, casting window location, and suggested parameter adjustments.

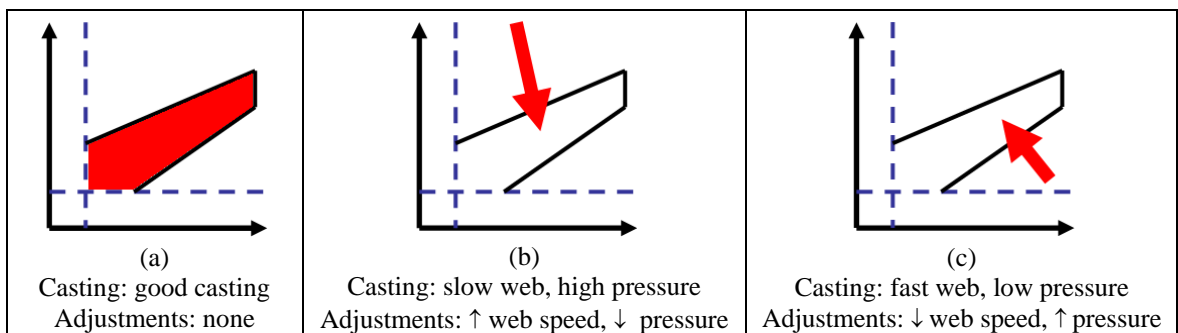


Figure 5.22: Casting window locations and recommendations in the GUI.

The GUI also provided the bi-directional thickness profile of the imaged area using the transmission density system, shown in Figure 5.23. The baseline influx was determined by capturing and averaging 20 successive 12 bit images with only the substrate on the backlight. Then when images were captured of the membrane, the

thickness profile was generated based the extinction coefficient entered by the user. This showed simple-to-understand thickness results for the user, such that if the thickness was not within tolerance, changes to the casting operating parameters could be made.

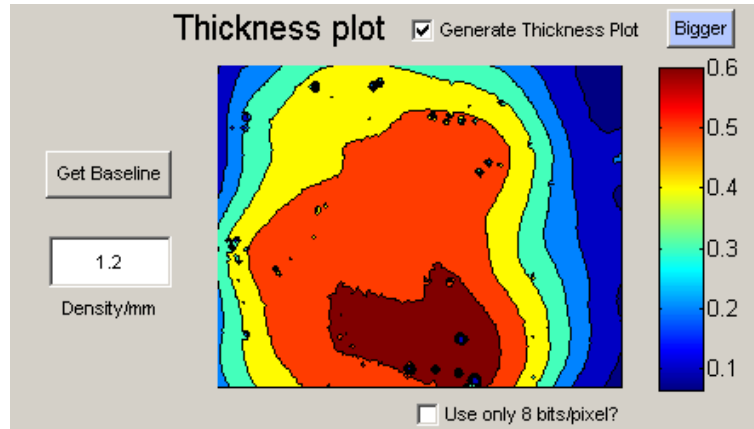


Figure 5.23: The thickness profilometry system.

The processing speed was the greatest challenge for the interface because for each defect that was located, the program was required to segment the ROI, calculate NN inputs, and classify the defect with the neural network. When there were a large number of defects, such as in Figure 5.20, this would take a significant amount of time. Using an inspection computer with 1.86 GHz Intel Core 2 processors and 2 GB of RAM, it took an average 0.017 s for each of the defects to be fully processed. Thus, the web speed was limited for castings with a large number of defects if 100% of the material was required for inspection. At high feed rates, the image processing would be unable to keep up with the image data rate, and some of the material would not be inspected. On the RFIS, the web speed was never set to a speed which the GUI could not continuously monitor, but for faster manufacturing operations this limitation must be considered.

CHAPTER 6: DISCUSSION OF RESULTS

A roll-to-roll casting system was designed and constructed to fabricate a range of thin films. The cast film was passed through an inspection system to continuously determine the thickness and quality of the casting, as well as determine the location on the casting window by classifying the types of defects. The inspection system had an escape rate of 1.2%, false positive rate of 7.1%, and classification accuracy was 96.1%. The density of the material was determined with a maximum error of 0.029 D and maximum standard deviation of 0.0065 D, but due to localized grayscale variation of the material, the thickness measurement had an average accuracy of 95.3% and standard deviation of 3.73%.

6.1 Defect Inspection

Although finding the correct threshold values and structural element sizes for the image processing took time and experience, once they were correctly set, the identification and classification system worked well near the casting window. If the casting shifted away from this location, the number of defects increased and caused (a) longer processing times, (b) greater density of defects and therefore more false positives, and (c) threshold adjustments to account for the different types of defects. For instance, when the casting was mostly good, defects were easily detected so the thresholds could be set aggressively to catch any grayscale deviation, whereas when the casting was outside the casting window, thinning, bubbles, or holes clustered together, so less aggressive thresholds were required in order to avoid combining blob regions and false positives.

The image processing variables had a large impact on defect identification and classification. When set correctly the system performed satisfactorily, but defect identification was highly sensitive to the threshold values. In some cases, changing the thresholds by as little as 3-5 gray levels drastically escalated the false alarm or escapement rates—typically due to small blobs entering or exiting the binarization. Therefore, the inspection system operator must be skilled in selecting the proper

thresholds and prepared to adjust them as necessary. The structural element sizes also were critical to defect identification because they provided the top- and bottom-hat images for thresholding. Fortunately, the structural elements were highly robust and a 20-pixel disk for the hot-hat and a 12-pixel disk for the bottom-hat produced acceptable results for nearly all images.

Despite reporting a 96.1% classification accuracy with the training data, when operating the NN in real-time, the number of misclassifications were significantly higher. This can be attributed to two factors: 1) the NN relied on top- and bottom-hat results so when the image processing values were not optimally adjusted these input features were different than in the training data, and 2) the training data was extracted from a single batch material which did not produce certain defect characteristics, so these defects were commonly misclassified. For example, there was one defect type severely unrepresented in the training data: large and often irregularly shaped bubbles at low pressure. As a result, these defects were commonly misclassified as gels or occasionally holes, shown in Figure 5.13.

6.2 Casting Window Determination

The location on the casting window was determined in the GUI using a heuristic algorithm; however, the casting window defect trends changed slightly based on the batch solution chemistry. It was noticed that each batch had different chemical compositions, so the surface tension, adhesion, and cohesion properties changed depending on which of the manufacturer-supplied bottles was chosen for the test. In some cases this caused the periodic thinning effects at low pressures to be replaced by periodic bubbles. As a result, the location on the casting window was incorrectly determined. Thus, in order to accurately determine the casting window location, the specific defect trends for the chemical composition must be known. In such cases, there would need to be supplemental or modified GUI rules applied to the casting window calculations to account for the changes in batch material.

6.3 Transmission Densitometry Depth Profilometry

The accuracy and repeatability of the full-field densitometer did not meet the design requirements. The average thickness error was 4.7% of the measured thickness which corresponded to an average error of 11.8 μm at 250 μm . The design objective was to measure the thin film within ± 10 μm of the true thickness. Furthermore, the measurement error had a standard deviation of 3.73% (9.3 μm at 250 μm), so instrument repeatability was also poor. However, some of this error and variation can be attributed to the local variations and defects in the membrane. Calibration results showed that the instrument had a standard deviation of 4.6 μm (2.5%) for membrane thicknesses of 186 μm .

The extinction coefficient for the thin film was crucial to densitometry because this value described the range of measurable thicknesses. The membrane solution had an extinction coefficient of 1.4 D/mm, which was fortunate given the desired thickness measurement range, because it avoided high density measurements. At higher densities the variance is greater due to dark noise. Thus, for highly dense materials, there is a narrow range of thicknesses which can be accurately measured using the densitometer, as shown in Figure 6.1. However, if the extinction coefficient is small, very thick films can be measured, but the thickness measurements would be inaccurate because even small amounts of noise in the density would be magnified in the conversion to thickness, i.e., divided by the small coefficient, as shown in Figure 6.1.

Therefore, only a limited range of extinction coefficients are suitable for accurate measurements between 200-400 μm . Using the model in Eq. (3.33) with influx grayscale = 4095 and efflux noise, $\text{Norm}(\mu_{\text{graylevel_dark}}, \sigma_{\text{graylevel_dark_temporal}}) = 10$, the trade-offs were quantified for different extinction coefficients in Table 6.1. From the table, it can be seen that the error has a local minimum where the dark camera noises are low but the material is dense enough to provide grayscale variation with depth. Plots of the error versus extinction coefficient for different dark noise levels are shown in Figure 6.2. This shows the best extinction coefficient for transmission densitometry is around 1.1 D/mm. Depending on the required accuracy and amount of noise in the system, the range of acceptable thickness coefficients changes. For instance, if the dark noise was 20

grayscale levels, and 10 μm of error was acceptable, materials with extinction coefficients of 0.30-2.85 could be measured at 400 μm .

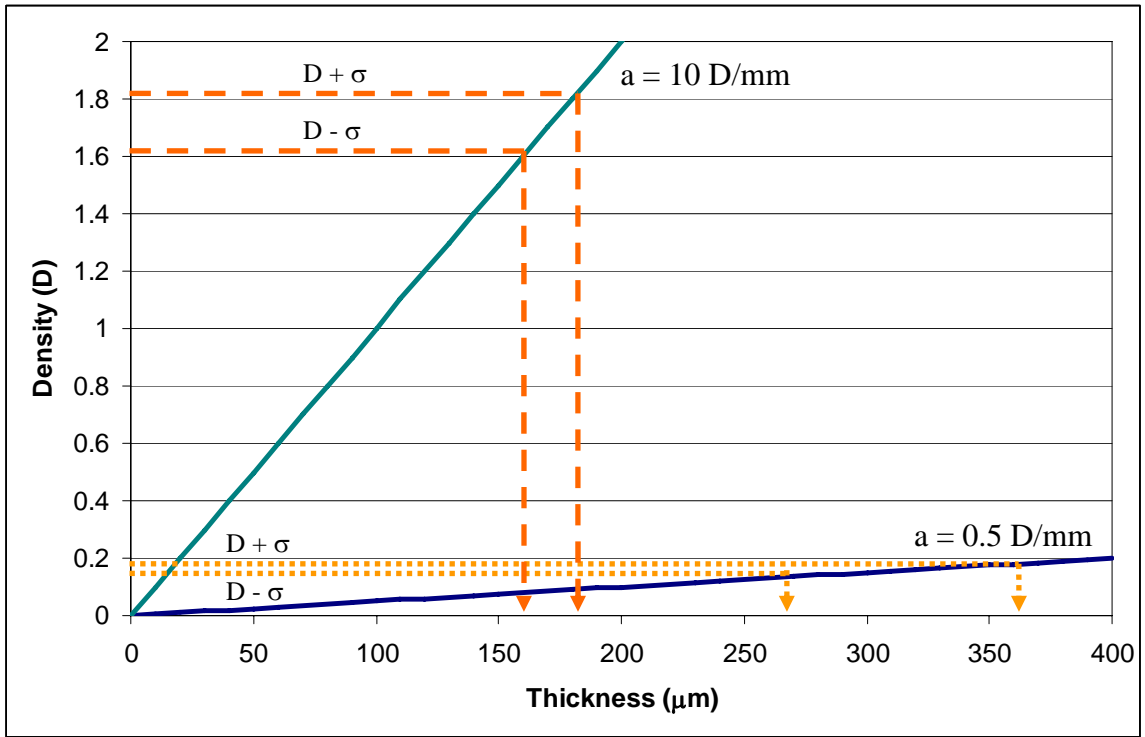


Figure 6.1: Theoretical density vs thickness profiles for two materials with a density measurement $\pm 1 \sigma$ shown to illustrate how noise is introduced into the measurement.

Table 6.1: Thickness errors for 400 μm measurements of different hypothetical thin films.

Extinction Coefficient	Density at 400 μm	Grayscale at 400 μm	Density with $z_{\text{dark}} = 10$	Density error	Density % error	Thickness error (μm)	Thickness % error
0.1	0.04	3735.59640	0.0388	0.0012	2.90	11.61	2.90
0.5	0.20	2584.40128	0.1983	0.0017	0.84	3.35	0.84
1.0	0.40	1630.64697	0.3973	0.0027	0.66	2.66	0.66
2.0	0.80	649.17225	0.7934	0.0066	0.83	3.32	0.83
3.0	1.20	258.44013	1.1835	0.0165	1.37	5.50	1.37
5.0	2.00	40.96000	1.9051	0.0949	4.74	18.97	4.74
10.0	4.00	0.40960	2.5949	1.4051	35.13	140.51	35.13

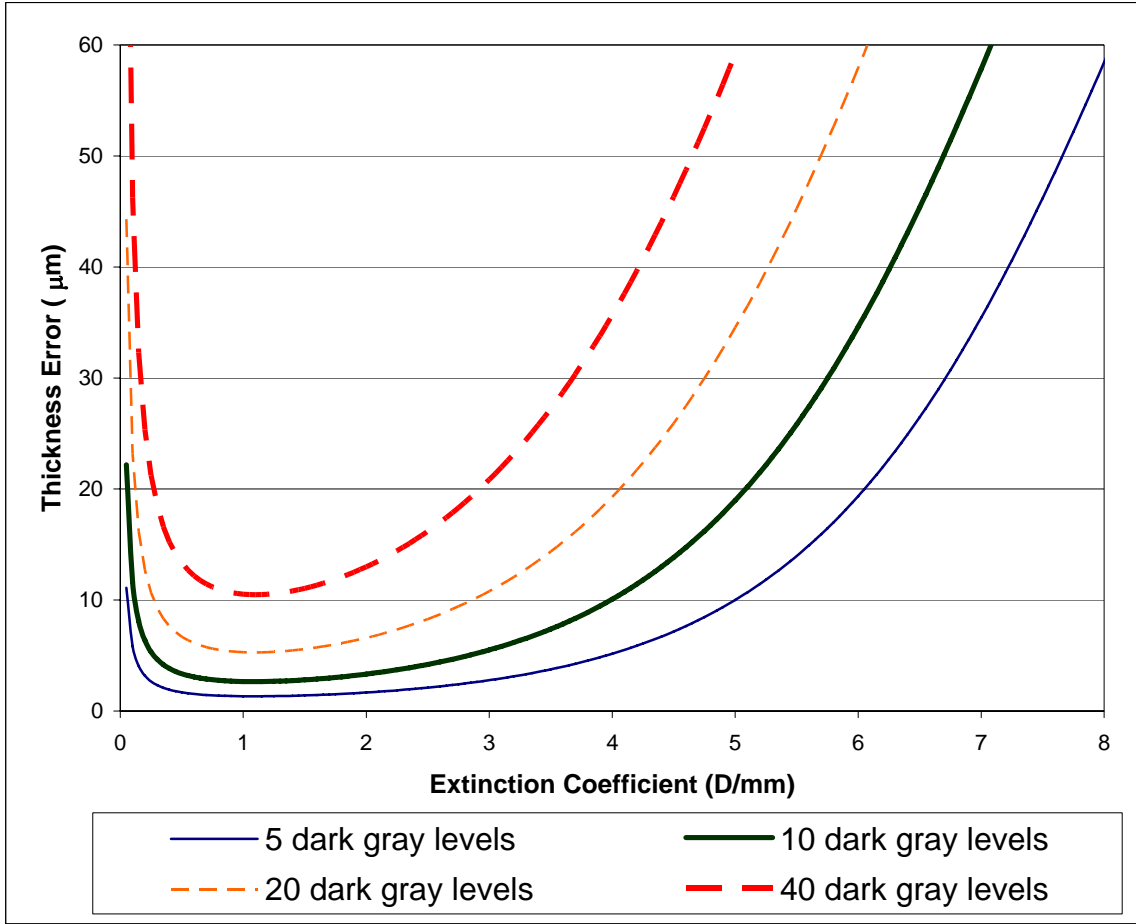


Figure 6.2: Theoretical thickness error at 400 µm vs extinction coefficient for different dark currents.

Depending on the thickness range of the material, a specific extinction coefficient can be determined which minimizes thickness error. This extinction coefficient may exist at a certain wavelength, so by tailoring the wavelength of light which passes through the material with monochromatic backlighting (e.g., with an LED array) or optical filters, the absorption could be optimized for accuracy. For example, if the RFIS manufactured a thin film at 400 ± 200 µm which had spectrophotometer results shown in Figure 6.3, the optimal wavelength could be determined. As shown in Figure 6.2, an extinction coefficient of about 1.1 D/mm was best for 400 µm measurements; thus, to match this absorbance, a wavelength should be selected such that the density is 0.44 D, based on:

$$D_{optimal} = a_{optimal} t_{mean} \tag{6.1}$$

The wavelengths which provided the optimal material density (absorbance) are indicated in Figure 6.3. However, this calculation does not take into consideration the quantum efficiency of the camera sensor, so to truly find the wavelength which minimizes error, a more thorough analysis of the full instrument must be performed.

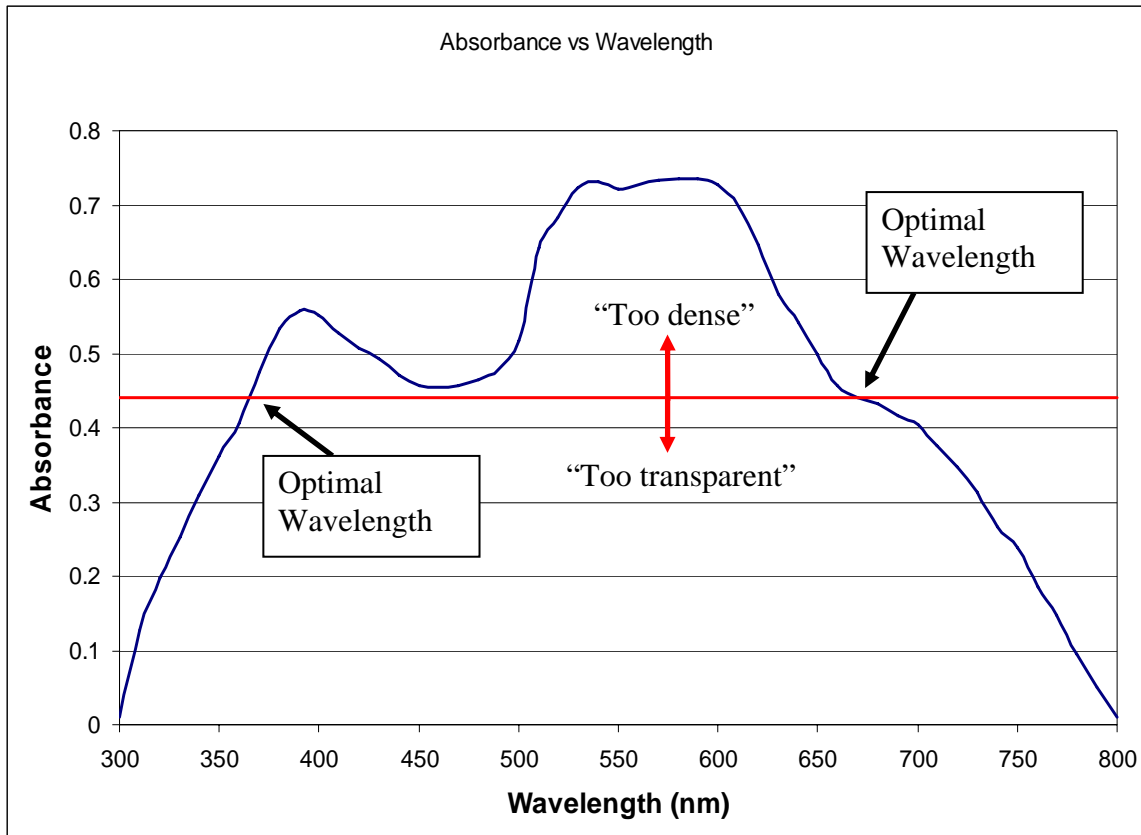


Figure 6.3: The spectral absorbance of a theoretical material shown with the two wavelengths which minimize error.

CHAPTER 7: CONCLUSIONS, CONTRIBUTION, AND FUTURE WORK

7.1 General Conclusions

Overall, the roll-feed imaging system prototype showed good preliminary results for a range of new inspection concepts. When the image processing parameters were set correctly, the defect identification and classification systems were highly accurate (better than 96%) and could determine the location on the casting window. The thickness profilometry tool was limited by material types and thicknesses, but with additional exploration, would be highly accurate, economical tool for measuring full-field, thin film thicknesses.

7.2 Contributions to Engineering and Science

The scope of this work was broad so the contributions to the engineering field cover a wide range of scientific and engineering topics. The primary contributions were:

1. expanding image processing techniques to a roll-feed imaging system, to detect, classify, and quantify defects for semi-transparent polymeric materials
2. exploring new defects and feature sets for neural network classification
3. creating a new technology to provide non-contact, real-time, full-field, nondestructive thickness profilometry with inexpensive components
4. autonomously generating casting parameter changes to improve manufacturing in real-time using the concept of a casting window

The image processing methodology developed in this thesis is expandable to a large variety of industries which utilize semi-transparent web materials, such as the pharmaceutical, microelectronics, biomedical, chemical, and food industries.

Based on the data mining results, a neural network classification routine using 19 characteristic features was selected to determine the defect type. The inclusion of top- and bottom-hat features in the NN input vector was novel to defect classification. Also, NN classifiers have been extensively studied for use in textile and lumber industries, but

this work expands NN classification to polymer-based products, which, as a field, have had limited classification studies.

A bi-directional thickness profilometry technique was created based on the ANSI standard for diffuse transmission density measurements and a CCD sensor array. The densitometry tool is applicable to many industries since it records the localized variation in semi-transparent films quickly. Unfortunately, the instrument is limited by the range of densities which provide accurate thicknesses, but for materials with extinction coefficients near 1.1 D/mm, 200-400 μm measurements can be consistently recorded with errors less than 20 μm . Employing a camera with a better SNR, e.g., one with active cooling, would further improve the thickness accuracy.

A graphical user interface was created, which utilized *a priori* information about the casting window to inform the user of proper casting parameter adjustments. By counting the types of defects in the membrane solution, the system determines the casting window location and informs the user to change casting properties, if necessary. Evaluating the manufactured product with monitoring equipment is highly common, and the automotive and food industries often use machine vision to ascertain manufacturing quality. However, these tools are commonly used to measure a single variable, such as the length of a weld, number of rivets, bar code, hose twist, or some other geometric or topological feature, which identifies a problem. What separates the RFIS is that once these variables are quantified, advisable solutions are surmised via casting causality relationships. If a hose is twisted, a rivet missing, or a weld is poor, there are a variety of reasons these errors could have occurred. Whereas, with the casting system (assuming uniform material properties and heating), there are only two parameters—tank pressure and web speed—which play a dominate role in the casting, so prognostic recommendations can be directly provided to the operator.

7.3 Future Work

A prototype system has been created to manufacture and inspect slot die cast materials. Many of the hardware and software solutions should be refined to provide better accuracy, repeatability, and speed. Additionally, due to variations in solution

chemistry, many inspection system features must be reconsidered to accommodate variations in rheology and optical characteristics.

7.3.1 Casting System Modifications

In terms of the casting system, many of the control programs, preparation procedures, and hardware fixtures should be improved with higher quality components or instruments. The web tension controller does not strictly maintain the setpoint due to roller irregularities, frictional changes from the cast material, and load cell error. With better rollers there will be more uniform loading on the load cells and the tension will be more stable. When preparing a casting, a number of components lead to imprecise castings. The slot die stand off height is set using a feeler gauge and coarse worm gears. To create a gap with less than 10 μm error, sensors (e.g., linear encoders) should be installed. Additionally, the plastic bushings which hold the tank and die system should be replaced with high quality guide blocks and rails to reduce slop in the die location.

7.3.2 Inspection Hardware

There are a number of hardware modifications which would improve defect identification and classification, as well as densitometric accuracy. First, the spatial resolution could be greatly improved with a line scan camera. This would provide better image quality of defect regions and classification would likely be improved, albeit at the cost of processing time.

Densitometric accuracy could be improved via hardware modifications. First, a liquid or air cooled industrial camera would reduce the number of dark current electrons and boost the SNR. Additionally, using a longer lens would reduce vignetting effects and allow for more pixels to operate in the high SNR grayscale region. However, this would reduce the amount of light incident on the sensor, so integration times would need to be larger, which would increase the dark current and image blur at large web speeds. Thus, there is a difficult optimization problem involving these parameters to produce the greatest thickness accuracy. This problem should be studied in more detail in the future.

There are a range of avenues for expanding the transmission densitometry technology to additional materials and opportunities for optimizing the system for

specific materials. As discussed in Section 6.3, the influx wavelength could be tailored to the material and sensor to minimize the thickness errors with optical filters or a monochromatic LED backlight. Also, materials which are visibly opaque may be semi-transparent at other wavelengths, so by installing alternative backlight and/or sensor array technologies these materials could be measured.

7.3.3 Image Processing Refinement

Accurate defect detection requires robust image processing algorithms. The algorithms implemented in the inspection system removed vignetting and thickness changes using the top- and bottom-hat operations, however defect identification was highly sensitive to the top- and bottom-hat thresholds. In the future, either a more robust algorithm for separating defects from the background should be identified, or a better method of selecting the thresholds implemented. To begin, methodologies based on the algorithm developed for removing batch bubble effects in Section 5.1.1 should be investigated based on its earlier success.

The feedforward neural network also was susceptible to errors from poorly selected image processing parameters because the input vector changed based on the blob regions. Thus, in the future, cross-validation should be performed when training the network. The largest problem encountered with the classification routine was that changes in batch chemistry changed the types of defects seen in the membrane, and as a result, the network had no training data for them. So, either multiple neural networks should be trained for each of the batch chemistries or a more encompassing selection of training data should be used to create a chemically robust network.

The speed and accuracy of the network is tied closely with the neural network structure, so a more thorough study of network structure (e.g, number of layers, numbers of input and hidden neurons, etc.) as well as other neural network classification tools should be conducted. If more accuracy is desired, increasing the hidden layer nodes would provide a slightly more accurate network; or if computational speed is required, decreasing the inputs or hidden layer nodes would reduce the operating time with a slight decrease in performance. The speed of the identification and classification system is poor

so optimizing the code for mathematical operations, data management, and memory usage would improve the image processing rate.

7.3.4 GUI modifications

The graphical user interface could be improved in a number of ways. The most useful addition would be a visualization tool for selecting top- and bottom-hat thresholds. Since this part of the processing is challenging, time consuming, and must be accurate, a simple feature to dynamically visualize the blobs would reduce time and effort locating the optimal gray level. Adding a similar feature for convolution structural element sizes would indicate if the top- and bottom-hat transformations were isolating candidate blob regions well. Also, reinvestigating the heuristic method for determining the casting window location would provide better results for changes in chemistry.

7.3.5 Full Automation

The next step for the roll-feed imaging system will be to remove the human intermediary from the processing control system. As opposed to informing an operator of the desired tank pressure and web speed adjustments, a control system in the GUI will autonomously change the processing parameters, shown in Figure 4.15. Consultation with *a priori* casting window information could indicate directionality, and the number of defects could act as the controller error magnitude, such that larger defects quantities would create larger adjustments. A properly controlled system would reduce production costs by simplifying the manufacturer tasks, the system operator would require less training, and less batch material would be wasted because the control system would be more accurate and faster than the human operator.

APPENDIX A: LABVIEW CONTROL PROGRAM

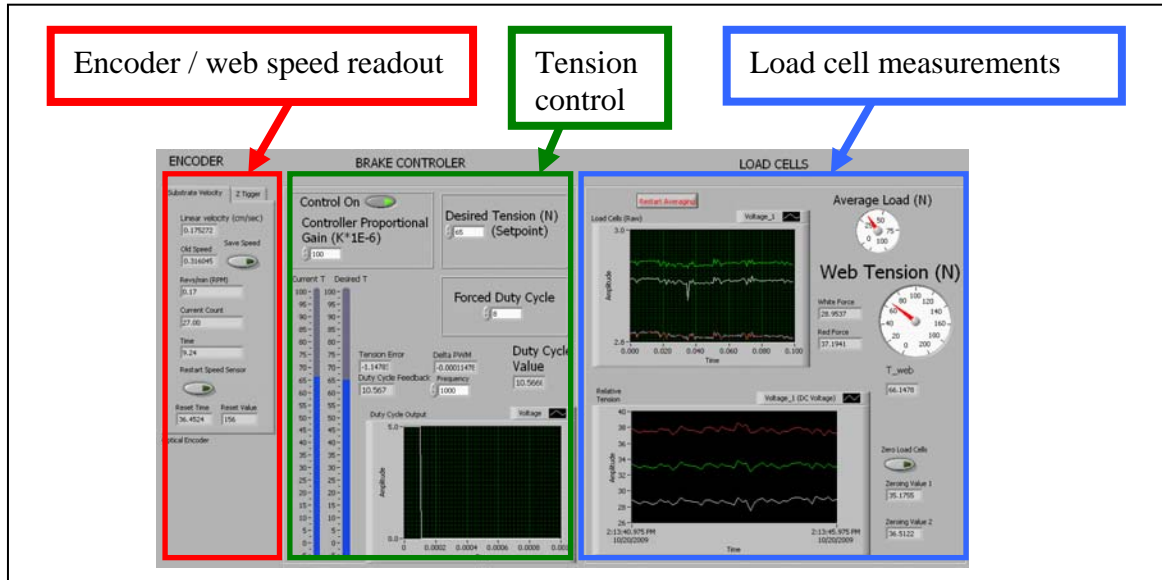


Figure A-1: The LabVIEW front panel.

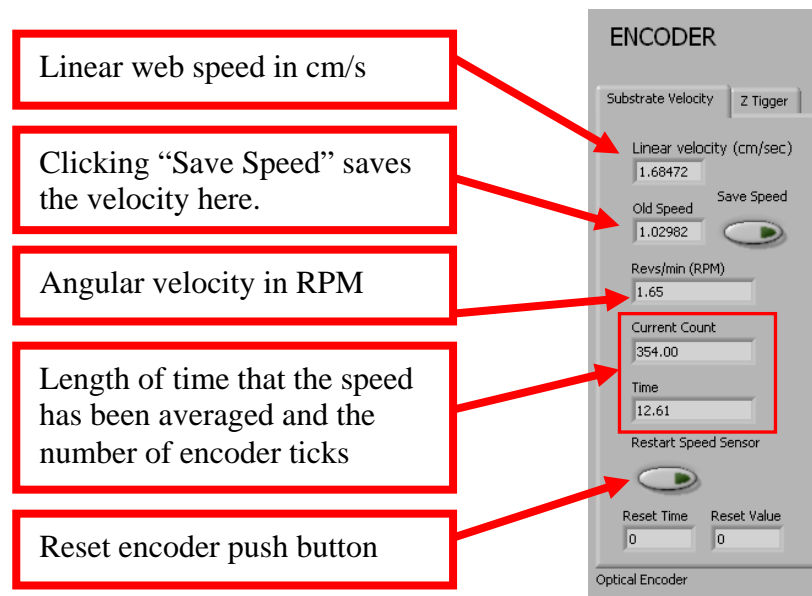


Figure A-2: Encoder front panel.

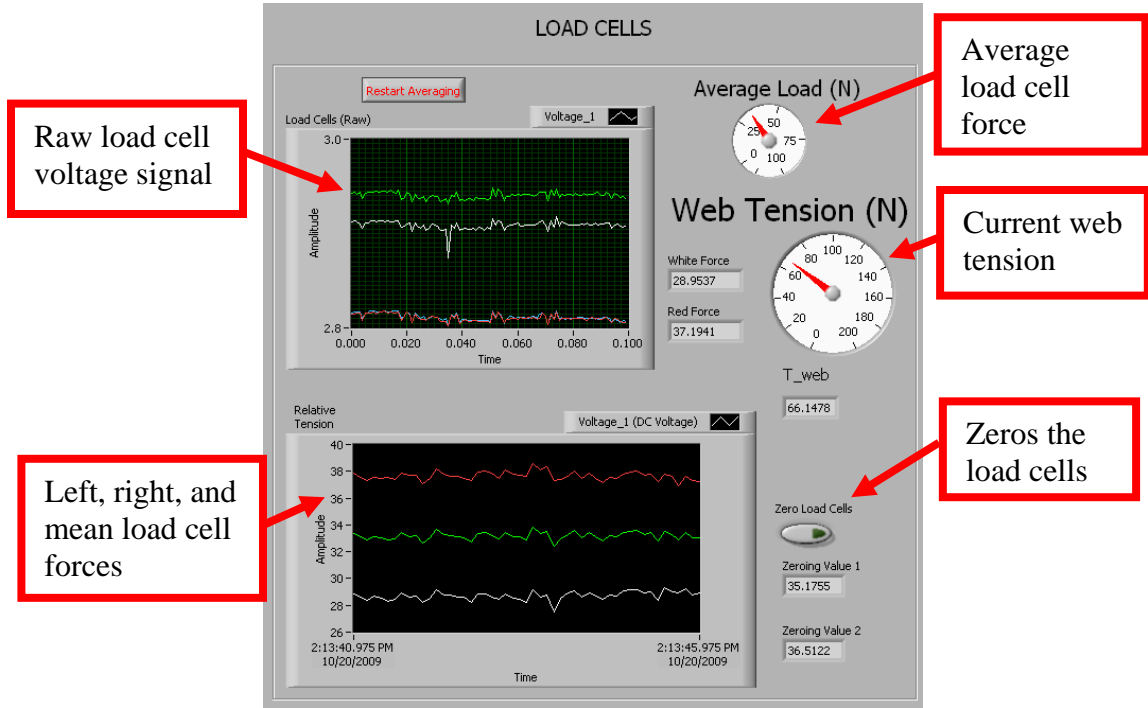


Figure A-3: Load cell front panel.

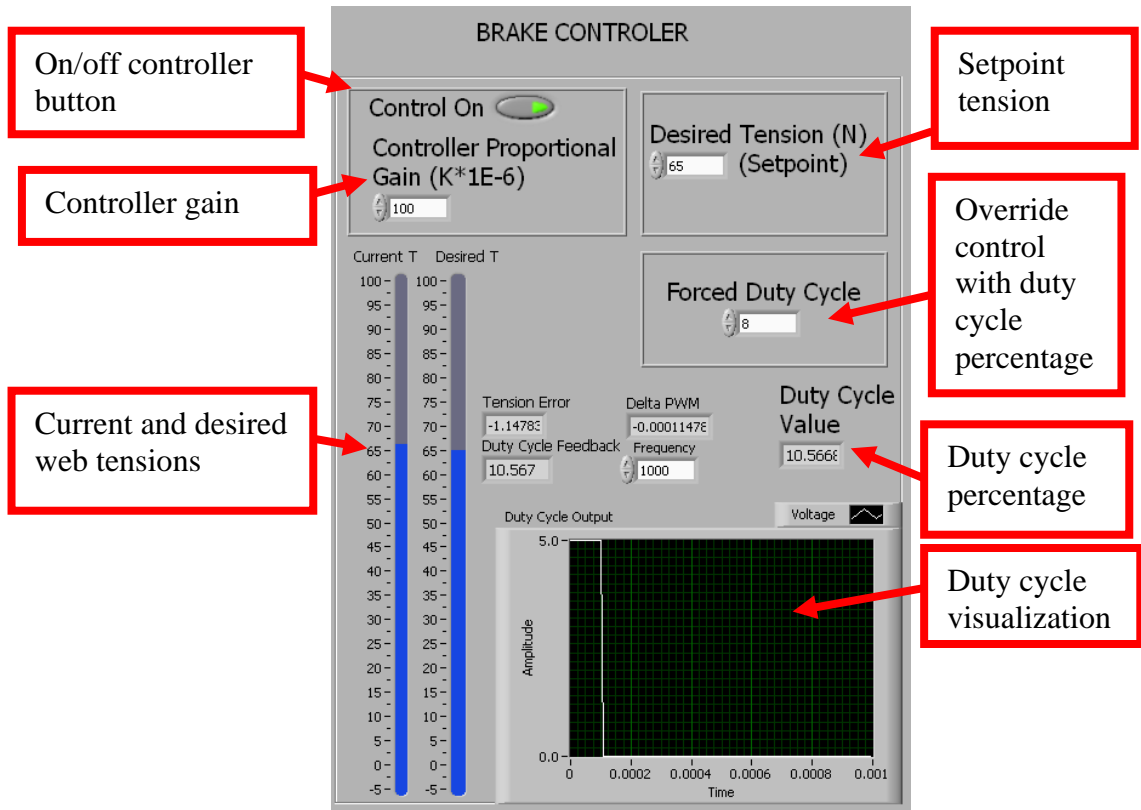


Figure A-4: Controller front panel.

APPENDIX B: WEB TENSION RESPONSES FOR DIFFERENT PROPORTIONAL CONTROLERS

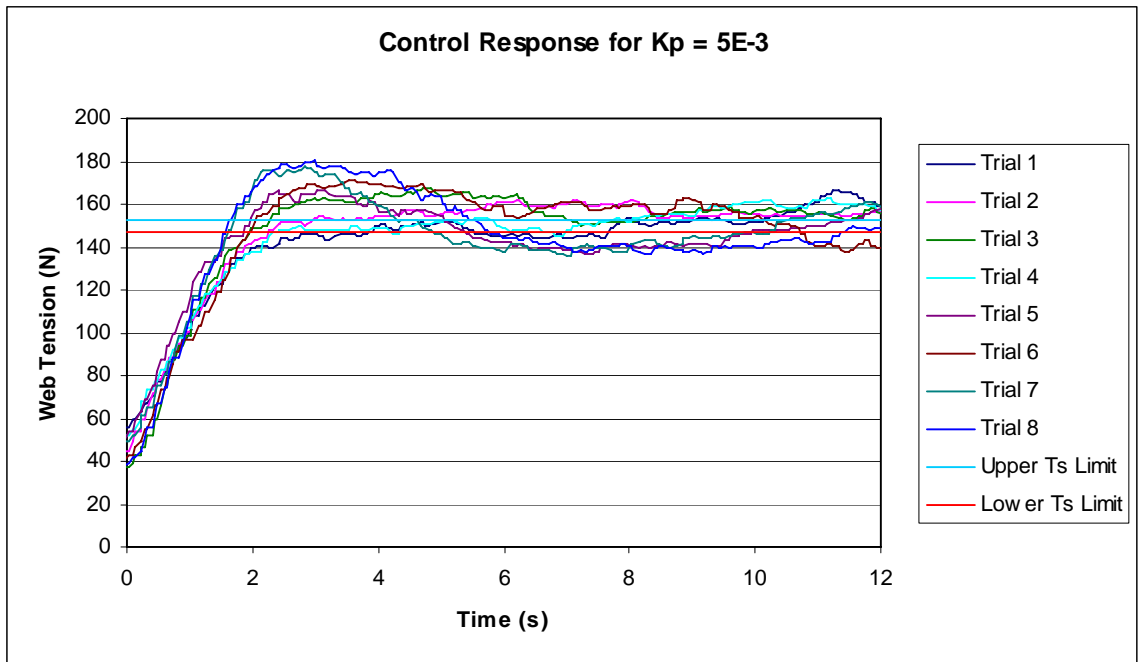


Figure B-1: Web tension vs time for a 0-150 N step in setpoint tension with $K_p = 5 \times 10^{-3}$.

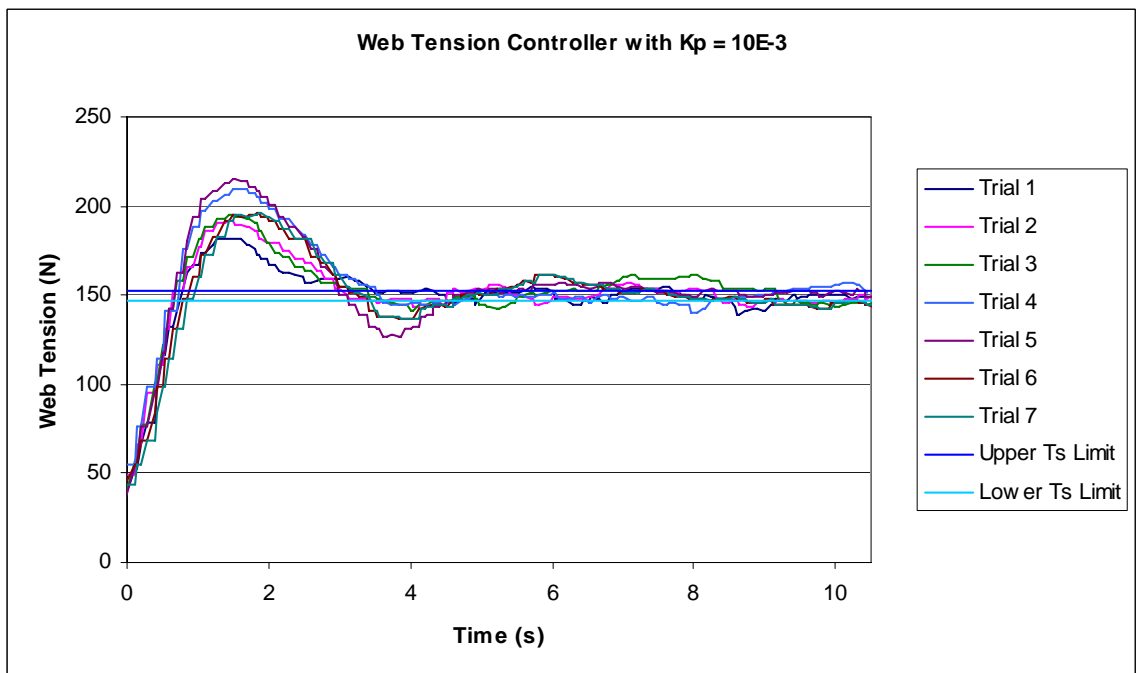


Figure B-2: Web tension vs time for a 0-150 N step in setpoint tension with $K_p = 10 \times 10^{-3}$. (The time datum in these tests was shifted to when the load cells first recorded a change in tension.)

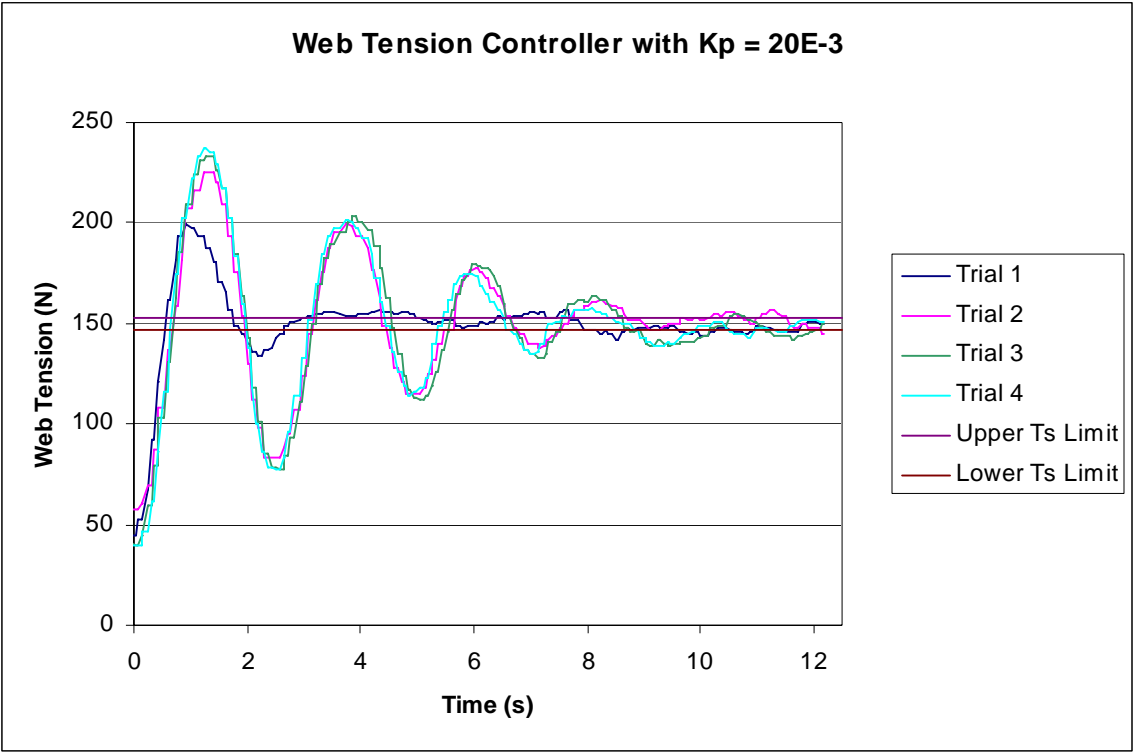


Figure B-3: Web tension vs time for a 0-150 N step in setpoint tension with $K_p = 20 \times 10^{-3}$.

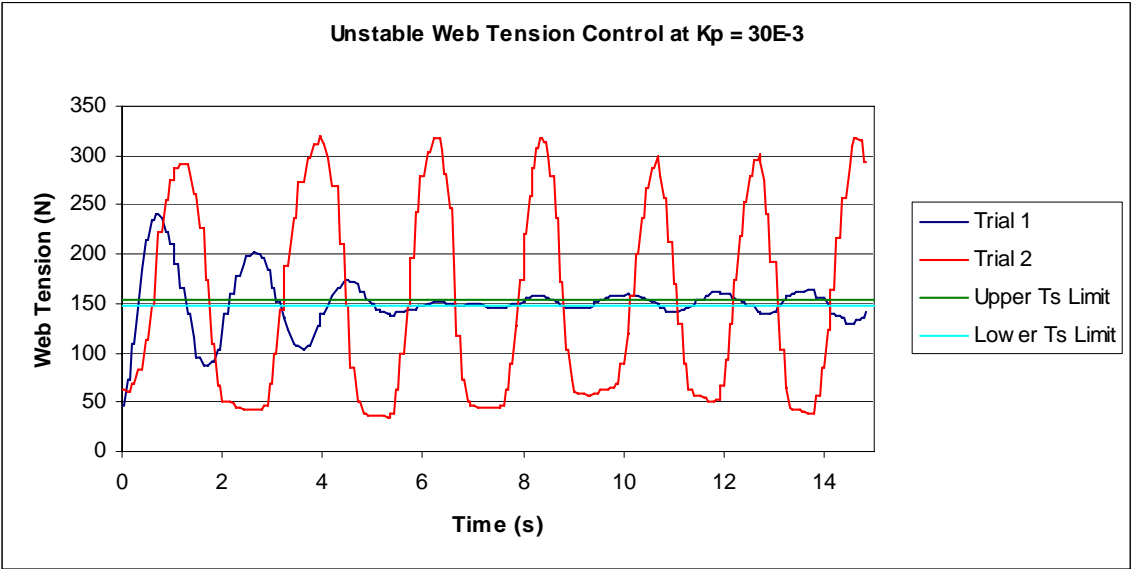


Figure B-4: Web tension vs time for a 0-150 N step in setpoint tension with $K_p = 30 \times 10^{-3}$.

APPENDIX C: CAMERA CHARACTERIZATION DATA FOR THE PHOTON TRANSFER METHOD

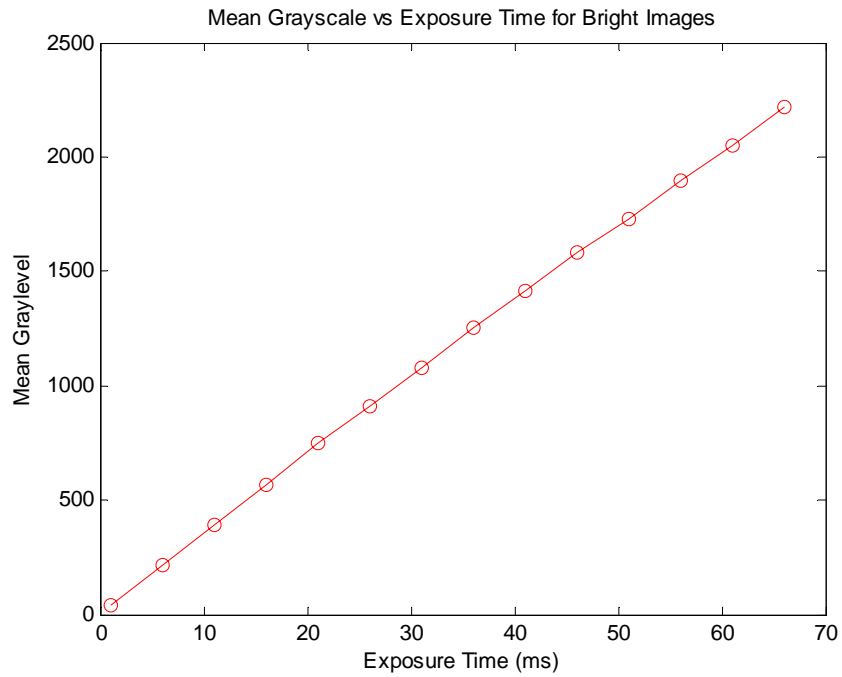


Figure C-1: The mean 12 bit grayscale for different integration times.

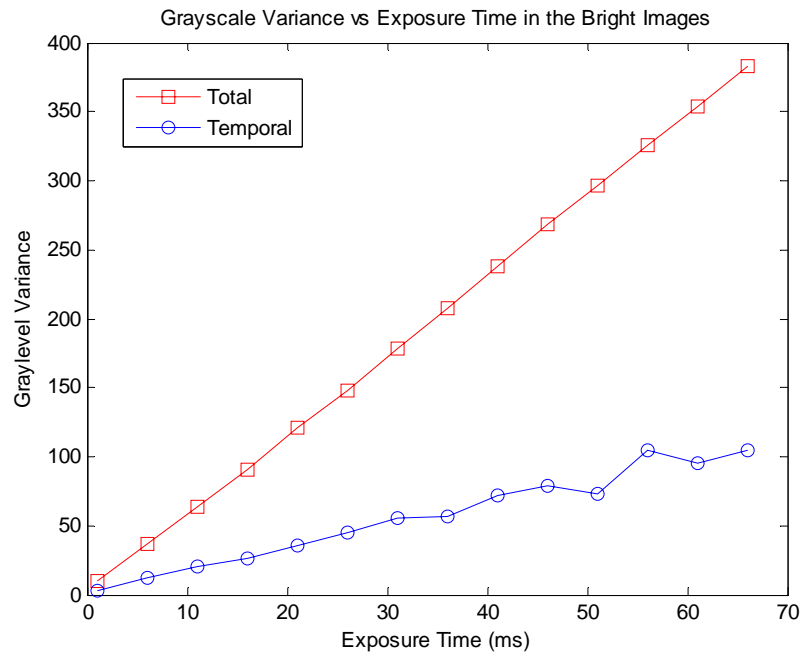


Figure C-2: Total and temporal pixel variance for different integration times.

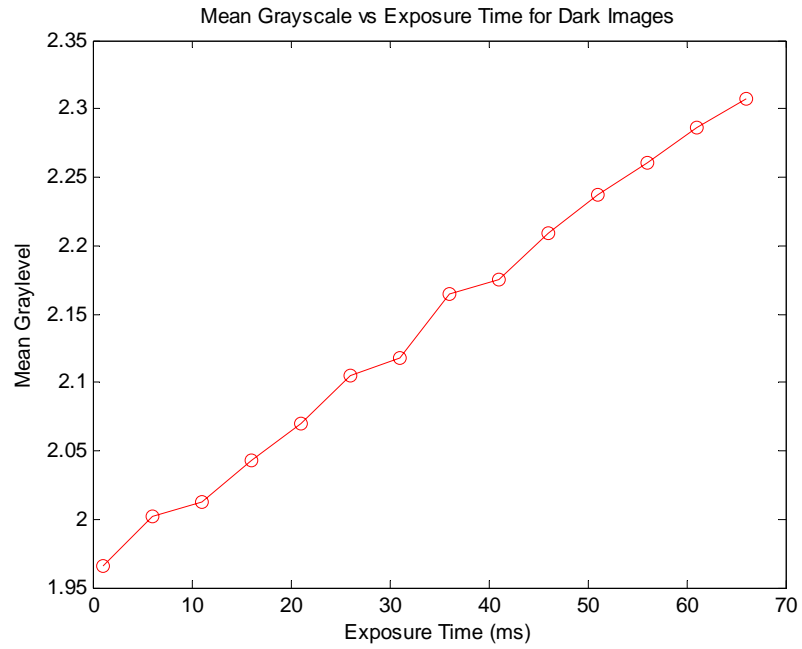


Figure C-3: Mean grayscale for dark images for different integration times.

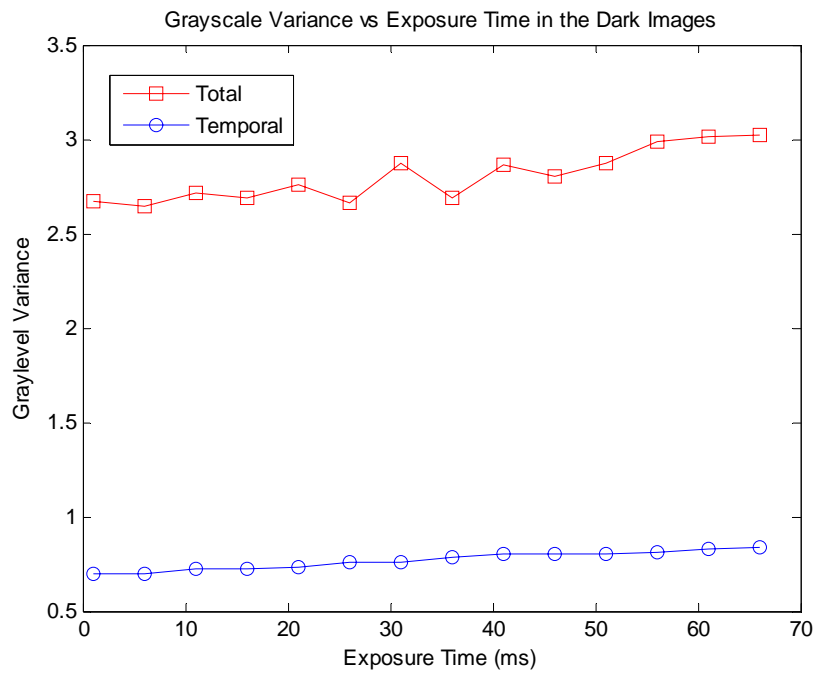


Figure C-4: Total and temporal variance for dark images for different integration times.

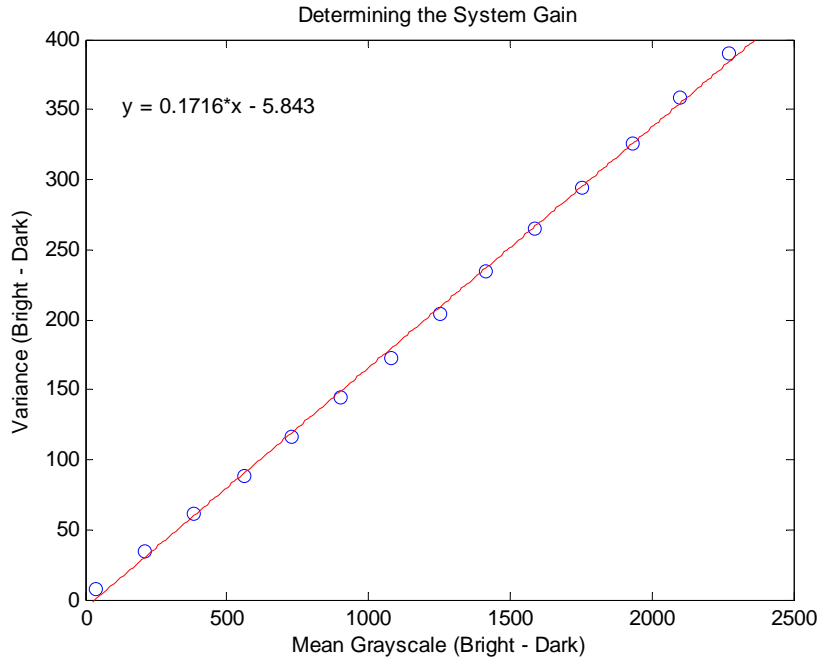


Figure C-5: Finding the system gain using the photon transfer method.

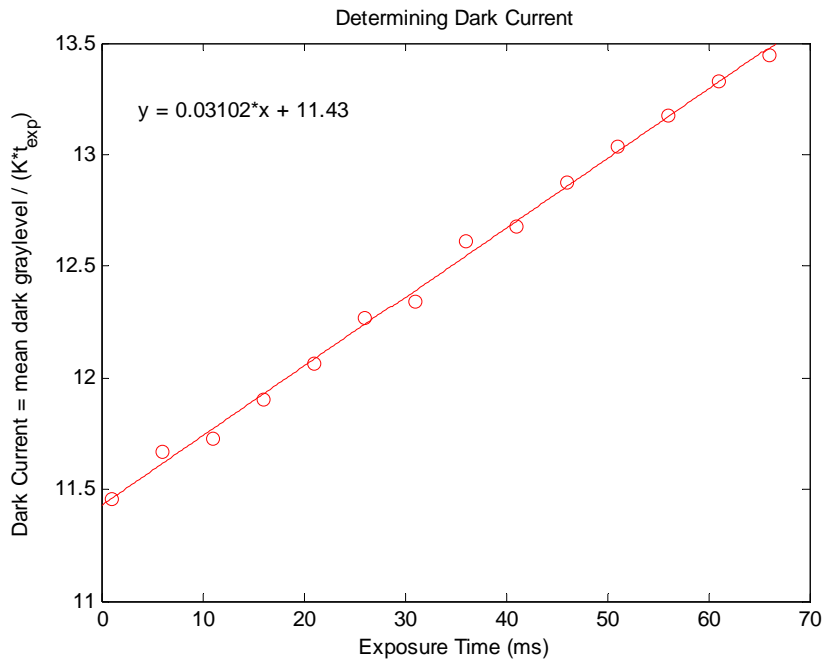


Figure C-6: Effect of integration time on dark current. Note that the dark current at zero integration time is from (in part) the capacitor not being fully cleared of charge during reset.

APPENDIX D: DENSITOMETRY RESULTS FOR REGIONS OF DIFFERENT INFLUX

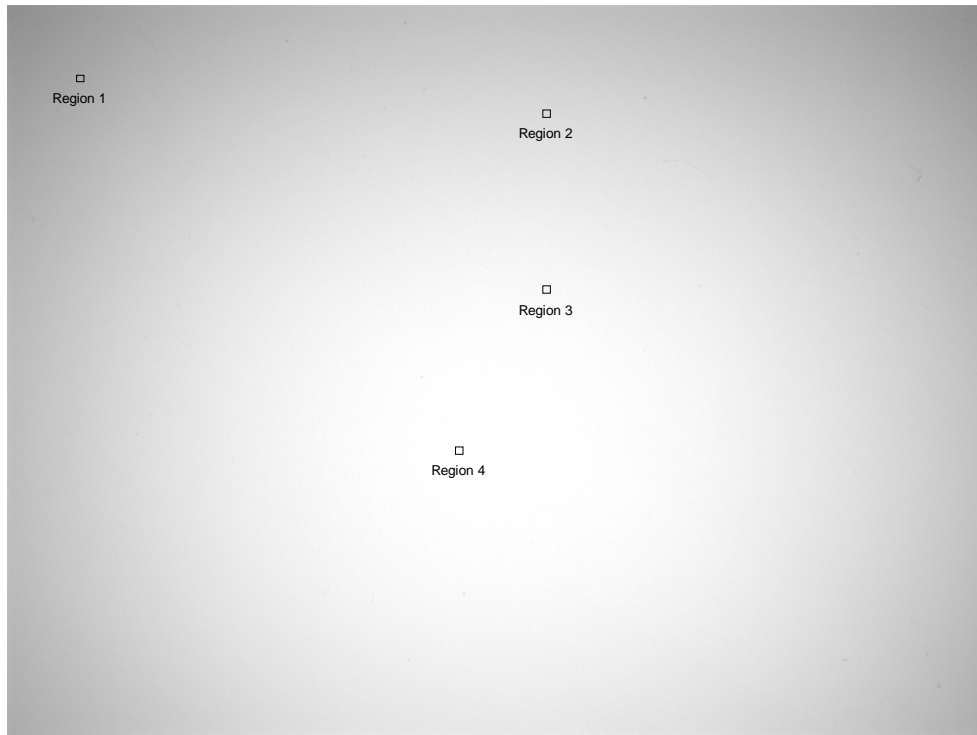


Figure D-1: Regions studied in the initial densitometry calibration. Images of these regions with 0.00, 0.06, 0.26, and 1.46 densities produced the following data.

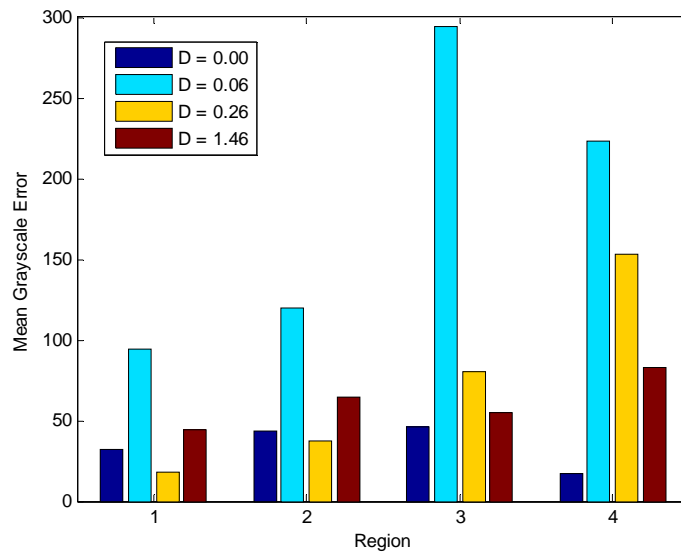
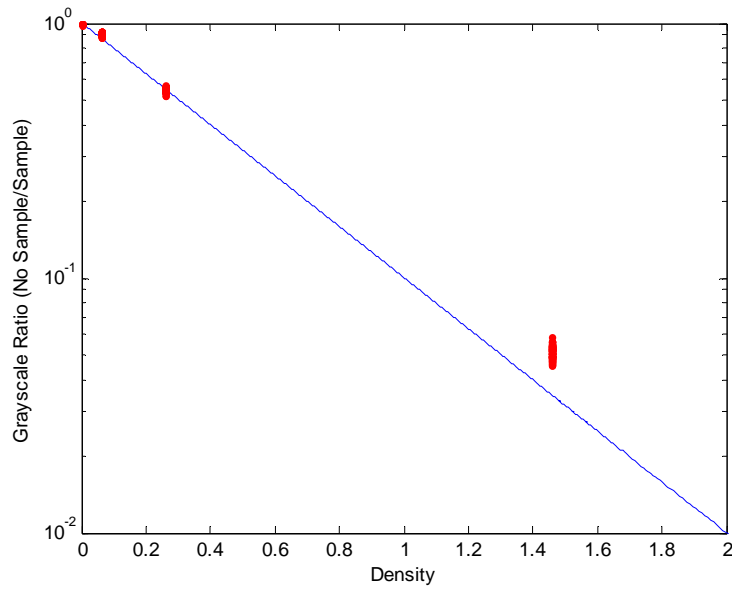
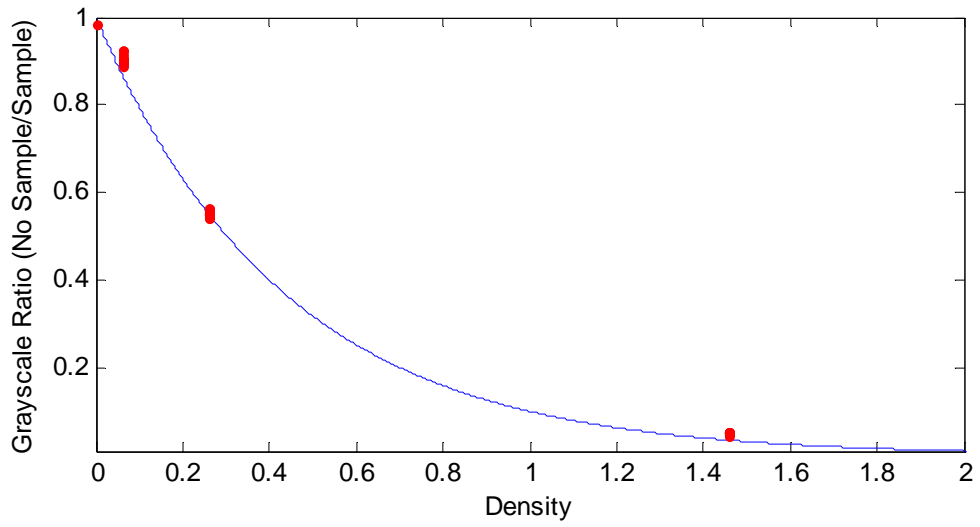
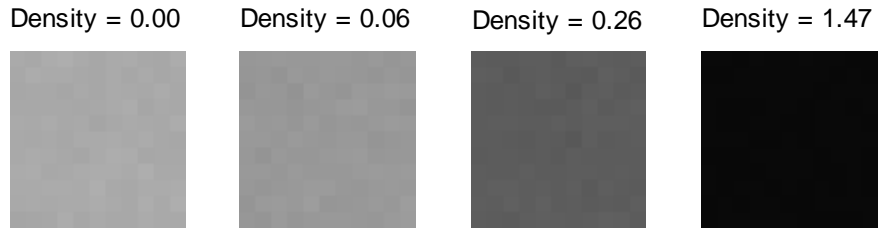
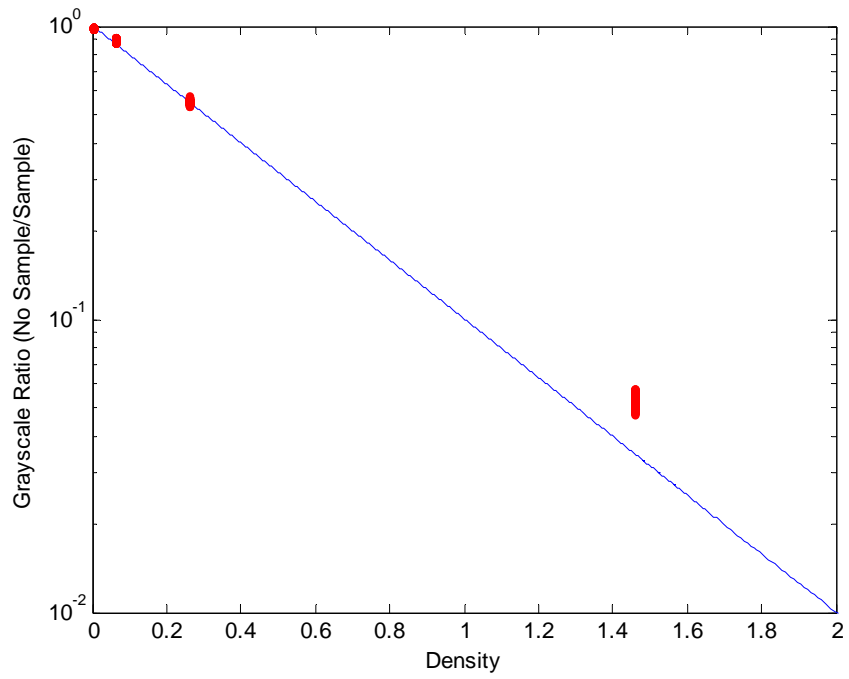
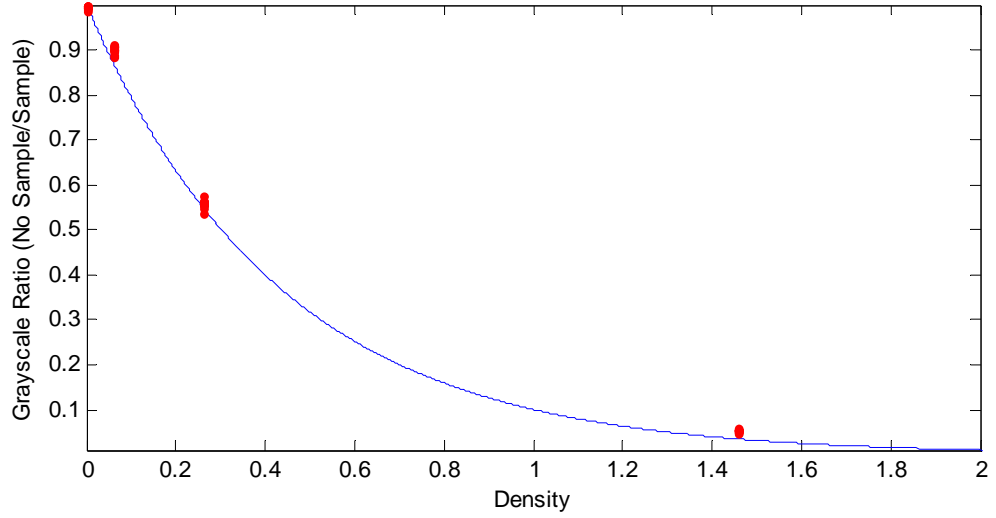
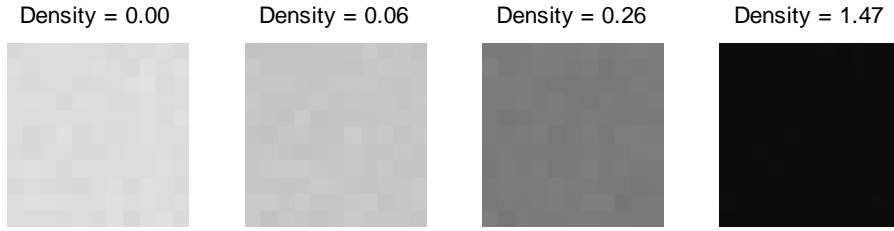


Figure D-2: The error in the grayscale for each region for densities of 0.00, 0.06, 0.26, and 1.46 D.

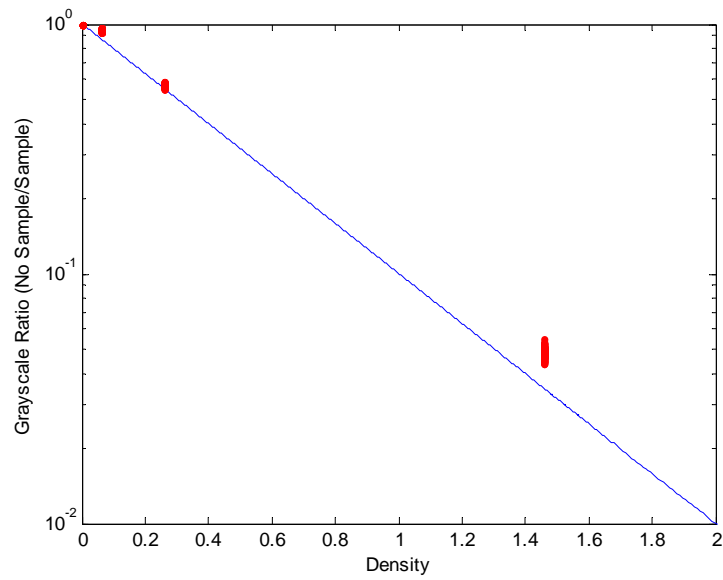
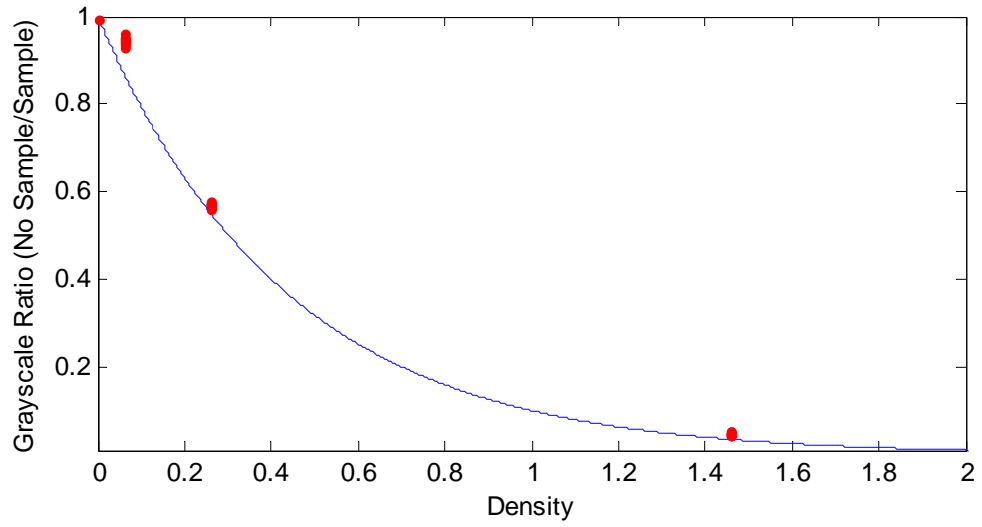
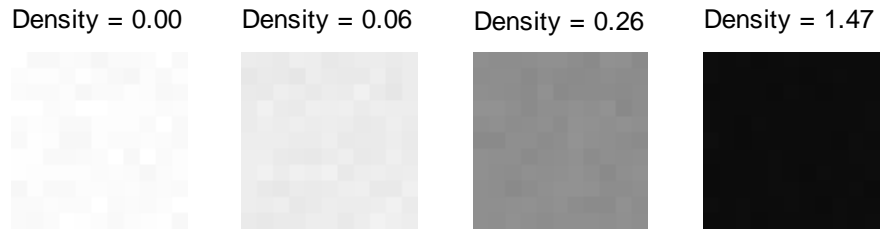
Region 1: $\mu_{\text{ref_grayscale}} = 2687$



Region 2: $\mu_{\text{ref_grayscale}} = 3503$



Region 3: $\mu_{\text{ref_grayscale}} = 3992$

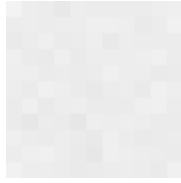


Region 4: $\mu_{\text{ref_grayscale}} = 4087$

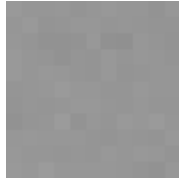
Density = 0.00



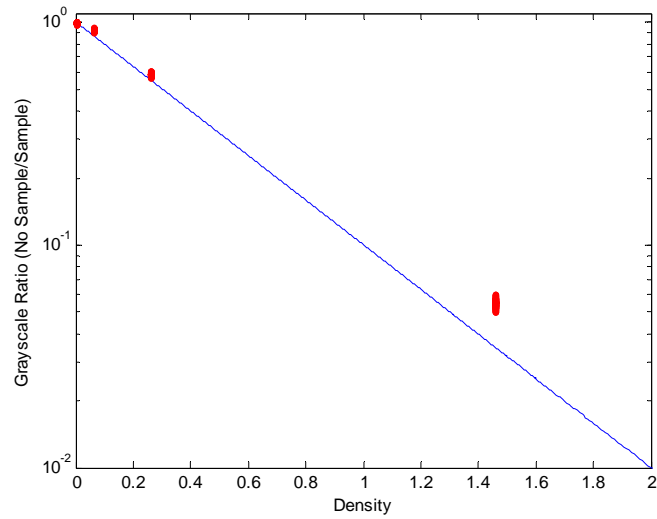
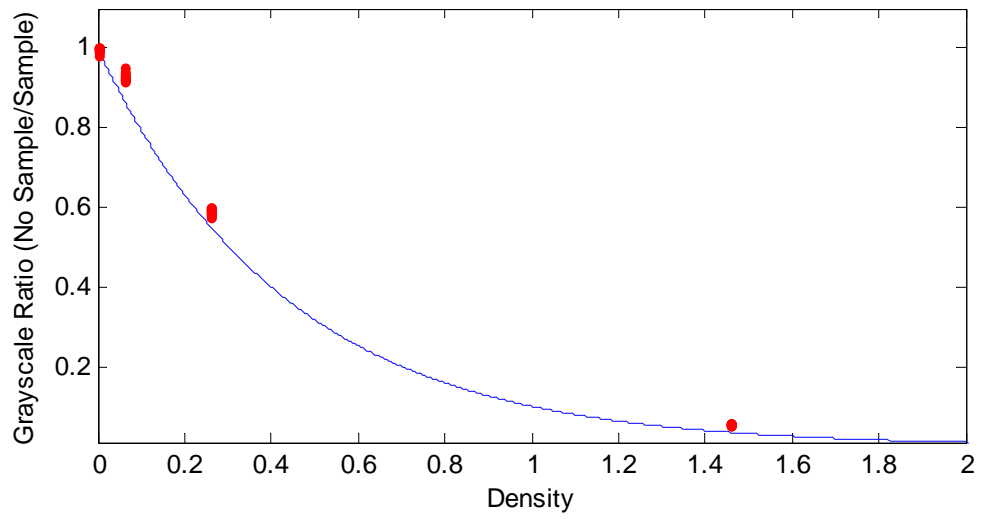
Density = 0.06






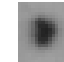
Density = 0.26



Density = 1.47



APPENDIX E: PARAMETERS FOR THE NEURAL NETWORK

	Parameter	In final feature set	Type	Hole	Bubble	Thinning	Gel
							
1	Width		Size	29.000	14.000	20.000	19.000
2	Height		Size	28.000	13.000	17.000	17.000
3	Gray - Mean Gray Value (μ)		Histogram	138.977	137.863	149.991	135.483
4	Gray - Median		Histogram	126.000	140.000	145.000	151.000
5	Gray - Mode		Histogram	121.000	143.000	140.000	156.000
6	Gray - Standard Deviation (σ)	x	Histogram	25.168	9.230	10.900	32.727
7	Gray - Skewness	x	Histogram	1.211	-1.093	0.907	-1.799
8	Gray - Peakedness (Kurtosis)		Histogram	3.108	3.802	2.582	5.073
9	Gray - Percentage of pixels less than μ	x	Histogram	66.133	35.165	61.471	26.316
10	Gray - Percentage of pixels less than $\mu - \psi$		Histogram	0.000	0.000	0.000	13.622
11	Gray - Percentage of pixels greater than $\mu + \psi$	x	Histogram	13.177	0.000	0.000	0.000
12	Gray - 3rd Darkest Pixel (used to account for 'noise' pixels)		Histogram	114.000	113.000	136.000	36.000
13	Gray - 3rd Lightest Pixel		Histogram	199.000	150.000	175.000	160.000
14	Gray - Threshold at $\mu - 1.5\sigma$, count white pixel percentage (light outliers)		Histogram	100.000	87.912	99.706	88.235
15	Gray - Threshold at $\mu + 1.5\sigma$, count white pixel percentage (dark outliers)	x	Histogram	13.916	0.549	11.765	0.000
16	Top-hat - Mean Gray Value (μ_{th})		Histogram	58.074	10.912	43.000	15.443
17	Top-hat - Median		Histogram	13.000	6.000	26.000	10.000
18	Top-hat - Mode		Histogram	6.000	0.000	13.000	0.000
19	Top-hat - Standard Deviation (σ)		Histogram	76.506	18.203	35.849	16.163
20	Top-hat - Skewness		Histogram	1.325	4.080	0.935	0.683
21	Top-hat - Peakedness (Kurtosis)		Histogram	3.330	25.128	2.615	2.162
22	Top-hat - Percentage of pixels less than μ_{th}		Histogram	69.704	64.835	62.647	57.276
23	Top-hat - Percentage of pixels less than $\mu_{th} - \psi$		Histogram	53.448	0.000	1.471	0.000
24	Top-hat - Percentage of pixels greater than $\mu_{th} + \psi$		Histogram	23.276	3.297	18.529	0.310
25	Top-hat - 3rd Darkest Pixel		Histogram	0.000	0.000	0.000	0.000
26	Top-hat - 3rd Lightest Pixel	x	Histogram	245.000	100.000	126.000	52.000
27	Bottom-hat - Mean Gray Value (μ_{bh})	x	Histogram	3.397	27.280	4.124	44.006

28	Bottom-hat - Median		Histogram	0.000	21.000	2.000	12.000
29	Bottom-hat – Mode	x	Histogram	0.000	15.000	0.000	4.000
30	Bottom-hat - Standard Deviation (σ)	x	Histogram	4.504	18.966	4.929	66.958
31	Bottom-hat - Skewness		Histogram	1.213	1.227	0.935	1.830
32	Bottom-hat - Peakedness (Kurtosis)	x	Histogram	4.003	4.075	2.807	5.158
33	Bottom-hat - Percentage of pixels less than μ_{bh}	x	Histogram	20.320	92.308	1.471	94.118
34	Bottom-hat - Percentage of pixels less than $\mu_{bh} - \psi$		Histogram	0.000	0.000	0.000	40.557
35	Bottom-hat - Percentage of pixels greater than $\mu_{bh} + \psi$		Histogram	35.837	2.198	37.353	0.000
36	Bottom-hat - 3rd Darkest Pixel		Histogram	0.000	2.000	0.000	0.000
37	Bottom-hat - 3rd Lightest Pixel		Histogram	19.000	81.000	17.000	247.000
38	Laplace Transform of Grayscale, largest value		Topography	10.000	46.000	13.000	54.000
39	Laplace Transform of Grayscale, Threshold at ξ , count white pixel %		Topography	0.862	9.890	3.235	9.288
40	Laplace Transform of Grayscale, Threshold at $\xi + \beta$, count white pixel %	x	Topography	0.000	6.593	0.294	8.050
41	Blob - Area of the region in pixels		Size	239.000	37.000	82.000	88.000
42	Blob - Large axis length		Size	17.804	8.848	11.457	11.292
43	Blob region properties - Eccentricity of an ellipse fit around the region	x	Geometry	0.265	0.615	0.574	0.453
44	Blob region properties - Extent (% of white pixels in bounding box)	x	Geometry	0.781	0.661	0.683	0.800
45	Blob region properties - Orientation		Geometry	-80.688	84.185	-81.003	89.122
46	Blob region properties - Centroid's x-value as % of width		Geometry	0.502	0.531	0.476	0.460
47	Blob region properties - Centroid's y-value as % of height		Geometry	0.522	0.498	0.501	0.502
48	Blob region properties - Euler number ($N_{blobs} - N_{holes}$)	x	Topology	1.000	0.000	1.000	1.000
49	Blob region properties - Solids within blob		Topology	0.968	0.841	0.932	0.967
50	Bounding box fully contained another box (1/0 flag)		Topology	0.000	1.000	0.000	0.000
51	Profile - Monotonically increasing		Topology	0.000	0.000	0.000	1.000
52	Profile - Monotonically decreasing	x	Topology	1.000	0.000	1.000	0.000
53	Profile - Increase more than 20 levels	x	Topology	0.000	1.000	0.000	1.000
54	Profile - Decrease more than 20 levels		Topology	1.000	1.000	1.000	0.000
55	Profile - Decrease more than 20 and then increase more than 20 levels		Topology	0.000	1.000	0.000	0.000
56	Profile - Increase more than 60 levels	x	Topology	0.000	0.000	0.000	1.000
57	Profile - Decrease more than 60 levels		Topology	1.000	0.000	0.000	0.000
58	Profile - Decrease more than 30 and then increase more than 30 levels		Topology	0.000	0.000	0.000	0.000
59	Center Pixel Grayscale	x	Topology	199.000	150.000	175.000	37.000

Note: $\psi = 40$, $\xi = 8$, $\beta = 4$

REFERENCES

1. Hua, L. and L. Jen Chung, *Using fuzzy logic to detect dimple defects of polished wafer surfaces*. Industry Applications, IEEE Transactions on, 1994. **30**(2): p. 317-323.
2. Dorundo, A.D., J.R. Mandeville, and F.Y. Wu. *Reference-based automatic visual inspection of electronic packaging using a parallel image processing system*. in *Machine Vision Applications in Industrial Inspection II*. 1994. San Jose, CA, USA: SPIE.
3. Larena, A., G. Pinto, and F. Millán, *Using the Lambert-Beer law for thickness evaluation of photoconductor coatings for recording holograms*. Applied Surface Science, 1995. **84**(4): p. 407-411.
4. Bowman, C.C., O.J. Olsson, G.T. Palmer, and D.W. Penman. *On-line high-resolution inspection of multilayered plastic bags*. in *Proc. SPIE, Machine Vision Applications, Architectures, and Systems Integration III*. 1994.
5. Gamage, P. and S. Xie, *A real-time vision system for defect inspection in cast extrusion manufacturing process*. The International Journal of Advanced Manufacturing Technology, 2008. **40**: p. 144-156.
6. Larena, A., F. Millán, M. Verdú, and G. Pinto, *Surface roughness characterisation of multilayer polymer films for graphic arts applications*. Applied Surface Science, 2001. **174**(3-4): p. 217-224.
7. Larena, A., F. Millán, G. Pérez, and G. Pinto, *Effect of surface roughness on the optical properties of multilayer polymer films*. Applied Surface Science, 2002. **187**(3-4): p. 339-346.
8. Ulbricht, M., *Advanced functional polymer membranes*. Polymer, 2006. **47**(7): p. 2217-2262.
9. Zuo, X., S. Yu, X. Xu, R. Bao, J. Xu, and W. Qu, *Preparation of organic-inorganic hybrid cation-exchange membranes via blending method and their electrochemical characterization*. Journal of Membrane Science, 2009. **328**(1-2): p. 23-30.
10. Brinker, C.J., *Sol-Gel Science*. 1990, New York, NY.: Academic Press.
11. Harris, T., *Design methodology, science, and technology to manufacture high temperature polymer electrolyte membranes for fuel cells*, in *Mechanical Engineering*. 2006, Rensselaer Polytechnic Institute: Troy, New York.

12. Malamas, E.N., E.G.M. Petrakis, M. Zervakis, L. Petit, and J. Legat, *A survey on industrial vision systems, applications and tools*. Image and Vision Computing, 2003. **21**: p. 171-188.
13. Soini, A. *Machine vision technology take-up in industrial applications*. in *Image and Signal Processing and Analysis, 2001. ISPA 2001. Proceedings of the 2nd International Symposium on*. 2001. Pula, Croatia.
14. Zuech, N., *Applying machine vision*. 1988, New York, NY: John Wiley & Sons.
15. Xu, W. and S.P. Floeder. *Industrial web inspection for manufacturing process understanding and control*. in *Machine Vision Applications in Industrial Inspection VII*. 1999. San Jose, CA: Proc. SPIE
16. Power, J.F., *Inverse problem theory in the optical depth profilometry of thin films*. Review of Scientific Instruments, 2002. **73**(12): p. 4057-4141.
17. Luke, I.F., *Evaluation of an ion exchange membrane fuel cell for space power*, Air Force Aero Propulsion Lab. 1974: Wright-Patterson AFB, OH.
18. Hopkinson, G.R., T.M. Goodman, and S.R. Prince, *A guide to the use and calibration of detector array equipment* 2004, Bellingham, WA: Sira Technology Ltd. and NPL.
19. Smith, R.D., *Roll and web defect terminology*. 1995, Atlanta, GA: Tappi Press.
20. To, H., D. Shin, and S. Ko, *On-Line Measurement of Wrinkle Using Machine Vision*, in *Computational Science and Its Applications – ICCSA 2007*. 2007. p. 931-940.
21. Kona, S.R., J.W. Foster, and J.V. Varughese, *A robust algorithm for detecting pinholes in transparent plastic films* Pattern Recognition, 1993. **26**(8): p. 1215-1227
22. Heavens, O.S., *Optical properties of thin films*. Reports on Progress in Physics, 1960. **23**(1): p. 1-65.
23. Larena, A. and S.J.d. Ochoa, *Use of different surface analysis techniques for the study of the photo-degradation of a polymeric matrix composite*. Applied Surface Science, 2004. **238**(1-4): p. 530-537.
24. Weber, K., *Apparatus for optically scanning a web of material*, U.S. Patent 4,866,288, 1989.
25. Weber, K., *Optical web monitoring apparatus*, U.S. Patent 4,775,238, 1986.
26. Matzan, E., *Dual laser web defect scanner*, U.S. Patent 6,934,029, 2005.

27. Polzleitner, W. and G. Schwingshakl, *Real-time surface grading of profiled wooden boards*. *Industrial Metrology*, 1992. **2**(3-4): p. 283-298.
28. Alcock, R., *Techniques for automated visual inspection of birch wood boards*, in *School of Engineering*. 1996, University of Wales, Cardiff: Cardiff.
29. Drake, P.R. and M.S. Packianather, *A decision tree of neural networks for classifying images of wood veneer*. *The International Journal of Advanced Manufacturing Technology*, 1998. **14**(4): p. 280-285.
30. Pham, D. and R. Alcock, *Plywood image segmentation using hardware-based image processing functions*. *Proceedings of the Institution of Mechanical Engineers, Part B: Journal of Engineering Manufacture*, 1999. **213**(4): p. 431-434.
31. Pham, D.T. and R.J. Alcock, *Automatic detection of defects on birch wood boards*. *Proceedings of the Institution of Mechanical Engineers. Pt.E. Journal of Process Mechanical Engineering*, 1996. **210**(1): p. 45-52.
32. Pham, D.T. and R.J. Alcock. *Automated visual inspection of birch wood boards*. in *Artificial Intelligence in Manufacturing (Digest No: 1997/060)*, *IEE Colloquium on*. 1997.
33. Packianather, M.S. and P.R. Drake, *Neural Networks for Classifying Images of Wood Veneer. Part 2*. *The International Journal of Advanced Manufacturing Technology*, 2000. **16**(6): p. 424-433.
34. Pham, D. and R. Alcock, *Artificial intelligence based techniques for processing segmented images of wood boards*. *Proceedings of the Institution of Mechanical Engineers, Part E: Journal of Process Mechanical Engineering*, 1998. **212**(2): p. 119-129.
35. Pham, D.T., A.J. Soroka, A. Ghanbarzadeh, E. Koc, S. Otri, and M. Packianather. *Optimising Neural Networks for Identification of Wood Defects Using the Bees Algorithm*. in *Industrial Informatics, 2006 IEEE International Conference on*. 2006.
36. Mitropulos, P., C. Koulamas, R. Stojanovic, S. Koubias, G. Papadopoulos, and G. Karayanis, *Real-time vision system for defect detection and neural classification of web textile fabric*. *Proc. SPIE Machine Vision Applications in Industrial Inspection VII*, 1999. **3652**: p. 59-69.
37. Dar, I.M., W. Mahmood, and G. Vachtsevanos. *Automated pilling detection and fuzzy classification of textile fabrics*. in *Machine Vision Applications in Industrial Inspection V*. 1997. San Jose, CA, USA: SPIE.
38. Ngan, H. and G. Pang, *Novel method for patterned fabric inspection using bollinger bands*. *Optical Engineering*, 2006. **45**(8): p. 1-15.

39. Escofet, J., R. Navarro, M.S. Millan, and J. Pladellorens, *Detection of local defects in textile webs using Gabor filters*. *Optical Engineering*, 1998. **37**(8): p. 2297-2307.
40. Parker, J.R., *Web monitoring for paper machines*, U.S. Patent 5,745,365, 1998.
41. Vanessa Pratt, J.W., *Defect inspection in transparent materials*. *Sensor Review*, 2000. **20**(4): p. 294-298.
42. Brasunas, J.C., G.M. Cushman, and B. Lakew, *Thickness Measurement*, in *The Measurement, Instrumentation and Sensors Handbook*, J.G. Webster, Editor. 1999, CRC Press: New York, NY. p. 1500.
43. Flournoy, P.A., R.W. McClure, and G. Wyntjes, *White-Light Interferometric Thickness Gauge*. *Appl. Opt.*, 1972. **11**(9): p. 1907-1915.
44. Alius, H. and R. Schmidt, *Interference method for monitoring the refractive index and the thickness of transparent films during deposition*. *Review of Scientific Instruments*, 1990. **61**(4): p. 1200-1203.
45. Tolansky, S., *Multiple beam interferometry of surface and films*. 1948, Clarendon Press: Oxford. p. pp. 147–50.
46. Shukla, R.P., D.V. Udupa, N.C. Das, and M.V. Mantravadi, *Non-destructive thickness measurement of dichromated gelatin films deposited on glass plates*. *Optics & Laser Technology*, 2006. **38**(7): p. 552-557.
47. Cox, G. and C.J.R. Sheppard, *Measurement of thin coatings in the confocal microscope*. *Micron*, 2001. **32**(7): p. 701-705.
48. Garini, Y., B.J. Vermolen, and I.T. Young, *From micro to nano: recent advances in high-resolution microscopy*. *Current Opinion in Biotechnology*, 2005. **16**(1): p. 3-12.
49. Jones, B.T. and J.D. Winefordner, *Molecular fluorescence in thin liquid films*. *Analytical Chemistry*, 2002. **58**(13): p. 2870-2872.
50. Power, J.F. and S.-w. Fu, *Apparatus and method for light profile microscopy*, U.S. Patent 6,614,532, 2003.
51. Doran, S.J. and N. Krstajic, *The history and principles of optical computed tomography for scanning 3-D radiation dosimeters*. *Journal of Physics: Conference Series*, 2006: p. 45.
52. West, G.A., J.J. Barrett, D.R. Siebert, and K.V. Reddy, *Photoacoustic spectroscopy*. *Review of Scientific Instruments*, 1983. **54**(7): p. 797-817.

53. Françon, M., *Polarization Interference Microscopes*. Appl. Opt., 1964. **3**(9): p. 1033-1036.
54. Kreis, T., *Handbook of holographic interferometry: optical and digital methods*. 2005: Wiley, John & Sons, Inc.
55. Cuche, D.E. *Large deformation analysis by holographic interferometry*. in *Holographic Systems, Components and Applications, 1989., Second International Conference on*. 1989.
56. Deck, L. and P. de Groot, *High-speed non-contact profiler based on scanning white light interferometry*. International Journal of Machine Tools and Manufacture, 1995. **35**(2): p. 147-150.
57. Soini, A., *New sensors for new machine vision applications*. Sensor Review, 2000. **20**(4): p. 287.
58. Blodgett, K.B. and I. Langmuir, *Built-Up Films of Barium Stearate and Their Optical Properties*. Physical Review, 1937. **51**(11): p. 964.
59. Shelley, P.H., K.S. Booksh, L.W. Burgess, and B.R. Kowalski, *Polymer Film Thickness Determination with a High-Precision Scanning Reflectometer*. Appl. Spectrosc., 1996. **50**(1): p. 119-125.
60. Warnecke, A.J. and P.J. LoPresti, *Refractive Index Dispersion in Semiconductor-related Thin Films*. IBM Journal of Research and Development, 1973. **17**(3): p. 256.
61. Pliskin, W.A., *Nondestructive optical techniques for thin-film thickness measurement*, in *Physical measurement and analysis of thin films*, E.M. Murt and W.G. Gulder, Editors. 1969, Plenum: New York.
62. Goodman, A.M., *Optical interference method for the approximate determination of refractive index and thickness of a transparent layer*. Appl. Opt., 1978. **17**(17): p. 2779-2787.
63. Wei, T. and I.C. Ume, *Warpage Measurement of Board Assemblies Using Projection Moiré*. Advanced Packaging, IEEE Transactions on, 2008. **31**(3): p. 447-453.
64. Hai, D., R.E. Powell, C.R. Hanna, and I.C. Ume, *Warpage measurement comparison using shadow Moire and projection Moire methods*. Components and Packaging Technologies, IEEE Transactions on, 2002. **25**(4): p. 714-721.
65. Altman, J.H., *Densitometry*, in *The Measurement, Instrumentation and Sensors Handbook*, J.G. Webster, Editor. 1999, CRC Press in Cooperation with IEEE Press: Boca Raton, FL.

66. Altman, J.H., *Chap. 17*, in *The Theory of the Photographic Process, 4th ed.*, T.H. James, Editor. 1977, MacMillan: New York.
67. ANSI/NAPT, *Part 2: Geometric Conditions for Transmission Density*, in *Density Measurements*. 1994.
68. Tobias Associates, Inc. *Transmission Densitometers*. 2009, cited Aug 25, 2009, Available from: <http://www.densitometers.net/transmission.asp>.
69. X-Rite, Inc. *500 Series Family: Measure any Density Status Quickly and Reliably*. 2009, cited Aug 25, 2009, Available from: http://www.xrite.com/product_overview.aspx?ID=278.
70. X-Rite, Inc. *361T Transmission Densitometer*. 2009, cited Aug 25, 2009, Available from: http://www.xrite.com/documents/literature/en/L11-010_361T_en.pdf.
71. Teasdale, P.R., S. Hayward, and W. Davison, *In situ, High-Resolution Measurement of Dissolved Sulfide Using Diffusive Gradients in Thin Films with Computer-Imaging Densitometry*. *Analytical Chemistry*, 1999. **71**(11): p. 2186-2191.
72. Pekcan, Ö., et al., *Photon transmission method for studying void-closure kinetics during coalescence of hard latex particles*. *Journal of Applied Polymer Science*, 1999. **72**(8): p. 981-988.
73. Pekcan, Ö., F. Kemeroglu, and E. Arda, *Measuring backbone activation energy at polymer-polymer interfaces during latex film formation by using a photon transmission method*. *European Polymer Journal*, 1998. **34**(9): p. 1371-1378.
74. Pekcan, Ö. and F. Kemeroglu, *Photon transmission technique for studying film formation from polystyrene latexes prepared by dispersion polymerization using various steric stabilizers*. *Journal of Applied Polymer Science*, 1998. **68**(8): p. 1257-1267.
75. Pekcan, Ö. and E. Arda, *Effect of molecular weight on latex film formation: Photon transmission study*. *Journal of Applied Polymer Science*, 1998. **70**(2): p. 339-351.
76. Parker, M.L., S. Chow, P.R. Steiner, and L.A. Jozsa, *Application of x-ray densitometry to determine density profile in waferboard: relationship of density to thickness expansion and internal bond strength under various cycles*. *Wood science* 1978. **11**(1): p. 48-55.
77. ExxonMobile Chemical Corporation. *Optical Density*. 2001, cited Aug 25, 2009, Available from: http://www.opffilms.com/Public_Files/OPPFilms/Oriented_PP_Films/NorthAmerica/Test_Method_Optical_density.pdf.

78. Zhu, Y., A.S. Kirov, V. Mishra, A.S. Meigooni, and J.F. Williamson, *Quantitative evaluation of radiochromic film response for two-dimensional dosimetry*. Medical Physics, 1997. **24**(2): p. 223-231.
79. Rushton, W.A.H., *Densitometry of Pigments in Rods and Cones of Normal and Color Defective Subjects*. Invest. Ophthalmol. Vis. Sci., 1966. **5**(3): p. 233-241.
80. Molloi, S., T. Xu, J. Ducote, and C. Iribarren, *Quantification of breast arterial calcification using full field digital mammography*. Medical Physics, 2008. **35**(4): p. 1428-1439.
81. Tarlton, J.F. and P.J. Knight, *Comparison of Reflectance and Transmission Densitometry, Using Document and Laser Scanners, for Quantitation of Stained Western Blots*. Analytical Biochemistry, 1996. **237**(1): p. 123-128.
82. Agar, A.W., *The measurement of the thickness of thin carbon films*. British Journal of Applied Physics, 1957. **8**(1): p. 35-36.
83. Larena, A., F. Millán, and G. Pinto, *Iterative method for the optical characterization of biaxially oriented poly(ethyleneterephthalate) films*. Optical Materials, 2006. **28**(8-9): p. 1013-1019.
84. Kotwaliwale, N., P.R. Weckler, and G.H. Brusewitz, *X-ray Attenuation Coefficients using Polychromatic X-ray Imaging of Pecan Components*. Biosystems Engineering, 2006. **94**(2): p. 199-206.
85. Ashford, R.D., *Beta gauge mechanism*, U.S. Patent 4,324,136, 1982.
86. Syré, H.-R., *Apparatus for the evaluation of the material properties of moved web*, U.S. Patent 5,822,070, 1996.
87. Flook, W.M. and C.B. Moore, *Automatic control apparatus for maintaining transverse thickness uniformity of extruded material*, U.S. Patent 3,212,127, 1965.
88. Workman, J.J., *Method and apparatus for controlling the manufacturing quality of a moving web*, U.S. Patent 6,452,679, 2002.
89. Harris, T.A.L., and Walczyk, D. F., *Development of a Casting Technique for Membrane Material Used in High-Temperature Pem Fuel Cells*. Journal of Manufacturing Processes, 2006. **8**(1): p. 8-20.
90. LabVIEW. 2009, National Instruments: Austin, TX.
91. Roisum, D.R., *The Mechanics of Web Handling*. 1998: TAPPI Press.
92. Cleveland Motor Controls. *Electromagnetic Particle Brake*. 2009, cited 30 May, 2009, Available from: http://www.cmcccontrols.com/downloads/web_tension_control/dsEMAG9.pdf.

93. Harris, T.A.L., D. Walczyk, R. Puffer, and R. O'Donnell. *Design of an Experimental Test Bed for Depositing Membrane Material for High Temperature Fuel Cells*. in *Proceedings of the 2004 SME North American Manufacturing Research Conference*. 2004.
94. Romero, O.J. and M.S. Carvalho, *Response of slot coating flows to periodic disturbances* *Chemical Engineering Science*, 2008. **63**(8): p. 2161-2173.
95. Laitinen, J. and I. Moring, *Method for evaluation of imaging in automated visual web inspection*. *Optical Engineering*, 1997. **36**(8): p. 2184-2196.
96. Bolhouse, A., *The fundamentals of Machine Vision: Sensors and Image Capture*. 2009, Vision Systems Design.
97. EMVA, *Standard Compliant*, in *Standard for Characterization and Presentation for Specification Data for Image Sensors and Cameras*. 2005.
98. Schuermeyer, F., et al., *Photometry and Radiometry*, in *The Measurement, Instrumentation and Sensors Handbook*, J.G. Webster, Editor. 1999, CRC Press: New York, NY. p. 1500.
99. Dierks, F. *Sensitivity and image Quality of Digital Cameras*. 2004, cited Sept 16, 2009, Available from: http://www.baslerweb.com/downloads/9835/Image_Quality_of_Digital_Cameras.pdf.
100. Lumenera Corporation. *Lm135: 1.4 Megapixel Mini Industrial USB 2.0 Camera*. 2009, cited Sept 20, 2009, Available from: <http://www.lumenera.com/products/industrial-cameras/lm135.php>.
101. Aggarwal, M., H. Hua, and N. Ahuja. *On cosine-fourth and vignetting effects in real lenses*. in *Computer Vision, 2001. ICCV 2001. Proceedings. Eighth IEEE International Conference on*. 2001.
102. Horn, B.K.P., *Robot Vision*. 1986: The MIT Press.
103. Young, H.D. and R.A. Freedman. *University Physics 11th Ed. Extra Topics* *University Physics* 2009, cited Sept 19, 2009, Available from: www.aw-bc.com.
104. Yu, W., *Practical anti-vignetting methods for digital cameras*. *IEEE Transactions on Consumer Electronics*, 2004. **50** (4): p. 975 - 983.
105. Yu, W., Y. Chung, and J. Soh, *Vignetting distortion correction method for high quality digital imaging*, in *17th International Conference on Pattern Recognition*. 2004. p. 666 - 669.
106. J. C. Mullikin, et al., *Methods for CCD Camera Characterization*. *Proc. SPIE*, 1994. **2173**: p. 73-84.

107. Chu, W.-B., J.-W. Yang, Y.-C. Wang, T.-J. Liu, C. Tiu, and J. Guo, *The effect of inorganic particles on slot die coating of poly(vinyl alcohol) solutions*. Journal of Colloid and Interface Science, 2006. **297**(1): p. 215-225.
108. Appleby, A.J., *Issues in fuel cell commercialization*. Journal of Power Sources, 1996. **58**(2): p. 153-176.
109. Carlson, E.J., et al., *Cost Analysis of PEM Fuel Cell Systems for Transportation: September 30, 2005*. . 2005 TIAX LLC: Cambridge, Massachusetts.
110. Knaggs, B., T. Niimura, and F. Ordubadi. *PEM fuel cells for improved grid reliability and power transfer*. in *Power Engineering Society General Meeting, 2004. IEEE*. 2004. Denver, CO, .
111. *Wind-to-Hydrogen Project*. Hydrogen & Fuel Cells Research 2008 October 27, 2008, Available from: http://www.nrel.gov/hydrogen/proj_wind_hydrogen.html.
112. Davis, U. *Green Transportation Laboratory*. 2009, cited Oct 5, 2009, Available from: <http://mae.ucdavis.edu/jwpark/>.
113. DuPont. *DuPont™ Nafion® Membranes and Dispersions*. 2009, Available from: http://www2.dupont.com/Fuel_Cells/en_US/products/nafion.html.
114. Xiao, L., et al., *Synthesis and Characterization of Pyridine-Based Polybenzimidazoles for High Temperature Polymer Electrolyte Membrane Fuel Cell Applications*. Fuel Cells, 2005. **5**(2): p. 287-295.
115. Mecerreyes, D., H. Grande, O. Miguel, E. Ochoteco, R. Marcilla, and I. Cantero, *Porous Polybenzimidazole Membranes Doped with Phosphoric Acid: Highly Proton-Conducting Solid Electrolytes*. Chemistry of Materials, 2004. **16**(4): p. 604-607.
116. He, R., Q. Li, G. Xiao, and N.J. Bjerrum, *Proton Conductivity of Phosphoric Acid Doped Polybenzimidazole and Its Composites with Inorganic Proton Conductors*. Journal of Membrane Science, 2003. **226**(1-2): p. 169-184.
117. Wainright, J.S., J.T. Wang, D. Weng, R.F. Savinell, and M. Litt, *Acid-Doped Polybenzimidazoles: A New Polymer Electrolyte*. Journal of the Electrochemical Society, 1995. **142**(7): p. 121-123.
118. Kamarudin, S.K., W.R.W. Daud, A. Md.Som, M.S. Takriff, and A.W. Mohammad, *Technical design and economic evaluation of a PEM fuel cell system* Journal of Power Sources, 2005. **157**(2): p. 641-649.
119. Tsuchiya, H. and O. Kobayashi, *Mass production cost of PEM fuel cell by learning curve* International Journal of Hydrogen Energy, 2003. **29**(10): p. 985-990.

120. Hogarth, M. and X. Glipa, *High Temperature Membranes for Solid Polymer Fuel Cells*, Department of Trade and Industry. 2001.
121. Lightner, V., *DOE Hydrogen Program Record*, D.H. Program, Editor. 2006.
122. Conti, A.B.L., A.R. Fragala, and J.R. Boyack, in *Proceedings of the Symposium on Electrode Materials and Processes for Energy Conversion and Storage*, D.E. McInyre, S. Srinivasan, and F.G. Will., Editors. 1977, The Electrochemical Society. p. 354.
123. Stucki, S., G.G. Sherer, S. Schlagowski, and E. Fischer, *PEM water electrolyzers: evidence for membrane failure in 100kW demonstration plants*. Journal of Applied Electrochemistry, 1998. **28**(10): p. 1041-1049.
124. Stanic, V. and M. Hoberecht, *Mechanism of pinhole formation in membrane electrode assemblies for PEM fuel cells*, in *Proton conducting membrane fuel cells IV*, M. Murthy, Editor. 2006, Electrochemical Society.
125. Bhamidipati, K.L. and Harris T. A. L. *Numerical Analysis of the Effects of Processing Conditions on The Casting Of High Temperature PEMFC Membrane Solutions*. in *Proceedings of FuelCell2009 Seventh International Fuel Cell Science, Engineering and Technology Conference*. 2009. Newport Beach, California, USA.
126. Liu, B., J.H. Chen, X.X. Zhong, K.Z. Cui, H.H. Zhou, and Y.F. Kuang, *Effect of inorganic particles on slot die coating of poly(vinyl alcohol) solutions*. Journal of Central South University of Technology, 2007. **14**(0): p. 386-388.
127. Bhamidipati, K.L., *Detection And Elimination of Defects During Manufacturing of High Temperature Polymer Electrolyte Membranes*, in *Ph.D. Proposal*. 2009, Georgia Tech: Atlanta, GA.
128. Bhamidipati, K.L. and T.A.L. Harris, *Numerical Simulation of a High Temperature Polymer Electrolyte Membrane Fabrication Process*. Journal of Fuel Cell Science and Technology, 2009.
129. Harris, T.A.L. and K.L. Bhamidipati, *Computational Modeling of a Polymer Electrolyte Membrane Fabrication Process*. ECS Transactions - 2007 Fuel Cell Seminar & Exposition, 2007. **12**(1): p. 251-262.
130. Gonzalez, R.C., R.E. Woods, and S.L. Eddins, *Digital Image Processing Using MATLAB 2nd Ed*. 2009: Gatesmark Publishing.
131. Otsu, N., *A Threshold Selection Method from Gray-Level Histograms*. IEEE Transactions on Systems, Man, and Cybernetics, 1979. **9**(1): p. 62-66.
132. MathWorks, *MATLAB*. 2009, The MathWorks: Cambridge, MA.

133. Witten, I.H. and E. Frank, *Data Mining: Practical machine learning tools and techniques, 2nd Edition*. 2005, San Francisco: Morgan Kaufmann.
134. Hall, M.A. and L.A. Smith. *Practical feature subset selection for machine learning*. in *Computer Science*. 1998. ACSC'98, Perth, 4-6 February 1998: Berlin: Springer.
135. Kohavi, R., *The Power of Decision Tables*, in *8th European Conference on Machine Learning*. 1995. p. 174-189.
136. Quinlan, R., *C4.5: Programs for Machine Learning*. 1993, San Mateo, CA: Morgan Kaufmann Publishers.
137. Ben-Gal, I., *Bayesian Networks*, in *Encyclopedia of Statistics in Quality & Reliability*, F. Ruggeri, F. Faltin, and R. Kenett, Editors. 2007, Wiley & Sons.
138. Rutkowski, L., *Neural networks and their learning algorithms*, in *Computational Intelligence*. 2008. p. 187-264.